

Transactions of the ASME®

Technical Editor, T. H. OKIISHI (1998)
Associate Technical Editors
Aeromechanical Interaction
R. E. KIELB (1996)
Gas Turbine
C. J. RUSSO (1995)
Heat Transfer
M. G. DUNN (1996)
Nuclear Engineering
H. H. CHUNG (1996)
Power
P. H. GILSON (1996)
Turbomachinery
N. A. CUMPSTY (1995)

BOARD ON COMMUNICATIONS
Chairman and Vice-President
R. D. ROCKE

Members-at-Large

T. BARLOW, N. H. CHAO, A. ERDMAN,
G. JOHNSON, L. KEER, W. MORGAN,
E. M. PATTON, S. PATULSKI, R. E. REDER,
S. ROHDE, R. SHAH, F. WHITE,
J. WHITEHEAD

OFFICERS OF THE ASME
President, P. J. TORPEY
Executive Director
D. L. BELDEN
Treasurer
R. A. BENNETT

PUBLISHING STAFF
Mng. Dir., Publ.,
CHARLES W. BEARDSLEY
Managing Editor,
CORNELIA MONAHAN
Sr. Production Editor,
VALERIE WINTERS
Production Assistant,
MARISOL ANDINO

Transactions of the ASME, *Journal of Turbomachinery* (ISSN 0889-504X) is published quarterly (Jan., Apr., July, Oct) for \$150.00 per year by The American Society of Mechanical Engineers, 345 East 47th Street, New York, NY 10017. Second class postage paid at New York, NY and additional mailing offices. POSTMASTER: Send address change to Transactions of the ASME, *Journal of Turbomachinery*, c/o THE AMERICAN SOCIETY OF MECHANICAL ENGINEERS, 22 Law Drive, Box 2300, Fairfield, NJ 07007-2300.

CHANGES OF ADDRESS must be received at Society headquarters seven weeks before they are to be effective. Please send old label and new address.

PRICES: To members, \$40.00, annually; to nonmembers, \$150.00.

Add \$24.00 for postage to countries outside the United States and Canada.

STATEMENT from By-Laws. The Society shall not be responsible for statements or opinions advanced in papers or printed in its publications (B7.1, Par. 3).

COPYRIGHT © 1995 by The American Society of Mechanical Engineers. Authorization to photocopy material for internal or personal use under circumstances not falling within the fair use provisions of the Copyright Act is granted by ASME to libraries and other users registered with the Copyright Clearance Center (CCC) Transactional Reporting Service provided that the base fee of \$3.00 per article is paid directly to CCC, 222 Rosewood Dr., Danvers, MA 01923. Request for special permission or bulk copying should be addressed to Reprints/Permission Department.

INDEXED by Applied Mechanics Reviews and Engineering Information, Inc. Canadian Goods & Services Tax Registration #126148048

Journal of Turbomachinery

Published Quarterly by The American Society of Mechanical Engineers

VOLUME 117 • NUMBER 2 • APRIL 1995

TECHNICAL PAPERS

- 205 Design and Development of an Advanced Two-Stage Centrifugal Compressor (94-GT-202)
D. L. Palmer and W. F. Waterman
- 213 A Simulation of the Unsteady Interaction of a Centrifugal Impeller With Its Vaned Diffuser: Flow Analysis (94-GT-105)
W. N. Dawes
- 223 Numerical Calculations of the Turbulent Flow Through a Controlled Diffusion Compressor Cascade
Shin-Hyoung Kang, Joon Sik Lee, Myung-Ryul Choi, and Kyung-Yup Kim
- 231 Experimental Investigation of the Flow in Diffusers Behind an Axial Flow Compressor (94-GT-347)
T. Zierer
- 240 Effects of Free-Stream Turbulence Intensity on a Boundary Layer Recovering From Concave Curvature Effects (93-GT-25)
M. D. Kestoras and T. W. Simon
- 248 *Darryl E. Metzger Memorial Session Paper:* Comparison of Calculated and Measured Heat Transfer Coefficients for Transonic and Supersonic Boundary-Layer Flows (94-GT-173)
C. Hürst, A. Schulz, and S. Wittig
- 255 Prediction of Turbulent Flow and Heat Transfer in a Ribbed Rectangular Duct With and Without Rotation (93-GT-206)
C. Prakash and R. Zerkle
- 265 Effect of Permeable Ribs on Heat Transfer and Friction in a Rectangular Channel (93-GT-301)
Jenn-Jiang Hwang and Tong-Miin Liou
- 272 Surface Heating Effect on Local Heat Transfer in a Rotating Two-Pass Square Channel With 60 deg Angled Rib Turbulators (93-GT-336)
Y. M. Zhang, J. C. Han, J. A. Parsons, and C. P. Lee
- 281 Experimental Study of the Effects of Bleed Holes on Heat Transfer and Pressure Drop in Trapezoidal Passages With Tapered Turbulators (93-GT-212)
M. E. Taslim, T. Li, and S. D. Spring
- 290 Detailed Heat Transfer Coefficient Measurements and Thermal Analysis at Engine Conditions of a Pedestal With Fillet Radii (93-GT-329)
Z. Wang, P. T. Ireland, and T. V. Jones
- 298 Flow Between Contrarotating Disks (93-GT-286)
X. Gan, M. Kilic, and J. M. Owen

ANNOUNCEMENTS

- 289 Change of address form for subscribers
- 306 Information for authors

Design and Development of an Advanced Two-Stage Centrifugal Compressor

D. L. Palmer

W. F. Waterman

AlliedSignal Engines,
Light Helicopter Turbine Engine Company,
Phoenix, AZ 85072

This paper describes the aeromechanical design and development of a 3.3 kg/s (7.3 lb/sec), 14:1 pressure ratio two-stage centrifugal compressor, which is used in the T800-LHT-800 helicopter engine. The design employs highly nonradial, splitter bladed impellers with swept leading edges and compact vaned diffusers to achieve high performance in a small and robust configuration. The development effort quantified the effects of impeller diffusion and passive inducer shroud bleed on surge margin as well as the effects of impeller loading on tip clearance sensitivity and the impact of sand erosion and shroud roughness on performance. The developed compressor exceeded its performance objectives with a minimum of 23 percent surge margin without variable geometry. The compressor provides a high-performance, rugged, low-cost configuration ideally suited for helicopter applications.

Introduction

Small turboshaft engines require high-pressure-ratio, high-efficiency compressors to provide low engine fuel consumption. However, being in a low-power class, these engines must be inexpensive to manufacture and operate, requiring that the compressor be a simple, rugged design having low parts count and ease of manufacture. Helicopter applications, especially military, are subjected to high levels of sand ingestion and inlet distortion, requiring a durable configuration with good surge margin. The compressor for these engines has traditionally been accomplished by either an axial-centrifugal or a two-stage centrifugal configuration.

Particularly in flow sizes less than 4.5 kg/s (10 lb/sec), engine and compressor sizing studies have indicated that the two-stage centrifugal compressor has several important advantages over an axial-centrifugal compressor:

- Good surge margin is achievable without use of variable geometry for steady-state operation, thereby reducing complexity, parts count, and manufacturing costs.
- Only two stages are required to achieve high pressure ratio (14:1 and greater) with good efficiency, again reducing complexity, parts count, and manufacturing costs.
- Greater blade thicknesses and rugged long chord blading improves foreign object damage (FOD) and sand erosion tolerance, thereby reducing overhaul costs.
- Reduced sensitivity to tip clearance can be achieved through low blade loading, thereby improving performance retention and reducing overhaul costs.

- High tolerance to inlet distortion is possible due to very low aspect ratio blading.

This paper describes the aeromechanical design and development of a 3.3 kg/s (7.3 lb/sec), 14:1 pressure ratio two-stage centrifugal compressor, which is used in the T800-LHT-800 helicopter engine (Fig. 1). The T800 is a 136 kg (300 lb), 895 kW (1200 hp) class engine developed for the U.S. Army by the Light Helicopter Turbine Engine Company (LHTEC), a partnership between Allison Engine Company and AlliedSignal Engines.

As shown in Fig. 1, this engine has a two-stage centrifugal compressor coupled to a two-stage gas-generator turbine with a two-stage fre shaft power turbine. The engine inlet is annular in nature and incorporates an integral inlet particle separator.

The compressor design employs highly nonradial, splitter bladed impellers with swept leading edges and compact vaned diffusers to achieve high performance in a small and robust configuration. The compressor development effort reported in this paper quantified the effects of impeller diffusion and passive inducer shroud bleed on surge margin as well as the effects of impeller loading on tip clearance sensitivity and the impact of sand erosion and shroud roughness on performance.

Compressor Design

Cycle analyses of turboshaft engines indicated that the following compressor design objectives would provide the required power with the improved fuel consumption desired:

- Pressure ratio = 14:1
- Referred flow = 3.3 kg/s (7.3 lb/sec)

Contributed by the International Gas Turbine Institute and presented at the 39th International Gas Turbine and Aeroengine Congress and Exposition, The Hague, The Netherlands, June 13-16, 1994. Manuscript received by the International Gas Turbine Institute February 18, 1994. Paper No. 94-GT-202. Associate Technical Editor: E. M. Greitzer.

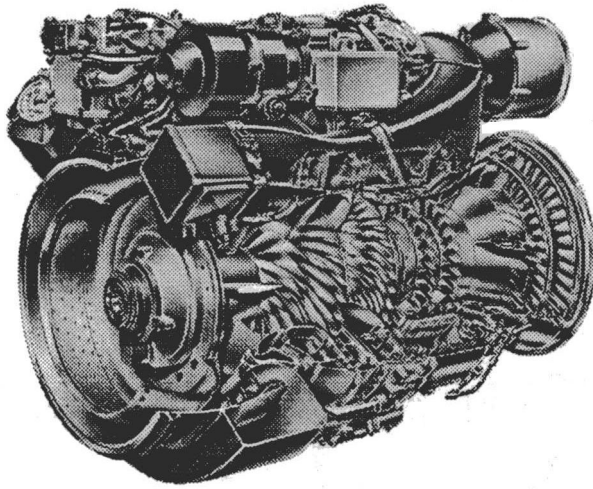


Fig. 1 The T800-LHT-800 engine

- Adiabatic efficiency > 0.80 (total-total including the inlet duct and rated to a combustor inlet Mach number of 0.15)
- Surge margin > 15 percent (constant speed)

Preliminary design studies of the compressor indicated that a rotational speed (corrected to compressor inlet conditions) of 43,800 rpm was necessary to achieve the compressor overall diameter and weight objectives (with acceptable turbine stresses) for the turboshaft engine applications. This speed, combined with a first-stage inducer hub-tip ratio of 0.51 and an inlet absolute Mach number of 0.52, results in an inlet tip relative Mach number of 1.37. The relatively high hub-tip ratio was selected for three reasons:

- To allow the largest blade count practical with integrally machined impellers for high efficiency
- To minimize upstream duct curvatures and diffusion for low losses (the upstream duct is included in the compressor rating)
- To permit a short bearing span in a configuration incorporating front end drive

The impeller inlet absolute Mach number was selected to minimize upstream duct diffusion when matched to an inlet particle separator.

High impeller backward curvature (approximately 47 deg) in both stages (Fig. 2) was used to improve efficiency through reduced impeller loading and to improve surge margin by providing a steeper, and therefore more stable, energy addition characteristic. The high impeller exit blade angles required a coordinated aeromechanical design effort, particularly for the first stage, to ensure acceptable blade aerodynamic loadings, stresses, and vibration characteristics.

High impeller blade count (14 main and 14 splitter blades) in the first stage was used to reduce blade loadings, thereby providing lower secondary flow losses and reduced sensitivity to tip clearance. To achieve high blade count while retaining low-cost manufacture, both impellers were designed with splitter blades. The blade surfaces were generated by straight-line elements, permitting the impellers to be integrally machined by flank milling with conical cutters on numerically controlled five-axis milling machines without encountering cutter tool interference with adjacent blading.

Because of the high inducer shroud Mach number on the first-stage impeller, blade angle distributions were selected to minimize inducer tip turning upstream of the throat, which, in conjunction with the high leading edge sweep, minimized shock losses and improved flow range [1]. The high specific speed of this stage would normally result in a significant inducer tangential lean, which causes high blade stresses.

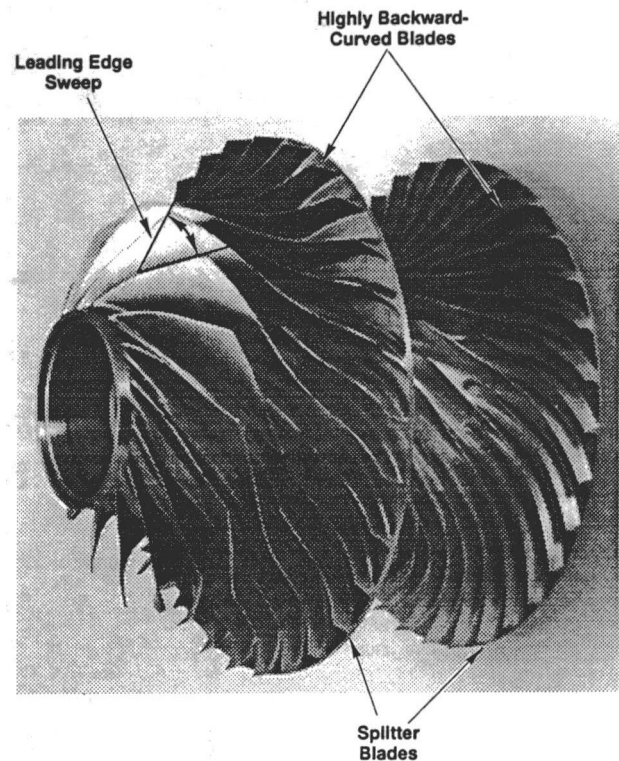


Fig. 2 Compressor rotating group illustrates impeller design philosophy

Constant Axial Plane Section at Inducer Tip

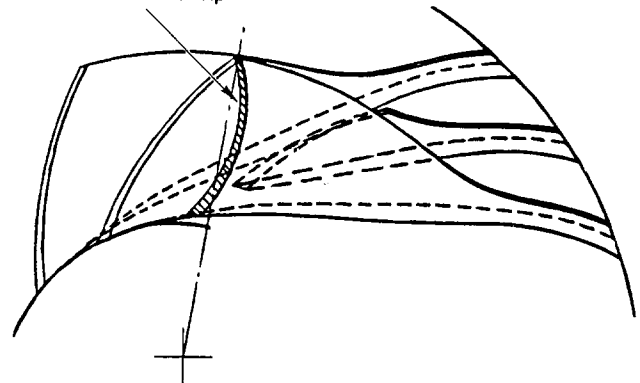


Fig. 3 Leading edge sweep minimizes inducer lean angles

However, by extending the leading edge hub ahead of the tip (i.e., adding leading edge sweep), these lean angles were significantly reduced, resulting in reduced stresses. The low inducer average lean angle is shown in a front view of the first-stage impeller (Fig. 3) with a cross section cut perpendicular to the axis of rotation through the inducer tip of the main blade. The resulting impeller blade stresses (Fig. 4) indicate a peak stress of 481 mPa (69.7 ksi) at the blade root, which is well below the allowable for forged titanium.

This design was accomplished prior to the availability of three-dimensional viscous analysis capabilities. Therefore, the impeller blade loadings were calculated using an axisymmetric radial equilibrium flow analysis for the meridional plane solution. Blade-to-blade analysis used the change in angular momentum through the impeller to calculate the surface relative Mach number distributions. Hub and tip loadings for the first-stage impeller are shown in Fig. 5. These loadings indicate that the primary diffusion is taken early in the impeller to minimize high-suction-surface Mach numbers,

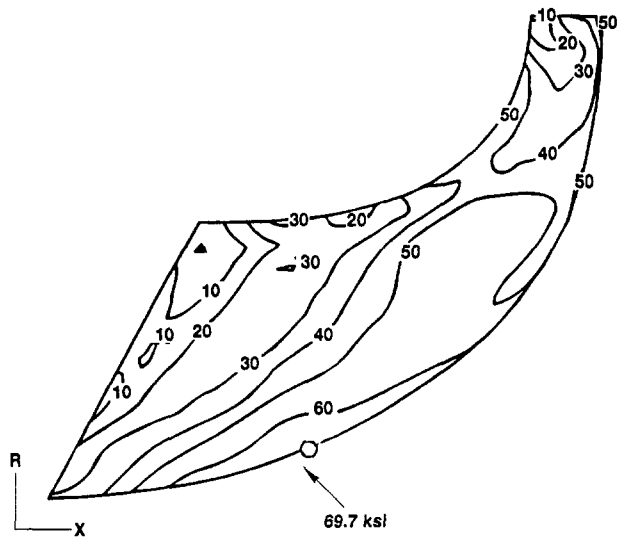


Fig. 4 Blade stresses are low due to low inducer lean angles

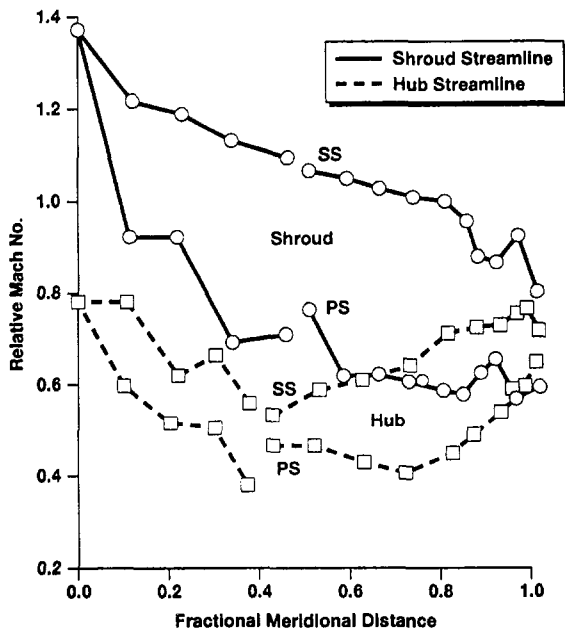


Fig. 5 First-stage impeller loadings indicate early diffusion and no over-velocity

shock losses, and resulting flow separation. Blade-to-blade loadings at the impeller exit are low as a result of using splitter blades. The splitter leading edges were positioned tangentially to minimize angle-of-attack losses as determined using an inviscid three-dimensional transonic flow analysis. As such, the splitters are not merely cut-off main blades.

To establish the choking flow capacity of the first-stage impeller and to verify the adequacy of the main and splitter blade designs, inviscid three-dimensional transonic flow analyses of the first-stage impeller were conducted using the method reported by Denton [2]. Results of this analysis at conditions just out of choke are shown in Fig. 6, which provides a view of the Mach number distributions on the suction surfaces of the main and splitter blades.

Two second-stage impeller designs were accomplished. The first design had 32 blades (16 main blades and 16 splitters) with a nearly uniform meridional distribution of blade loading.

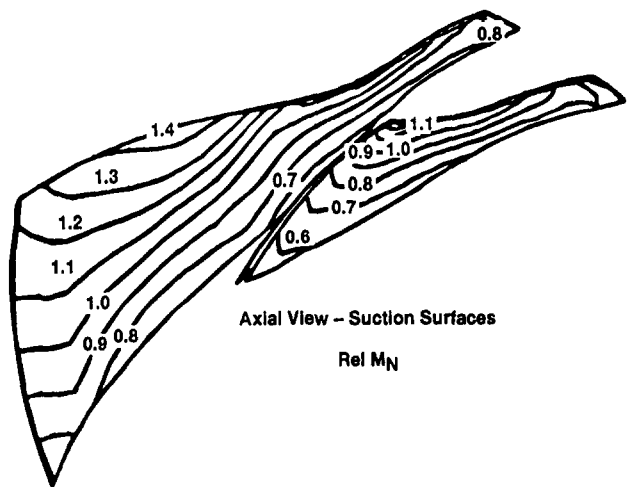


Fig. 6 Three-dimensional transonic analysis verifies flow capacity

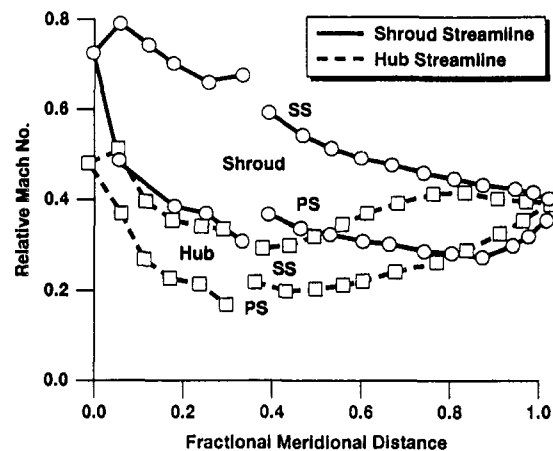


Fig. 7 Second-stage impeller has low exit loadings for clearance insensitivity

The major design goal of the other second-stage impeller was to reduce impeller exit loading significantly, since low loadings reduce sensitivity to axial clearance. Low loadings were achieved by designing for 38 blades at the exit (19 main blades and 19 splitters) using similar techniques as described for the first-stage impeller. In addition, impeller blade angles were configured to accomplish nearly all of the required diffusion ahead of the splitter to further reduce impeller exit loadings. These loadings, from the radial equilibrium analysis, are shown in Fig. 7 for both hub and shroud streamlines.

The compressor flowpath and diffusion system blading are shown in Fig. 8. To reduce the first-stage overall diameter to minimize weight, the first-stage diffuser uses sheet metal vanes and splitters to maximize diffusion in a small radial envelope. The first-stage diffuser splitter vane is positioned tangentially to maximize the recovery of the two adjacent channels with uniform exit static pressure. The vanes were made of steel for FOD and sand erosion resistance and ease of manufacture.

The crossover duct between the two stages consists of a 180-deg annular bend followed by a radial inflow deswirl vane system, which provides zero net swirl to the second-stage impeller. A small amount of bleed air is taken off at the slot ahead of the second-stage impeller to simulate turbine cooling requirements. Acceleration bleed at this point is also provided for rapid transient operation.

The second-stage diffuser is a conventional vane-island design with through bolts. It achieves high recovery through a

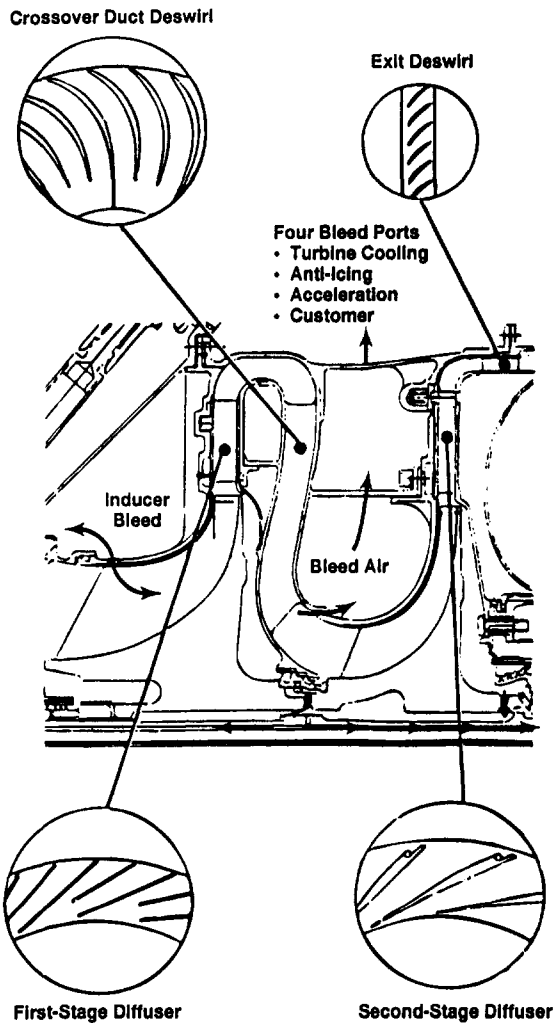


Fig. 8 Compressor stationary diffusion systems

high divergence angle, which is optimum for low-throat aspect ratios. Splitter vanes were not used because sufficient radial envelope was available to provide the required recovery with a more conventional design. This diffuser is followed by a 90-deg annular bend and an axial deswirl row, which reduces exit swirl to 30 deg and exit Mach number to 0.15 entering the combustor.

The compressor design and performance rating includes an upstream transition duct and five service struts. During early development, this duct included the re-entry slots for a first-stage impeller passive inducer shroud bleed system similar to that reported by Chapman [3] for single-stage centrifugal compressors. This system was developed for this two-stage centrifugal compressor during the rig test effort described below.

The initial passive inducer shroud bleed system, shown schematically in Fig. 9, allows communication of the first-stage inducer flow with the inlet duct. When operating at part speed, the impeller pressure at the bleed port location is higher than duct pressure; therefore, outflow occurs naturally (without controls) from the impeller. This outflow, which returns to the duct at the reentry slot, relieves inducer stall through natural low-flowing of the impeller and provides improvement in part-speed surge and efficiency (the recirculation occurs entirely within the compressor and losses are, therefore, properly accounted for in the compressor rating). At high speeds, the inducer approaches choke, resulting in a low pressure at the port location. This causes inflow to occur

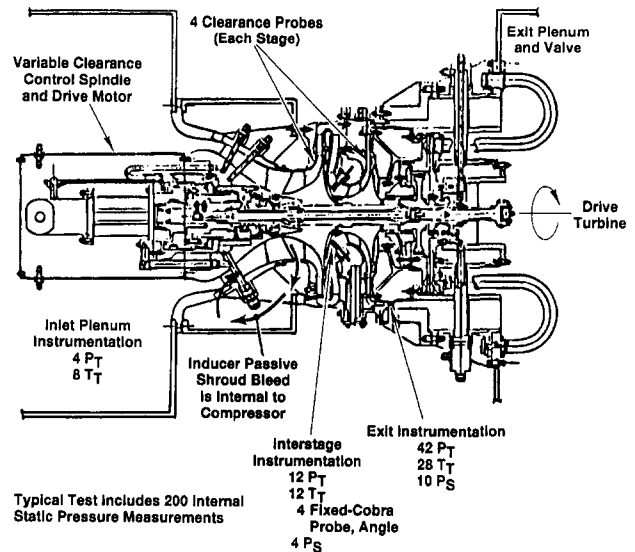


Fig. 9 Compressor test rig provided performance and diagnostic instrumentation

from the upstream duct, which reduces inducer choke losses with resultant increases in overspeed flow capacity and efficiency.

Compressor Development

Development testing of this compressor was conducted using the test rig shown in Fig. 9. This rig has a translating rotor group to control running axial tip clearances to match engine requirements. The rig can accept slip rings for strain gage testing, and a distortion generator can be attached upstream for pressure distortion testing.

Instrumentation for performance testing is also indicated on Fig. 9. This instrumentation allows measurement of individual stage and overall performance, as well as providing diagnostic measurements of component static pressure distributions. Clearance is monitored with capacitive-type clearance probes. Testing at several axial clearance levels was conducted to establish compressor performance sensitivities. At high speeds, surge data were taken at approximately 0.25 mm (0.010 in.) increased clearance to avoid rubs. Previous testing has demonstrated that the spatial position of the compressor surge line on the map is not affected by this magnitude of clearance change.

Significant development testing was conducted to optimize the performance and surge margin of the compressor. During this development effort, a number of important factors affecting compressor performance and surge margin were tested. These factors included the effects of:

- First-stage impeller diffusion on surge margin
- Inducer shroud bleed system on surge margin
- Axial clearance on compressor performance
- Blade loading on axial clearance sensitivity
- Second-stage shroud roughness on compressor performance
- Sand erosion on compressor performance

Baseline Test. This first test of the as-designed hardware served as the baseline for the development program. The baseline test map is shown in Fig. 10 along with a representative nominal engine operating line. Tip clearance testing during this build established clearance sensitivity for the original design second stage. This test showed good efficiency but was short of the objective surge margin at part speed.

Inducer Shroud Bleed. Since design point performance levels were close to objectives but surge margin was low,

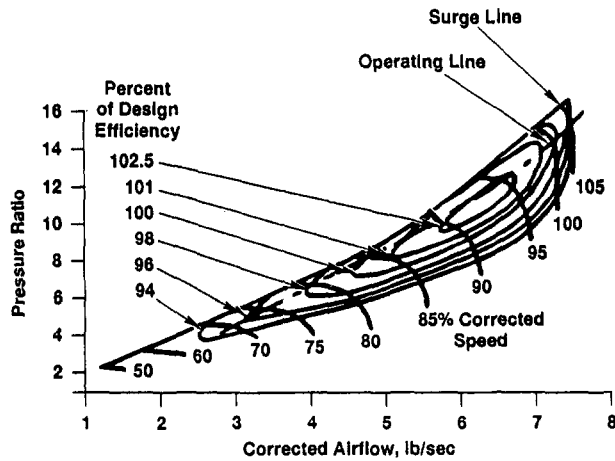


Fig. 10 Baseline compressor test is short of goal surge margin at part speed

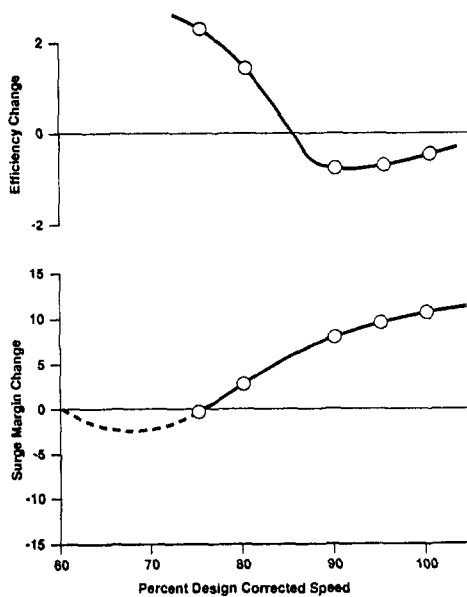


Fig. 11 Early shroud bleed configuration significantly improved surge margin over baseline

testing concentrated on surge margin improvement. Based on the work of Chapman and previous experience with passive inducer shroud bleed on two-stage centrifugal compressors, it was decided to incorporate such a concept for this two-stage centrifugal compressor. To facilitate changing the meridional position and area of the bleed ports along the first-stage impeller shroud, round holes through the shroud were used since they could readily be plugged or reduced in area as required.

This test used hardware from the baseline test with the first-stage inducer bleed system added. Tests were conducted with various hole positions and areas to optimize surge margin and performance. Inducer bleed flow was recirculated to the compressor inlet downstream of the inlet-measurement station, thereby accounting for all losses in the recirculation system. This testing showed that for an inducer bleed system using round bleed holes through the shroud, the best configuration consisted of a dual row of holes located in the throat region of the first-stage impeller.

Figure 11 shows the efficiency and surge margin test results for the dual row of holes compared to the baseline test. The following observations are made from this test:

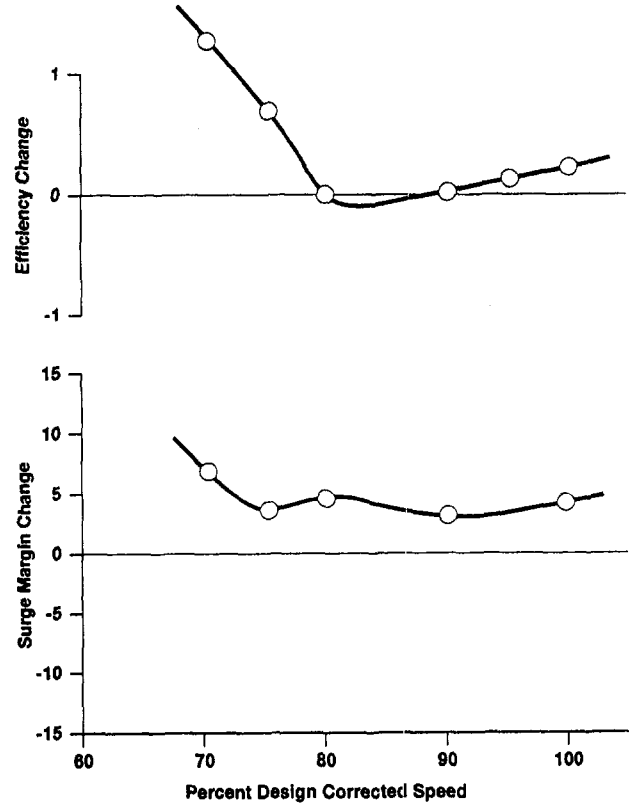


Fig. 12 Reduced first-stage impeller diffusion improved part-speed surge margin over baseline

- Surge margin above 80 percent speed was nearly doubled with the inducer bleed.
- High-speed choke flow was increased.
- Surge margin at 75 percent speed was reduced. Prior testing without the bleed system had shown that at this speed and below, the first-stage impeller inducer tip region is fully stalled, providing a stable internal recirculation. Under these conditions, adding a higher pressure drop external recirculation path actually reduces the recirculated flow and therefore the surge margin benefit.

Impeller Diffusion. This test was conducted to determine whether reduced first-stage impeller diffusion, achieved by reducing the first-stage impeller exit and diffuser passage heights, could improve surge margin without significant loss in high-speed performance. Results of this testing, compared to the baseline, are shown in Fig. 12. Again, improvements in surge margin above 80 percent speed were realized, although they were not as large as those achieved with the inducer bleed. Good high-speed performance was retained and no loss in surge margin occurred at 75 percent speed, as happened with the inducer bleed.

Shroud Roughness. Next, the redesigned second stage was introduced. This configuration is that described in the design section of this paper. At the same time, the second-stage shroud abradable coating material was changed, which resulted in a surface roughness of approximately $9.0 \mu\text{m}$ ($350 \mu\text{in.}$) compared to the previous configurations, which had a roughness of approximately $1.8 \mu\text{m}$ ($70 \mu\text{in.}$).

This test was conducted with the baseline first stage, the new design second stage, and the $9.0 \mu\text{m}$ ($350 \mu\text{in.}$) roughness second-stage impeller shroud. Overall performance was disappointingly low and, as a result, a study of surface roughness effects in centrifugal stages was undertaken. The objective was to determine whether the change in second-

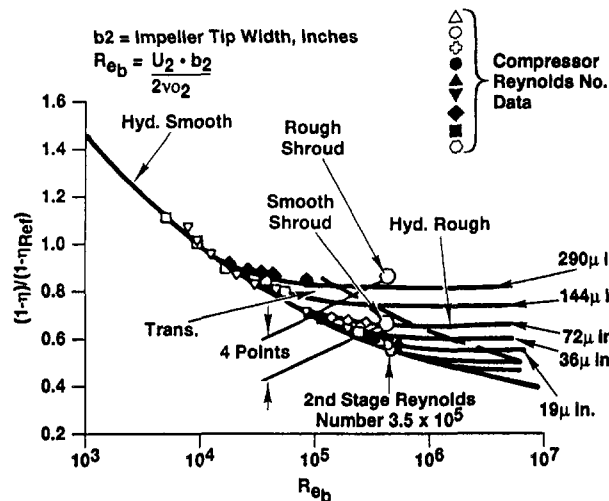


Fig. 13 Single-stage centrifugal compressor's loss versus roughness for 0.3 in. exit tip width

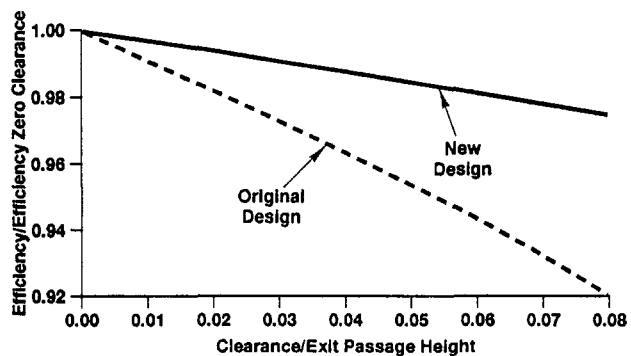


Fig. 14 Improved clearance sensitivity of the second-stage compressor by reduced blade loading

stage shroud roughness could account for the low performance observed on this test.

Using a pipe-flow analogy for a centrifugal stage, the characteristic length for similarity is the hydraulic diameter (which is nearly equal to the impeller exit tip width). On this basis, centrifugal compressor Reynolds number effects can be correlated, as shown in Fig. 13, which shows the effects of surface roughness at high Reynolds numbers. The Reynolds number of the second stage, operating in the two-stage compressor, is indicated on the figure ($Re_b = 3.5 \times 10^5$). As can be seen, the second stage lies in the hydraulically rough regime with a roughness of $9.0 \mu\text{m}$ ($350 \mu\text{in.}$) and in the transition region between hydraulically rough and hydraulically smooth with a roughness of $1.8 \mu\text{m}$ ($70 \mu\text{in.}$). The predicted change in second-stage efficiency for this change in roughness is 4.0 points, which converts to approximately 1.6 points in overall two-stage efficiency for the compressor.

As a result of this analysis, the second-stage shroud coating material was restored to that used previously and the compressor retested. An improvement of over 2.0 points in overall efficiency was obtained at the design point.

The sensitivity of the second stage to changes in impeller axial clearance was evaluated using the variable clearance feature of the compressor rig. Comparison of the clearance sensitivity of the original 16 main blade/splitter bladed second-stage impeller to the new design having 19 main blades/19 splitters is shown in Fig. 14. Clearly, the reduced impeller loadings due to increased blade count and revised blade angle distributions have had a significant effect on the

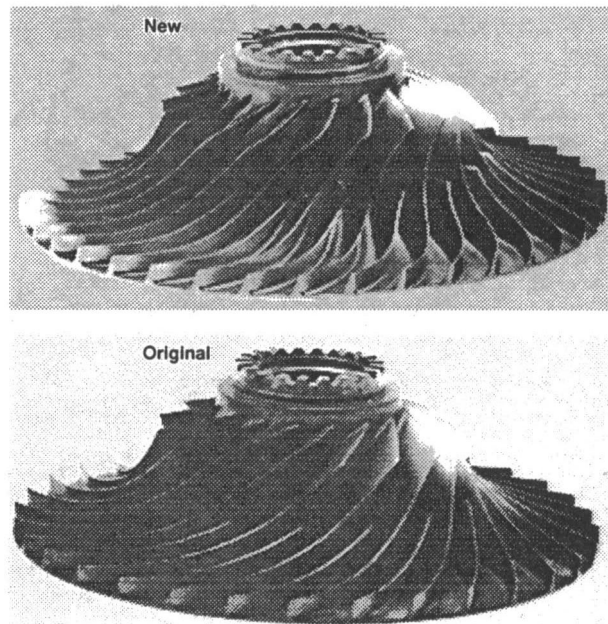


Fig. 15 Original and new second-stage impellers show revised blade angle distributions

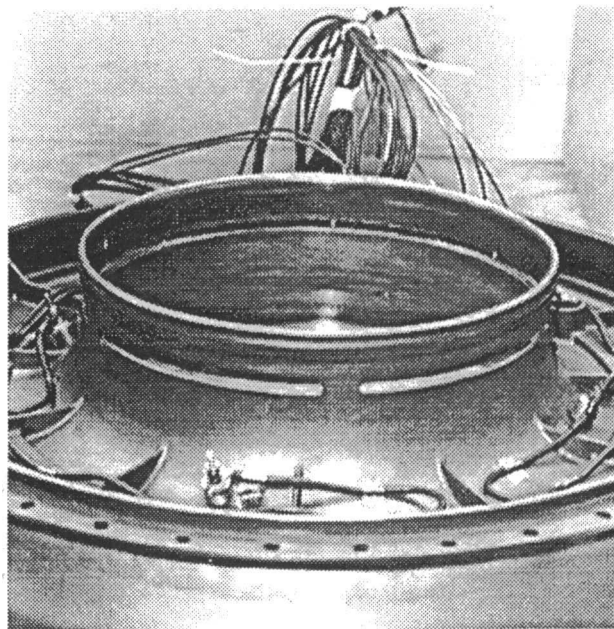


Fig. 16 Inducer bleed slotted shroud test configuration

rate of efficiency loss with increasing axial tip clearance. The low clearance sensitivity allows the second stage to operate efficiently at a robust 6 percent axial clearance needed for the extremely rapid helicopter acceleration requirements. Comparison of these impellers is made in Fig. 15.

Annular Shroud Slot Inducer Bleed. An annular slot inducer bleed configuration was also tested. The annular slot was located in a similar position on the first-stage impeller shroud as the dual row of round holes. The slot was approximately $2/3$ the area of the round hole configuration due to the expected higher flow coefficient of the slot. A photograph of the slotted shroud is shown in Fig. 16.

Comparative results of the two inducer bleed arrangements are shown in Fig. 17. These results indicate that the

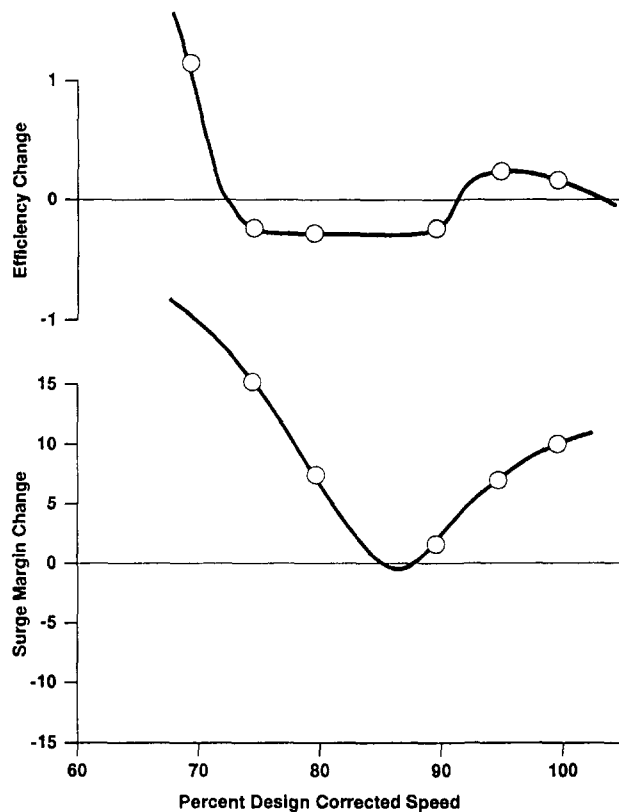


Fig. 17 Inducer bleed shroud slot improved surge margin over hole

annular bleed significantly improves surge margin over the dual hole configuration, particularly in the 70 to 85 percent speed region. The annular bleed design provided the compressor with a minimum of 13.5 percent surge margin over the entire steady-state operating region. However, detailed examination of the test data indicated that a modest re-matching of the first-stage diffuser would improve performance, particularly in the important part speed (80 to 90 percent) region. This was accomplished by reducing the first-stage diffuser vane height by 3 percent, converging the vaneless space, and reducing the diffuser throat and exit areas. This test resulted in the compressor achieving the efficiency objective and the minimum surge margin objective of 15 percent.

Overboard Venting of the Inducer Bleed. Additional testing was accomplished on an inducer bleed system with two changes: (1) The inducer bleed air was ducted outside of the engine, and (2) the impeller shroud slot area increased by 22 percent.

This configuration, used in the T800 qualification engines, yielded a large improvement in surge margin with a minimum of 23 percent and resulted in the map shown in Fig. 18.

Strain Gage Testing. Strain gage testing was conducted with 1, 2, 3, and 4/rev circumferential distortion patterns, and strain responses at critical locations on both the first- and second-stage impellers were measured. In no instance were the measured strains high enough to precipitate blade failures. Without distortion, strain responses were low enough that high-cycle-fatigue failures were not likely to occur even with FOD impellers simulated by stress concentration factors of three.

Sand Erosion. The T800 engine was also subjected to a 50-hour C-spec sand ingestion test, an AC-fine sand test, and

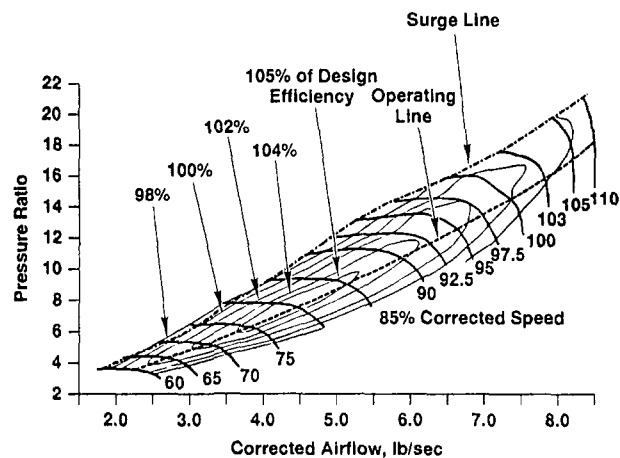


Fig. 18 T800 final compressor map with overboard inducer bleed achieves objectives

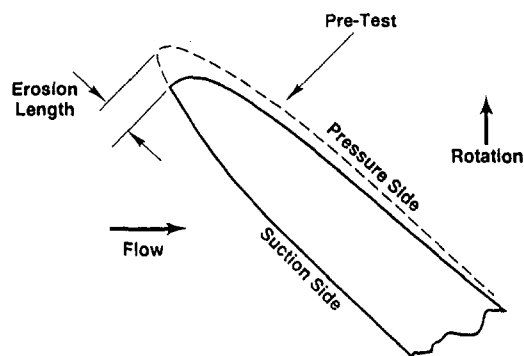


Fig. 19 First-stage impeller leading edge sand erosion

an AC-course sand test. The C-spec sand is generally considered to have the most potential for damage due to the high percentage of large particles. This test encompassed 50 hours of engine operation at maximum continuous rated power with sand contaminant introduced into the engine inlet at 53 mg per cubic meter of engine inlet air. Since the engine is equipped with an integral particle separator with a very high separation efficiency, most of the sand did not reach the compressor. However, approximately 10.8 kg (2.39 pounds) of sand went through the engine core.

Engine performance deterioration was only about 5 percent horsepower loss at 25 hours and 8.3 percent at 50 hours. Diagnostic analysis of the pre- and post-test data indicated the compressor efficiency was decreased 1.1 to 1.3 percent over the range of 85 to 100 percent speed and was the major cause of the engine performance loss.

Post-test inspection of the compressor hardware showed:

- The leading edges of the first-stage impeller blades were eroded back about 0.50 to 0.85 mm (0.020–0.034 in.), as shown in Fig. 19, with the higher value near the hub.
- A slight channel 0.38 mm (0.015 in.) deep on the pressure side of each blade and splitter at the exducer of the first-stage impeller
- An increase in roughness on the first-stage shroud abrasion coating
- No visual signs of second-stage impeller leading edge erosion were noted
- The second-stage shroud had a polished appearance
- Only minor evidence of erosion was noted on the first- and second-stage diffusers and deswirl assembly.

Conclusions

The design and development work described in this paper has shown that a high-pressure-ratio, two-stage centrifugal compressor is capable of high performance and that good surge margin and distortion tolerance, necessary for helicopter applications, can be achieved without resorting to variable geometry.

The passive inducer bleed concept was shown to improve surge margin, and part-speed and overspeed performance. In addition, the concept also improved the already exceptional pressure distortion tolerance of this compressor configuration as described by Cousins et al. [4, 5].

Development testing also showed that:

- First-stage impeller diffusion levels impact surge margin
- Shroud roughness of high-pressure centrifugal stages has a significant effect on performance
- Tip clearance sensitivity can be reduced with lower blade loadings

The developed T800 compressor provides a fully defined,

high-performance, and robust configuration ideally suited for helicopter applications.

References

- 1 Wennerstrom, A. J., and Puterbaugh, S. L., "A Three-Dimensional Model for the Prediction of Shock Losses in Compressor Blade Rows," *ASME Journal of Engineering for Gas Turbines and Power*, Vol. 106, 1984, pp. 295–299.
- 2 Denton, J., "An Improved Time-Marching Method for Turbomachinery Flow Calculation," *ASME Journal of Engineering for Gas Turbines and Power*, Vol. 105, 1983, pp. 514–524.
- 3 Chapman, D. C., "Model 250-C30/C281 Compressor Development," *AGAED Compressor Proceedings No. 282, Centrifugal Compressors, Flow Phenomenon, and Performance*, May 1980.
- 4 Cousins, W. T., Dalton, K. K., Andersen, T. T., and Bobula, G. A., "Pressure and Temperature Distortion Testing of a Two-Stage Centrifugal Compressor," *ASME Journal of Engineering for Gas Turbines and Power*, Vol. 116, 1994, pp. 567–573.
- 5 Cousins, W. T., Miller, R. E., and Dalton, K. K., "Distortion Tolerance of the T800-LHT-800 Turboshift Engine," *Proceedings, American Helicopter Society 47th Annual Forum and Technology Display*, Vol. 2 (A92-14326 03-01), 1992, pp. 1147–1155.

A Simulation of the Unsteady Interaction of a Centrifugal Impeller With Its Vaned Diffuser: Flow Analysis

W. N. Dawes

Whittle Laboratory,
Cambridge, United Kingdom

The aim of this paper is to help advance our understanding of the complex, three-dimensional, unsteady flow associated with the interaction of a splintered centrifugal impeller and its vaned diffuser. A time-resolved simulation is presented of the Krain stage performed using a time-accurate, three-dimensional, unstructured mesh, solution-adaptive Navier–Stokes solver. The predicted flowfield, compared with experiment where available, displays a complex, unsteady interaction, especially in the neighborhood of the diffuser entry zone, which experiences large periodic flow unsteadiness. Downstream of the throat, although the magnitude of this unsteadiness diminishes rapidly, the flow has a highly distorted three-dimensional character. The loss levels in the diffuser are then investigated to try and determine how time-mean loss levels compare with the levels expected from “equivalent” steady flow analysis performed by using the circumferentially averaged exit flow from the impeller as inlet to the diffuser. It is concluded that little loss could be attributed directly to unsteady effects but rather that the principal cause of the rather high loss levels observed in the diffuser is the strong spanwise distortion in swirl angle at inlet, which initiates a strong hub/corner stall.

Introduction

The performance of a centrifugal impeller is often very good, but when the wheel is combined with a vaned diffuser the performance of the overall stage is often disappointing. The diffuser performance is known to be very sensitive to inlet blockage distribution and distortion and so it seems likely that the performance of the diffuser is adversely affected by the jet-wake phenomena emerging from the wheel. The extent to which this performance degradation is due to unsteady interactions or to the time-mean axially distorted inlet flow is not known.

An experimental study of the nature of impeller–vaned diffuser interaction was published by Krain (1981). Substantial periodic flow unsteadiness was observed in the entry zone to the vaned diffuser with large temporal variations of swirl angle, of the order of 10–15 deg, and large spanwise variations from hub to shroud, of the order of 20–25 deg. However, and perhaps because the diffuser inlet Mach numbers were not supersonic, the presence of the vaned diffuser was observed to cause little unsteady variation in the impeller internal flow. In a subsequent lecture Krain (1984) presented

some measurements downstream of the diffuser vane throat, which showed that despite the large periodic unsteadiness in the entry zone, levels of unsteadiness decreased rapidly downstream of the throat.

Inoue (1980) published a similar study, albeit for a much more lightly loaded stage than that of Krain and with a lower solidity diffuser, and found the same large periodic flow unsteadiness in the diffuser vane entry zone. He too found that the magnitude of this periodic unsteadiness diminished rapidly downstream of the throat so that in the outer part of the diffuser no periodic unsteadiness could be observed.

In neither study did the impeller flow mix out before arriving at the diffuser vane leading edges as is sometimes assumed in design (see for example Johnston and Dean, 1966). For vaneless diffusers Senoo et al. (1977) report that spanwise (hub–tip) distortions mix out less rapidly than circumferential distortions and there is a suggestion that this is true also for vaned diffusers in both Krain’s and Inoue’s work. In any case this calls into doubt much of the current basis for design of vaned diffusers.

The purpose of this paper is to help advance our understanding of this complex flow by presenting a time-resolved simulation of the Krain splintered centrifugal impeller–vaned diffuser interaction using a time-accurate three-dimensional unstructured mesh, solution-adaptive Navier–Stokes solver. The predicted flowfield, compared with experiment where

Contributed by the International Gas Turbine Institute and presented at the 39th International Gas Turbine and Aeroengine Congress and Exposition, The Hague, The Netherlands, June 13–16, 1994. Manuscript received by the International Gas Turbine Institute February 4, 1994. Paper No. 94-GT-105. Associate Technical Editor: E. M. Greitzer.

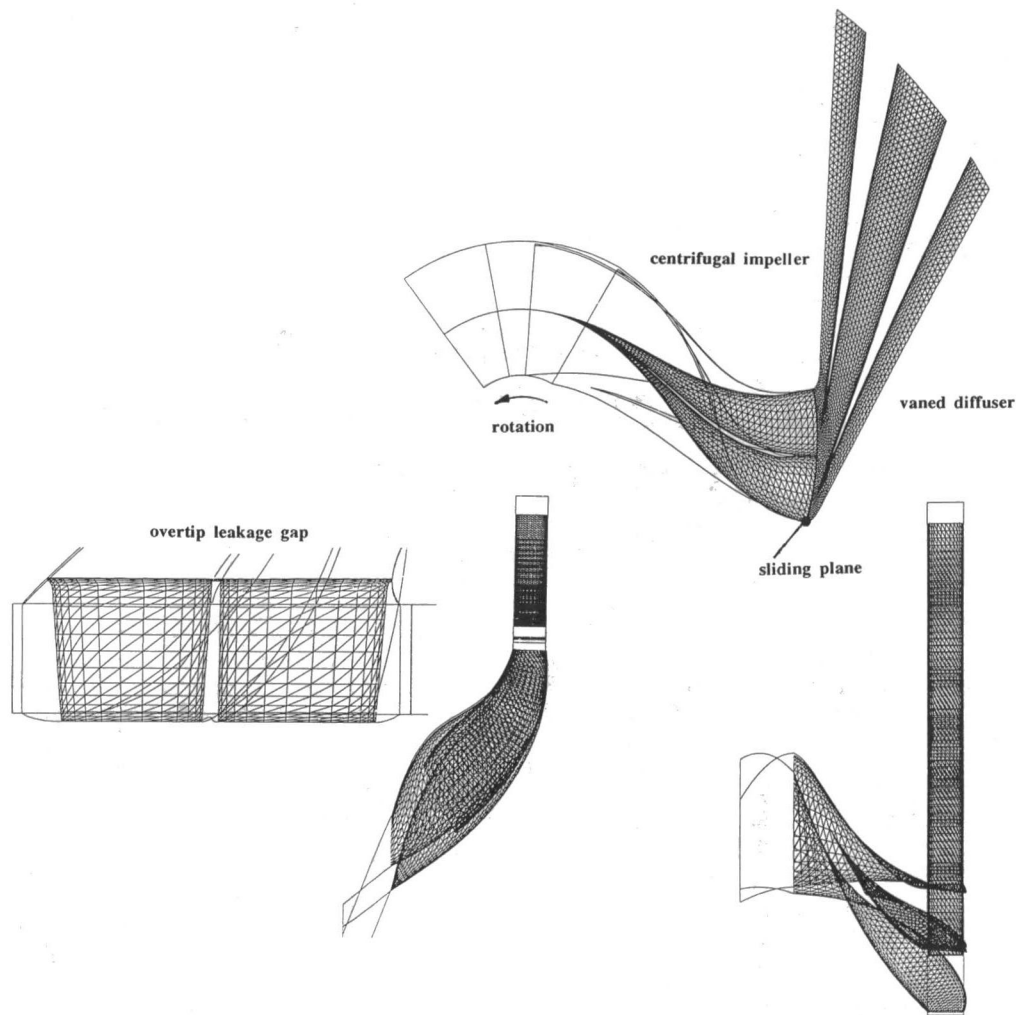


Fig. 1 The unstructured mesh generated for the splattered centrifugal impeller-vaned diffuser stage

available, confirms a complex, unsteady interaction especially in the neighborhood of the diffuser leading edges and a highly distorted three-dimensional flow downstream of the diffuser throat. The loss levels in the diffuser are then investigated to try and determine how time-mean loss levels compare with the levels expected from "equivalent" steady flow analysis performed by using the circumferentially averaged exit flow from the impeller as inlet to the diffuser.

Numerical Approach

Equations of Motion. The equations solved are the fully three-dimensional unsteady, compressible, Reynolds-averaged, Navier-Stokes equations expressed in strong conservation form. The full stress tensor is retained, including the full viscous energy equation. Turbulence is modeled via $k-\epsilon$

transport equations (Patel et al., 1985) together with appropriate low-Reynolds-number terms (Lam and Bremhorst, 1981) to handle smoothly the approach to the blade surfaces should the mesh be sufficiently fine. The application to mixed rotating-stationary frames is greatly eased if the equations are cast in the absolute frame and this is done here. This necessitates detail changes to impermeable surface boundary conditions but otherwise presents no analytic or algorithmic difficulty.

Mesh. An unstructured mesh system was adopted consisting of a set of tetrahedra. The generation of the mesh is based on a simple multiblock procedure described in detail by Dawes (1993a). The mesh generated for the subject of the present study, a splattered centrifugal impeller followed by a vaned diffuser, is shown in Fig. 1. This initial mesh contained

Nomenclature

PO1 = impeller inlet absolute stagnation pressure
 PS = pressure side of passage
 SS = suction side of passage
 t = time

T = periodic time; static temperature
 U = wheel speed
 V = total velocity
 α = absolute swirl angle referenced to the meridional direction

Subscripts

mer = meridional
 rms = root mean square
 2 = wheel exit

Superscripts

\sim = time mean value
 $'$ = instantaneous time mean value

around 100,000 nodes; for these exploratory simulations advantage was not taken of the solution-adaptive capability. It is recognized that the number of nodes is rather low but nevertheless effected a good compromise between accuracy and solution time. Solutions obtained in the past with on the order of 40,000 nodes per blade element (for example Krain and Hoffman, 1989) have been able to capture sufficient flow physics and be in sufficiently good agreement with data to make the exercise worthwhile.

During the simulation the impeller mesh rotates at a specified rate while the diffuser mesh remains fixed. Once the impeller has rotated through whatever is the periodic unit, the whole mesh is then indexed back and the rotation restarted. The surface between the rotating and stationary frames is referred to as the "sliding surface." The flow variables must be interpolated across this sliding surface each time step during the simulation. To ensure conservation, a volume-weighted interpolation procedure is adopted. This type of moving-to-fixed block interpolation is well known and described in more detail by Rai (1985) and Rao and Delancy (1990), among others. It must be stressed that the sliding surface is intended to act as a transparent internal boundary between the rotating and stationary frames transferring any axial and circumferential distortions in the flow *without* modification; circumferential averaging is *not* employed to mix out the flow across the sliding surface.

The strategy in the current approach is to model the nearest convenient integer multiple of blades in the impeller and diffuser. In this case it meant matching 14 impeller blades plus 14 splitter blades to 28 diffuser vanes (instead of the 27 in the true geometry). This strategy was adopted because of its simplicity and the advantages with respect to convergence rate and solution and postprocessing storage requirements when compared with the other available methods of handling noninteger blade ratios. In particular, the "time-tilting" method of Giles (1990) has a limited range of applicability and in practical use has to be supplemented by computing an integer ratio of blades but the solution then has to be reconstructed by Fourier analysis of a large number of storage-intensive solution levels throughout the cycle; the phase-shifted periodic boundary method of Erdos (see Hodson, 1985) leads to slow convergence rates and again to unacceptably large storage requirements for three-dimensional simulations.

The Solution Algorithm. The solution algorithm will be described here only in outline; for further details see Dawes (1992, 1993a, b). The seven equations of motion are discretized in finite volume form on each of the tetrahedral control volumes with vertex variable storage. The primary variables are assumed to have a piecewise linear variation over cell faces between the vertices so that the flux sum for a given cell is evaluated to second-order accuracy in space. The derivative terms in the viscous stresses are piecewise constant over the cell (since the primary variables are piecewise linear) and are computed by simple application of the Gauss divergence theorem. Using all the cells surrounding each individual node as a control volume then allows the evaluation of the viscous stress terms at that node. Artificial diffusion is added to control shock capture and solution decoupling. The smoothing consists of a classical blend of fourth derivatives as a general background and second derivative terms controlled in magnitude by the local strength of the pressure gradient.

At inflow boundaries the total pressure, total temperature, turbulent kinetic energy and dissipation rate, and two flow angles are specified and the derivative of static pressure in the streamwise direction set to zero; at the outflow boundaries the static pressure is specified and the other variables extrapolated from the interior. At present the inflow bound-

ary is not treated in a truly nonreflecting manner; however, the outflow uses a simple one-dimensional nonreflecting treatment based on the work of Giles (1988, 1990). On solid surfaces zero normal fluxes of mass, momentum, and energy are imposed. The wall shear stress can be computed either from the laminar sublayer or log law wall functions depending on whether the local value of the wall coordinate Y^+ is less than or greater than 10, respectively. Similarly the wall heat flux can be computed either from the wall normal temperature derivative if Y^+ is less than 10 or from a wall function based on Reynolds analogy. In a similar spirit if Y^+ is less than 10 the turbulent kinetic energy and the normal gradient of dissipation rate are set to zero on the surface; otherwise k and ϵ are set to be consistent with the assumed log law at values of $u_w^2/\sqrt{c_1}$ and $u_w^3/\kappa Y_w$, respectively, with Y_w the normal distance to the wall. For the present simulations the relative coarseness of the mesh means that wall Y^+ values were in the range 30 to 70 and so all viscous boundary conditions were implemented via the various wall functions.

The net flux imbalance into each cell is used to update the flow variables themselves via a four-step Runge-Kutta time marching algorithm with residual smoothing inspired by the pioneering work of Jameson and Baker (1987). Standard fractional step coefficients of 1/4, 1/3, 1/2, and 1 are used, conferring second-order time accuracy (fourth-order for linear equations). Residual smoothing (Jameson and Baker, 1987) is applied after each fractional step to extend the stability domain of the algorithm. For calculations with a steady-state solution as the objective the algorithm is run with spatially varying time steps (i.e., a constant CFL number imposed everywhere) and correspondingly with a spatially constant residual smoothing coefficient selected. Clearly, unsteady simulations must use a spatially constant time step, which will invariably be limited by the very fine mesh in the viscous-dominated regions near wetted surfaces. To alleviate this limit and make numerical simulation practical, a spatially varying residual smoothing is used, as suggested by Jorgenson and Chima (1989), which has the effect that in the inviscid part of the flow no residual smoothing is used and the algorithm reduces to a simple explicit time accurate integration. In the viscous-dominated regions near wetted surfaces the allowable time step is increased substantially beyond the local explicit limit; nevertheless the formal second-order temporal accuracy is not disrupted provided the magnitude of the residual smoothing coefficient is carefully controlled.

As well as interpolating the basic flow variables across the "sliding surface" between the rotating impeller mesh and the stationary diffuser mesh as described earlier, all the fluxes, viscous stress terms, and artificial smoothing terms are also interpolated in an attempt to ensure no loss of time accuracy across this interior boundary.

Postprocessing. To aid the interpretation of the unsteady simulation certain unsteady statistics are extracted:

$$\text{time-average } \bar{D} = \frac{1}{N} \sum_n^{n+N} D(n)$$

$$\text{rms fluctuation } D_{\text{rms}} = \sqrt{\left[\frac{1}{N} \sum_n^{n+N} \{D(n) - \bar{D}\}^2 \right]}$$

where $D(n)$ is the instantaneous value at time step n of a selected variable, D , and N the number of time steps in a period. Thus plots can be made of instantaneous values, either averaged quantity or the (instantaneous-averaged) value at a selected instant during the simulation.

The averages are extracted on the fly as the computation proceeds such that during a given period the current time average is that from the previous period and the current rms

fluctuation is based on the instantaneous values in the previous period and the time average of the next previous period. Limitations of computer storage have prevented the accumulation of ensemble averages.

Application to the Centrifugal Impeller-Vaned Diffuser Simulation

Background. The pioneering paper by Krain (1981) seems to contain the only public-domain stage geometry and experimental data concerning centrifugal impeller–vaned diffuser interaction. The geometry he studied consisted of a split-tered, radial discharge impeller, with 14 main blades and 14 splitter blades, together with a straight channel diffuser containing 27 blades. The key details of the vaned diffuser’s geometry are:

Radius ratio of diffuser LE/impeller exit	1.1
Radius ratio of diffuser discharge/impeller exit	1.905
Throat aspect ratio	1.6
Length/width ratio of the channel diffuser	11.46
Channel divergence angle	7.54 deg
Diffuser vein stagger angle	17.32 deg

Detailed measurements were made at the DFVLR using laser-two-focus velocimetry within the impeller and diffuser vane entry zone at the following operating point:

Rotational speed	14,000 rpm
Mass flow	5.8 kg/s
Total–total pressure ratio (nominal)	2.

The unstructured mesh generated for the present numerical simulation was shown in Fig. 1. For economy the number of diffuser blades was increased to 28 to allow a periodic unit of one main impeller blade per two diffuser vanes; the alternative of modeling the entire annulus was considered excessive for a preliminary study of this nature. The impeller overtip leakage gap was not known; nominal clearances are 1.1 mm at zero rpm and 0.2 mm at 22,500 rpm (Krain, 1993). Assuming that clearance scales with rotational speed squared (which might be true for radial clearance but not necessarily for the axial clearance at the impeller exit) suggested setting the clearance to 0.8 mm for the simulations and this was done with three nodes across the gap. The resulting mesh contains roughly 100,000 nodes and with the maximum CFL number set to around 3 required of order 1000 time steps per periodic blade passing scale. The code was run on a simple IBM RISC/6000 workstation at a processing rate of around 0.8 ms/node/time step. The boundary conditions to the simulation consisted of the rpm, inlet boundary conditions to the impeller, and the diffuser exit static pressure. Some difficulty was experienced in finding a matched operating point, nevertheless the following:

Rotational speed	14,000 rpm
Mass flow	5.6 kg/s
Static–total pressure ratio	1.70
Total–total pressure ratio	1.85
Total–total stage efficiency	71.2 percent

was predicted to be a converged, periodic solution. Convergence was judged by monitoring velocity levels in the most sensitive part of the flowfield—the diffuser leading edge. Figure 2 shows the variation with time from the start of the simulation of predicted velocities in midpitch of the diffuser vane leading edge plane at 10, 50, and 90 percent span. About 14 blade passing periods were required to produce a solution judged to be acceptably periodic over the last three to four cycles.

The Impeller Flow. The predicted impeller flow exhibits, by the exit from the blading, the expected development of

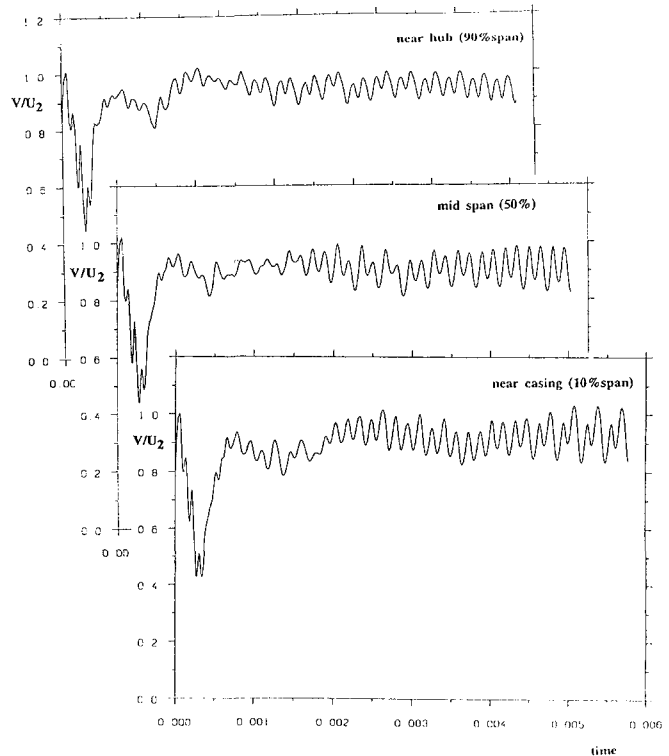


Fig. 2 Variation with time of predicted velocities in midpitch of the diffuser vane leading edge at 10, 50, and 90 percent span

the jet-wake structure. Figure 3 summarizes the rotor flow by showing predicted time-averaged relative velocity vectors near the casing, predicted time-averaged midpassage relative Mach numbers and a comparison of predicted and measured time-averaged meridional velocities in a crossflow plane toward the wheel exit at 87 percent of the streamwise distance through it. The predicted wake is slightly larger and pushed somewhat further over to the suction sides of the passages than in the measurements; the wake depth is nevertheless well represented. Clearly, a finer mesh and more sophisticated turbulence modeling might reduce these discrepancies somewhat. Nevertheless, in the context of the current effort aimed at advancing our understanding of the flow physics, the predicted wake structure was judged acceptable, particularly as the wake deficit itself was well predicted, and it is primarily this that produces the expected velocity and flow angle variations in the diffuser entry zone.

To assess the level of unsteadiness induced in the impeller by the interaction with the diffuser, the rms-averaged static pressure fluctuation was derived. It was found that the majority of the impeller experienced very low levels of periodic flow fluctuation except over the last 10 percent of the flow passage toward the suction side, where the rms pressure fluctuations were of order 5 percent of the local time-mean level. This lack of influence of the diffuser on the impeller was observed by Krain (1981) who measured very similar meridional velocity distributions in the 87 percent meridional distance plane when the impeller was tested both with and without the diffuser.

The Flow in the Vaned Diffuser; the Entry Zone. Next the flowfield in the “entry zone” of the vaned diffuser (i.e., the zone from impeller discharge to diffuser throat) will be considered. The jet-wake discharge from the impeller sweeps periodically over the diffuser and induces a very strongly varying, periodic flow in the entry zone.

The variation with time of predicted meridional velocity at midpitch of the diffuser vane leading edge plane is compared

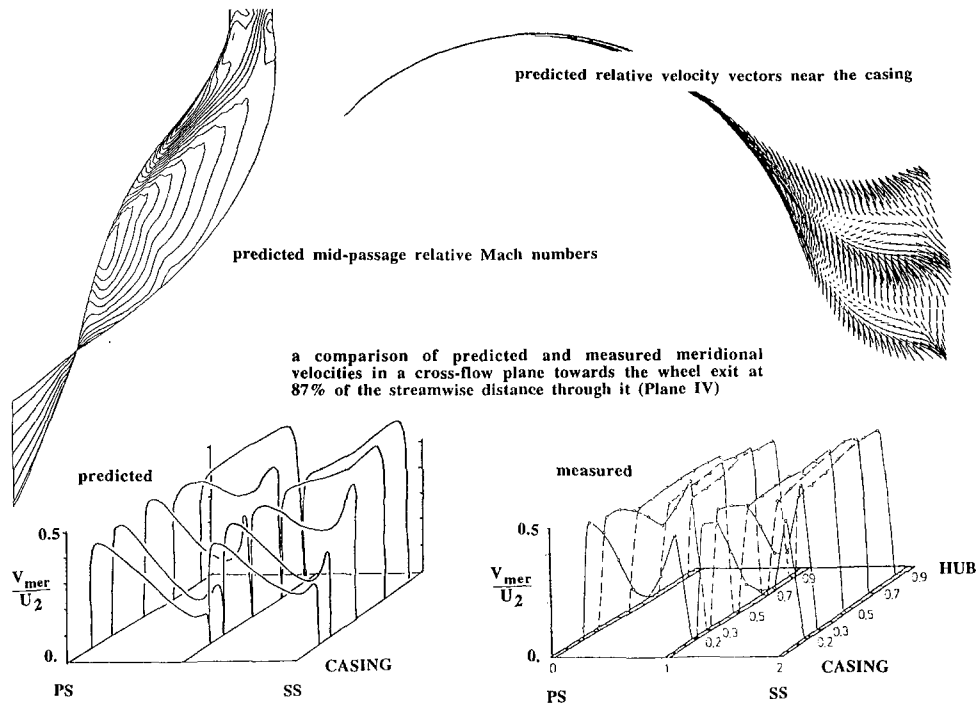


Fig. 3 A summary of the rotor flow showing the development of the jet-wake

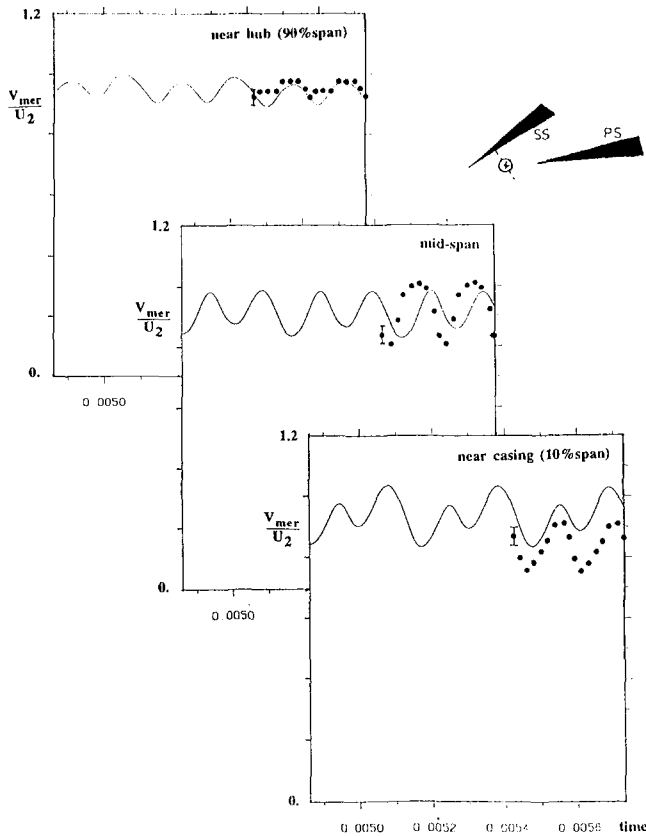


Fig. 4 The variation with time of predicted meridional velocity at midpitch of the diffuser vane leading edge plane compared with measurements (line = prediction; symbol = experiment)

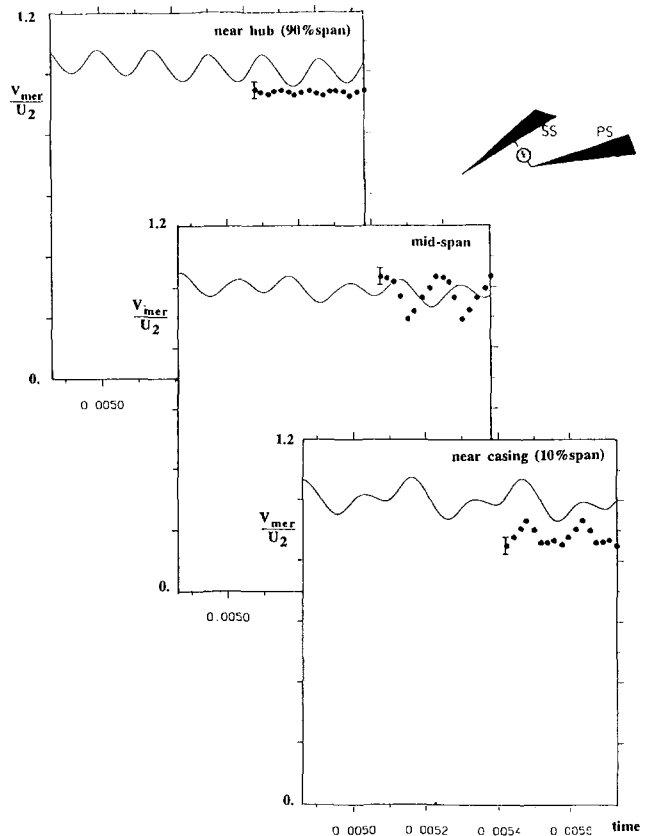


Fig. 5 The variation with time of predicted meridional velocity at midpitch of the diffuser vane throat plane compared with measurements (line = prediction; symbol = experiment)

with Krain's laser measurements in Fig. 4 for about three periodic time scales. The amplitude of the periodic variation is very large: around ± 5 percent near the hub but nearer ± 10 percent at midspan and near the casing. The agreement between predicted and measured amplitude is good. The Krain data have been ensemble averaged over 28 blades

whereas in fact the flow emerging from the two different passages of the impeller is not identical (see Fig. 3) and so the correct time scale for averaging should have been that associated with the number of main blades, i.e., 14 blades. In terms of phase, the agreement between prediction and measurement near the hub and near the casing is also good. In

midspan there is a small phase shift between the predicted and measured variations and this is associated with the slightly different locations of the wake in the prediction and the experiment discussed in the previous section.

Figure 5 shows the variations with time of predicted meridional velocity at midpitch of the diffuser vane throat plane and compares them with Krain's measurements. The flow is still strongly periodic in the diffuser throat in terms of blade passing time scales but the amplitudes of the variations are noticeably reduced. At midspan and near the casing the

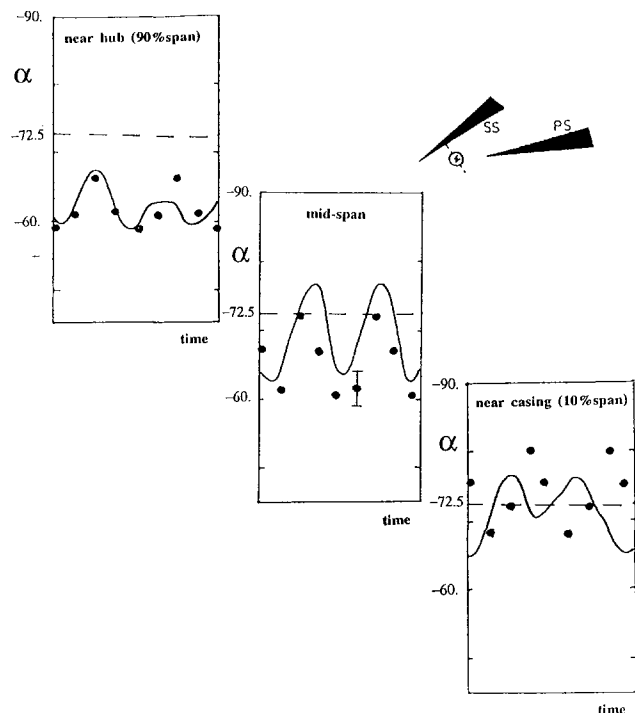


Fig. 6 The variation with time of predicted swirl angle at midpitch of the diffuser vane leading edge plane compared with measurements (line = prediction; symbol = experiment)

predicted amplitude agrees well with that measured, although there is disagreement over the mean level of meridional velocity near the casing and the midspan phase shift referred to earlier still persists. The only serious discrepancy between measurement and prediction is near the hub; the reason for this has not yet been determined but is believed to be associated with uncertainty as to the precise location of the onset of the highly three-dimensional distorted flow in the diffuser downstream of the throat (to be described in the next section). The noticeable phase shifts between all the data in the throat when compared with the corresponding locations in the vane leading edge plane are simply associated with the time taken for the phenomena to convect from one location to the next.

Associated with the substantial periodic variations of meridional velocity described above are large variations of the absolute swirl angle at diffuser entry. Figure 6 plots the variations with time of predicted swirl angle at midpitch of the diffuser vane leading edge plane compared with Krain's measurements. The amplitude of the angle variation is very large, being as high as ± 7 deg in midspan and around ± 5 deg near the hub and the casing. The agreement between prediction and measurement is good near the casing and in midspan and fair near the hub. It is very noticeable both in the predictions and the measurements that considerable flow angle variations exist from hub to casing. Near the casing the flow vector has a mean angle roughly equal to the blade inlet angle; in midspan the mean angle corresponds to around 5 deg negative incidence (i.e., flow direction closer to radial) onto the vanes; and near the hub the mean incidence angle is about 10 deg negative incidence. These are large flow incidences for vanes such as these, with very sharp leading edges, and as the next section describes, a large stall is provoked in the hub-pressure side corner of the diffuser main passage.

It is clear from the previous observations that the jet-wake flow emerging from the impeller gives rise to substantial circumferential and spanwise distortions. These distortions do not mix out before arriving at the diffuser vanes' entry zone. This mixing is assumed in some design theory (e.g., Dean and Senoo, 1960, and Johnston and Dean, 1966); doubt this must therefore be placed on the validity of design procedures of this type.



Fig. 7 Predicted time-mean velocities on slices through the diffuser flow near the hub, in midspan, and near the casing

It seems reasonable to conclude from this section that good qualitative and quite fair quantitative agreement has been achieved between the predicted and measured flowfields in the entry zone to the diffuser. The next section concerns the development of this flowfield downstream of the throat in the diffuser passage as a whole.

The Flow in the Vaned Diffuser; the Passage as a Whole. The predicted flow pattern in the diffuser was quite similar near the shroud and in midspan but dramatically different toward the hub where a substantial hub-pressure side corner stall was predicted. Figure 7 shows contours of predicted time-averaged total velocity on slices through the diffuser flow near the hub, in midspan, and near the casing. The contours show the corner stall to be initiated just downstream of the vane throat; the vanes run near the hub with a flow incidence varying from 5 to 12 deg with a mean level of around 10 deg. The stalled zone expands rapidly downstream extending all across the vane passage before the trailing edge is reached. There is evidence of the corner stall even in the midspan plane, which is in fact virtually tangential to the separated zone over the aft half of the passage. Krain (1984) has presented some extra data for two stations downstream

of the throat. In these, a zone of blockage is measured developing in the hub/pressure side corner with velocity levels fallen as low as around 25 percent of the passage mean value. The measurements do not indicate reverse flow, however, nor are they made far enough downstream to see if the low-velocity zone develops into a reversed flow as predicted. The observations of Inoue (1980) also support the likelihood of the development of a corner blockage aft in the diffuser passages. It seems safest to conclude that a substantial blockage does develop in the hub/pressure side corner at this operating point but that its extent is somewhat overpredicted in the current effort.

Also of some interest is the extent to which the periodic, highly unsteady flow in the diffuser entry zone propagates downstream. The behavior is illustrated in Fig. 8, which shows two plots of (instantaneous-averaged) velocity vectors in the midspan slice a quarter of a blade-passing time apart. The magnitudes of the velocity fluctuations decay rapidly away from the entry zone; this is already happening quite strongly by the throat region (compare also Figs. 5 and 6). This sort of behavior was observed by Inoue (1980) who found that the magnitude of the periodic flow unsteadiness in the diffuser vane entry zone diminished rapidly down-

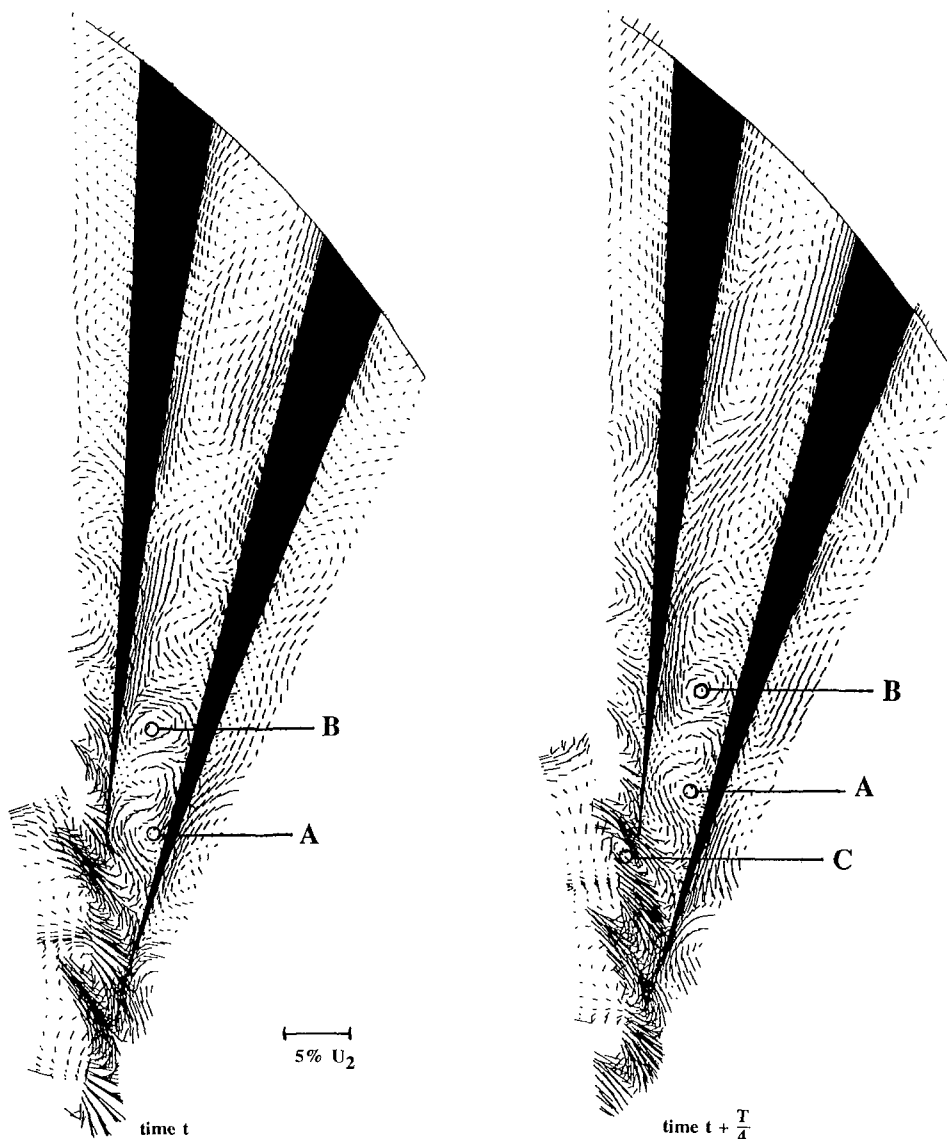


Fig. 8 (Instantaneous-averaged) velocity vectors in the midspan slice a quarter of a blade-passing time period apart

stream of the throat so that in the outer part of the diffuser no periodic unsteadiness could be observed. The physical mechanism seems to be as follows. The unsteady perturbation flow takes the form in the blade-blade plane of train of vortices, which can be seen quite clearly emanating from the entry zone. Vortices "A" and "B" are propagating downstream and vortex "C" is the next one forming. This pattern of propagation is periodic and locked to the blade passing time scale. Also clear in the figure is the way the vortices are damped as they propagate, seemingly being absorbed into the irregular fluctuations associated with the edge of the corner stall. The large corner stall with its relatively large natural time scale seems not to respond quickly enough to the rapid fluctuations in the entry zone but rather absorbs them and acts to damp them away.

A final point related to Fig. 8 is that the time-averaged flow in alternate diffuser passages is not identical. This is because the averaging is conducted on the fly over a single blade passing period whereas in fact the diffuser flow was predicted to be slowly varying over a time scale of the order of five to seven blade passing periods. This may be a result of conducting a simulation with a relative blade count of 14:28 instead of the true 14:27. Nevertheless it is quite plausible in a flow such as this that there could be a variety of time scales present: short scales associated with trailing edge vortex shedding phenomena, medium ones associated with the blade passing time scale, and large ones associated with the large separated zone in the long ductlike diffuser passages.

Overall the diffuser flow is characterized by the growth of a substantial corner blockage/stall and a rapid decay of periodic unsteadiness downstream of the throat. It seems likely that the corner stall is initiated by the very unfavorable flow incidence near the hub at this operating point. The spanwise variation of flow property, especially swirl angle, seems to exert a more significant influence on the diffuser performance than does the unsteady, circumferential variation in flow. There is some evidence to support this view from Senoo et al. (1977), who found that spanwise (axial)

distortions persisted further downstream than did circumferential distortions in vaneless diffusers.

Unsteady Loss Production; Average Versus Steady Operating Point. Finally, the predicted flowfield was interrogated from the perspective of loss production to try to determine the contribution of the unsteady flow to the loss levels in and hence to the time-average performance of the stage.

The only scientific measure of loss in an unsteady flow is entropy. The unsteady transport equation for entropy, s , takes the following form for *adiabatic* flow:

$$\rho \frac{Ds}{Dt} = \frac{1}{T} \tau_{ij} \frac{\partial u_i}{\partial x_j} + \frac{k}{T^2} \frac{\partial T}{\partial x_i} \frac{\partial T}{\partial x_i}$$

where τ_{ij} is the stress tensor, ρ the density, u_i the velocity field, x_i the space coordinate, and k the thermal conductivity. The right-hand side can be interpreted as the source of entropy; the left-hand side represents the unsteady convection of that entropy. All the entropy produced within the flowfield will eventually pass through the exit boundary from the stage and be perceived as the "stage" loss. For a periodically varying flow the instantaneous rate of entropy production will also vary periodically.

The dominant production term is the tensor product of the stress and the strain and this is quadratic in velocity. If the velocity is represented by the sum of a time-averaged and a fluctuating part, $u = \bar{u} + u'$ then the time average of a quadratic velocity "production" term is

$$\overline{u^2} = \bar{u}^2 + \overline{u'^2}$$

The first term on the right-hand side represents the loss production associated with the time-averaged flow; this may be indirectly affected by unsteadiness in that the time-averaged flow may differ from an "equivalent steady flow." The second term represents the nonlinear contribution to loss production *directly* attributable to the unsteady flow itself.

For comparative purposes an "equivalent steady flow simulation" was performed by modeling just the diffuser and

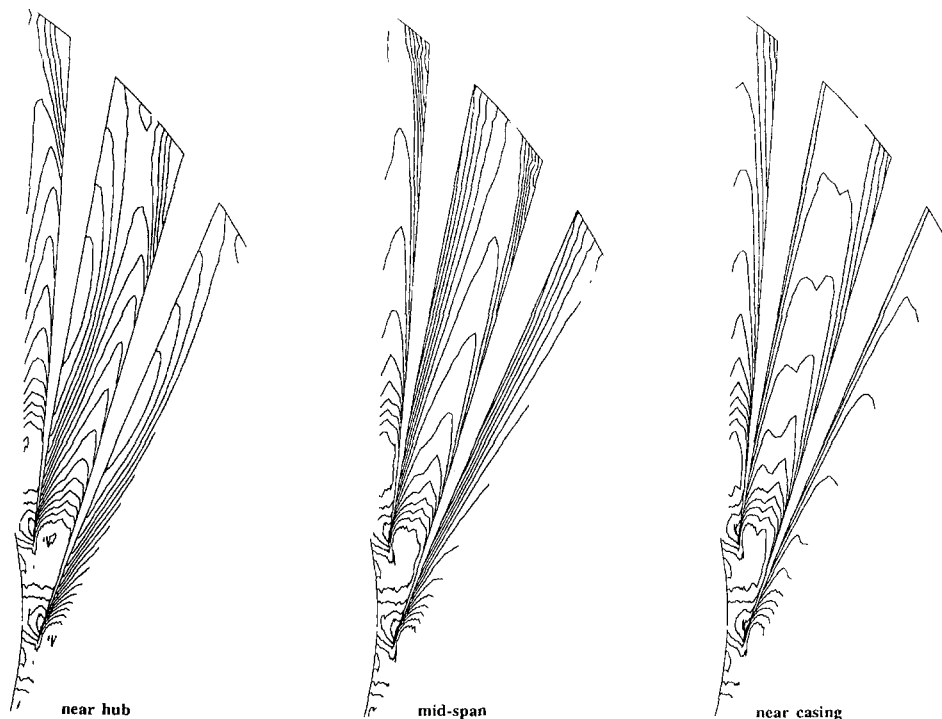


Fig. 9 Predicted velocities on slices through the diffuser flow near the hub, in midspan, and near the casing for the "equivalent steady flow"

with the circumferentially averaged impeller exit flow used as inlet boundary conditions (in particular modeling the spanwise variation of flow incidence). Running to the same back pressure as the stage, the diffuser was predicted to pass the same mass flow (i.e., the basic operating point did not change). The resulting predicted contours of velocity are shown in Fig. 9, which should be compared with the time-averaged velocities in Fig. 7. A hub/corner stall is seen to be present also in the “equivalent steady flow.” The extent of the corner blockage is not quite as great as in the time-averaged flow and the reason would seem to be that in the unsteady flow the corner stall is absorbing the unsteadiness propagating from the entry zone, as discussed earlier, and this act to increase the time-averaged size of the stalled zone.

A comparison is now made of the time-averaged entropy production rate, the production rate that would be associated with the time-averaged flow and the production rate of the “equivalent steady flow.” The first represents the actual performance of the stage. The difference between the first two should correspond to loss production directly attributable to the unsteady flow itself. The result is shown below:

	<i>Impeller</i>	<i>Diffuser</i>
Time-averaged entropy production	8.15 kW/m ³ kg K	11.13
Entropy production of the time-averaged flow	8.13	10.63
Entropy production of the “equivalent steady flow”	—	9.47

This shows little loss directly attributable to unsteady effects in the rotor. The diffuser is seen to contribute nearly two thirds of the overall loss. In the diffuser vanes, despite the highly unsteady flow in the entry zone, only around 5 percent of the loss production could be directly associated with the unsteady flow (and this is really the impeller discharge mixing out in the diffuser entry zone rather than diffuser loss per se). The principal cause of the rather high loss levels observed in the diffuser seems to be the strong hub/corner stall, which is initiated by the strong spanwise distortion in swirl angle at inlet. The bulk of this loss (85 percent of the predicted actual time-averaged total) is in fact captured by the “equivalent steady flow” simulation. The mixing loss arising from the circumferential averaging of the rotor flow was not included in the equivalent steady flow loss above. The difference therefore between the time-averaged losses and the equivalent steady result gives a measure of the magnitude of the mixing loss itself (about 6 percent of the total stage loss).

Kirtley and Beach (1992) simulated a low-speed centrifugal stage with a steady flow Navier–Stokes solver using the passage-averaging approach of Adamczyk (1985) to model deterministic unsteadiness arising from blade row interactions. Their simulations also showed that while in the entry zone to the diffuser deterministic unsteadiness was important, aft of the throat only the spanwise incidence variation onto the diffuser was important. A very useful future exercise would be to use the present unsteady simulations to help in the formulation of such passage-averaged models.

Conclusions

- Except over the critical zone near the impeller trailing edges, the impeller flow was observed to be essentially steady; this result might change if the diffuser entry velocities were supersonic.
- The highly distorted jet-wake flow emerging from the impeller did not appear to mix out before arriving at the

diffuser vanes’ entry zone as assumed in some design methods.

- Very large periodic variations of velocity and flow angle were observed in the entry zone to the diffuser.
- Good qualitative and quite fair quantitative agreement was achieved between the predicted and measured flowfields both in the impeller and in the entry zone to the diffuser.
- Flow unsteadiness at blade passing scale in the vaned diffuser was confined largely to the entry zone and diminished rapidly further outboard in the diffuser. Outboard, although the flow was predicted to be unsteady, the unsteadiness did not appear to be periodic on blade passing time scales and in any case was much lower in magnitude than in the entry zone.
- The flow pattern in the diffuser downstream of the throat was quite similar near the shroud and in midspan but dramatically different near the hub where a substantial hub–pressure side corner stall was predicted; this corner stall seems largely to be caused by the spanwise variation of flow angle at diffuser inlet.
- The irregular fluctuations associated with the corner stall seem to overwhelm and damp out any periodic, propagating unsteadiness from the entry zone.
- The spanwise variation of flow property, especially swirl angle, seems to exert a more significant influence on the diffuser performance than does the unsteady, circumferential variation in flow.
- A comparison was made of the time-averaged entropy production rate with the production rates, which would be associated with the time-averaged flow and with the “equivalent steady flow.” This showed little loss directly attributable to unsteady effects. The principal cause of the rather high loss levels observed in the diffuser seems to derive from the strong spanwise distortion in swirl angle at inlet, which initiates a strong hub/corner stall.
- It is very important therefore that design methods that mix out the impeller flow before entry to the diffuser should only perform such mixing circumferentially so that the crucial spanwise variation of flow property be preserved and passed on to impact the diffuser performance.

References

- Adamczyk, J. J., 1985, “Model Equation for Simulating Flows in Multi-stage Turbomachinery,” ASME Paper No. 85-GT-226.
- Dawes, W. N., 1992, “The Simulation of Three-Dimensional Viscous Flow in Turbomachinery Geometries Using a Solution-Adaptive Unstructured Mesh Methodology,” ASME JOURNAL OF TURBOMACHINERY, Vol. 114, pp. 528–537.
- Dawes, W. N., 1993a, “The Extension of a Solution-Adaptive Three-Dimensional Navier–Stokes Solver Toward Geometries of Arbitrary Complexity,” ASME JOURNAL OF TURBOMACHINERY, Vol. 115, pp. 283–295.
- Dawes, W. N., 1993b, “Simulating Unsteady Turbomachinery Flows on Unstructured Meshes Which Adapt Both in Time and Space,” ASME Paper No. 93-GT-104.
- Dean, R. C., and Senoo, Y., 1960, “Rotating Wakes in Vaneless Diffusers,” ASME *Journal of Basic Engineering*, Vol. 82, pp. 563–570.
- Giles, M. B., 1988, “Calculation of Unsteady Wake/Rotor Interaction,” *AIAA J. of Propulsion and Power*, Vol. 4, No. 4, pp. 356–362.
- Giles, M. B., 1990, “Stator/Rotor Interaction in a Transonic Turbine,” *AIAA J. of Propulsion and Power*, Vol. 6, No. 6.
- Holmes, D. G., and Connell, S. D., 1992, “Unstructured, Adaptive, Finite Volume Solution Methods for Fluid Dynamics,” presented at the 7th IMACS Conference on the Computer Simulation of pde’s, Rutgers, NJ, July.
- Hodson, H. P., 1985, “An Inviscid Blade-to-Blade Prediction of a Wake-Generated Unsteady Flow,” ASME *Journal of Engineering for Gas Turbines and Power*, Vol. 107, pp. 337–344.
- Inoue, M., 1980, “Centrifugal Compressor Diffuser Studies,” PhD Dissertation, Cambridge University, United Kingdom.
- Jameson, A., and Baker, T. J., 1987, “Improvements to the Aircraft Euler Method,” AIAA Paper No. 87-0452.
- Johnston, J. P., and Dean, R. C., 1966, “Losses in Vaneless Diffusers of Centrifugal Compressors and Pumps,” ASME *Journal of Engineering for Power*, Vol. 88, pp. 49–60.
- Jorgensen, P., and Chima, R., 1989, “An Unconditionally Stable

Runge-Kutta Method for Unsteady Flows," AIAA Paper No. 89-0205.

Kirtley, K. R., and Beach, T. A., 1992, "Deterministic Blade Row Interactions in a Centrifugal Compressor Stage," *ASME JOURNAL OF TURBOMACHINERY*, Vol. 114, pp. 304-311.

Krain, H., 1981, "A Study on Centrifugal Impellor and Diffuser Flow," *ASME Journal of Engineering for Gas Turbines and Power*, Vol. 103, Oct.

Krain, H., 1984, "Experimental Observations of the Flow in Impellers and Diffusers," VKI Lecture Series, 1984-07.

Krain, H., and Hoffmann, W., 1989, "Verification of an Impeller Design by Laser Measurements and 3D Viscous Flow Calculations," ASME Paper No. 89-GT-159.

Krain, H., 1993, private communication.

Lam, C. K. G., and Bremhorst, K. A., 1981, "Modified Form of the $k-\epsilon$

Model for Predicting Wall Turbulence," *ASME Journal of Fluids Engineering*, Vol. 103.

Patel, V. C., Rodi, W., and Scheuerer, G., 1985, "Turbulence Models for Near-Wall Flows and Low Reynolds Numbers: a Review," *AIAA Journal*, Vol. 23, No. 9.

Rai, M. M., 1985, "Navier-Stokes Simulations of Rotor-Stator Interaction Using Patched and Overlaid Grids," Paper No. AIAA-85-1519.

Rao, K., and Delaney, R., 1990, "Investigations of Unsteady Flow Through Transonic Turbine Stage Part I: Analysis," Paper No. AIAA-90-2408.

Senoo, Y., Kinoshita, Y., and Ishida, M., 1977, "Asymmetric Flow in Vaneless Diffusers of Centrifugal Blowers," *ASME Journal of Fluid Engineering*, Vol. 99, pp. 104-114.

Shin-Hyung Kang
Mem. ASME

Joon Sik Lee
Mem. ASME

Myung-Ryul Choi

Kyung-Yup Kim

Department of Mechanical Engineering,
Seoul National University,
Kwan-Ak Ku,
Seoul, Korea 151-742

Numerical Calculations of the Turbulent Flow Through a Controlled Diffusion Compressor Cascade

The viscous flow through a controlled diffusion (CD) compressor cascade was calculated and compared with the measured data for two different test conditions. A control volume method was used, which has been developed for a generalized nonorthogonal coordinate system. The discretized equations for the physical covariant velocity components were obtained by an algebraic manipulation of the discretized equations for the Cartesian velocity components. Low Reynolds number $k-\epsilon$ turbulence models were used to obtain the eddy viscosity. The numerical scheme using the low Reynolds number $k-\epsilon$ turbulence model reasonably predicted the general performance, i.e., mean outlet flow angle and loss coefficients. The development of the shear layer along the pressure and suction sides was well estimated, and the physical features found in the experiment were reasonably well confirmed in the simulation. However, the calculated profiles of mean velocity and turbulent kinetic energy in the near wake show considerable disagreement with the measured values.

Introduction

Reliable and accurate prediction of turbulent flows in turbomachinery over a wide range of flow conditions is very important for the design and performance prediction of new machines. An efficient method is required that correctly simulates complex flows containing viscous effects, namely, transition, leading edge separation, reattachment, nonequilibrium turbulent shear flow, and boundary layer separation. Various numerical methods have been developed in the past for passage flows. Reviews of CFD techniques were recently reported by McNally and Sockol (1985) and Lakshminarayana (1991). Numerical calculations with some approximations, i.e., two- or three-dimensional flows, steady or unsteady flows, incompressible or compressible flows, and viscous or inviscid flows, have been applied for design purposes. However, there is still a strong need to validate viscous calculational methods for two-dimensional, steady-state, and incompressible flow through cascades.

Experimental studies have been carried out to obtain flow data to validate a computational method for the design and off-design behavior of a cascade. Recently, Deutsch and Zierke (1987, 1988a, b) and Zierke and Deutsch (1990) used an LDV system to measure the boundary layers on the surfaces of a double circular arc (DCA) blade compressor cascade. The viscous flow was numerically investigated by Hobson and Lakshminarayana (1991). Controlled diffusion

(CD) compressor cascades have been designed and tested by Hobbs and Weingold (1984) and Behlke (1986). The CD blade shape was reported to avoid significant boundary layer separation over a wide range of incidence angle. Sanger and Shreeve (1986), Elazar and Shreeve (1990), and Shreeve et al. (1991) redesigned a CD blade and measured the velocity field and turbulence intensity as well as general performance parameters. The data identify a leading-edge separation bubble on the suction side at high incidence angles, and are well suited for viscous code assessment and calibration.

A fully elliptic numerical calculation for the CD blade was reported by Kang et al. (1992). The viscous flows through the CD blade in a cascade were calculated and compared with the measured data. A control volume method recently reported by Karki (1986) and Karki and Patankar (1988) was used. The scheme was developed for a generalized nonorthogonal coordinate system and the discretized equations for the physical covariant velocity components were obtained by an algebraic manipulation of the discretized equations for the Cartesian velocity components. A low-Reynolds-number $k-\epsilon$ turbulence model (Launder and Sharma, 1974) was used to obtain the eddy viscosity. The predicted mean outlet flow angle and the loss coefficients were in good agreement with the measured values. The development of the shear layer along the pressure and suction sides was generally well estimated. However, there was still a large discrepancy in the predicted profiles of mean velocity and turbulent kinetic energy. There are several points to be considered in depth to improve accuracy in the prediction, even if uncertainty in the measurement is taken into account.

Contributed by the International Gas Turbine Institute for publication in the JOURNAL OF TURBOMACHINERY. Manuscript received at ASME Headquarters February 1994. Associate Technical Editor: H. Lukas.

One of the important points is to simulate shear layer development reasonably over the transition region on a blade. The importance of transition in the flows through turbomachinery was summarized by Mayle (1991). Effects of free-stream turbulence intensity and length scale on the transition and heat transfer on turbomachinery blading are important. A model for the correct prediction of the transition point on the blade and the transport of turbulence under strong pressure gradient and free-stream turbulence does not yet exist. However, the low-Reynolds-number $k-\epsilon$ turbulence model used in the previous study (Kang et al., 1992) was surely one of the candidates, which was developed to simulate the near-wall damping effects. The model was successful in the prediction of the Reynolds number at which the pipe flow became turbulent, and the relaminarization of the turbulent boundary layer under a large accelerating pressure gradient. Schmidt and Patankar (1991 a, b) evaluated characteristics of low-Reynolds $k-\epsilon$ turbulence models, predicting the transition in the flat plate boundary layer over a range of free-stream turbulence conditions. Then, a modified low-Reynolds-number $k-\epsilon$ turbulence model was proposed that limited the production term in the turbulent kinetic energy equation. However, the modified one was not extended to the more general cases under the strong pressure gradient. The model was adopted in the present study and its performance was investigated.

Governing Equations and Boundary Conditions

Governing Equations. For a steady turbulent flow, the continuity and Reynolds-averaged Navier-Stokes equations are given as follows:

$$\frac{\partial}{\partial x_i}(\rho u_i) = 0 \quad (1)$$

$$\frac{\partial}{\partial x_j}(\rho u_i u_j) = -\frac{\partial p}{\partial x_i} + \frac{\partial}{\partial x_j} \left[\mu \left(\frac{\partial u_i}{\partial x_j} + \frac{\partial u_j}{\partial x_i} - \frac{2}{3} \frac{\partial u_k}{\partial x_k} \delta_{ij} \right) - \overline{\rho u_i' u_j'} \right] \quad (2)$$

where u_i is the mean velocity and u_i' is the fluctuating

velocity components. The Reynolds stresses are related to the mean rates of strain and an isotropic eddy-viscosity:

$$-\overline{\rho u_i' u_j'} = \mu_t \left(\frac{\partial u_i}{\partial x_j} + \frac{\partial u_j}{\partial x_i} \right) - \frac{2}{3} \rho k \delta_{ij} \quad (3)$$

The eddy viscosity μ_t is obtained by the low-Reynolds-number $k-\epsilon$ model (Launder and Sharma, 1974). The transport equations for k and ϵ are written as:

$$\mu_t = C_\mu f_\mu \rho \frac{k^2}{\epsilon} \quad (4)$$

$$\frac{\partial}{\partial x_i}(\rho u_i k) = \frac{\partial}{\partial x_i} \left[\left(\mu + \frac{\mu_t}{\sigma_k} \right) \frac{\partial k}{\partial x_i} \right] + \mu_t \frac{\partial u_j}{\partial x_i} \left(\frac{\partial u_i}{\partial x_j} + \frac{\partial u_j}{\partial x_i} \right) - \rho \epsilon - 2 \mu \left(\frac{\partial k^{1/2}}{\partial x_j} \right)^2 \quad (5)$$

$$\frac{\partial}{\partial x_i}(\rho u_i \epsilon) = \frac{\partial}{\partial x_i} \left[\left(\mu + \frac{\mu_t}{\sigma_\epsilon} \right) \frac{\partial \epsilon}{\partial x_i} \right] + C_1 \mu_t \frac{\epsilon}{k} \frac{\partial u_j}{\partial x_i} \times \left(\frac{\partial u_i}{\partial x_j} + \frac{\partial u_j}{\partial x_i} \right) - C_2 f_2 \frac{\rho \epsilon^2}{k} + 2 \frac{\mu \mu_t}{\rho} \left(\frac{\partial^2 u_i}{\partial x_j \partial x_k} \right)^2 \quad (6)$$

The functions and model constants are summarized as follows:

$$f_\mu = \exp \left[-\frac{3.4}{(1 + \text{Re}_t/50)^2} \right], \quad f_2 = 1 - 0.3 \exp(-\text{Re}_t^2),$$

$$\times \text{Re}_t = \frac{\rho k^2}{\mu \epsilon},$$

$$C_\mu = 0.09, \quad C_1 = 1.44, \quad C_2 = 1.92, \quad \sigma_k = 1.0, \quad \sigma_\epsilon = 1.3 \quad (7)$$

Schmidt and Patankar (1991b) modified the value of the function f_μ , and limited the production rate of turbulent kinetic energy as follows (Production Term Modification Model):

Nomenclature

a = coefficient in the discretized equation	n^+ = dimensionless distance normal to the blade surface = nu_τ/ν	x, y = Cartesian coordinates with the origin at the leading edge
b = source term in the discretized equation	p = pressure	x', y' = Cartesian coordinates with the origin at the trailing edge
C = blade chord length	Re = Reynolds number = $\rho V_1 C/\mu$	β_1, β_2 = inlet and outlet flow angle
C_f = skin-friction coefficient = $2\tau_w/\rho V_1^2$	Re_t = turbulent Reynolds number = $\rho k^2/\mu \epsilon$	Γ_ϕ = diffusion coefficient
C_p = pressure coefficient = $2(p - p_1)/\rho V_1^2$	S_ϕ = source term in the governing equations	ϵ = dissipation rate of turbulence energy
C_μ, C_1, C_2 = turbulence model constants	s = blade spacing	θ = momentum thickness
c_1, c_2, c_3 = coordinate transformation parameters	Tu = turbulence intensity = $100\sqrt{2k/3}/V_1$	μ = viscosity
f_2, f_μ = empirical functions in turbulence model	u, v = Cartesian velocity components	μ_t = eddy viscosity
G^1, G^2 = velocity components normal to grid cell boundary	u_ξ, u_η = velocity components in ξ, η directions	μ_{eff} = effective viscosity = $\mu + \mu_t$
J = Jacobian of the inverse coordinate transformation	V_1, V_2 = magnitudes of inlet and outlet velocity	ξ, η = general curvilinear coordinate system
k = turbulence kinetic energy	X, Y = Cartesian coordinates with the origin at the leading edge	ρ = density
n = distance normal to the blade surface		ϕ = dependent variable
		$\bar{\omega}$ = mass-averaged total pressure loss coefficient = $(\bar{p}_{11} - \bar{p}_{12})/(\bar{p}_{11} - p_1)$

$$f_\mu = \min\{f_{\mu 0}, 1.0, 0.5 + 0.0025 \text{Re}_t\} \quad (8)$$

$$P_k = 0, \quad \text{for } \text{Re}_\theta < \text{Re}_{\theta,C} \quad (9)$$

$$\frac{dP_{k,\max}}{dt} = A \cdot P_k + B, \quad \text{for } \text{Re}_\theta > \text{Re}_{\theta,C} \quad (10)$$

where Re_θ is the Reynolds number based on the momentum thickness and $\text{Re}_{\theta,C}$ is 100. The coefficient A and B are functions of the free-stream turbulence intensity. These were determined considering the following empirical correlations of Reynolds numbers at the starting and ending locations of transition, $\text{Re}_{\theta,S}$, $\text{Re}_{\theta,E}$, by Abu-Ghannam and Shaw (1980).

$$\text{Re}_{\theta,S} = 163 + \exp(6.91 - 100Tu_c) \quad (11)$$

$$\text{Re}_{\theta,E} = 2.667\text{Re}_{\theta,S} \quad (12)$$

Boundary Conditions. A flow domain bounded by two neighboring blades is considered, which is extended from the far upstream to the downstream locations (Fig. 1). The boundary conditions are specified at the inlet and outlet sections, on the surface of the blade, and the periodic lines between the blades. At the inlet boundary $A-A'$, all dependent variables must be specified. A uniform flow distribution is assumed with a given flow angle β_1 . The constant values of k and ϵ are given on $A-A'$, i.e., $k_1 = 1.5 \cdot (0.014 \cdot V_1)^2$, $\epsilon_1 = C_\mu k_1^3 / 0.01s$. On the outlet boundary $D-D'$, the streamwise derivatives of all the dependent variables are zero. On the suction side $B-C$ and the pressure side $B'-C'$ of the blade, the no-slip condition is enforced. Since the low-Reynolds-number $k-\epsilon$ model is used, the boundary conditions $k=0$ and $\epsilon=0$ are applied on the blade surfaces. The periodicity condition on $A-B$, $A'-B'$ and $C-D$, $C'-D'$ is imposed in an implicit manner. The variables have the same values at the corresponding periodic points along the periodic lines.

Method of Calculation

Calculations are carried out in a nonorthogonal curvilinear coordinate (ξ, η) . The governing equations for a dependent variable ϕ can be transformed into the following general form:

$$\begin{aligned} \frac{1}{J} \frac{\partial}{\partial \xi} (\rho G^1 \phi) + \frac{1}{J} \frac{\partial}{\partial \eta} (\rho G^2 \phi) \\ = \frac{1}{J} \frac{\partial}{\partial \xi} \left[\frac{\Gamma_\phi}{J} \left(c_1 \frac{\partial \phi}{\partial \xi} - c_2 \frac{\partial \phi}{\partial \eta} \right) \right] \\ + \frac{1}{J} \frac{\partial}{\partial \eta} \left[\frac{\Gamma_\phi}{J} \left(c_3 \frac{\partial \phi}{\partial \eta} - c_2 \frac{\partial \phi}{\partial \xi} \right) \right] + S_\phi(\xi, \eta) \end{aligned} \quad (13)$$

where

$$\begin{aligned} G^1 &= uy_\eta - ux_\eta, \quad G^2 = ux_\xi - uy_\xi, \\ c_1 &= x_\eta^2 + y_\eta^2, \quad c_2 = x_\xi x_\eta + y_\xi y_\eta, \quad c_3 = x_\xi^2 + y_\xi^2, \\ J &= x_\xi y_\eta - x_\eta y_\xi \end{aligned} \quad (14)$$

The discretized equations are obtained following a finite volume method (Karki and Patankar, 1988). A staggered grid arrangement is used in which the scalar variables are located at the geometric center of a control volume, while the physical covariant velocity components, u_ξ and u_η , are located on the midpoints of the control faces (Fig. 1). A power law differencing scheme is employed to evaluate the combined convection-diffusion fluxes on the control surfaces. The discretized equation for the scalar variables at a grid P is written as:

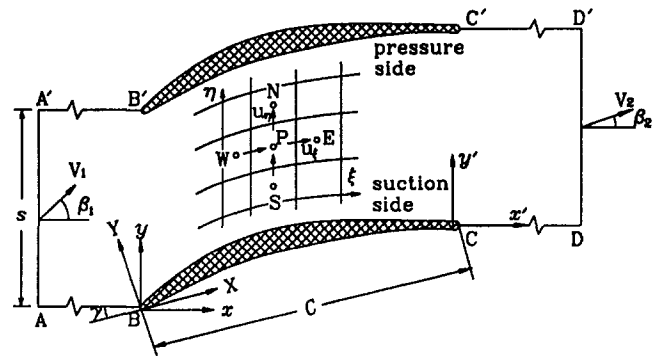


Fig. 1 Configuration of a cascade and coordinate system

Table 1 Parameters of the CD cascade

Parameters	Values
Chord	12.73 cm
Solidity	1.67
Leading edge radius	0.114 cm
Trailing edge radius	0.157 cm
Thickness	7 percent
Section angle	14.2 deg
Stagger angle	14.4 deg
Span	25.4 cm

$$a_P \phi_P = a_E \phi_E + a_W \phi_W + a_N \phi_N + a_S \phi_S + b \quad (15)$$

where the coefficients a denote the combined convection-diffusion coefficients and b includes the explicitly calculated terms as well as the source terms.

The physical covariant velocity components, which are directed along the coordinate lines, are used as the dependent variables in the momentum equations. The discretization is performed by using Cartesian velocity components in a locally fixed coordinate system at a grid point P (Karki and Patankar, 1988). This procedure is reported to avoid complicated curvature source terms that would appear if the full transformation of the equations was used. The discretization equation for $u_{\xi,P}$, for example, can be written as:

$$a_P u_{\xi,P} = a_E u'_{\xi,E} + a_W u'_{\xi,W} + a_N u'_{\xi,N} + a_S u'_{\xi,S} + b'_\xi \quad (16)$$

where the primed velocities are the velocity components parallel to $u_{\xi,P}$ at the neighboring points. Introducing the covariant velocity components, i.e., $u_{\xi,E}$, $u_{\xi,W}$, etc., the discretized equation becomes as follows:

$$\begin{aligned} a_P u_{\xi,P} &= a_E u_{\xi,E} + a_W u_{\xi,W} + a_N u_{\xi,N} + a_S u_{\xi,S} + b'_\xi \\ &+ a_E (u'_{\xi,E} - u_{\xi,E}) + a_W (u'_{\xi,W} - u_{\xi,W}) \\ &+ a_N (u'_{\xi,N} - u_{\xi,N}) + a_S (u'_{\xi,S} - u_{\xi,S}) \end{aligned} \quad (17)$$

In Eq. (17), the terms such as $a_E (u'_{\xi,E} - u_{\xi,E})$ and similar terms included in the source term b'_ξ represent the effect of curvature. Equation (17) is rewritten in a compact form, with the pressure difference term appearing explicitly, as follows:

$$a_P u_{\xi,P} = \sum a_{nb} u_{\xi,nb} + \frac{\Delta V}{h_\xi} (p_w - p_c) + b_\xi \quad (18)$$

A pressure correction equation is obtained by the SIMPLE (Patankar, 1980) algorithm. The velocity components are corrected to satisfy the continuity equation. However, the pressures are obtained by the SIMPLER (Patankar, 1980) scheme using the full momentum equations. The pressure correction and pressure equations are represented by the same form with Eq. (15).

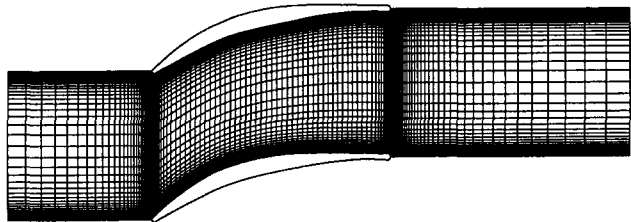


Fig. 2 Grids for computation

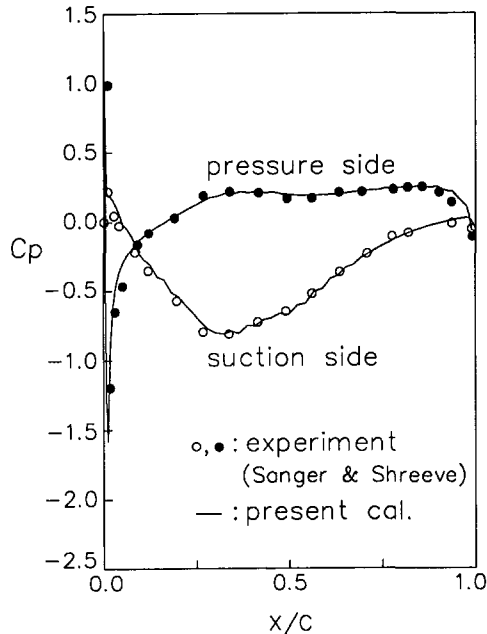


Fig. 3 Distributions of calculated and measured pressure coefficient for $\beta_1 = 28.0$ deg

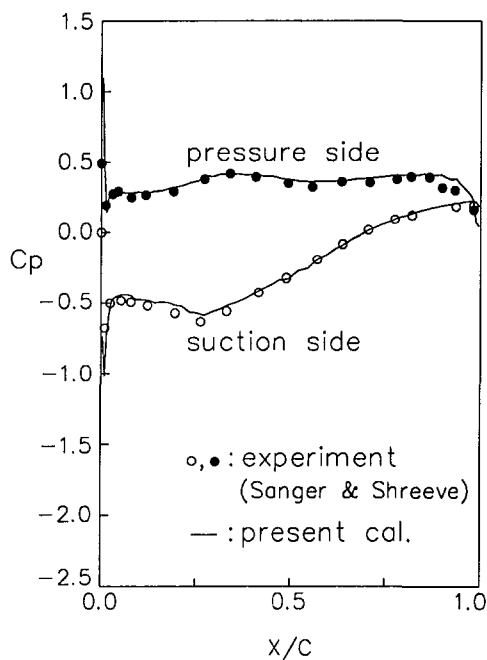


Fig. 4 Distributions of calculated and measured pressure coefficient for $\beta_1 = 39.0$ deg

A cyclic TDMA (Ramamurti et al., 1988) is used to obtain a numerical solution of the discretized equation. Convergence is assumed when the maximum relative error in the pressure field is less than 10^{-5} .

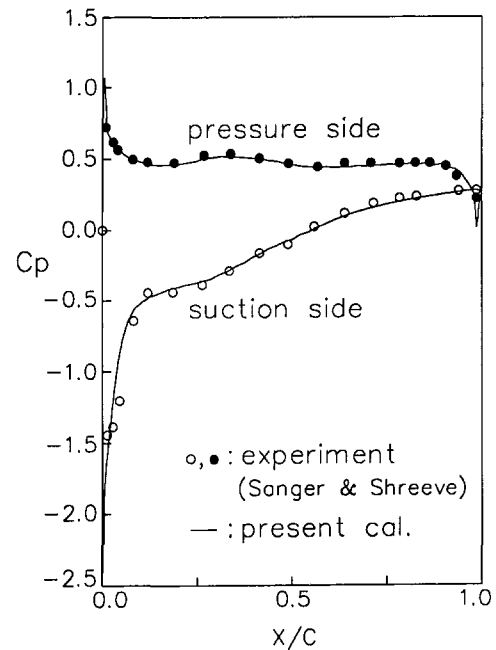


Fig. 5 Distributions of calculated and measured pressure coefficient for $\beta_1 = 46.0$ deg

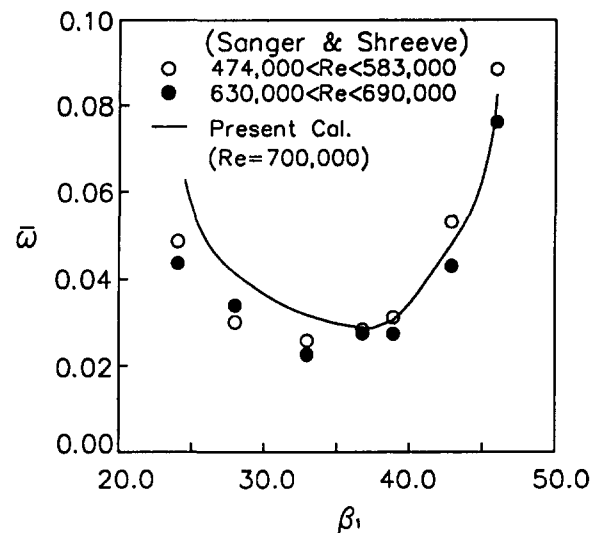


Fig. 6 Predicted and measured loss coefficients

Results and Discussion

Before going further, the important results of the previous study (Kang et al., 1992) using the low-Reynolds-number $k-\epsilon$ model are introduced below. Flow calculations were carried out for the controlled-diffusion (CD) compressor blade, which has been experimentally evaluated at design and off-design conditions by Sanger and Shreeve (1986), Elazar and Shreeve (1990), and Shreeve et al. (1991). The parameters of the cascade are given in Table 1. The blade was tested at a Reynolds number of 700,000 and Mach number of 0.25. Measurements included conventional cascade performance and blade surface pressures (Sanger and Shreeve, 1986), velocity distributions using LDV (Elazar and Shreeve, 1990), and mean velocity and turbulence intensity in the wake (Shreeve et al., 1991). Nonuniform grids were generated, i.e., fine grid spacings near the leading and trailing edges as well as the pressure and suction surfaces (Fig. 2). The inlet and outlet boundaries were located at $-0.6 C$ and $1.0 C$, respec-

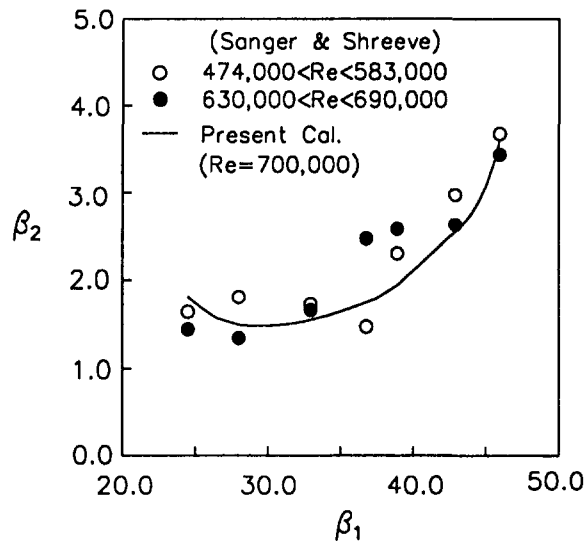


Fig. 7 Predicted and measured outlet flow angles

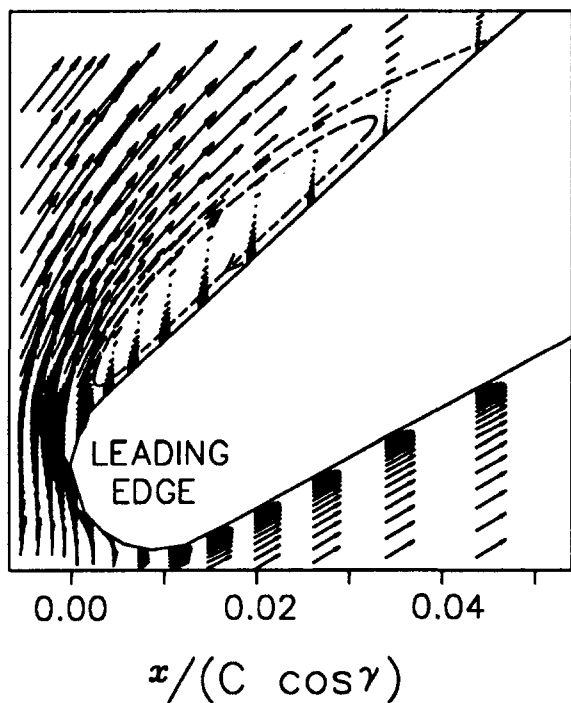


Fig. 8 Calculated velocity vectors over leading edge for $\beta_1 = 46.0$ deg

tively. The number of grids was 158×78 in the ξ and η directions. The values of n^+ ($= u_\tau n/\nu$) at the grids next to the solid surfaces were 0.9–1.2 to ensure the low-Reynolds-number $k-\epsilon$ model would work. These values were decided after several sensitivity tests by Kim (1991). The magnitude of the inlet velocity was fixed at the experimental condition, 85.0 m/s. The inlet angle was changed from 24.0 to 46.0 deg.

Calculated pressure coefficients on the pressure and suction surfaces for three inlet angles, i.e., 28.0 deg (negative incidence), 39.0 deg (design angle), and 46.0 deg (positive incidence), are presented in Figs. 3, 4, and 5, respectively. Calculated results are in good agreement with the measured values (Sanger and Shreeve, 1986); especially near the trailing edge where viscous effects are strong. The strong adverse pressure gradient along the suction surface for the inlet angle of 46.0 deg is also predicted well. Calculated loss coefficients

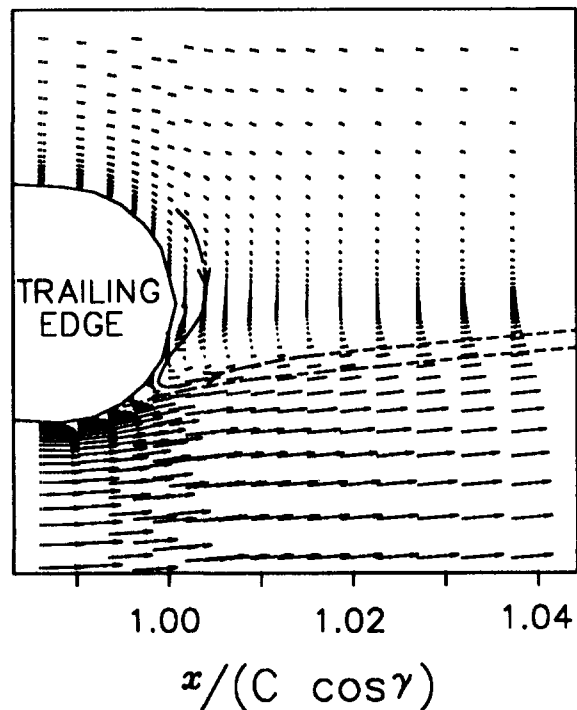


Fig. 9 Calculated velocity vectors over trailing edge for $\beta_1 = 46.0$ deg

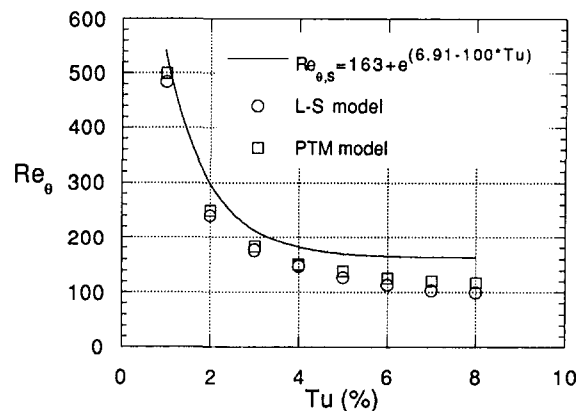


Fig. 10 Variation of starting location of transition on the flat plate with free-stream turbulence intensity

(obtained by mass averaging total pressure at the outlet boundary) show good agreement with measured values at the high flow angles toward stall (Fig. 6). The mass-averaged outlet flow angles are also predicted well as shown in Fig. 7. The leading edge separation bubble detected in the experimental study (Elazar and Shreeve, 1990) is also simulated for the inlet flow angle of 46.0 deg (Fig. 8). The separation bubble becomes smaller as the inlet flow angle decreases, and does not appear when the inlet angle is less than 40.0 deg. Velocity vectors near the trailing edge are also shown in Fig. 9. The thick boundary layer on the suction side makes velocity small and pressures high, and the pressures along the pressure side decrease over the trailing edge (Fig. 5). Therefore, flow particles at the trailing edge were accelerated to the pressure side. For this reason, the center of the wake for $\beta_1 = 46.0$ deg (Fig. 9) is shifted to the pressure side. The blunt trailing edge makes a small backflow region over the trailing edge. The wake becomes more symmetric as the inlet flow angle is reduced. These results are in accord with experiments (Elazar and Shreeve, 1990). The growths of the

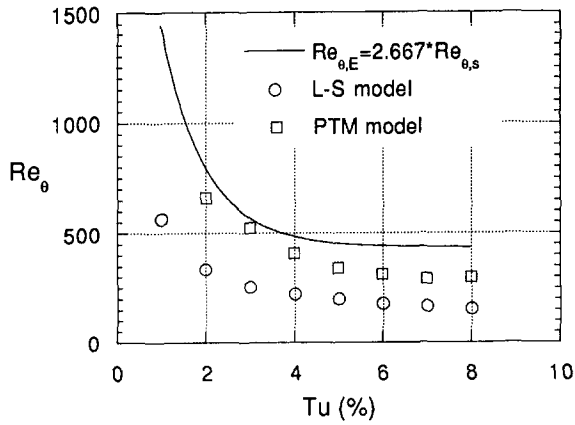


Fig. 11 Variation of ending location of transition on the flat plate with free-stream turbulence intensity

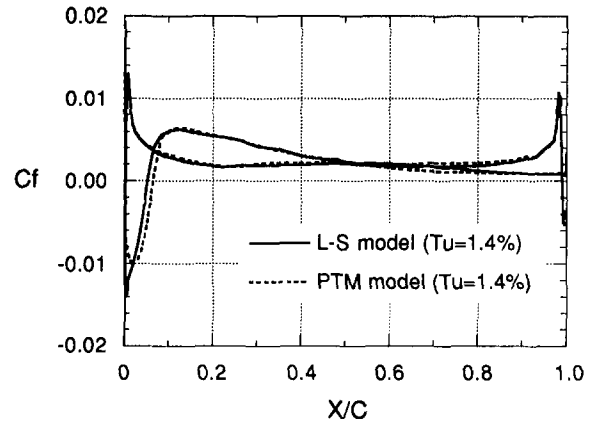


Fig. 14 Distributions of calculated skin-friction coefficient on the blade; $\beta_1 = 46.0$ deg

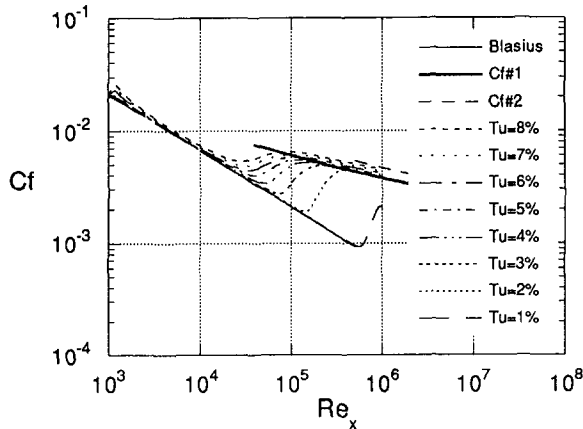


Fig. 12 Skin-friction coefficients along the flat plate for various values of free-stream turbulence intensity (the PTM model used)

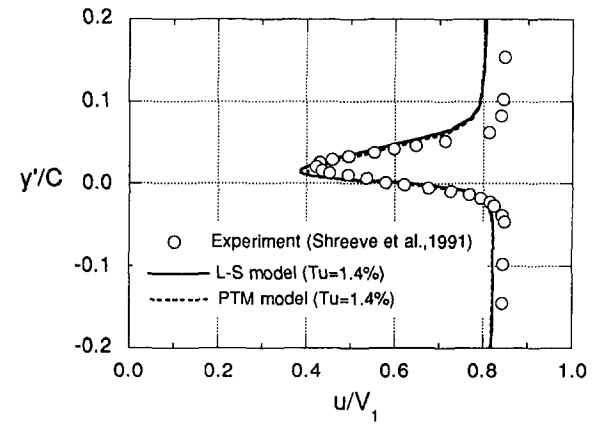


Fig. 15 Profiles of (a) mean velocity and (b) turbulence intensity at $x/C = 212$; $\beta_1 = 39.0$ deg

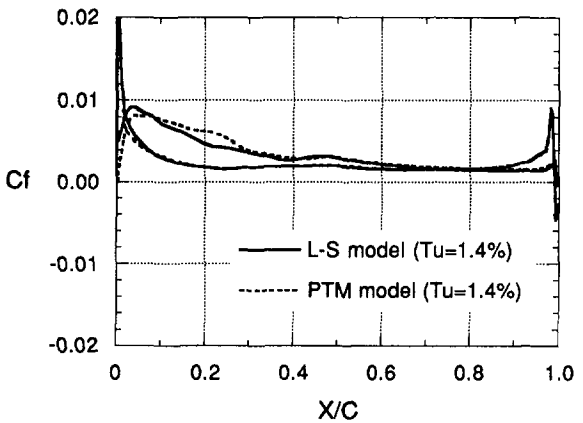
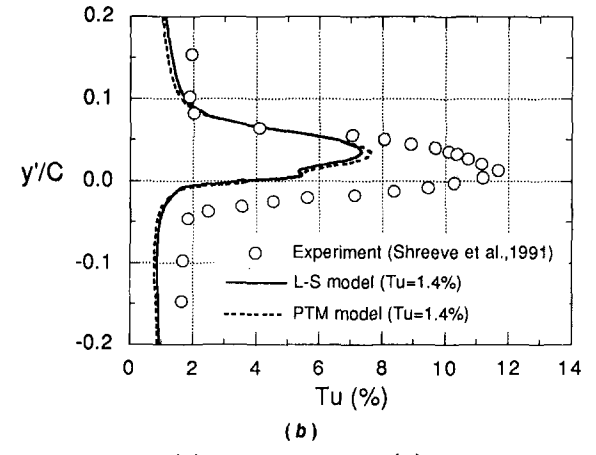


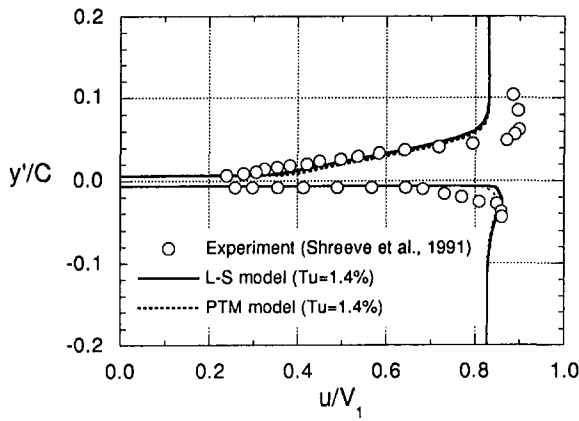
Fig. 13 Distributions of calculated skin-friction coefficient on the blade; $\beta_1 = 39.0$ deg



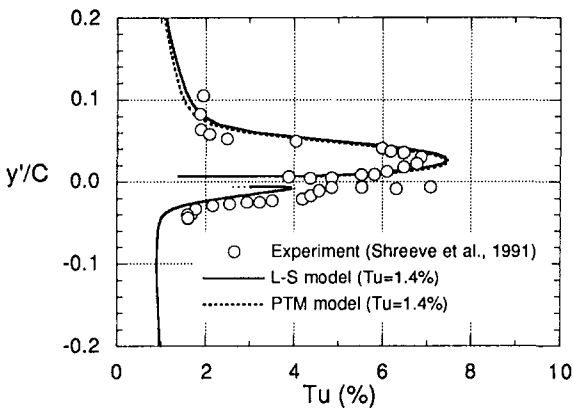
boundary layers on the suction and pressure surfaces were investigated. Variations of the displacement thicknesses and the shape factors were in accord with measured values (not shown here). The boundary layer occupies 20 percent of the passage and the blockage effect on the pressure loss becomes important. The distributions of the tangential and normal velocity components and turbulence intensity in the boundary layer were qualitatively in accord with measurements (Elazar and Shreeve, 1990).

However, it is important to investigate the coincidence of the simulated mean velocity and turbulent kinetic energy

profiles with measured ones. Since there is considerable uncertainty in the measurement of thin boundary layer on the surface, the profiles at the trailing edge and in the near wake were mainly investigated. All the numerical errors as well as the effects of turbulence model through the whole flow field upstream would accumulate in the wake. Since the transition may strongly affect the development of the mean velocity as well as turbulence intensity profiles along the blade, not only the low-Reynolds-number $k-\epsilon$ model of Launder and Sharma (L-S model) but also a low-Reynolds $k-\epsilon$ turbulence model with transition model (PTM model)



(a)

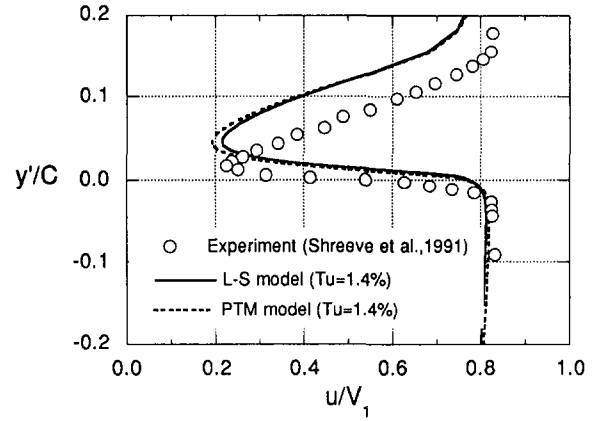


(b)

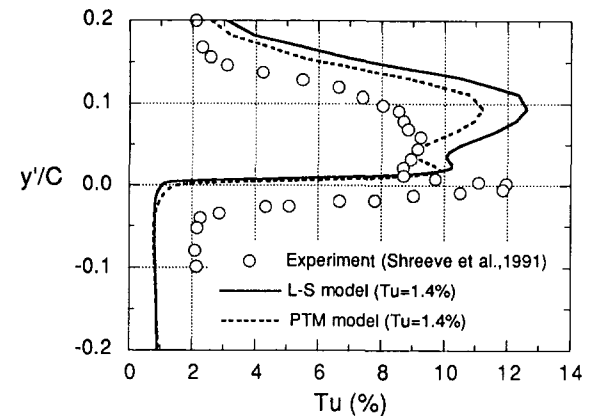
Fig. 16 Profiles of (a) mean velocity and (b) turbulence intensity at trailing edge; $\beta_1 = 39.0$ deg

was used in the present study. The PTM model was applied for the boundary layer flow on the flat plate with different values of free-stream turbulence intensity. The predicted locations of the starting and ending point of transition are shown in Figs. 10 and 11. The lengths of the transition, $Re_{\theta,e} - Re_{\theta,s}$, are reasonably estimated by the modified model. If the coefficients A and B in Eq. (10) were adjusted further, the predicted values would coincide with those of the correlations. Variations of skin-friction coefficient are shown in Fig. 12. As the value of free-stream turbulence intensity increases, the skin-friction coefficient increases in the whole range of speed.

The validity of the PTM model is not fully tested yet for the curved blade surface under a strong pressure gradient. Flows through the cascade at the design angle of 39.0 deg and near the stall angle of 46.0 deg were recalculated using the PTM model without any further verifications in the present study. Noticeable changes in the pressure as well as skin-friction coefficients did not appear. The value of free-stream turbulence intensity of 1.4 percent was not high enough for the PTM model to predict quite different values in the transition region (cf. Figs. 13 and 14). However, the skin-friction coefficients near the leading edge separation bubble especially for $\beta_1 = 46.0$ deg were considerably changed. The bubble became longer and thicker when the PTM model was used. It should be noted that the validity of the model is not fully confirmed yet for separated flow. The flow in the transition region over the surface of the blade was not clearly identified not only in the measurement but also in the simulation. Considering variations of the mean velocity and turbulence intensity profiles as well as variations of



(a)



(b)

Fig. 17 Profiles of (a) mean velocity and (b) turbulence intensity at $x/C = 0.212$; $\beta_1 = 46.0$ deg

turbulence production and eddy-viscosity, we concluded that the transition occurs between $X/C = 0.057$ and 0.130 on the pressure side and before $X/C = 0.057$ (over the bubble for $\beta_1 = 46.0$ deg) on the suction side.

At the design angle of flow, the profiles at the location of $0.212 C$ downstream from the trailing edge are presented in Fig. 15. The highly asymmetric shape of velocity profile was nicely simulated; however, the magnitudes of velocity outside the boundary layer, i.e., in the core region, are smaller than the measured values. This may be due to the AVDR (Axial Velocity Density Ratio) of 1.04 in the experiment. The effects of the AVDR are not taken into account in the present two-dimensional calculations. The turbulent intensity is considerably underestimated and the effects of the turbulence models are small. The profiles of mean velocity and turbulent kinetic energy at the trailing edge are shown in Fig. 16. It is noted that the turbulent intensity is considerably well-estimated in the boundary layer and a little underestimated in the core region. It is not clear what is the mechanism of high production of turbulent kinetic energy within a short distance from the trailing edge to the location of $0.212 C$.

In Fig. 17, mean velocity and turbulence intensity profiles at the location of $0.212 C$ are shown when the angle of incoming flow is 46.0 deg. The growth of the boundary layer on the suction side is faster than that in the measurement and the location of the centerline shifted more to the suction side. The turbulent intensity is overestimated on the suction side and underestimated on the pressure side in this case. The higher value of turbulence intensity generally results in the larger eddy viscosity and makes the boundary layer thicker on the suction side. When the modified model was used, the

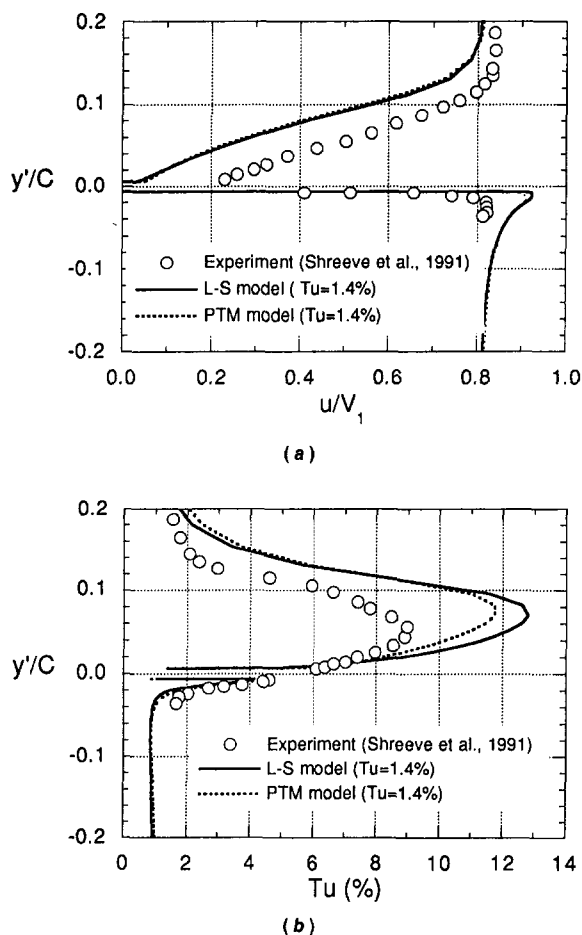


Fig. 18 Profiles of (a) mean velocity and (b) turbulence intensity at trailing edge; $\beta_1 = 46.0$ deg

values of turbulence intensity were reduced by 10 percent, but still higher than the measured values. On the other hand, noticeable differences were not observed on the pressure side. The profiles at the trailing edge are presented in Fig. 18. Considering that a similar discrepancy already appears at the trailing edge, prediction errors accumulated along the blade surface, especially on the suction side where the leading edge bubble appeared.

It was experimentally determined that the thickness of the boundary layer increased on the suction side and decreased slightly on the pressure side as the incidence was increased. The values of turbulence intensity showed the typical value of a fully turbulent boundary layer on the suction side and reduced on the pressure side with the incidence (Shreeve et al., 1991). Even though there are some discrepancies in the predicted mean velocity and turbulent intensity profiles, the physical features of flows were reasonably well confirmed in the present simulation.

Conclusion

The results of the numerical calculations of the flows in the controlled diffusion blade in the cascade are summarized as follows:

- 1 The numerical scheme using the low-Reynolds-number $k-\epsilon$ turbulence model reasonably predicts the mean outlet flow angle and the loss coefficients. Calculated flows are in accord with the measurement.
- 2 The development of the shear layer along the pressure and suction sides is generally well estimated. The measured

leading edge separation bubble for a high inlet flow angle is confirmed, which has large effects on the flow development downstream. The boundary layer on the suction side is not separated after reattachment for large incidence angles; however, a small back flow region appears over the trailing edge.

3 Noticeable changes in the pressure as well as skin-friction coefficients did not appear using the PTM model with small values of free-stream turbulence intensity. However, noticeable changes were observed in the flow over the leading edge, i.e., the thicker and longer separation bubble was predicted.

4 The calculated profiles of mean velocity and turbulent kinetic energy in the near wake, wherein accumulated all the effects of numerical errors as well as turbulence model through the whole flow field upstream, show considerable disagreement with the measured values. However, the physical features found in the experiment were reasonably well confirmed in the simulation. Refinement of the numerical technique and turbulence models is required to achieve closer agreement.

Acknowledgments

The authors would like to extend their appreciation to the Turbo and Power Machinery Research Center and the Korean Science and Engineering Foundation for supporting the present work.

References

- Abu-Ghanam, B. J., and Shaw, R., 1980, "Natural Transition Boundary Layer—The Effects of Turbulence, Pressure Gradient, and Flow History," *J. Mech. Eng. Science*, Vol. 22, No. 5, pp. 213–228.
- Behlke, R. F., 1986, "The Development of a Second Generation of Controlled Diffusion Airfoils for Multistage Compressors," *ASME JOURNAL OF TURBOMACHINERY*, Vol. 108, pp. 32–41.
- Davis, R. L., Hobbs, D. E., and Weingold, H. D., 1988, "Prediction of Compressor Cascade Performance Using a Navier–Stokes Technique," *ASME JOURNAL OF TURBOMACHINERY*, Vol. 110, pp. 520–531.
- Deutsch, S., and Zierke, W. C., 1987, "The Measurement of Boundary Layers on a Compressor Blade in Cascade: Part 1—A Unique Experimental Facility," *ASME JOURNAL OF TURBOMACHINERY*, Vol. 109, pp. 520–526.
- Deutsch, S., and Zierke, W. C., 1988a, "The Measurement of Boundary Layers on a Compressor Blade in Cascade: Part 2—Suction Surface Boundary Layers," *ASME JOURNAL OF TURBOMACHINERY*, Vol. 110, pp. 138–145.
- Deutsch, S., and Zierke, W. C., 1988b, "The Measurement of Boundary Layers on a Compressor Blade in Cascade: Part 3—Pressure Surface Boundary Layers and the Near Wake," *ASME JOURNAL OF TURBOMACHINERY*, Vol. 110, pp. 146–152.
- Elazar, Y., and Shreeve, R. P., 1990, "Viscous Flow in a Controlled Diffusion Compressor Cascade With Increasing Incidence," *ASME JOURNAL OF TURBOMACHINERY*, Vol. 112, pp. 256–266.
- Hobbs, D. E., and Weingold, H. D., 1984, "Development of Controlled Diffusion Airfoil for Multistage Compressor Applications," *ASME Journal of Engineering for Gas Turbines and Power*, Vol. 106, pp. 271–278.
- Kang, S. H., Lee, J. S., Kim, Y. H., and Kim, K. Y., 1992, "Numerical Calculations of the Turbulent Flow Through a Controlled Diffusion Compressor Blade in Cascade," *Proceeding of ISROMAC-4*.
- Karki, K. C., 1986, "A Calculation Procedure for Viscous Flows at All Speeds in Complex Geometries," Ph.D. Thesis, University of Minnesota, Minneapolis.
- Karki, K. C., and Patankar, S. V., 1988, "Calculation Procedure for Viscous Incompressible Flows in Complex Geometries," *Numerical Heat Transfer*, Vol. 14, pp. 295–307.
- Kim, Y. H., 1991, "Numerical Study on Viscous Flows Around the Two-Dimensional Compressor Cascade," M.S. Thesis, Seoul N. University.
- Lakshminarayana, B., 1991, "An Assessment of Computational Fluid Dynamic Techniques in the Analysis and Design of Turbomachinery—The 1190 Freeman Scholar Lecture," *ASME Journal of Fluids Engineering*, Vol. 113, pp. 315–352.
- Lauder, B. E., and Sharma, B. I., 1974, "Application of the Energy-Dissipation Model of Turbulence to the Calculation of Flow Near a Spinning Disc," *Letters in Heat and Mass Transfer*, Vol. 1, p. 131.
- Mayle, R. E., 1991, "The Role of Laminar–Turbulent Transition in Gas Turbine Engines, The 1991 IGTI Scholar Lecture," *ASME JOURNAL OF TURBOMACHINERY*, Vol. 113, pp. 509–537.

Experimental Investigation of the Flow in Diffusers Behind an Axial Flow Compressor¹

T. Zierer

Gas Turbine Development,
ABB Power Generation Limited,
Baden, Switzerland

The flow fields of four diffusers situated at the rear of a one-stage axial flow compressor were experimentally investigated. Through modification of the compressor operating point, a wide range of variations of the side wall boundary layers and the radial velocity distribution outside of the boundary layers at diffuser inlet could be achieved. The three-dimensional flow field at both diffuser inlet and outlet is analyzed. Changes of inlet blockage and radial velocity distribution and their resulting effects on pressure recovery are thoroughly presented. Compared with the results of measurements at diffusers, typically with ducted flow inlet conditions, higher values of pressure recovery are observed. Established design rules, based on investigations of diffusers with carefully developed inlet flow, are checked regarding their applicability for diffusers in turbomachine environments.

1 Introduction

Annular diffusers are used in turbomachine environments for a reduction of the velocity at the exit of the bladed duct. Due to the application of a diffuser downstream of a compressor, the pressure ratio from flange to flange is increased. A diffuser downstream of a turbine extends the effective enthalpy difference for the bladed part of the machine. A good diffuser design is very important especially for efficiency and performance of one-stage machines, because the kinetic energy at the blading exit can be up to 50 percent of the energy that is transformed by the machine. Nevertheless, diffusers for multistage machines also require a careful design. Due to the large power of such machines, the kinetic energy at the blading exit can be in the magnitude of several MW.

Up to the present, most investigations of diffusers were carried out without a turbomachine installed upstream of the diffuser. They contributed fundamental knowledge about the design of diffusers and the flow in diffusers at different operating conditions. The most notable contribution concerning annular diffusers is perhaps that due to Sovran and Klomp (1967), who tested more than 100 annular diffuser geometries with different area and length ratios. All the tests were carried out with ducted flow inlet conditions and a thin inlet boundary layer.

A variation of the inlet conditions was often carried out by

changing the inlet blockage B_1 . As a result of their investigations of plane and conical diffusers, Reneau et al. (1967) and Sprenger (1959) concluded that an increase of inlet blockage leads to a poorer pressure recovery. Another parameter that influences the flow in the diffuser is the swirl at the diffuser inlet. The radial pressure gradient resulting from the swirl leads to poorer turbulent mixing in the hub boundary layer of annular diffusers. Lohmann et al. (1979) report as a result of their investigation of the swirling flow in annular diffusers, that the onset of flow separation at the diffuser hub occurs earlier than with axial inlet flow. Wolf and Johnston (1969) investigated the influence of nonuniform inlet flow distributions on the pressure recovery in plane diffusers. Inlet profiles with a radial velocity gradient in the core flow resulted in a heavily distorted outlet flow with a larger velocity gradient than at the inlet, due to the deceleration of the flow. Because of this nonuniform velocity distribution at the diffuser exit, the authors obtained a lower pressure recovery than Reneau et al. (1967), who carried out their experiments with plane inlet conditions.

It is characteristic for the inlet flow of a diffuser in turbomachine environments to have a high level of turbulence and to have the wakes of the blading situated upstream of the diffuser. Compared to ducted flow inlet conditions, a better pressure recovery may be observed because of the increased turbulent mixing in the diffuser. Both Stevens and Williams (1980) and Hoffmann and Gonzales (1984) obtained a considerable increase in pressure recovery compared to ducted flow inlet conditions, when they increased the turbulence level at the diffuser inlet.

Beside investigations showing the basic influence of these parameters, experimental investigations with a real turbomachine situated upstream of the diffuser are also important. Only such experiments show which magnitude those param-

¹The investigation was carried out during the author's previous affiliation at the Thermal Turbomachinery Department, Technische Hochschule Darmstadt, Darmstadt, Federal Republic of Germany.

Contributed by the International Gas Turbine Institute and presented at the 38th International Gas Turbine and Aeroengine Congress and Exposition, Cincinnati, Ohio, May 24–27, 1993. Manuscript received at ASME Headquarters March 17, 1993. Paper No. 93-GT-347. Associate Technical Editor: H. Lukas.

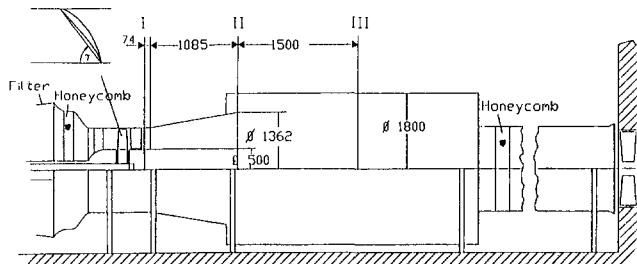


Fig. 1 Test facility with control surfaces I, II, III

ters have in the turbomachine and how they influence the flow in the diffuser, when they are superimposed by other parameters such as swirl and velocity distribution at the diffuser inlet.

The present paper is a summary of a detailed investigation of the flow in annular diffusers with inlet conditions typical for an axial flow compressor (Zierer, 1992). Due to the wakes of the compressor blading the inlet flow is characterized by a high level of nonuniformity in the velocity distribution versus radius and versus circumference as well as a high degree of turbulence. As in most of the cases the last row of a compressor is a stator, the inlet flow of the diffuser situated downstream of a compressor is without swirl, independent of the operating conditions.

The measurements were carried out with a one-stage axial flow compressor. They cover a wide operating range of the machine. This results in a wide range of different inlet conditions for the following diffuser. Their impact on the flow in diffusers with different area ratios but constant length shall be discussed. Furthermore, established design rules, based on experimental investigations of diffusers with ducted flow inlet conditions, shall be checked regarding their applicability for diffusers in turbomachine environments.

2 Experimental Apparatus

Figure 1 shows a cross section of the test rig. The air is drawn from the laboratory through a nozzle to the compres-

or blading. The annular diffuser is mounted behind the stage. The diffuser walls are hydraulically smooth. Behind the diffuser the flow expands into a settling section followed by a tube where the mass flow can be determined.

The compressor stage is designed for constant work versus radius. The design volume flow coefficient is $\varphi = 0.335$. The blading profiles are based on the NACA 65 series according to a design procedure of Lieblein (1965). The solidity of the stator ranges from 2.4 at the hub to 1.1 at the tip (25 vanes). The ratio of compressor hub to tip is 0.5. The flow in the rotor has been thoroughly investigated by Pfeil and Sieber (1986b).

During the measurements, the volume flow in the system was varied at constant 2000 rpm by adjusting a throttle device at the exit of the facility. A desired volume flow coefficient could be regulated within 1 percent. The investigations were carried out at design stagger angle of the rotor blading $\Delta\gamma = 0$ deg as well as at a smaller stagger angle $\Delta\gamma = -8$ deg, respectively. The stagger angle of the stator was kept constant throughout all measurements. Due to the sufficient solidity of the stage blading, the swirl at the exist of the stage did not exceed ± 5 deg. At maximum mass flow ($\Delta\gamma = 0$ deg) the mean velocity at the stator exit amounted to 40 m/s. The corresponding Reynolds number $Re = (c_1 \cdot h_1)/\nu$ is 6.6×10^5 , the Mach number $M = 0.1$.

All measurements were carried out with pneumatic probes (five-hole probes and pitot probes). Both at diffuser inlet and diffuser outlet probe traverses were carried out versus radius and circumference. The static pressure distribution along the diffuser was measured with static pressure taps at hub and casing.

Probe positioning as well as data recording was performed by a microcomputer. Depending on the measuring position, the signals have different fluctuations versus time. To obtain a representative mean value, a sufficient number of samples was taken, from which a mean value was calculated. The required number of samples was determined during the measurements for each measurement position. The confidence interval achieved, resulting from the standard deviation of the fluctuations and the number of samples taken ensures that the difference between the real mean value and

Nomenclature

A = cross-sectional area
 AR = area ratio = A_2/A_1
 B_1 = blocked area at diffuser inlet
 c = velocity
 c_p = pressure recovery coefficient
 d = diameter
 h = channel height
 H_{12} = $\delta_{1ax}/\delta_{2ax}$
 l = approach length before the diffuser
 L = averaged wall length for annular diffusers
 \dot{m} = mass flow
 M = Mach number
 p = static pressure
 P = total pressure
 r = radius
 Re = Reynolds number
 t = pitch
 u = axial velocity
 U_∞ = velocity at the edge of the boundary layer
 u_t = rotor speed at blade tip
 \dot{V} = volume flow

Δx_i = distance diffuser inlet/tip of cone
 y' = coordinate in circumferential direction
 y^* = coordinate perpendicular to centerline, counting from the wall
 α = energy parameter

$$= \frac{1}{A} \int_A \frac{c^2 c_{ax}}{\bar{c}_{ax}^3} dA$$

 β = momentum parameter

$$= \frac{1}{A} \int_A \frac{c_{ax}^2}{\bar{c}_{ax}^2} dA$$

 $\Delta\gamma$ = deviation of the rotor stagger angle from the design point stagger angle
 δ = boundary layer thickness
 δ_{1ax} = axisymmetric displacement thickness
 δ_{2ax} = axisymmetric momentum thickness

ζ_D = total pressure loss coefficient
 ν = kinematic viscosity
 ρ = density
 φ = volume flow coefficient

$$= \dot{V}/(A \cdot u_t)$$

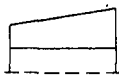
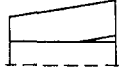
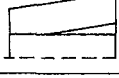
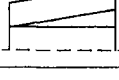
Subscripts

ax = axial
 i = inner
 o = outer
 t = tip
 1 = diffuser inlet (control surface I in Fig. 1)
 2 = diffuser outlet (control surface II in Fig. 1)
 3 = settling section (control surface III in Fig. 1)

Superscripts

$\bar{\quad}$ = area averaged
 \sim = mass averaged
 $'$ = fluctuating quantity

Table 1 Tested diffuser geometries

	d_{1i} [mm]	d_{1a} [mm]	d_{2i} [mm]	d_{2a} [mm]	Δz_i [mm]	l_{ax} [mm]	$\frac{L}{h_1}$ [-]	AR [-]
	500	1000	500	1362	-	1085	4.36	2.14
	500	1000	627	1362	713	1085	4.37	1.95
	500	1000	738	1362	389	1085	4.39	1.75
	500	1000	855	1362	40	1085	4.40	1.50

the mean value averaged from the samples is less than 0.4 percent of the measuring range with a statistic security of 95 percent. The resulting statistic security of velocity and pressure recovery is $c/\bar{c} = 1.5$ percent (diffuser inlet), $c/\bar{c} = 5.5$ percent (diffuser outlet), and $c_p = 4.5$ percent. This was solely not reached at total pressure measurements in separated flow regions.

The diffuser geometries tested are listed in Table 1. At a constant length ratio $L/h_1 = 4.4$ the area ratio AR ranges from 1.5 to 2.14. The total area ratio from diffuser inlet to the settling section amounts to $A_3/A_1 = 4.4$. The diffuser with $AR = 1.95$ is designed from maximum pressure recovery at a prescribed length according to the design criteria of Sovran and Klomp. It is located on the c_p^* line in the diffuser performance map of the authors. Therefore, even at healthy inlet conditions in the larger diffuser with $AR = 2.14$ a flow separation at the diffuser exit must be expected. The remaining two diffusers are designed more conservatively. At the same length ratio they have lower area ratios.

The investigations of Sovran and Klomp showed that the influence of the wall shape is small compared to the influence of the main dimensions, area ratio and length ratio. Investigations of plane diffusers by Carlson et al. (1967) showed that a slight increase in c_p could be reached for diffusers situated below the c_p^* line when the side walls had a bell shape. Considering these results, the reduction of the area ratio at constant length ratio was incorporated by moving a cone at the diffuser hub toward the diffuser inlet. The cone was divided in three axial parts, so that casing and hub of the diffuser always ended at the same axial position. The resulting geometries all lead to a favorable increase rate of cross-sectional area versus diffuser length, because the diffusion rate is reduced at the end of the diffuser where the boundary layers are thick. Therefore, it was expected that a difference in pressure recovery at a fixed operation point is predominantly caused by a different area ratio and not by the different wall shapes.

3 Velocity Distributions

Due to the streamline curvature at the diffuser inlet, the static pressure in this plane is not constant. Preparatory measurements with a five-hole probe showed that the static pressure distribution versus radius could be approximated well by a linear interpolation between three measurement points (hub, half-channel height, and casing). Therefore, all velocity distributions and the performance coefficients ζ and c_p were evaluated with a static pressure distribution interpolated from the three measuring points mentioned above.

Figure 2 shows the velocity distribution behind a stator blade. Probe traverses were carried out behind three differ-

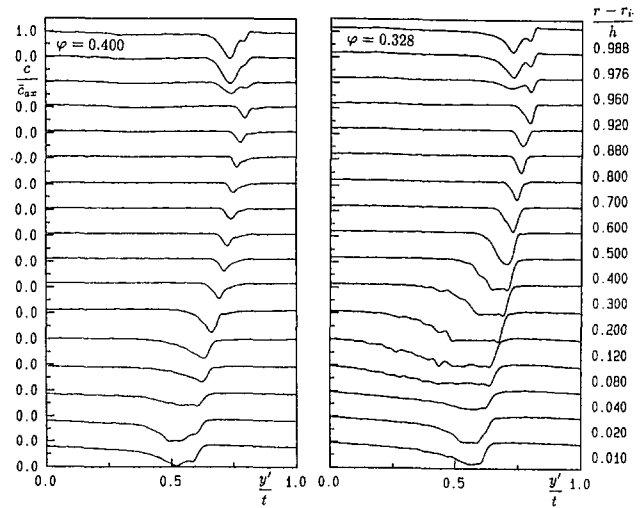


Fig. 2 Comparison of the flow field at diffuser inlet at different volume flow coefficients ($AR = 2.14$, $\Delta\gamma = 0$ deg)

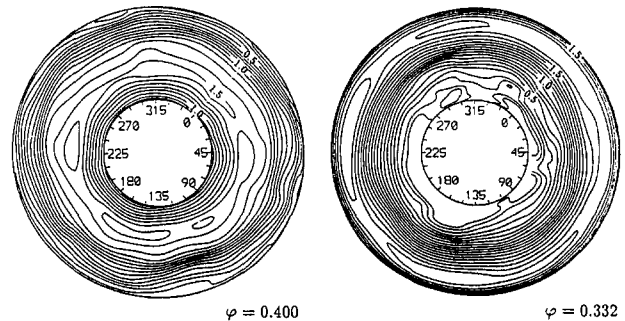


Fig. 3 Contour lines of constant velocity c_2 / \bar{c}_{ax} at diffuser exit ($AR = 2.14$, $\Delta\gamma = 0$ deg)

ent stator blades. Thereby, good circumferential symmetry was observed. The largest wakes occur at the hub. Here the flow separates at the suction side at small volume flow coefficients ϕ due to the increased loading of the blading.

For almost the same operation points the velocity distribution at diffuser exit is shown in Fig. 3. In this plane, a good circumferential symmetry was observed as well. At small volume flow coefficients a separated region at the hub can be seen. Only in this zone the flow is not axisymmetric. In fact, the flow here was very unsteady, so that the time-averaged mean values could not be evaluated with the statistical security mentioned above. Furthermore, the velocity gradient in this zone is very small. Both effects contribute to comparatively large deflections of the contour lines of constant velocity in the separated zone.

In Figs. 4 and 5 the circumferentially area-averaged velocity distributions at diffuser inlet are compared with their corresponding velocity distributions at the diffuser outlet. At the design point stagger angle the inlet velocity profiles are characterized by a constant velocity in the core flow. When the mass flow is reduced, the hub sidewall boundary layer increases strongly.

The inlet velocity distributions at smaller stagger angle ($\Delta\gamma = -8$ deg) differ from the profiles at design point stagger angle. Here the core flow is characterized by a radial velocity gradient combined with a high energetic maximum near the hub. As in the case $\Delta\gamma = 0$ deg the boundary layer at the hub increases when the volume flow is reduced.

The velocity distributions of the hub and casing boundary layer at both diffuser inlet and diffuser outlet were compared with the two-dimensional velocity model of Pfeil and Müller

(1989). For turbulent flows, this model is an extension of Cole's model. Except for the cases with strong separation at the stator blading (i.e., $\Delta\gamma = 0$ deg, small φ) a good agreement with the model was observed. Therefore, the circumferentially averaged flow field in the diffuser may be considered as two dimensional, if stage loading is not too high.

In Figs. 6 and 7 the axisymmetric displacement thickness δ_{1ax} and the shape parameter H_{12} are plotted:

$$\delta_{1ax} = \int_0^\delta \left(1 - \frac{u}{U_\infty}\right) \left(1 + \frac{y^*}{r_i}\right) dy^* \quad (1)$$

For the casing wall r_i must be replaced by $-r_o$. Due to the nonuniformity of the core flow the distinction between the boundary layer and the core flow is difficult. Therefore, the boundary layer thickness δ resulting from the velocity model was taken as the upper integration boundary and displacement thickness calculated by integration of the measured distribution up to this boundary.

At constant stagger angle the loading of the blading in-

creases with decreasing volume flow coefficient. This results in a strong growth of the displacement thickness at the hub at the diffuser inlet. Nevertheless, the shape parameter remains almost constant and at low values. At the casing the flow is nearly independent of the loading.

Focusing on the results with constant velocity versus radius in the inlet coreflow (i.e., $\Delta\gamma = 0$ deg), it can be seen that increasing displacement thickness leads to flow separation along the diffuser at the hub. As expected, the separation occurs earlier (i.e., at a larger volume flow coefficient) when the area ratio is increased. As mentioned above, in contrast to the displacement thickness, the shape parameter at the diffuser inlet remains nearly constant throughout all operating points. Therefore, it can be concluded from the present experiments that the shape parameter is not the quantity that determines the behavior of the flow in a diffuser downstream of a compressor when the operation point is changed. While the displacement thickness of the sidewall boundary layer increases with the stage loading, the shape parameter remains nearly constant. Therefore, the displacement thickness

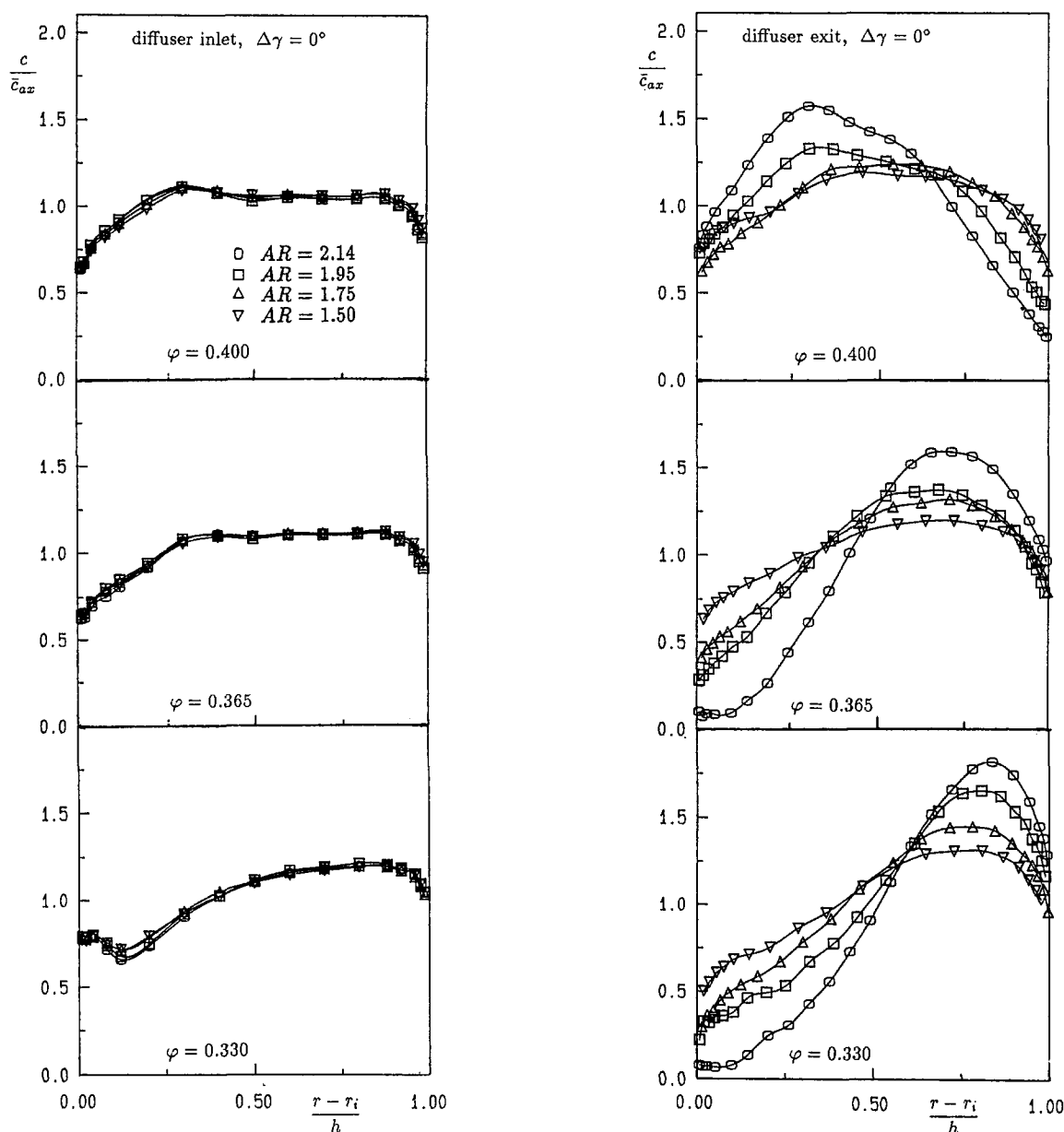


Fig. 4 Dependence of the velocity profiles at diffuser exit on the pitch-averaged inlet profile and the area ratio ($\Delta\gamma = 0$ deg)

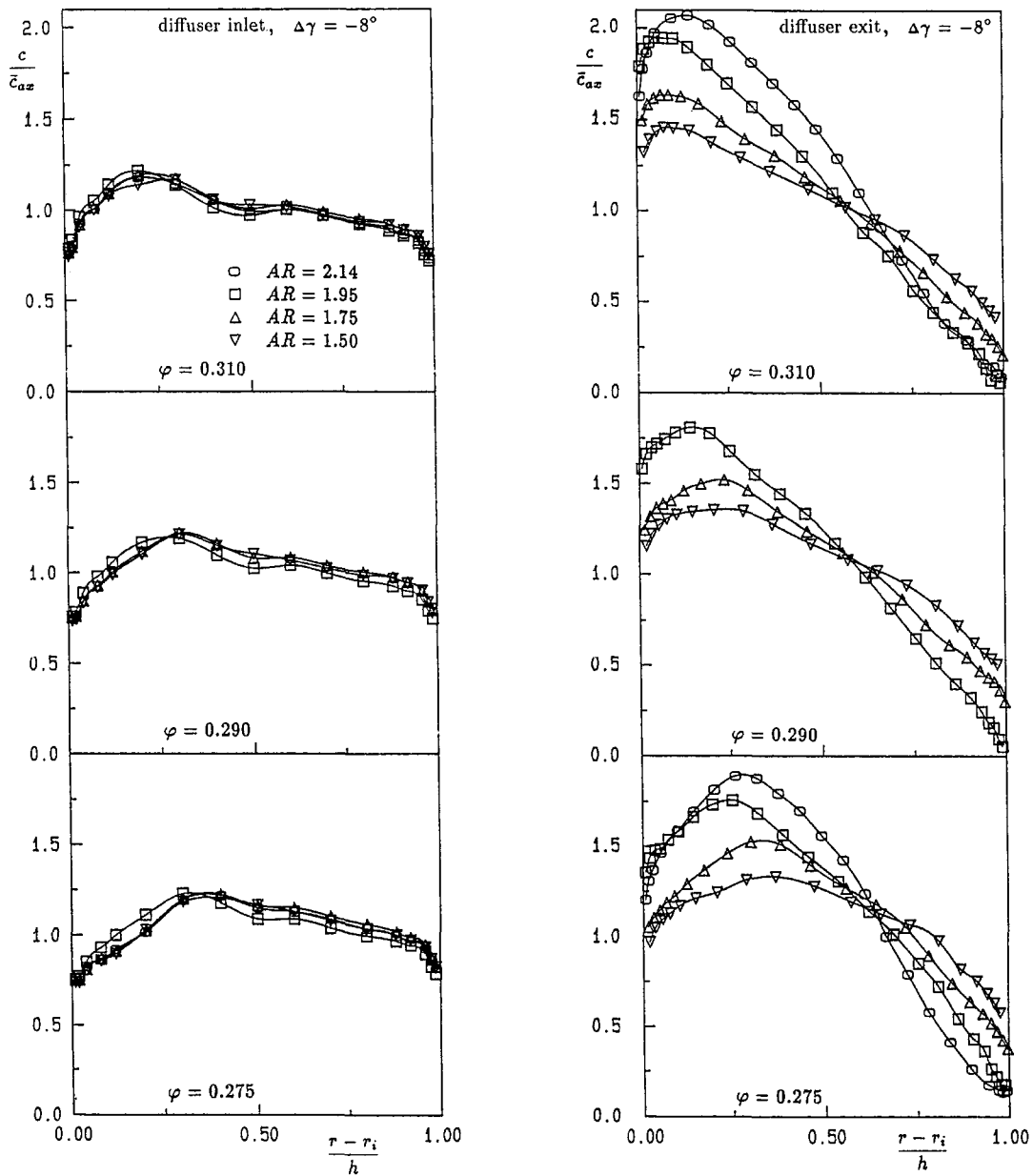


Fig. 5 Dependence of the velocity profiles at diffuser exit on the pitch-averaged inlet profile and the area ratio ($\Delta\gamma = -8$ deg)

is the determining boundary layer parameter. Moreover, as a result of their numerical investigation of the flow in conical diffusers, Schlichting and Gersten (1961) state that the growth of the boundary layer along a diffuser depends only weakly on the shape parameter at the diffuser inlet. They established the momentum thickness as the determining quantity. The results of this paper also indicate that the thickness of the boundary layer is an important parameter for the flow downstream in the diffuser. Because the shape parameter did not vary in the course of the experiments, no conclusions can be made here as to whether displacement thickness or momentum thickness has the determining influence.

Besides the influence of the inlet boundary layer on the flow in the diffuser, there is also a strong influence of the radial velocity distribution outside the boundary layers. This is shown by a comparison of the measurements at different stagger angles. At the design point stagger angle of the rotor ($\Delta\gamma = 0$ deg), the velocity distribution versus radius remains almost constant in the core flow for all volume flow rates. Here, the flow separates along the hub of the diffuser as the

hub boundary layer at the diffuser inlet increases. In the case $\Delta\gamma = -8$ deg the inlet velocity is characterized by a radial velocity gradient combined with a high energetic maximum at the hub. Although the inlet boundary layers are almost the same as in the case $\Delta\gamma = 0$ deg, i.e., the hub boundary layer is much thicker than the casing boundary layer, a separation at the diffuser casing occurs here. The resulting nonuniformity at the diffuser exit is much bigger than at hub separation.

In sum it may be said that small changes of the inlet profile do have a large influence on the flow in the diffuser, especially when the area ratio of the diffuser is large at a small length ratio. Thereby, axisymmetric separation at one sidewall leads to a more stable flow pattern at the opposite wall.

The boundary layer parameters δ_1 and H_{12} describe the circumferentially averaged velocity profiles at one wall. An integral quantity describing the velocity distribution in an entire cross section is the energy coefficient α . To give a measure of the magnitude of the flow nonuniformity the energy coefficient is plotted in Fig. 8. At the diffuser inlet it

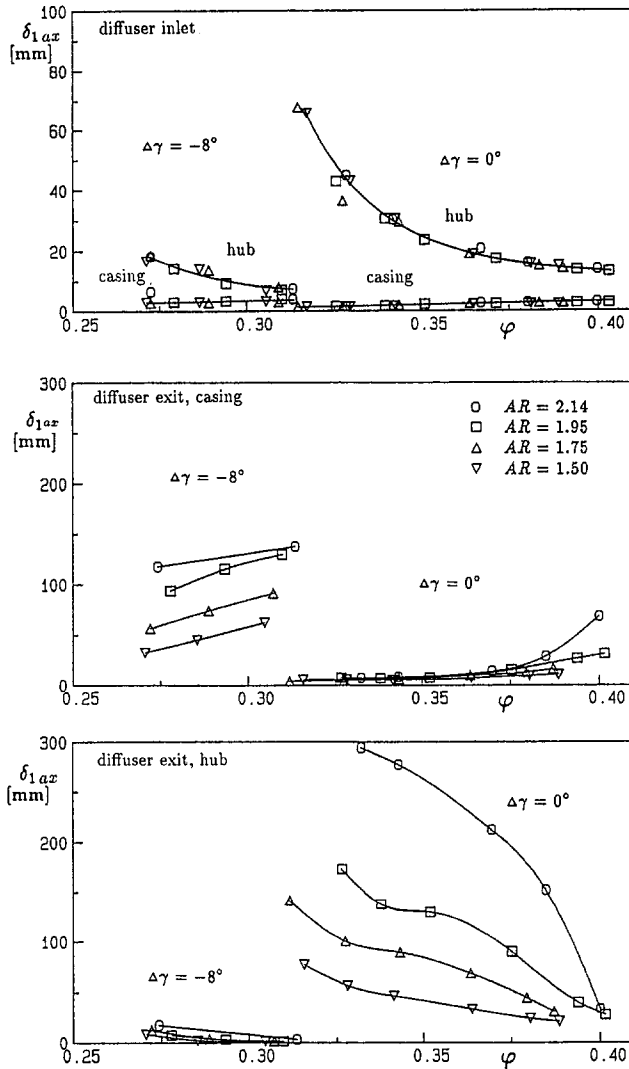


Fig. 6 Displacement thickness δ_{1ax} at both diffuser inlet and diffuser exit

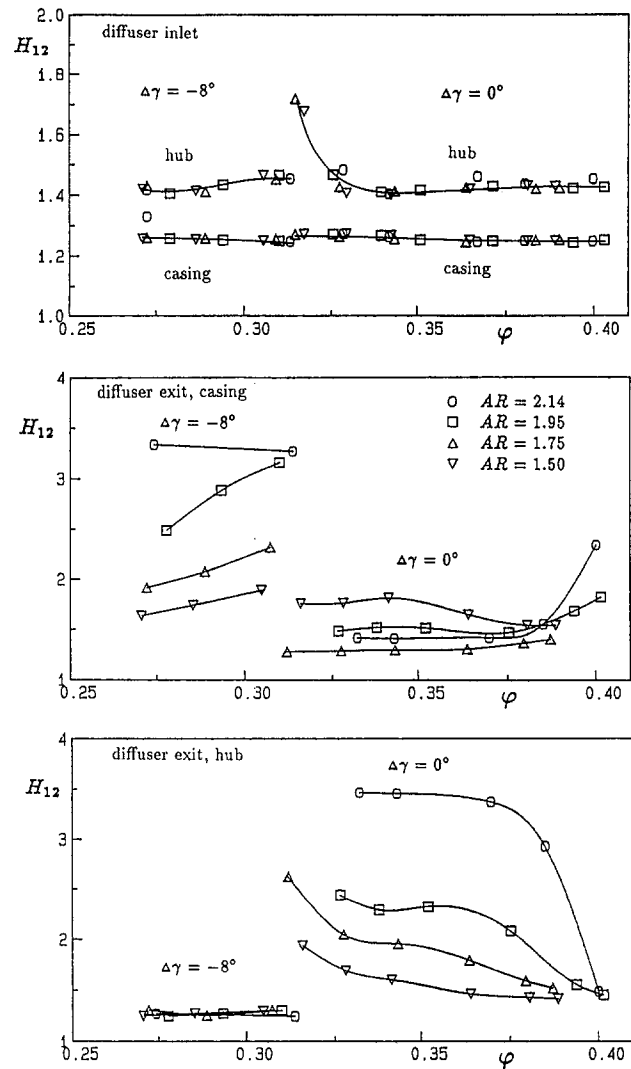


Fig. 7 Shape parameter H_{12} at both diffuser inlet and diffuser exit

is determined half from the radial velocity distribution and half from the wakes of the blading, respectively. At the diffuser exit, the portion due to circumferential nonsymmetry is negligible. This shows that at turbomachinery inlet conditions the energy coefficient is considerably higher compared to ducted flow inlet conditions. For example, Stevens and Williams (1980) report energy coefficients between 1.02 and 1.06, depending on the approach length of the annular duct upstream of the diffuser.

4 Performance Evaluation

From the previous section it may be concluded that the radial velocity distribution and the displacement thickness are the most important inlet flow parameters influencing the flow in the diffuser when the operating point of the compressor is altered. In this section, the impact on pressure recovery of varying these parameters shall be discussed in more detail.

For a one-dimensional description of the diffuser flow, the total pressure loss coefficient and the pressure recovery coefficient are applied. These are defined by

$$\zeta = \frac{2\Delta\bar{P}}{\rho\alpha_1\bar{c}_{1ax}^2} \quad (2)$$

and

$$c_p = \frac{2(\bar{p}_2 - \bar{p}_1)}{\rho\alpha_1\bar{c}_{1ax}^2} \quad (3)$$

The energy parameter α is defined by the energy equation and describes the additional kinetic energy the flow contains due to its radial and circumferential nonuniformity compared to a flow with a plug profile:

$$\bar{p}_1 + \frac{\rho}{2}\alpha_1\bar{c}_{1ax}^2 = \bar{p}_2 + \frac{\rho}{2}\alpha_2\bar{c}_{2ax}^2 + \Delta\bar{P} \quad (4)$$

The analysis of the measurements showed that the difference between the area-weighted and mass-weighted mean value of the static pressure was negligible. To simplify the evaluation procedure the area-weighted mean value was applied for the calculation of both the pressure recovery coefficient and the total pressure loss coefficient.

For the one-dimensional description of the influence of both hub and casing boundary layer the blocked area (Sovran and Klomp, 1967; Klein, 1981) is applied:

$$B_1 = \frac{2\pi(r_{li}\delta_{1axi} + r_{lo}\delta_{1axo})}{\pi(r_{lo}^2 - r_{li}^2)} \quad (5)$$

When the operating point of the compressor is altered, several parameters influencing pressure recovery in the diffuser are changing. Therefore, the pressure recovery coefficient c_p is plotted in Fig. 9 versus the volume flow coefficient

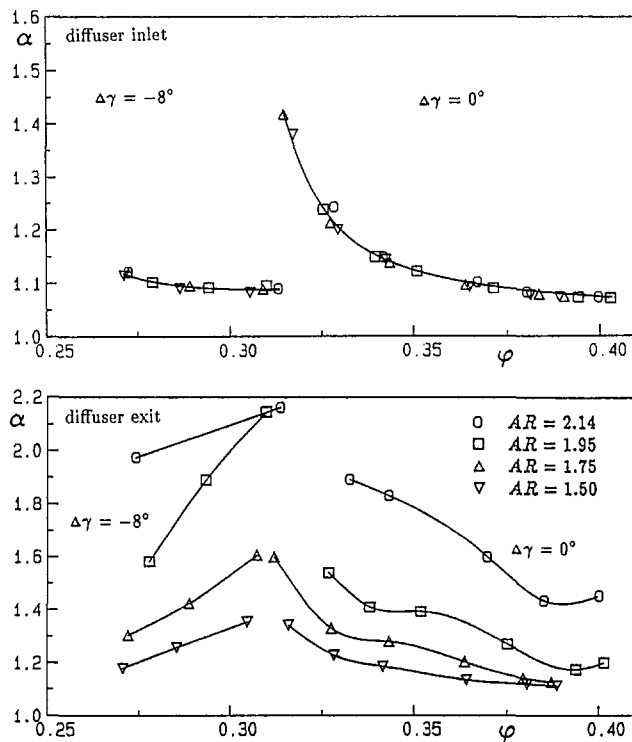


Fig. 8 Energy parameter α at both diffuser inlet and diffuser outlet

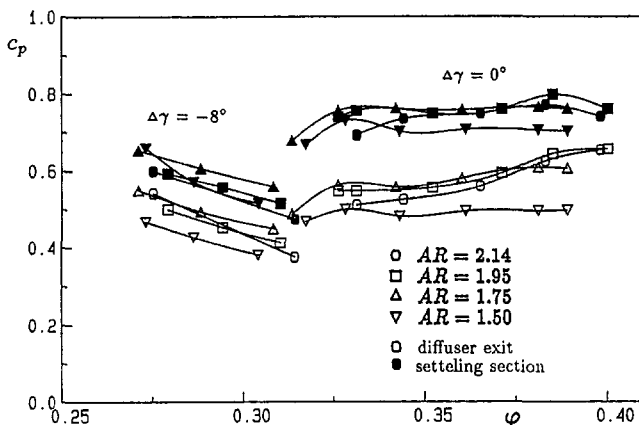


Fig. 9 Dependence of pressure recovery c_p on area ratio and operation point of the compressor

ϕ . Obviously the volume flow coefficient is not a determining parameter for the flow in the diffuser. It is only used for a distinction of the different inlet conditions resulting from the different operating points.

In the control plane diffuser exit at the design stagger angle ($\Delta\gamma = 0$ deg) the maximum pressure recovery is obtained at an area ratio of 1.95, almost independent of the operating point. Here, over all operating points the change of the flow field at the diffuser inlet is dominated by the change in the inlet blockage. The independence of the optimum area ratio on the inlet blockage is in close agreement with Sovran and Klomp's analysis (1967) of the flow in conical and plane diffusers having ducted flow inlet conditions. They report only a negligible change in the c_p^* line when the blockage at the diffuser inlet was increased, implying that the optimum area ratio, leading to maximum pressure recovery at constant length ratio, is independent of the inlet blockage. This also applies to diffusers in turbomachine environments. Moreover, the diffuser with the area ratio 1.95 agrees very well with the c_p^* line in the diffuser performance map by Sovran

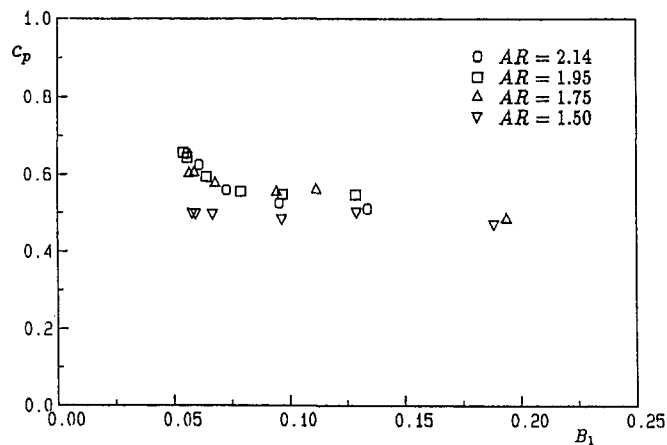


Fig. 10 Dependence of pressure recovery c_p at diffuser exit on inlet blockage B_1 (constant velocity versus radius in the inlet core flow)

and Klomp. This demonstrates that the results of their systematic investigation are often a good tool for designing diffusers in turbomachine environments, even though the data were derived from ducted flow inlet conditions. Nevertheless, the use of these correlations should be restricted to inlet conditions that resemble those used by Sovran and Klomp. Typically, for a turbomachine situated upstream of a diffuser, the increased inlet turbulence and the wakes present a slight improvement of these inlet conditions, leading to a higher pressure recovery yet no change in the optimum area ratio. This is no longer true for heavily distorted inlet flows, as the measurements at $\Delta\gamma = -8$ deg show. Compared to the increasing blockage, the particular radial velocity gradient imposed on the core flow at the experiments represents a much worse distortion of the inlet flow. Therefore, the maximum pressure recovery is obtained at smaller area ratios.

In the settling section a considerable increase of the pressure recovery is observed. This indicates the importance of such a device behind a diffuser. The additional pressure recovery is caused by both an increase of the area ratio and an equalization of the velocity profile. From the momentum equation

$$\Delta c_p = 2 \left(\frac{A_1}{A_3} \right)^2 \left(\beta_2 \frac{A_3}{A_2} - \beta_3 \right) \quad (6)$$

with

$$\beta = \int_A \frac{c^2}{c_{ax}^2} dA \quad (7)$$

it can be concluded that a high pressure recovery is obtained both by means of large area ratios A_3/A_2 and by a high nonuniformity of the flow field at the diffuser exit resulting in large momentum parameters β_2 . Therefore, the differences concerning c_p , resulting from different inlet conditions or diffuser area ratios, become smaller in the settling section. At constant area ratios, a decrease in c_p in plane II due to a distorted inlet flow results in a larger nonuniformity of the velocity at diffuser exit increasing the pressure recovery in the settling section. By analogy, poor pressure recovery due to a small diffuser area ratio A_2/A_1 is also compensated by an increased pressure recovery in the settling section because of the increased area ratio A_3/A_2 .

The examination of the velocity plots shows that the displacement thickness is an important quantity, which influences the flow in the diffuser if the radial velocity distribution at the inlet remains constant. Figure 10 shows the dependence of the pressure recovery coefficient on inlet

blockage and area ratio. With increasing blockage a poorer pressure recovery is obtained. When the area ratio is increased, a growing influence of the inlet blockage on pressure recovery can be established: Here a change of blockage especially at small values of B_1 is accompanied by a rapid decrease of c_p . From the velocity plots it can be seen that in this particular case the change of the inlet blockage is accompanied by the onset of separation at the diffuser hub.

Obviously, compared to the influence of the inlet blockage, a change in the radial velocity distribution outside the boundary layer has a more pronounced effect on pressure recovery. The operating points at $\Delta\gamma = -8$ deg are characterized by a radial velocity gradient in the inlet core flow, leading to a high energetic maximum near the hub. The displacement thickness is of the same magnitude as at $\Delta\gamma = 0$ deg and large volume flow coefficients; however, there the velocity versus radius in the core flow at the diffuser inlet is constant. At $\Delta\gamma = -8$ deg the particular radial velocity gradient at the experiments combined with the bend at the casing causes a separation at the casing leading to a considerably lower pressure recovery. The flow has to overcome a higher pressure rise at the diffuser casing than at the diffuser hub due to the convex turning, whereby the inlet flow has the lowest energy level at the casing resulting from the radial velocity distribution. Here, at $\Delta\gamma = -8$ deg even a rise in pressure recovery can be observed with increasing blockage, which increases with decreasing volume flow coefficient. Thus the improved pressure recovery is caused by the equalization of the inlet core flow at lower volume flow coefficients.

Table 2 lists typical values of total pressure loss. Besides the diffuser loss depending on area ratio and radial velocity distribution at the diffuser inlet, this total pressure drop also contains the loss due to the decay of the wakes of the compressor. The lowest total pressure losses are achieved at small area ratios due to the weak deceleration of the flow. Stevens and Wray (1985) report losses between 14 and 18 percent in a precombustor diffuser behind a one-stage axial flow compressor.

From the energy equation the relation

$$c_p = 1 - \frac{\alpha_2 \bar{c}_2^2}{\alpha_1 \bar{c}_1^2} - \zeta_{12} \quad (8)$$

can be derived. This shows that poor pressure recovery is caused by total pressure losses and poor velocity deceleration. Depending on operating conditions and area ratio the total pressure loss amounts to 5–14 percent of the dynamic

Table 2 Typical values of total pressure loss $\zeta_{12} = 2(\bar{p}_1 - \bar{p}_2) / \rho \alpha_1 \bar{c}_1^2$

	$AR = 1.5$	$AR = 1.95$
$\varphi = 0.38$ ($\Delta\gamma = 0^\circ$)	5%	8%
$\varphi = 0.33$ ($\Delta\gamma = 0^\circ$)	5%	13%
$\varphi = 0.30$ ($\Delta\gamma = -8^\circ$)	6%	8%
$\varphi = 0.28$ ($\Delta\gamma = -8^\circ$)	6%	12%

pressure at the diffuser inlet. Therefore, the total pressure loss as a fraction of the difference between the maximum obtainable pressure recovery and the measured value only amounts to

$$\frac{\zeta_{12}}{1 - c_p} = 0.1 \dots 0.3. \quad (9)$$

The larger portion is caused by an insufficient diffusion. At large area ratios the reason for insufficient diffusion is a nonuniform velocity distribution at the diffuser exit. At smaller area ratios the energy parameter at the diffuser exit decreases, but this decrease is accompanied by a corresponding increase of the area-averaged velocity \bar{c}_2 .

A comparison of the pressure recovery obtained at the diffuser exit with the results from other authors shows that in diffusers situated downstream of a turbomachine a higher c_p value is obtained. Table 3 lists the results of several experimental investigations of diffusers with nearly identical geometries. Stevens and Williams (1980) report a c_p value of 0.5 for ducted flow inlet conditions. Comparable, regarding the inlet blockage, are the measurements at high volume flow coefficient at $\Delta\gamma = 0$ deg where a c_p value of 0.67 is obtained. Compared to the present investigations, Quest and Scholz (1981) report a considerably higher pressure recovery in a diffuser situated downstream of a one-stage axial turbine. This may be caused by smaller sidewall boundary layers and the leakage flow at the casing. The mean values of the state variables are calculated using an averaging procedure by Kreitmeier (1992), which takes into account all balance equations and is characterized by hypothetical reversible and irreversible equilibration processes. For incompressible flow without swirl the reversible mean values are close to the mean values used in this paper. The pressure recovery measured by Adenubi (1976) in a compressor diffuser is considerably smaller. Moreover, he relates the pressure rise to the dynamic pressure calculated from the area-averaged mean value of the velocity, which leads to larger c_p values. The poor pressure recovery may be explained by the inlet conditions, which were characterized by a radial velocity gradient with a maximum near the hub as in the case $\Delta\gamma = -8$ deg in the present investigations. The c_p value of this operating point calculated with the area-averaged mean value of the velocity is of the same magnitude as in Adenubi's investigations.

The higher pressure recovery in turbomachine environments is due to the increased turbulence at the diffuser inlet. The compressor used upstream of the diffusers investigated in this paper is the same as that described by Pfeil and Göing (1987). He reported an axial degree of turbulence

$$Tu = \frac{\sqrt{u'^2}}{\bar{u}} = 7 \text{ percent} \quad (10)$$

outside of the stator wakes and outside of the sidewall boundary layers. The averaged value must be considerably higher. A part of this turbulence is due to the periodic oscillations, induced by the rotor, but Adenubi (1976) reports from his measurements behind a one-stage axial flow com-

Table 3 Comparison of several experimental diffuser investigations; *) $c_p = (\bar{p}_2 - \bar{p}_1) / (\rho / 2 c_1^2)$

Author	AR	L/h_1	$Re = \frac{\rho \bar{c}_1 h_1}{\mu}$	B_1	c_p	inlet conditions
Stevens/Williams	2.0	5.0	$0.55 \cdot 10^5$	0.028	0.505	annular duct, approach length $l/h_1 = 7.3$
Stevens/Williams	2.0	5.0	$0.55 \cdot 10^5$	0.109	0.445	annular duct, approach length $l/h_1 = 44.0$
Stevens/Williams	2.0	5.0	$0.55 \cdot 10^5$	0.044	0.595	annular duct, approach length $l/h_1 = 7.3$ with coarse grid for turbulence increase
Quest/Scholz	2.05	4.0	$2.0 \cdot 10^5$		0.71	diffuser behind turbine
Adenubi	2.0	4.5	$6.0 \cdot 10^5$	0.085	0.58*	diffuser behind compressor
Zierer	1.95	4.4	$6.5 \cdot 10^5$	0.056	0.67	diffuser behind compressor ($\varphi = 0.40$)
Zierer	1.95	4.4	$4.5 \cdot 10^5$	0.054	0.56*	diffuser behind compressor ($\varphi = 0.28$) radial velocity gradient

pressor, that the rotor-induced periodic oscillations amount to only 1 percent. He reports area-averaged axial stochastic turbulence intensities between 5 and 7 percent. Also, Stevens observed an increase in c_p after he increased the turbulence level at the diffuser inlet with application of a coarse grid in front of the diffuser. The increased turbulence produces a better momentum transport perpendicular to the main flow direction. This results in a later onset of separation and a higher pressure recovery.

5 Conclusions

The flow fields in four diffusers with inlet conditions typical for an axial flow compressor were experimentally investigated. Characteristic for the diffuser inlet flow in turbomachine environments are the wakes of the blading upstream of the diffuser and a high degree of turbulence. The operating point of the compressor situated before the diffusers was varied in a wide range. As a result of these investigations it was found that of the parameters changing with the operating point of the compressor, those having the most influence on the flow in the diffuser were the displacement thickness and the radial velocity distribution in the core flow at the diffuser inlet.

For a wide operating range of the compressor, when the change of the inlet conditions is dominated by a variation of the inlet blockage but velocity versus radius remains constant in the core flow, design rules for annular diffusers based on ducted-flow inlet conditions may also be applied for diffuser design in turbomachine environments.

Compared with diffusers, typically with ducted-flow inlet conditions, diffusers in turbomachine environments achieve a considerably higher pressure recovery. This is due to the increased turbulent mixing resulting in a later onset of separation.

In addition to inlet blockage influence the flow in the diffuser is strongly influenced by the radial velocity distribution in the core flow at the diffuser inlet. The particular radial velocity gradient imposed during the experiments combined with the bend at the casing caused a considerably lower pressure recovery than in the case of constant velocity.

Regarding the influence of the radial velocity distribution, a potential for increasing turbomachine efficiency is inherent, when the diffuser and the turbomachine are well matched to one another. During the design of the blading special attention should be taken of the exit velocity profile, which can be easily calculated using through flow codes. Further information about the influence of the radial inlet velocity distribution on the flow in diffusers is still sought. There is no doubt that the optimum inlet distribution will depend on the meridional shape of the diffuser, as the flow direction often must be turned in diffusers due to design limitations very strongly. This is an area where further investigations about the influence of the inlet conditions on the flow in diffusers should be pursued.

Dedication

This paper is dedicated to Prof. Dr.-Ing. H. Pfeil, who

initiated and greatly supported this work, but died before the preparation of this manuscript.

References

- Adenubi, S. O., 1976, "Performance and Flow Regime of Annular Diffusers With Axial Turbomachine Discharge Inlet Conditions," *ASME Journal of Fluids Engineering*, Vol. 98, pp. 236–243.
- Carlson, J. J., Johnston, J. P., and Sagi, C. J., 1967, "Effects of Wall Shape on Flow Regimes and Performance in Straight, Two-Dimensional Diffusers," *ASME Journal of Basic Engineering*, Vol. 89, pp. 151–160.
- Hoffmann, J. A., and Gonzales, G., 1984, "Effects of Small-Scale, High Intensity Inlet Turbulence on Flow in a Two-Dimensional Diffuser," *ASME Journal of Fluids Engineering*, Vol. 106, pp. 121–124.
- Johnson, I. A., and Bullock, R. O., 1965, "Aerodynamic Design of Axial-Flow Compressors," National Aeronautics and Space Administration, Washington, DC.
- Klein, A., 1981, "Review: Effects of Inlet Conditions on Conical-Diffuser Performance," *ASME Journal of Fluids Engineering*, Vol. 103, pp. 250–257.
- Kreitmeier, F., 1992, "Spacing-Averaging 3D Flows Using Strictly Formulated Balance Equations in Turbomachinery," presented at the ASME Cogen 1992.
- Lohmann, R. P., Markowski, S. J., and Brookman, E. T., 1979, "Swirling Flow Through Annular Diffusers With Conical Walls," *ASME Journal of Fluids Engineering*, Vol. 101, pp. 224–229.
- Pfeil, H., and Sieber, J., 1986a, "Characteristic Factors of a Compressor Rotor in Comparison With Two-Dimensional Cascade Data," ASME Paper No. 86-GT-29.
- Pfeil, H., and Sieber, J., 1986b, "Velocity Distribution and Decay Characteristics of Wakes Behind a Compressor Rotor-Blade," ASME Paper No. 86-GT-115.
- Pfeil, H., and Göing, M., 1987, "Measurements of the Turbulent Boundary Layer in the Diffuser Behind an Axial Flow Compressor," *ASME JOURNAL OF TURBOMACHINERY*, Vol. 109, pp. 405–412.
- Pfeil, H., and Müller, T., 1989, "Velocity Profile Model for Two-Dimensional Zero-Pressure Gradient Transitional Boundary Layers," *AIAA Journal*, Vol. 27, pp. 1127–1132.
- Quest, J., and Scholz, N., 1981, "Experimentelle Untersuchungen von Nabendiffusoren hinter Turbinenstufen," *Abschlussbericht zum FVV-Vorhaben*, No. 4468 Nabendiffusoren, DFVLR, Institut für Antriebstechnik, Köln, Germany.
- Renau, L. R., Johnston, J. P., and Kline, S. J., 1967, "Performance and Design of Straight, Two-Dimensional Diffusers," *ASME Journal of Basic Engineering*, Vol. 89, pp. 141–150.
- Schlichting, H., and Gersten, K., 1961, "Berechnung der Strömung in rotationssymmetrischen Diffusoren mit Hilfe der Grenzschichttheorie," *Zeitung für Flugwissenschaften*, Vol. 9, pp. 135–140.
- Sovran, G., and Klomp, E. D., 1967, "Experimentally Determined Optimum Geometries for Rectilinear Diffusers With Rectangular, Conical or Annular Cross-Section," *Fluid Mechanics of Internal Flow*, Elsevier Publishing Company, Amsterdam–London–New York.
- Sprenger, H., 1959, "Experimentelle Untersuchungen an geraden und gekrümmten Diffusoren," Dissertation, ETH Zürich, Switzerland.
- Stevens, S. J., Nayak, U. S. L., Prentson, J. F., Robinson, P. J., and Scrivener, C. T. J., 1980, "The Influence of Compressor Exit Conditions on the Performance of Combustor Dump Diffusers," *Journal of Aircraft*, Vol. 15, No. 8, pp. 482–488.
- Stevens, S. J., and Williams, G., 1980, "The Influence of Inlet Conditions on the Performance of Annular Diffusers," *ASME Journal of Fluids Engineering*, Vol. 102, pp. 357–363.
- Stevens, S. J., and Wray, A. P., 1985, "The Influence of Blade Wakes on the Performance of Outwardly Curved Combustor Pre-diffusers," AIAA Paper No. 85-1291.
- Wolf, S., and Johnston, J. P., 1969, "Effects of Nonuniform Inlet Velocity Profiles on Flow Regimes and Performance in Two-Dimensional Diffusers," *ASME Journal of Basic Engineering*, Vol. 91, pp. 462–474.
- Zierer, Th., 1992, "Experimentelle Untersuchung der Strömung in Diffusoren mit verschiedenen Erweiterungsverhältnissen hinter einem Axialverdichter," Doctoral Thesis, TH Darmstadt, Darmstadt, Germany.

Effects of Free-Stream Turbulence Intensity on a Boundary Layer Recovering From Concave Curvature Effects

M. D. Kestoras

ISITEM,
University of Nantes,
Nantes, France

T. W. Simon

Department of Mechanical Engineering,
University of Minnesota,
Minneapolis, MN 55455

Experiments are conducted on a flat recovery wall downstream of sustained concave curvature in the presence of high free-stream turbulence ($TI \sim 8\%$). This flow simulates some of the features of the flow on the latter parts of the pressure surface of a gas turbine airfoil. The combined effects of concave curvature and TI , both present in the flow over a turbine airfoil, have so far been little studied. Computation of such flows with standard turbulence closure models has not been particularly successful. This experiment attempts to characterize the turbulence characteristics of this flow. In the present study, a turbulent boundary layer grows from the leading edge of a concave wall, then passes onto a downstream flat wall. Results show that turbulence intensities increase profoundly in the outer region of the boundary layer over the recovery wall. Near-wall turbulent eddies appear to lift off the recovery wall and a "stabilized" region forms near the wall. In contrast to a low-free-stream turbulence intensity flow, turbulent eddies penetrate the outer parts of the "stabilized" region where sharp velocity and temperature gradients exist. These eddies can more readily transfer momentum and heat. As a result, skin friction coefficients and Stanton numbers on the recovery wall are 20 and 10 percent, respectively, above their values in the low-free-stream turbulence intensity case. Stanton numbers do not undershoot flat-wall expectations at the same Re_{Δ_2} values as seen in the low- TI case. Remarkably, the velocity distribution in the core of the flow over the recovery wall exhibits a negative gradient normal to the wall under high-free-stream turbulence intensity conditions. This velocity distribution appears to be the result of two effects: (1) cross transport of kinetic energy by boundary work in the upstream curved flow and (2) readjustment of static pressure profiles in response to the removal of concave curvature.

Introduction

The effects of high free-stream turbulence intensity have been under study for more than 30 years. Early studies (e.g., Kestin, 1966; Feiler and Yeager, 1962) reported conflicting results on the effects of high TI on heat transfer over a flat plate for TI in the range 0.7–8 percent. Simonich and Bradshaw (1978) suggested that the conflicting results are due mainly to a Reynolds number effect, the effect diminishing as the Reynolds number increases. They noted a 5 percent increase in Stanton number for every 1 percent increase in free-stream turbulence intensity ($TI < 7$ percent) at $Re_{\delta_2} = 6500$ (relatively high). Elevated TI suppressed the wake of temperature profiles, the effect increasing with increased TI . The results section of this paper will show that the wake of temperature profiles over the recovery wall is also suppressed

by high TI . Hancock and Bradshaw (1983) observed that the free-stream length scale, L_∞^u , is also important in describing the effects of free-stream turbulence. They found that the empirical parameter, $(\sqrt{u^2}/U) \times 100/(L_\infty^u/\delta_{99.5} + 2.0)$ correlates changes in skin friction coefficients, $(C_f - C_{f0})/C_{f0}$, quite satisfactorily. Blair (1983) conducted experiments in a heated turbulent boundary layer over a flat plate. He stated that the effects of elevated TI follow the functional relation $\Delta(C_f, St, U(y), T(y)) = f(\sqrt{u_\infty^2}/U_\infty, L_\infty^u/\delta_{99.5}, Re_{\delta_2})$ and extended Hancock's correlation by including an empirical term, $\beta = 3\exp(-Re_{\delta_2}/400) + 1$, as a multiplier to Hancock's correlating term to account for low Re_{δ_2} effects. He also observed that the logarithmic regions in velocity and temperature profiles were unaffected by free-stream turbulence intensity. As shown in the present work, the logarithmic region of a boundary layer over a recovery wall also remains unaffected by the elevated TI .

Data on the effects of TI on turbulent boundary layers over curved surfaces are very limited. Brown and Burton

Contributed by the International Gas Turbine Institute and presented at the 38th International Gas Turbine and Aeroengine Congress and Exposition, Cincinnati, Ohio, May 24–27, 1993. Manuscript received at ASME Headquarters February 12, 1993. Paper No. 93-GT-25. Associate Technical Editor: H. Lukas.

(1977) reported no effect of TI (1.6–9.2 percent) on Stanton numbers over convexly curved surfaces. You et al. (1989) studied the effects of two levels of free-stream turbulence intensity (0.65–1.85 percent) on a heated turbulent boundary layer over a convex surface for which $\delta_{99.5}/R = 0.03$. They reported that free-stream turbulence intensity enhances the stabilizing effects of convex curvature on mean and turbulence quantities.

Data on the effects of TI on turbulent boundary layers over a concave wall are few. Nakano et al. (1981) studied the effects of stable free-stream flow (positive shear) and unstable free-stream flow (negative shear) on a turbulent boundary layer over a concave wall. Under unstable free-stream flow conditions, shear-stress values in the boundary layer over the concave wall increase relative to values under stable free-stream flow conditions. Kim et al. (1991) reported mean and turbulence measurements over the same concave wall used in the present study. In the high- TI case (8 percent), they reported cross-transport of momentum taking place even in the core of the flow. Kestoras and Simon (1992) reported mean momentum and heat transfer measurements in a boundary layer recovering from sustained concave curvature under low- TI conditions ($TI = 0.6$ percent). Skin friction coefficients dropped abruptly at first, slowly thereafter, approaching flat-wall values. Stanton numbers showed a similar behavior, with one important difference: They quickly dropped below flat-wall values, then reached near-constant values and remained well below equivalent flat-wall values by the end of the test section, $33\delta_0$ from the bend exit. This behavior was attributed to a thickening of the viscous sub-layer and a lifting of the large-scale eddies off the wall. Velocity and temperature profiles reached a self-preserving shape over the recovery wall, exhibiting unusually sharp gradients near the wall.

In the present study, data taken on a flat wall downstream

of a concave wall under high- TI conditions are presented. To the authors' knowledge, this is the first time that the combined effects of high free-stream turbulence intensity and recovery from concave curvature are documented.

Test Facility and Instrumentation

The facility is an open-circuit, blown-type wind tunnel (Fig. 1). Details of the flow delivery section are given by Wang (1984). Measurements are taken at a nominal velocity of 17.2 m/s. This velocity is uniform to within 0.3 percent across the face of the nozzle. The free-stream temperature of the flow is uniform to within 0.1°C.

A free-stream turbulence intensity of ~ 8 percent at the inlet of the test channel is achieved using an insert section downstream of the contraction nozzle (Russ, 1989). This insert consists of a biplane grid of 4.2 cm OD PVC pipes on 10.8 cm centers. Downstream of the grid there is a 96.5-cm-long development region. The grid is similar to that used by O'Brien and vanFossen (1985). Data show that turbulence decays more quickly with streamwise distance on the upstream part of the concave wall. On the recovery wall, the decay of turbulence is very slow ($TI \sim 4$ percent). A power density spectrum taken at the nozzle exit shows that 19.6 percent of the turbulent energy in the free-stream is distributed over frequencies below 25 Hz.

The test channel is rectangular, 68 cm wide, 11 cm deep, and 284 cm long. The test wall consists of two major segments (concave wall and recovery wall) that are designed and assembled to provide a smooth, uniformly heated surface. Both segments were fabricated similarly. For example, the recovery wall consists of a layer of fiberglass insulation, a sheet of Plexiglas, an electrical resistance heater, a thin spacer, a stainless steel sheet, and, adjacent to the flow, a layer of liquid crystal. Thermocouples embedded into the

Nomenclature

C_f = skin friction coefficient	T = local mean temperature	y^+ = normal distance from the wall in wall units = yU_τ/ν
C_{f0} = skin friction coefficient at very low turbulence intensity	TI = free-stream turbulence intensity = $\sqrt{u'^2}/U_{cw}$	β = multiplier accounting for the Reynolds number effect on skin friction coefficients in the presence of high TI effects = $3\exp(-\text{Re}_{\delta_2}/400) + 1$
C_p = constant-pressure specific heat	T_∞ = free-stream temperature	δ = momentum boundary layer thickness
C_{p_c} = static pressure coefficient = $(P - P_{\text{ref}})/(0.5\rho U_{cw}^2)$	T_w = wall temperature	δ_0 = boundary layer thickness at the entrance to the recovery wall
H = shape factor δ_1/δ_2	T^+ = temperature in wall units = $((T_w - T)/(T_w - T_\infty)) \times \sqrt{C_f/2}/\text{St}$	δ_1 = displacement thickness
L_∞^u = free-stream length scale = $(\overline{u^2})^{3/2}/\left(U_\infty \frac{du_\infty^2}{dx}\right)$	U = mean streamwise velocity	δ_2 = momentum thickness
P = static pressure	U_c = local mean velocity obtained by extrapolating the velocity distribution in the core of the flow	$\delta_{99.5}$ = boundary layer thickness based on 99.5 percent of the local U_c
P_d = dynamic pressure = $1/2\rho U^2$	$\sqrt{u'^2}$ = root-mean-square fluctuation of streamwise velocity	Δ_2 = enthalpy thickness
Pr = molecular Prandtl number	$\sqrt{u_\infty'^2}$ = root-mean-square fluctuation of free-stream velocity	Δ_3 = Clauser thickness = $\int_0^{\delta_{99.5}} ((U_p - U)/U_\tau) dy$
P_{ref} = static pressure at the most upstream pressure tap 2 cm from the concave surface	U_p = potential flow velocity	$\Delta_{99.5}$ = thermal boundary layer thickness based on 99.5 percent of the wall-to-free-stream temperature difference
P_t = total pressure = $P + P_d$	U_∞ = free-stream mean velocity	ΔC_f = change in skin friction coefficient relative to the zero TI value = $C_f - C_{f0}$
q_w = convective heat flux at the wall	U_{cw} = value of U_c at the wall	θ = angular position around the bend
R = radius of curvature (negative for a concave surface)	U^+ = velocity in wall coordinates = U/U_τ	ν = molecular kinematic viscosity
Re_x = Reynolds number based upon distance from the beginning of the test wall	U_τ = shear velocity	ρ = density
Re_{δ_1} = Reynolds number based upon displacement thickness	x = streamwise distance from the leading edge of the concave wall	
Re_{δ_2} = Reynolds number based on momentum thickness	y = distance normal to the wall	
St = Stanton number = $q_w/\rho C_p (T_w - T_\infty) U_{cw}$		

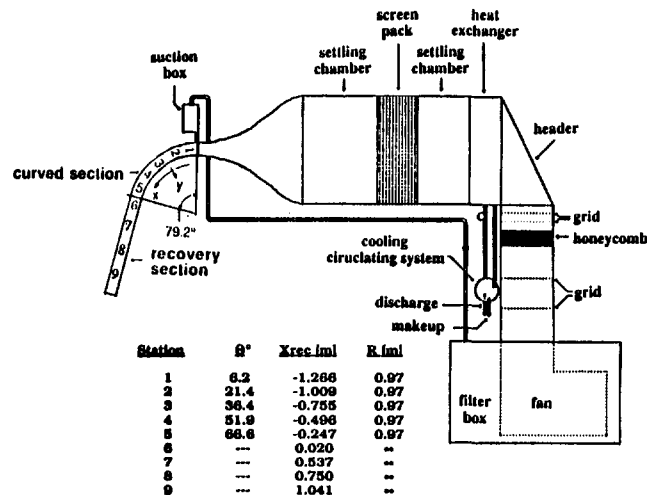


Fig. 1 Wind tunnel test facility

spacer are distributed both in the streamwise and spanwise directions.

The concave wall has a radius of 0.97 m and is 1.38 m long. The recovery wall is 1.452 m long and is tangent to the concave wall. The outer wall is adjusted to obtain negligible streamwise acceleration: static pressure coefficients, C_{p_c} , are kept to within 0.03 for the entire test length. Such C_{p_c} values are based upon static pressures taken at a radial distance of 2 cm from the test wall. Static pressures were measured using an array of static pressure taps on an end wall. The taps were distributed both in the x and y directions.

At the entry to the recovery section Re_x , Re_{δ_1} , and Re_{δ_2} are 1.4×10^6 , 1487, and 1174, respectively.

Data acquisition and processing are performed by a Hewlett Packard series 200, Model 16 personal computer. Mean and fluctuating velocities are measured using a hot-wire (TSI 1218-T1.5) probe on which the prongs are bent 90 deg to the probe holder to minimize flow interference. A constant-temperature, four-channel bridge (TSI-IFA-100) is used to power the hot wires. Analog output signals are digitized using an HP3437A system voltmeter. For statistical quantities, the sampling rate is 100 Hz and the sampling duration is at least 40 seconds.

Velocities are measured when the walls are not heated. The free-stream temperature is continuously monitored and the hot-wire voltage output is corrected for any temperature variations. The uncertainty in $\overline{u^2}$ is 3 percent.

Heat transfer experiments are conducted with the test walls uniformly heated to nominally 193 W/m^2 within a 1 percent nonuniformity (Wang, 1984). Wall temperatures are measured with $76\text{-}\mu\text{m}$ -dia embedded chromel-alumel thermocouples. The thermocouples were calibrated against a platinum-resistance standard. The spacings of the thermocouples in the streamwise direction are 2.54 and 5.08 cm over the concave and recovery walls, respectively. Surface temperatures are obtained by correcting the thermocouple readings for temperature drops between the embedded thermocouple beads and the test wall surface. Such corrections for the concave and the recovery walls, respectively, were typically 1.2°C and 0.3°C of the 5.5°C thermocouple-to-free-stream temperature difference. The uncertainty in the wall temperature readings thus obtained, is 0.2°C . Careful measurements of wall material conductivity, contact resistance values, and surface emissivity were needed to achieve this uncertainty. An energy balance was performed by comparing the enthalpy thicknesses calculated from the measured velocity and temperature profiles and the enthalpy thicknesses obtained by integration in the streamwise direction of wall values. On the

concave wall, where the wall temperature correction is largest, a closure within 5 percent was obtained.

Profiles were taken using a stepping motor assembly. The motor is capable of 400 half-steps per revolution, each half-step equivalent to $5 \mu\text{m}$ of travel in the y direction.

Determination of $\delta_{99.5}$ presents some difficulty in the high-turbulence case: No analytical equation is available for determining the velocity distribution outside the boundary layer over the recovery wall. The velocity distribution in the core of the flow is different from the distribution in a low-turbulence case, primarily because of cross transport of momentum by boundary work over the upstream concave wall (Eckert, 1987). Eckert suggests that this cross transport of momentum is dependent on the unsteadiness of the flow and the bending of the flow path-lines. Both factors are nearly constant across the core of the flow over the upstream concave wall: This implies a nearly uniform cross transport of momentum across the channel toward the concave wall but outside the boundary layer. Though the slope of the linear distribution of velocities in the core of the flow over the concave wall changes from that observed in a low-turbulence case (Kestoras and Simon, 1992) the velocity distribution in the core of the flow remains linear when high TI is introduced. The velocity profile in the core of the flow throughout the recovery section also remains linear. In this work, velocities in the core of the flow are least-square fitted with a straight line, capitalizing on this linearity; the resulting equation is used to provide the velocities that would be obtained in the vicinity of the wall if the boundary layer were not present. The velocities, thus obtained, are used instead of U_p (used previously in the low-turbulence cases) to determine $\delta_{99.5}$, δ_1 , and δ_2 .

Results

Under high free-stream turbulence conditions ($TI \approx 8$ percent) the flow appears fully turbulent, in terms of the wall skin friction and heat transfer, from the leading edge of the concave wall. Stable Görtler-like vortices do not appear in the high-turbulence case, in contrast to a previous case taken under low- TI conditions. Spanwise nonuniformities, which would indicate the presence of such vortices, do not appear on the liquid crystal covering the test surface; moreover, spanwise profiles of streamwise mean velocity do not show the maxima or minima observed in the low-turbulence case. Turbulence measurements (Kestoras, 1993) indicate that a scenario whereby Görtler-like vortices exist but meander with time may not be correct. Indeed, it appears that there is no coherent vortex activity. The effects of high TI are most profound in the outer region of the boundary layer over the recovery wall. In the inner region, the high- TI effects are important but the removal of concave curvature is more influential.

The structural changes of the boundary layer over the upstream concave wall, brought about by high TI , can be described as follows: at the bend exit, the near-wall velocity profiles exhibit sharper gradients than in a low- TI case. These sharp velocity gradients are the result of the following two effects taking place over the concave wall: (1) High free-stream turbulence provides large-scale, high-streamwise-momentum eddies outside the boundary layer. These eddies are accelerated toward the concave surface and induce an increase in eddy scale within the boundary layer. (2) Cross transport of energy by boundary work proceeds even outside of the boundary layer over the concave wall (Eckert, 1987) raising the streamwise momentum near the wall.

This paper documents the effects of the removal of concave curvature under high- TI conditions. Measurements are presented and their significance discussed. Effects of TI are

Table 1 Boundary layer parameters: concave-wall stations 4H and 5H; joint: station 6H; recovery wall stations 7H–9H

	Station 4H	Station 5H	Station 6H	Station 7H	Station 8H	Station 9H
x , m	0.875	1.133	1.390	1.912	2.124	2.416
R , cm	97	97	∞	∞	∞	∞
U_{cw} , m/s	16.71	17.09	16.41	17.17	16.77	16.95
$T_{i,core}$	5.201	4.631	4.618	4.150	4.135	4.127
$\delta_{99.5} \times 10^2$, m	3.87	3.60	2.40	2.69	2.86	2.89
$\delta_1 \times 10^3$, m	1.987	2.129	1.452	2.052	2.308	2.473
$\delta_2 \times 10^3$, m	1.618	1.746	1.146	1.586	1.776	1.411
$(y/\delta_{99.5})_{y^+ = 10}$	0.006	0.005	0.008	0.007	0.007	0.007
$R_{cx} \times 10^3$	9.44	12.05	14.23	20.84	23.26	25.68
Re_{δ_1}	2144	2264	1487	2236	2527	2630
Re_{δ_2}	1746	1857	1174	1728	1944	2033
H	1.228	1.219	1.267	1.294	1.300	1.294
$C_f \times 10^3$	5.00	4.93	4.85	4.45	4.36	4.19
$(\partial U/\partial y)_{core}$	10.1	15.4	15.7	-10.1	-9.5	-9.6
$\Delta_{99.5}$, cm	3.312	4.538	6.062	6.157	7.693	8.817
Δ_2 , mm	1.602	2.372	2.478	2.304	4.042	4.104
T_w	27.74	27.77	27.74	27.68	27.60	27.67
T_w , °C	31.32	31.35	31.74	31.94	31.88	32.13
Re_{Δ_2}	1662	2517	2521	2451	4203	4310
q_w	165.6	165.4	172.1	163.8	163.6	162.6
$St \times 10^3$	2.376	2.321	2.251	1.922	1.957	1.846
$2St/C_f$	0.951	0.941	0.928	0.864	0.898	0.881

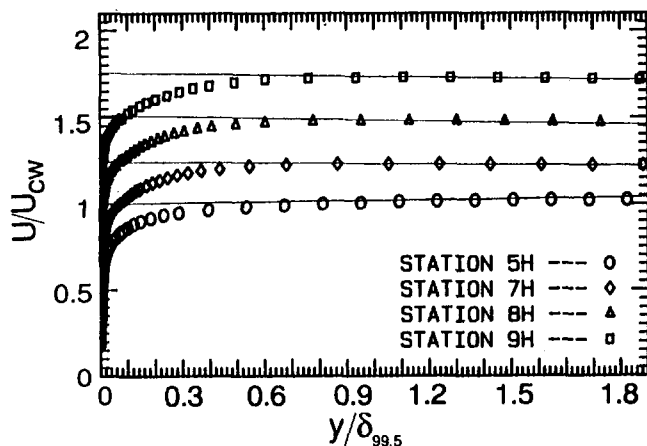


Fig. 2 Velocity profiles on recovery wall (stations 7H–9H). Station 5H; concave wall. Profiles shifted in the vertical direction.

isolated by comparing with data from a low- TI case (Kestoras and Simon, 1992; $TI = 0.6$ percent). Important parameters of the study are shown in Table 1.

Nondimensional Velocity Profiles. Nondimensional velocity profiles over the recovery wall (stations 7H–9H) are shown in Fig. 2. The velocity profile taken over the concave wall, 24 cm upstream of the bend exit (station 5H), is also shown for comparison. On the recovery wall, the velocity profiles in the core of the flow exhibit negative gradients whereas the profile gradient at station 5H is positive outside the boundary layer (Fig. 2). This unexpected behavior may be explained as follows: On the concave wall, cross transport of energy takes place in the core of the flow toward the concave wall, resulting in total pressure profiles that increase toward the concave surface (Kestoras, 1993). This cross transport in the core of the flow requires streamline curvature as discussed by Eckert (1987). It is, thus, shut off on the recovery section. The total pressure distribution profile at the bend exit is essentially maintained throughout the recovery section since no efficient means for transport remains. Readjustment to flat-wall static pressure profiles (centrifugal forces are removed) results in dynamic pressure ($P_d = P_t - P$) profiles with negative y gradients. Thus, the velocity profile ($P_d = 0.5\rho U^2$) also exhibits a negative y gradient.

After the removal of curvature, the boundary layer thick-

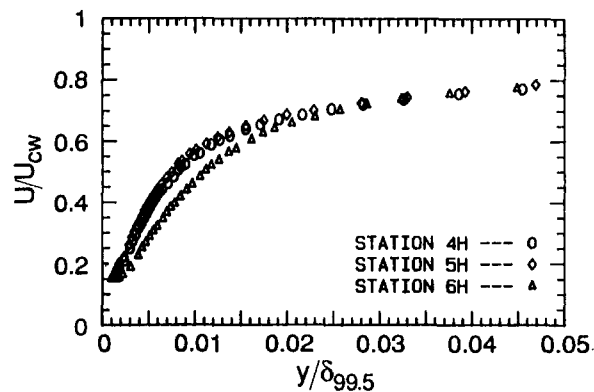


Fig. 3 Near-wall velocity profiles in the vicinity of the joint of the concave and recovery walls

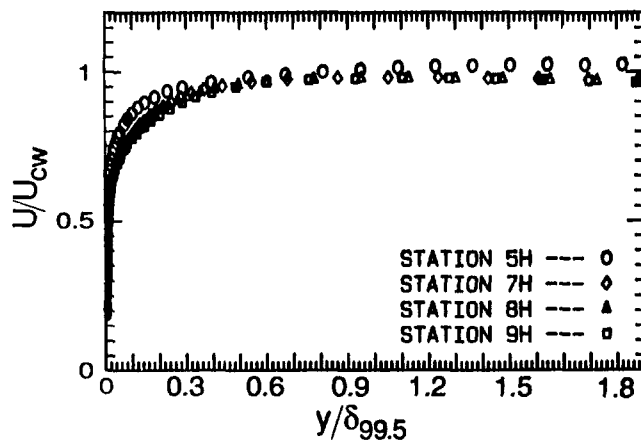


Fig. 4 Asymptotic behavior of velocity profiles on the recovery wall under high- TI conditions (stations 7H–9H)

nesses, $\delta_{99.5}$, δ_1 , and δ_2 decrease (Station 7H in Table 1). Values of $\delta_{99.5}$, δ_1 , and δ_2 increase monotonically for the test of the recovery wall. Their values however, do not rise above the pre-bend-exit value (station 5H) before the mid-downstream location of the recovery wall (station 8H). It therefore appears that there is a mechanism in the vicinity of the bend exit that transports streamwise momentum away from the wall quite efficiently. Before the bend exit (station 5H in Fig. 2) streamwise momentum increases with y . By conservation of angular momentum, the fluid layers with the higher streamwise momentum may tend to lift off the test wall whereas fluid layers close to the surface show a smaller tendency to lift off. This impulse of cross transport of momentum away from the test wall in the vicinity of the bend exit is consistent with the readjustment of the shape of the local velocity profiles. At the joint between the concave and recovery walls (station 6H), the near-wall, $y/\delta_{99.5} < 0.03$ velocity gradient, is shallower than for the upstream profiles (stations 4H and 5H in Fig. 3). This may at first seem strange since readjustment of static pressure profiles would tend to produce near-wall acceleration at this point. It is believed to be a result of the lifting of the vortices.

As with the low- TI case, the recovery wall velocity profiles assume a near-asymptotic shape (stations 7H–9H in Fig. 4). This behavior is especially true near the wall ($y/\delta_{99.5} < 0.13$). Moreover, near the wall ($y/\delta_{99.5} < 0.13$), self-similarity is established by station 6H (only 2 cm downstream of the bend exit, not shown in Fig. 4) suggesting that the redistribution of momentum discussed above begins slightly upstream of the bend exit and is complete soon after the beginning of recovery.

High- TI results in fuller velocity profiles (e.g., station 8H in Fig. 5) than profiles under low- TI conditions (stations 8U

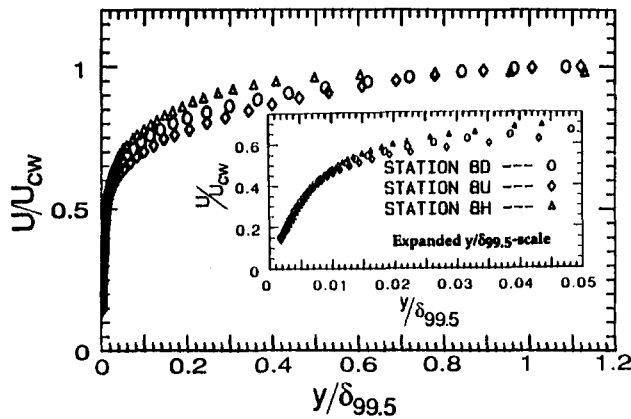


Fig. 5 Effect of high TI on nondimensionalized velocity profiles at station 8 on the recovery wall. Stations 8U and 8D; upwash and downwash sites of Görtler-like vortices—low- TI case. Station 8H; high- TI case.

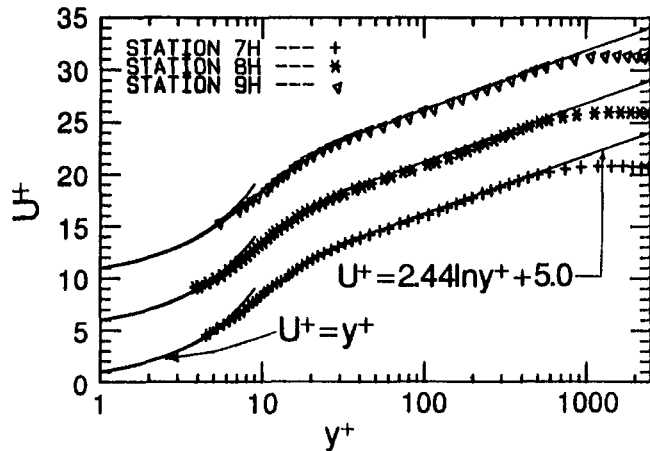


Fig. 6 Streamwise evolution of mean velocity profiles on the recovery wall in wall coordinates

and 8D). It is remarkable, however, that the near-wall velocity profiles, $y/\delta_{99.5} < 0.01$, (insert in Fig. 5) are the same for all. This near-wall similarity, because of its importance in determining mean and turbulence quantities, appears to be the reason for the many common features over the recovery wall for both the high- and low- TI cases. It will be shown later that a “stabilized” region appears near the recovery wall. It is presumed that, for the most part, the “stabilized” region is depleted of turbulent eddies and, therefore, should be little affected by the external high TI . It can therefore be argued that, since the velocity profile in the region ($y/\delta_{99.5} < 0.01$) remains unaffected by elevated TI , the “stabilized” region is about one-hundredth of the boundary layer thickness.

Velocity Profiles in Wall Coordinates. Over the recovery wall, the law of the wall appears to be valid up to $y^+ \sim 300$ (stations 7H–9H, Fig. 6) whereas over the concave wall, the logarithmic region extends only to $y^+ \sim 80$ (Kestoras, 1993). Similar enlargement of the logarithmic region over the recovery wall was observed in the low- TI case (e.g., stations 8U and 8D in Fig. 7). Elevated TI appears to affect only the wake region of the velocity profile in wall coordinates. Negligible effects of TI on the logarithmic region of a velocity profile were also reported in boundary layers over a flat plate (Blair, 1983).

The wake, suppressed in the high- TI case over the concave wall (Kestoras, 1993), begins to re-establish very early after the removal of curvature (station 6H, not shown) and contin-

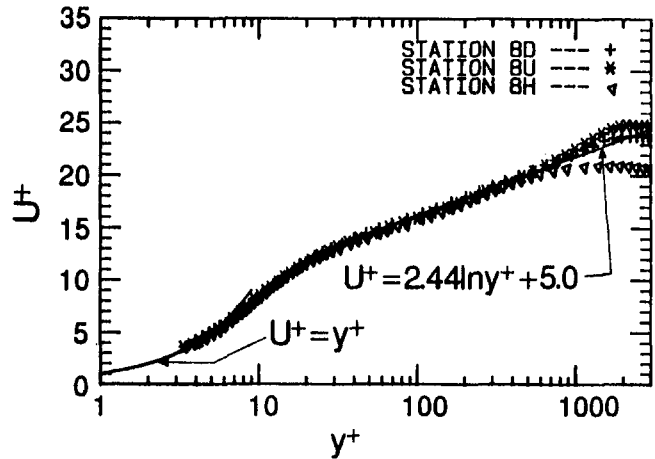


Fig. 7 Effect of high TI on velocity profiles on the recovery wall in wall coordinates. Stations 8U and 8D; upwash and downwash sites of Görtler-like vortices—low- TI case. Station 8H; high- TI case.

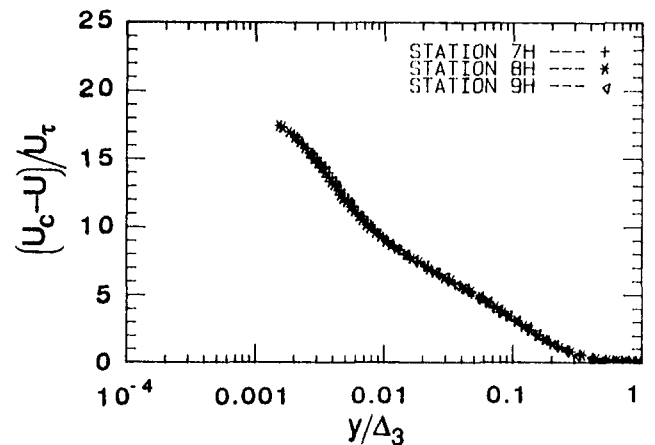


Fig. 8 Inner- and outer-region similarity exhibited by velocity profiles on the recovery wall under high- TI conditions

ues to do so throughout the recovery wall (stations 7H–9H, Fig. 6). Nevertheless, a negative wake persists (see station 9H). Similar re-emergence of the wake is observed in the low- TI case (Kestoras and Simon, 1992). However, the persistence of negative wakes over the recovery wall in the high-turbulence case (station 8H in Fig. 7, for example) is in contrast to the positive wakes exhibited under low- TI conditions (station 8U and 8D).

Velocity Profiles in Outer-Region Similarity Coordinates. The experiment is conducted under a condition of negligible streamwise acceleration, and thus would display equilibrium boundary layer characteristics under flat-wall conditions. Equilibrium boundary layers exhibit outer-region similarity when plotted in the coordinates of Fig. 8. Thus, if the residual effects of curvature would not preclude such behavior, the self-similarity exhibited over the recovery wall (stations 7H, 8H, and 9H) in the outer region ($y/\Delta_3 > 0.1$) is expected. However, self-similarity is also exhibited in the inner region. Velocity profiles in the low- TI case also exhibit both inner- and outer-region similarity. As explained by Kestoras and Simon (1992), this inner-region similarity may be an implication of the existence of a “stabilized” region near the recovery wall. Similar behavior was observed in strongly accelerated boundary layers where a near-wall “stabilized” layer (“laminar-like”) was also documented (Kays and Moffat, 1975).

Streamwise Turbulence Intensity Profiles. At the bend exit, turbulence intensity values in the presence of high TI

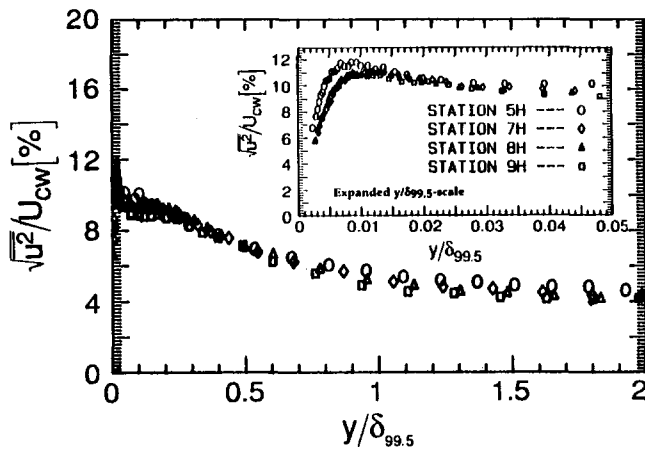


Fig. 9 Streamwise evolution of turbulence intensities on the concave wall (station 5H) and recovery wall (stations 7H-9H)

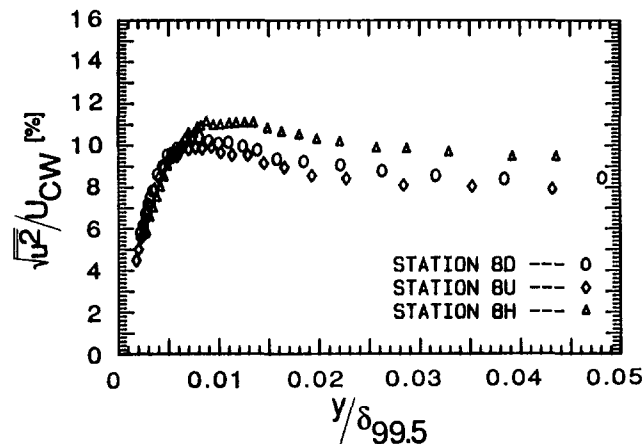


Fig. 10 Effect of high TI on near-wall turbulence intensities on the recovery wall. Stations 8U and 8D; upwash and downwash sites of Görtler-like vortices—low- TI case. Station 8H; high- TI case.

(stations 7H-9H in Fig. 9) drop only slightly from the enhanced concave-wall values (station 5H). This reduction is only one-tenth the reduction observed between the same stations in the low- TI case (Kestoras and Simon, 1992). It appears that the turbulent eddies at the edge of the boundary layer are large enough to dominate both the core of the flow and the boundary layer flow.

Near the surface of the recovery wall, $y/\delta_{99.5} < 0.012$ (inset in Fig. 9), turbulence intensity profiles do assume a self-similar shape (stations 7H-9H). This self-similar shape first appears at station 6, only 2 cm downstream of the bend exit (not shown). Turbulence intensity values under high- TI conditions deviate from those in the low- TI case for $y/\delta_{99.5} > 0.006$ (Fig. 10, only station 8 is shown). This may indicate that turbulent eddies penetrate deeper into the “stabilized” region under high- TI conditions. Deeper penetration couples the turbulent eddies with the sharp velocity gradients in this region, resulting in more efficient transport of momentum and, thus, a quicker recovery.

Immediately after the bend exit, the viscous sublayer appears to grow faster than does $\delta_{99.5}$, indicated by near-wall turbulence intensity profiles in insert in Fig. 9 where lower near-wall gradients are shown for stations 7H-9H than for 5H. This may indicate a thickening of the viscous sublayer after the bend exit, which is consistent with observations in temperature profiles (to be presented). A thickening of the viscous sublayer upon recovery is also observed in the low- TI case. The peaks in profiles 7H-9H are at the same location for both low- and high- TI cases, indicating that the eddies lift off the recovery wall in a manner that is independent of TI .

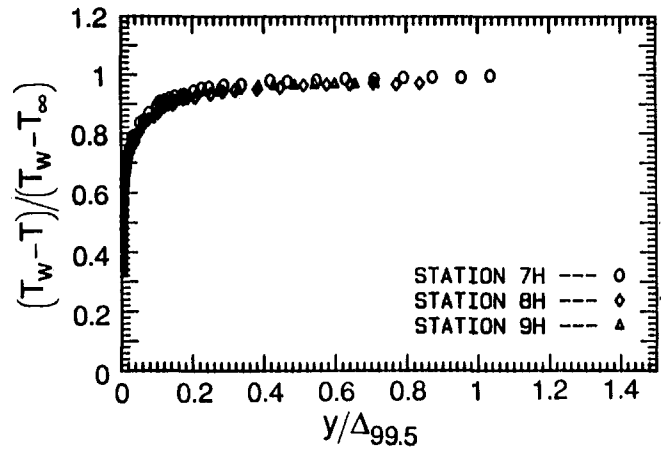


Fig. 11 Asymptotic behavior of nondimensionalized mean temperature profiles on the recovery wall under high- TI conditions

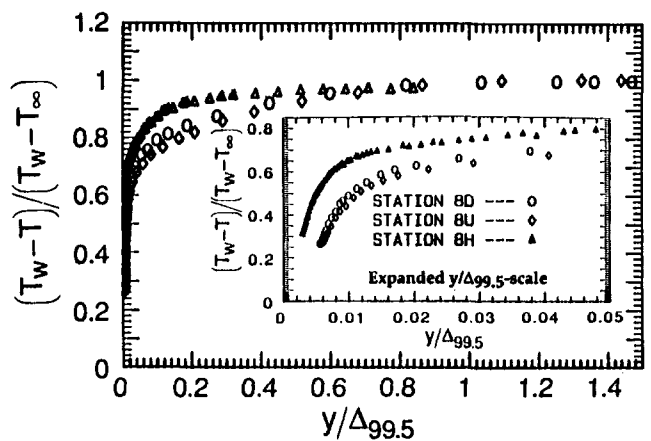


Fig. 12 Effect of high TI on nondimensionalized mean temperature profiles on the recovery wall under high- TI conditions. Stations 8U and 8D; upwash and downwash sites of Görtler-like vortices—low- TI case. Station 8H; high- TI case.

Nondimensionalized Mean Temperature Profiles. On the recovery wall, temperature profiles (stations 7H-9H, Fig. 11) exhibit a near-self-similar behavior starting from the exit of the bend. Similar behavior was also observed in the low- TI case (Kestoras and Simon, 1992).

High free-stream turbulence effects fuller mean temperature profiles on the recovery wall (Fig. 12) than in the low- TI case. The innermost 20 percent of the boundary layer accounts for almost 95 percent of the wall-to-free-stream temperature difference; less than 85 percent in the low- TI case. Such a high near-wall thermal resistance indicates a “stabilized” layer, as reported in the low- TI case (Kestoras and Simon, 1992). However, in the presence of high TI , temperatures in the region are higher than values under low- TI conditions (inset in Fig. 12). Furthermore, temperature profiles in the inner part of the “stabilized” region ($y/\delta_{99.5} < 0.005$) possess sharper gradients (station 8H in inset in Fig. 12) than temperature profiles in the low- TI case (stations 8U and 8D). In contrast, velocity profiles in the near-wall region ($y/\delta_{99.5} < 0.01$ in inset in Fig. 5) are not affected by TI level.

Temperature Profiles in Wall Coordinates. Temperature profiles (stations 7H-9H in Fig. 13) show little evolution in the conduction layer and the logarithmic region under high- TI conditions. However, the wake appears to be slowly re-emerging. Over the concave wall, the wake is suppressed by high TI and concave curvature (Kestoras, 1993). A re-emer-

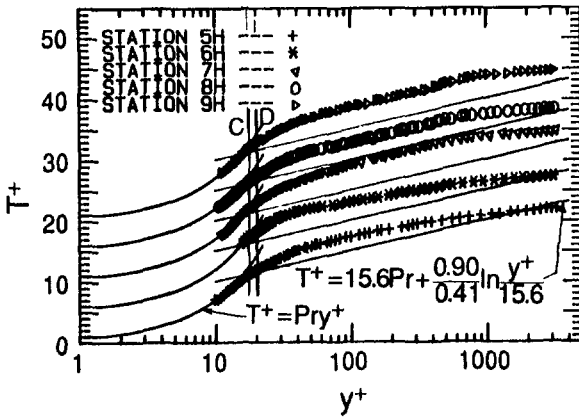


Fig. 13 Streamwise evolution of mean temperature profiles in wall coordinates on the recovery wall (Station 7H–9H). Concave wall; station 5H; joint station 6H.

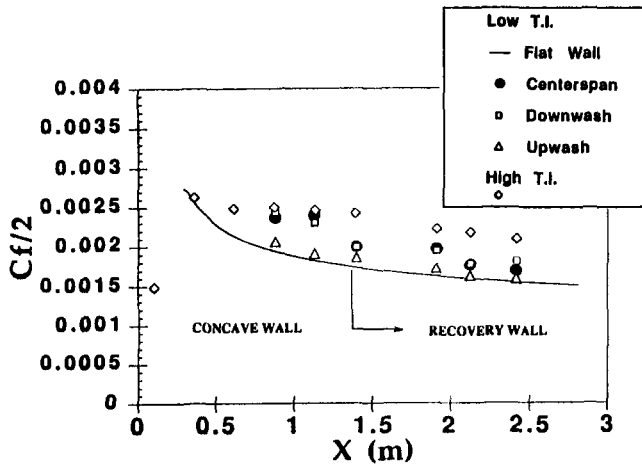


Fig. 14 Skin friction coefficients on the concave and the recovery walls. Centerspan, downwash and upwash are the respective sites of Görtler-like vortices; low- TI case. Flat-wall line calculated using mixing length modeling

gence of the wake on the recovery wall is also observed in the low- TI case (Kestoras and Simon, 1992).

A thickening of the conduction layer appears at the joint between the concave and recovery walls. To indicate this increase, the y^+ position where the conduction layer equation, $T^+ = Pr y^+$, first departs from the data is marked, for each station (Fig. 13) and vertical lines C and D are drawn to indicate these points for station 5H, and for stations 6H, 7H, 8H, and 9H, respectively. A single line suffices for the last four stations. The locations of lines C and D can be taken as measures of the thicknesses of the respective conduction layers. The conduction layer thicknesses rise at the end of the bend, then remain the same throughout the recovery wall length. A thickening of the conduction layer after the bend exit is also observed in the low- TI case. It appears that free-stream turbulence has a minimal effect in the inner part of the boundary layer.

Friction Coefficients. On the recovery wall, the effect of elevated TI on skin friction coefficients is very profound (Fig. 14). In the low- TI case, skin friction coefficients at the bend exit drop as much as 20 percent from the enhanced concave-wall values. In contrast, the corresponding drop in the high- TI case is only 8 percent. Thus, skin friction coefficients on the recovery wall increase by 20 percent when TI is elevated. This sensitivity to TI may be caused by penetration of eddies into the outer part of the “stabilized” region. Effective mix-

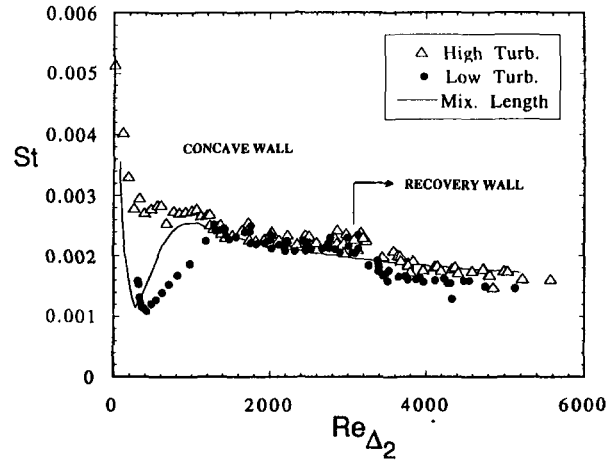


Fig. 15 Comparison of streamwise behavior of Stanton numbers under low- and high- TI conditions. Flat wall expectations calculated using mixing length modeling.

ing, resulting from the coupling of the penetrating eddies with the sharp velocity gradients in the “stabilized” region greatly boosts the cross-stream transport of momentum.

Stanton Numbers. Stanton numbers show that the boundary layer is turbulent-like essentially from the leading edge of the concave wall (Fig. 15). In contrast, a transition zone is present under low- TI conditions (Kestoras and Simon, 1992).

The response of Stanton numbers to elevated TI on both the concave and recovery walls (Fig. 15) is similar to the response of skin friction coefficients. On the recovery wall, Stanton numbers rise 10 percent when TI is elevated, half the corresponding increase in skin friction coefficients.

As in the low- TI case, Stanton numbers drop at the bend exit, then level off, assuming a near-constant value for the remainder of the recovery wall. The qualitative similarity in Stanton numbers of the two cases may be a result of dominance of near-wall phenomena, which appear to be independent of TI . Such a phenomenon is the thickening of the conduction layer, which adversely affects heat transfer (Kays and Moffat, 1975).

The high Stanton numbers on the recovery wall in the high- TI case may be the result of turbulent eddies penetrating the “stabilized” region, where velocity gradients are sharper. Temperature profiles, however, exhibit sharper gradients in the inner part and shallower gradients in the outer part of the “stabilized” region under high- TI conditions. Therefore, the eddies that penetrate the outer parts of the “stabilized” region do not enhance heat transfer as much as they enhance momentum transfer. Thus, over the recovery wall, the increase in Stanton numbers with elevated TI is only half the increase in skin friction coefficients.

Conclusions

In this study the combined effects of high TI and the removal of concave curvature are documented. These data are important for real turbine airfoil flow where high- TI conditions prevail. At the bend exit, the velocity and temperature profiles are fuller than profiles in the low- TI case (Kestoras, 1993). As in the low- TI case, turbulent eddies lift off the recovery wall and the viscous sublayer thickens relative to the boundary layer thickness on the concave wall (Fig. 16). The “stabilized” region remains largely unaffected in the mean by the elevated TI . However, measurements show that turbulent eddies do penetrate the outer layers of the “stabilized” region (Fig. 16). As they do, eddy action on the sharp velocity and temperature gradients of the “stabilized” region

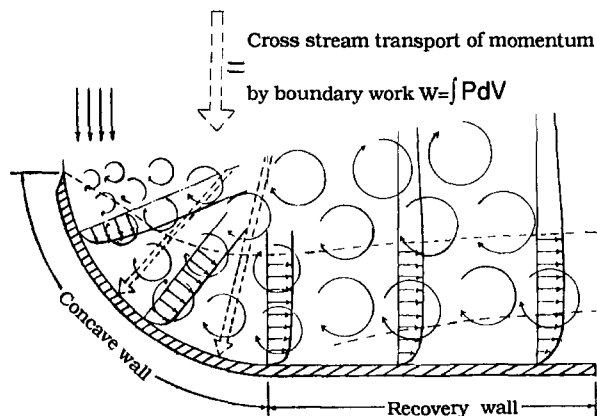


Fig. 16 Schematic diagram of structural changes effected by introduction and removal of concave curvature under high- TI conditions

result in an increase in momentum and heat transfer. Cross transport of momentum by boundary work, which is active over the concave wall, ceases over the recovery wall. Since turbulent eddies lift off the recovery wall, the momentum that has accumulated near the surface over the concave wall has no efficient way of diffusing away from the wall on the recovery section. As in the low- TI case, this excess momentum persists over the recovery wall (Fig. 16). The main conclusions of this study are:

- 1 On the recovery wall, at least part of the "stabilized" region near the surface remains unaffected by elevated TI . Mean velocity profiles in this part of the "stabilized" region show no response to elevated TI .
- 2 Turbulence intensity profiles show that eddies in the high- TI case penetrate the outer 40 percent of the "stabilized" region. It is suggested that C_f and St values increase substantially over the recovery wall, with enhanced TI because the eddies penetrate this region.
- 3 As in the low- TI case, velocity profiles over the recovery wall exhibit inner- and outer-region similarity.
- 4 On the recovery wall, sharper temperature gradients are established in the inner layers of the "stabilized" region relative to gradients in the low- TI case. Conversely, gradients in the outer part of the "stabilized" region are reduced. Thus the effectiveness of the mixing resulting from the eddies penetrating the outer parts of the "stabilized" region is reduced. As a result, heat transfer on the recovery wall does not increase with increased TI as much as does momentum transfer.
- 5 The boundary layer over the recovery wall appears to be free of spanwise nonuniformities. It is suggested that

Görtler-like vortices do not form under high- TI conditions.

- 6 For $y^+ < 300$, the momentum law of the wall remains valid over the recovery wall.

Acknowledgments

This work was supported by the Air Force Office of Scientific Research. The project (grant number AF/AFOSR-91-0322) monitor was Maj. D. Fant.

References

- Blair, M. F., 1983, "Influence of Free-Stream Turbulence on Turbulent Boundary Layer Heat Transfer and Mean Profile Development, Part II—Analysis of Results," *ASME Journal of Heat Transfer*, Vol. 105, pp. 41–47.
- Brown, A., and Burton, R. C., 1977, "The Effects of Free-Stream Turbulence Intensity and Velocity Distribution on Heat Transfer to Curved Surfaces," ASME Paper No. 77-GT-48.
- Eckert, E. R. G., 1987, "Cross Transport of Energy in Fluid Streams," *Wärme- und Stoffübertragung*, Vol. 21, pp. 73–81.
- Feiler, C. E., and Yeager, E. B., 1962, "Effect of Large-Amplitude Oscillations on Heat Transfer," NASA Tech. Report R-142.
- Hancock, P. E., and Bradshaw, P., 1983, "The Effect of Free-Stream Turbulence on Turbulent Boundary Layers," *ASME Journal of Fluids Engineering*, Vol. 105, pp. 284–289.
- Kays, W. M., and Moffat, R. J., 1975, "The Behavior of Transpired Turbulent Boundary Layers," Report HMT-20, Thermosciences Division, Department of Mechanical Engineering, Stanford University, CA.
- Kestin, J., 1966, "The Effects of Free-Stream Turbulence on Heat Transfer Rates," *Advances in Heat Transfer*, Vol. 3, T. F. Irvine, Jr., and J. P. Hartnett, eds., Academic Press, London.
- Kestoras, M. D., and Simon, T. W., 1992, "Hydrodynamic and Thermal Measurements in a Turbulent Boundary Layer Recovering From Concave Curvature," *ASME JOURNAL OF TURBOMACHINERY*, Vol. 114, No. 4, pp. 891–898.
- Kestoras, M. D., 1993, "Heat Transfer and Fluid Mechanics Measurements in a Turbulent Boundary Layer Recovering From Concave Curvature," Ph.D. Thesis, University of Minnesota.
- Kim, J., Simon, T. W., and Russ, S. G., 1991, "Free-Stream Turbulence and Concave Curvature Effects on Heated, Transitional Boundary Layers," *ASME Journal of Heat Transfer*, Vol. 114, No. 2, pp. 339–347.
- Nakano, S., Takahashi, A., Shizawa, T., and Honami, S., 1981, "Effects of Stable and Unstable Free-Streams on a Turbulent Flow Over a Concave Surface," *Proc. 3rd Symposium on Turbulent Shear Flows*, Davis, CA.
- O'Brien, J. E., and vanFossen, G. J., 1985, "The Influence of Jet Grid Turbulence on Heat Transfer From the Stagnation Region of a Cylinder in Cross Flow," ASME Paper No. 85-HT-58.
- Russ, S. G., 1989, "The Generation and Measurement of Turbulent Flow Fields," MSME Thesis, Dept. of Mech. Eng., University of Minnesota.
- Simonich, J. C., and Bradshaw, P., 1978, "Effect of Free-Stream Turbulence on Heat Transfer through a Turbulent Boundary Layer," *ASME Journal of Heat Transfer*, Vol. 100, pp. 671–677.
- Wang, T., 1984, "An Experimental Investigation of Curvature and Freestream Turbulence Effects on Heat Transfer and Fluid Mechanics in Transition Boundary Layer Flows," PhD Thesis, University of Minnesota.
- You, S. M., Simon, T. W., and Kim, J., 1989, "Free-Stream Turbulence Effects on Convex-Curved Turbulent Boundary Layers," *ASME Journal of Heat Transfer*, Vol. 111, pp. 66–72.

Comparison of Calculated and Measured Heat Transfer Coefficients for Transonic and Supersonic Boundary-Layer Flows

C. Hürst

A. Schulz

S. Wittig

Lehrstuhl und Institut für
Thermische Strömungsmaschinen,
Universität Karlsruhe (T.H.),
Karlsruhe, Federal Republic of Germany

The present study compares measured and computed heat transfer coefficients for high-speed boundary layer nozzle flows under engine Reynolds number conditions ($U_\infty = 230 \div 880$ m/s, $Re^ = 0.37 \div 1.07 \times 10^6$). Experimental data have been obtained by heat transfer measurements in a two-dimensional, nonsymmetric, convergent-divergent nozzle. The nozzle wall is convectively cooled using water passages. The coolant heat transfer data and nozzle surface temperatures are used as boundary conditions for a three-dimensional finite-element code, which is employed to calculate the temperature distribution inside the nozzle wall. Heat transfer coefficients along the hot gas nozzle wall are derived from the temperature gradients normal to the surface. The results are compared with numerical heat transfer predictions using the low-Reynolds-number $k-\epsilon$ turbulence model by Lam and Bremhorst. Influence of compressibility in the transport equations for the turbulence properties is taken into account by using the local averaged density. The results confirm that this simplification leads to good results for transonic and low supersonic flows.*

Introduction

Modern gas turbine blades are characterized by extremely high thermal and mechanical loading due to increasing turbine inlet temperatures and higher overall pressures. Since the hot gas temperatures exceed by far the allowable material temperatures, a highly efficient turbine blade cooling is necessary for reliable blade design. To validate numerical codes for the solution of the boundary layer equations, exact experimental heat transfer data are necessary. The numerical codes and turbulence models used for predicting hot gas side boundary layer flow and heat transfer have to take into account the various influencing parameters such as free-stream turbulence, pressure gradients, wall cooling, surface roughness, and wall curvature. Among these parameters, free-stream turbulence and pressure gradients are of major importance, since they are of dominant influence on boundary layer transition and hot gas side heat transfer. Free-stream turbulence affects production and dissipation of turbulent kinetic energy and boundary layer stability. Strong main-stream velocity acceleration directly influences boundary layer thickness, increases stability, and controls turbulence dissipation. In addition, for strong favorable pressure gradients,

boundary layer reverse transition from turbulent to laminar state has to be considered. The increase of heat transfer rates in the case of strong wall cooling is primarily due to the change of fluid properties. Wall roughness stimulates the turbulence motion and, therefore, increases the friction coefficient and consequently heat transfer. Wall curvature dampens turbulence intensity for convex curvature (suction side of turbine blades) and vice versa.

The flow field along modern gas turbine blades is characterized by high Mach numbers and high heat transfer to the walls. Therefore, compressibility effects have to be taken into account. Heat is generated by direct dissipation and transferred by the turbulent fluctuations. For high-speed boundary layer flows, the large amount of dissipation in the near wall region leads to high static temperatures and hence to a strong coupling of the aerodynamic and thermal boundary layer. The increase of the static temperature results in a higher kinematic viscosity. Compared with an incompressible boundary layer, the viscous sublayer is thicker.

The goal of the present study is a comparison of measured and calculated heat transfer distributions for transonic boundary layer flows. The main objectives include: (1) the presentation of heat transfer data for a complex flow, and (2) checking whether a numerical code well suited for subsonic boundary layer flows can be employed for transonic and supersonic boundary layer flows. The vast majority of the available experimental heat transfer data for transonic flow

Contributed by the International Gas Turbine Institute and presented at the 39th International Gas Turbine and Aeroengine Congress and Exposition, The Hague, The Netherlands, June 13-16, 1994. Manuscript received by the International Gas Turbine Institute February 15, 1994. Paper No. 94-GT-173. Associate Technical Editor: E. M. Greitzer.

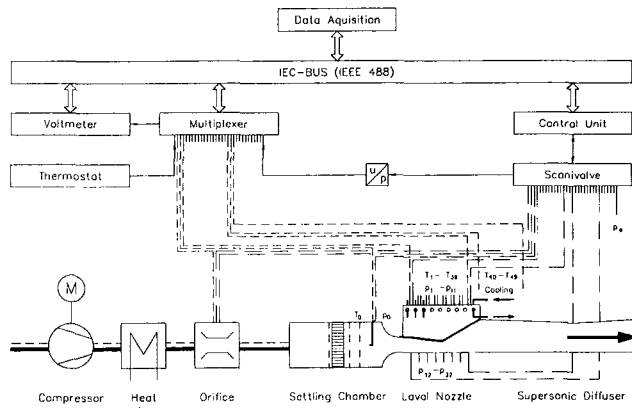


Fig. 1 Experimental setup (schematic)

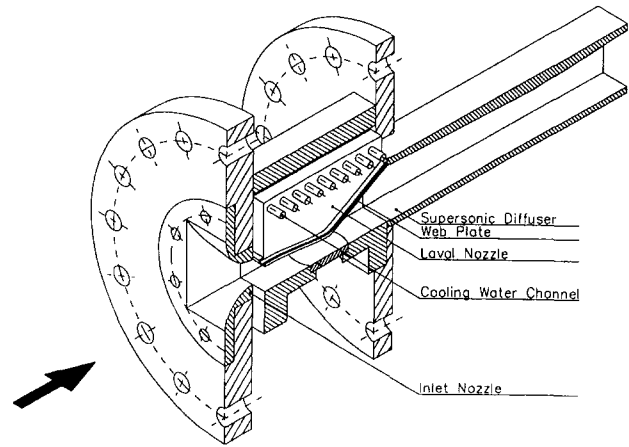


Fig. 2 Test section

were taken during the 1960s (i.e., Back et al. [2–5], Bartz [6], Boldman et al. [7, 8]). However, detailed heat transfer measurements in the high subsonic and low supersonic flow region (Mach number range $0.5 \leq M \leq 2.0$) as demanded for gas turbine applications are rather scarce. Therefore, a new test section for heat transfer measurements was designed. Experiments and calculations have been performed for a two-dimensional nonsymmetric Laval nozzle (Figs. 1 and 2). Specific to the nozzle studied is the small throat radius of curvature. This includes a nonuniform acceleration and results in a nonequilibrium boundary layer. However, for the Mach number range under consideration ($M \leq 2.5$) there is no significant change in turbulence structure compared to an incompressible boundary layer (Maise and McDonald [16]).

Experiments

The heat transfer measurements were conducted under steady-state conditions in the high-pressure–high-temperature test facility of the Institute for Thermal Turbomachinery. The experimental setup is shown schematically in Fig. 1. Maximum values for total pressure and total temperature in the settling chamber are $p_0 = 11$ bar and $T_0 = 1100$ K, respectively. Maximum mass flow rate is $\dot{m} = 1$ kg/s. A honeycomb and three screens in the settling chamber provide a uniform temperature distribution upstream of the inlet nozzle. The Laval nozzle accelerates the flow to supersonic

speed; the exit Mach number of the nonsymmetric two-dimensional convergent-divergent nozzle is $M_{ex} = 2.5$ when fully expanded.

Cross-sectional area in the throat is 27 mm wide and $h^* = 18$ mm high. Maximum channel height in the divergent section is $3 \cdot h^*$. The supersonic diffuser downstream of the Laval nozzle (Fig. 2) improves the flow behavior of the nozzle when not fully expanded by reducing the shock strength. The nozzle wall is convectively cooled using nine water passages. Coolant mass flow rate through the pipes can be adjusted separately for every cooling water pipe. Inflow and outflow temperatures of the coolant are measured. The flow properties for every water channel are calculated with the mean temperature of the cooling water. Mass flow rates are obtained from flow measurements with calibrated orifices. The heat transfer coefficients inside the water pipes are calculated using an equation proposed by Schlünder [23]:

$$\alpha_c = \frac{\xi/8(\text{Re}_c - 1000)\text{Pr}_c}{1 + 12.7\sqrt{\xi/8}(\text{Pr}_c^{2/3} - 1)} \left[1 + \left(\frac{d}{L}\right)^{2/3} \right] \left(\frac{\lambda_c}{d}\right). \quad (1)$$

The friction coefficient ξ for hydraulically smooth passages in Eq. (1) is given by $\xi = (1.82 \log \text{Re}_c - 1.64)^{-2}$ [23]. The assumption of turbulent flow in the pipes is fulfilled for the pipe geometry. Surface temperatures of the Laval nozzle are

Nomenclature

a = velocity of sound
 $c_\mu, c_{\epsilon 1}, c_{\epsilon 2}$ = turbulence model constants
 f_1, f_2, f_μ, f_{cv} = turbulence model functions
 d = pipe diameter
 h = channel height
 H = static enthalpy
 k = turbulent kinetic energy
 K = acceleration parameter
 L = pipe length
 \dot{m} = mass flow rate
 M = Mach number
 p = pressure
 P = production term
 Pr = Prandtl number
 \dot{q} = heat flux
 n = direction perpendicular to surface
 \dot{q} = heat flux
 Re = Reynolds number

S = curvature parameter
 T = temperature
 T^+ = normalized temperature
 Tu = level of turbulence
 U, \tilde{V} = mass-averaged velocities
 U^+ = normalized mean velocity
 u', v' = instantaneous fluctuating components of velocities
 u_τ = friction velocity
 x = mainstream direction
 y = direction perpendicular to the wall
 y^+ = normalized space coordinate
 α = heat transfer coefficient
 ϵ = dissipation rate of k
 κ = ratio of specific heats = 1.4
 λ = heat conductivity
 μ = dynamic viscosity

ξ = friction coefficient
 ρ = density
 $\sigma_k, \sigma_\epsilon$ = turbulence model constants
 τ = shear stress

Subscripts and Superscripts

$[\]_0$ = total
 $[\]_\infty$ = free-stream
 $[\]_a$ = ambient
 $[\]_c$ = cooling
 $[\]_{\text{calc}}$ = calculated
 $[\]_{cv}$ = curvature
 $[\]_{ex}$ = exit
 $[\]_g$ = gas
 $[\]_{is}$ = isentropic
 $[\]_l$ = laminar
 $[\]_m$ = measured
 $[\]_s$ = start
 $[\]_t$ = turbulent
 $[\]_w$ = wall
 $[\]^*$ = throat

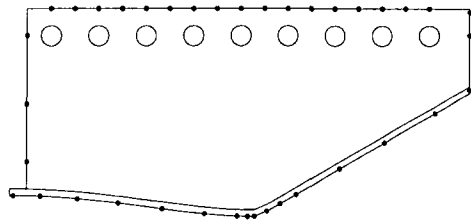


Fig. 3 Position of thermocouples in the midplane

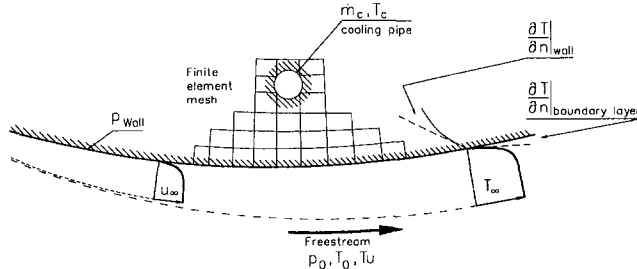


Fig. 4 Comparison of measured and calculated heat transfer distribution

Table 1 Reynolds number $Re^* \times 10^{-6}$ for the operating conditions

T_0 [K]	p_0 [bar]					
	4	5	6	7	9	
565			0.715	0.834	0.953	1.072
630			0.629	0.733	0.838	0.943
700	0.371	0.463	0.556	0.649		

measured with Ni-NiCr thermocouples of \varnothing 0.25 mm attached in the midplane (Fig. 3) and the side walls.

The method used to obtain the heat transfer coefficients is based on the work of Turner [22] and has been applied by us extensively (Rüd [20]). The technique was slightly modified according to Schulz [25] to reduce the uncertainty of measurements. Basically, the temperature distribution inside the nozzle wall is obtained by solving the three-dimensional Laplace equation with a finite-element code [10]. As boundary conditions for the calculation serve the surface temperature distribution of the Laval nozzle and the heat transfer coefficients inside the cooling water pipes (Eq. (1)). Since the number of thermocouples is much smaller than the number of nodes of the computational mesh, measured temperatures have to be interpolated onto the grid points. In this study, the modified Hermite spline interpolation method of Akima [1] is employed, which gives a very smooth temperature distribution without the wiggles known from rational spline interpolation methods. The interpolation method is applied (1) along the circumference of the nozzle body and (2) between the thermocouples at the contact surface of the web plates and the side walls (Fig. 2).

The local hot gas side heat transfer coefficients can be directly evaluated from temperature distribution inside the nozzle wall (see Fig. 4):

$$\alpha_g = \frac{\dot{q}}{T_0 - T_w} = \frac{-\lambda_w \frac{\partial T_w}{\partial n}}{T_0 - T_w} \quad (2)$$

The total temperature instead of the adiabatic wall temperature is used in Eq. (2) because static temperatures on the hot gas side are not measured. The method described provides good spatial resolution of the heat transfer distribution. Even local hot spots can be caught if the number of the thermo-

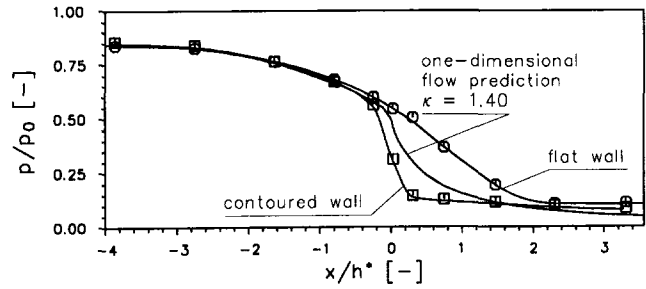


Fig. 5 Pressure distribution

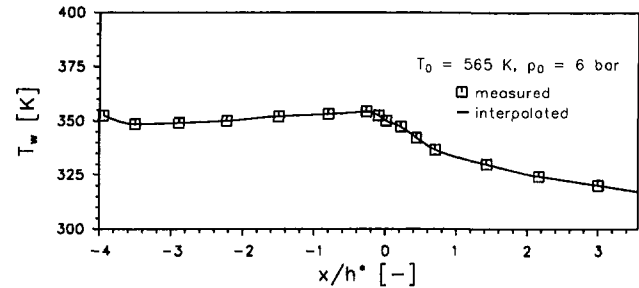


Fig. 6 Hot gas side wall temperature

couples in that specific region is sufficiently high. Moreover, no disturbing probes have to be placed in the flow channel, which is advantageous especially in the near-sonic and super-sonic flow region.

Small pressure taps on both the contoured and the flat nozzle wall give the pressure distribution near the nozzle walls. Total pressure and total temperature in the settling chamber are measured with a traversable probe.

Uncertainties in measurements are given in the following:

Temperature measurement:	0.2 K
Thermocouple positioning:	0.1 mm
Pressure measurement:	0.5 percent
Cooling water mass flow rate:	2 percent

Experimental Results

In the following sections only fully expanded flow is considered. Results of heat transfer measurements are shown for the contoured nozzle wall. The streamwise coordinate x is normalized by the channel height in the nozzle throat h^* . The value $x/h^* = 0$ denotes the nozzle throat; $x/h^* = -4$ represents the entrance of the Laval nozzle. The throat Reynolds number $Re^* = \rho^* a^* h^* / \mu^*$ for the different operating conditions is summarized in Table 1. To reduce the uncertainty in measuring temperature differences, moderate free-stream temperatures were chosen.

The normalized static pressure distributions of both the contoured and the flat wall are shown in Fig. 5. For ambient pressure downstream of the supersonic diffuser a total pressure of $p_0 = 4$ bar at the entrance of the nozzle is necessary to insure a fully expanded flow. On the flat surface, the velocity becomes sonic upstream of the throat. In the divergent section for $x/h^* \geq 1.6$ the measured static pressures are higher than the values derived from one-dimensional flow prediction.

A typical measured wall temperature distribution is shown in Fig. 6. The straight line represents the interpolated temperatures for the heat transfer calculations. Wall temperatures increase toward the throat and obtain their maximum one third channel height upstream of the throat. The local temperature maximum at the beginning of the Laval nozzle (at $x/h^* = -3.9$) is due to the uncooled web plate (see Figs. 2 and 3). To determine the influence of this uncooled web

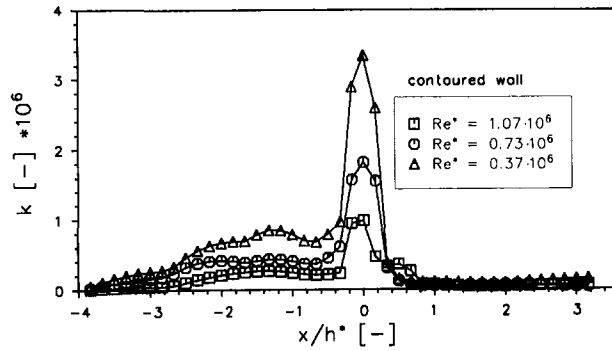


Fig. 7 Acceleration parameter for different test conditions

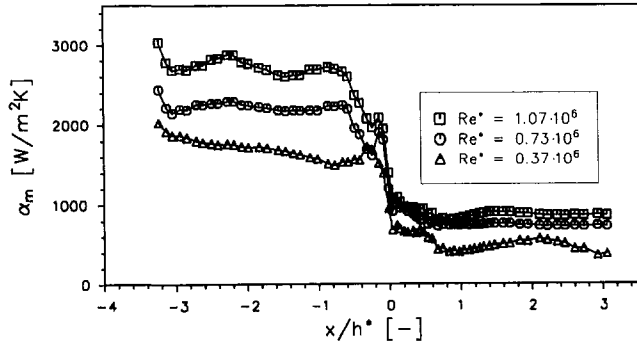


Fig. 8 Typical measured heat transfer distributions

plate on the heat transfer distribution downstream, additional finite-element calculations were performed. The results indicate that there is only a spatially limited effect. The heat transfer in the nozzle throat, however, is unaffected.

The acceleration parameters $K = \mu_c / (\rho_e U_c^2) \cdot dU_c/dx$ (see Moretti and Kays [18]) for the entire range of Reynolds numbers Re^* are shown in Fig. 7. The values are derived from the measured pressure distributions assuming isentropic expansion and constant free-stream enthalpy. For low turbulence levels, a threshold value of $K \approx 3 \times 10^{-6}$ for boundary layer reverse transition is generally accepted [17]. Since the threshold value is exceeded only for the minimum Reynolds number Re^* near the throat, it is assumed that an initially turbulent boundary layer remains in the turbulent state throughout the entire nozzle.

The turbulence level, defined as $\sqrt{u'^2}/U$, was measured by means of a two-component laser-Doppler velocimeter and was found to be $Tu = 1.8$ percent just in front of the Laval nozzle.

Measured heat transfer distributions for the entire range of Reynolds numbers are shown in Fig. 8. Heat transfer levels are very high in the subsonic region and decrease instantaneously as the flow becomes supersonic. In the supersonic region the heat transfer coefficients decrease slightly as the Mach number increases. The rapid drop in heat transfer upstream of the throat corresponds with the strong decrease of pressure and mass flux in that region. Unlike typical heat transfer distributions in rocket nozzles [4, 6] showing the heat transfer maximum in the throat region, the results of the present study show a decrease of the heat transfer coefficients in approaching the throat. The reason for this is the relatively high Mach number at the entrance of the Laval nozzle ($M_{is} \approx 0.5$) and a very thin boundary layer due to the strong acceleration in the inlet nozzle, which lead to very strong velocity and temperature gradients in the boundary layer.

Immediately upstream of the throat at the location $x/h^* \approx -0.25$ the decrease of heat transfer is nonmonotonic. This

can be explained by the position of the thermocouples (Fig. 3 and Eq. (2)). Small errors due to deviations from the correct position of the thermocouples are amplified when calculating the temperature gradients. This problem especially arises if the spatial density of thermocouples is high as in the throat region.

Heat Transfer Calculations

Heat transfer calculations are performed with a modified version of the two-dimensional finite difference boundary layer code ALFA [24, 21]. The boundary layer code accounts for all fundamental effects influencing the heat transfer: boundary layer transition with advanced transition models, favorable and adverse pressure gradients, free-stream turbulence, wall curvature, wall temperature gradients, variable fluid properties, wall roughness, and compressibility.

The Favre approach is used in the averaged transport equations for mass, momentum, and stagnation enthalpy and transformation into a body-fitted coordinate system is employed. The turbulent shear stress can be expressed as follows:

$$\tau_t = -[\overline{\rho'(v+v')} + \rho v']u' = -\overline{\rho u'v'} - \overline{v\rho'u'} - \overline{\rho'v'u'} \quad (3)$$

The last two terms of Eq. (3) account for the compressibility. Since experimental data for $-\overline{v\rho'u'}$ and $-\overline{\rho'v'u'}$ are scarce, most of the turbulence models neglect these terms, i.e., the expression for the turbulent shear stress reduces to the Reynolds shear stress of incompressible flows. The equation for the turbulent shear stress can be extended from the incompressible to the compressible case by simply using the local averaged density.

In the present study, the low-Reynolds-number $k-\epsilon$ turbulence model proposed by Lam and Bremhorst [14] is employed for the description of turbulent momentum and heat transport. The Reynolds stresses and the turbulent heat flux are related to the gradients of the mean velocity and total enthalpy by the eddy viscosity $\mu_t = c_{\mu} f_{\mu} f_{cv} k^2/\epsilon$ and a turbulent Prandtl number Pr_t , respectively:

$$-\overline{\rho u'v'} = \mu_t \frac{\partial U}{\partial y} \quad -\overline{\rho v'h'} = \frac{\mu_t}{Pr_t} \frac{\partial H}{\partial y} \quad (4)$$

The function f_{cv} according to Leschziner and Rodi [15] in the definition of the eddy viscosity accounts for the wall curvature. The equations for the turbulent kinetic energy k and its dissipation rate ϵ in a body-fitted (x, y) -coordinate system are:

$$\rho U \frac{\partial k}{\partial x} + \rho \tilde{V} \frac{\partial k}{\partial y} = \frac{\partial}{\partial y} \left[\left(\mu + \frac{\mu_t}{\sigma_k} \right) \frac{\partial k}{\partial y} \right] + \underbrace{\mu_t \left[\left(\frac{\partial U}{\partial y} \right) (1-S) \right]^2}_{P_k} - \rho \epsilon \quad (5)$$

$$\rho U \frac{\partial \epsilon}{\partial x} + \rho \tilde{V} \frac{\partial \epsilon}{\partial y} = \frac{\partial}{\partial y} \left[\left(\mu + \frac{\mu_t}{\sigma_{\epsilon}} \right) \frac{\partial \epsilon}{\partial y} \right] + \underbrace{c_{\epsilon 1} f_1 \frac{\epsilon}{k} P_k - \rho c_{\epsilon 2} f_2 \frac{\epsilon^2}{k}}_{P_{\epsilon}} \quad (6)$$

where the factor $(1-S)$ of the production terms P_k and P_{ϵ} depends on the local radius of curvature, the velocity U , and its gradient normal to the wall.

The empirical constants in Eqs. (4), (5), and (6) are given by Rodi [19] and Kays and Moffat [13]:

c_{μ}	$c_{\epsilon 1}$	$c_{\epsilon 2}$	σ_k	σ_{ϵ}	Pr_t
0.09	1.44	1.92	10	1.3	0.86

Numerous modifications of two-equation turbulence models to account for compressibility effects are given in the literature (i.e., [11, 9, 12]). The modifications primarily are additional terms for the transport equations for k and ϵ , Eqs. (5), (6), or modify the eddy viscosity.

Horstman [12] investigated three different modifications of the Jones–Launder turbulence model: (i) modification of the production term of the ϵ equation, (ii) addition of compressibility terms in the transport equations for the turbulence properties, (iii) multiplication of the eddy viscosity with a factor depending on the turbulent kinetic energy k , the local velocity of sound, and the local Mach number. Galmes et al. [11] introduced additional terms in the transport equations of the turbulence model by Jones and Launder to calculate two-dimensional boundary layers with pressure gradient. They also proposed a modification of the eddy viscosity based on the balance between production and dissipation terms in the k equation. The modifications are based on the assumption of the strong Reynolds analogy and, therefore, are not valid for the present problem (see below). The model of Dussauge and Quine [9] for the pressure-velocity correlation employs a modified eddy viscosity, which is obtained by a simplification of the Reynolds stress equations. No additional terms appear in the transport equations for the turbulence properties. They applied their model to a supersonic shear layer and could predict the decrease of the spreading rate of the shear layer with increasing Mach number, while the Jones–Launder turbulence model shows no influence of the Mach number. The applicability for boundary layer flow problems is not discussed. Since the modifications described above are not generally valid for the present flow problem, the standard form of the low-Reynolds-number k – ϵ turbulence model, Eqs. (4) to (6), is employed.

Boundary Conditions. The measured wall temperature distribution is employed as wall boundary condition for the energy equation. The wall boundary conditions for the turbulence properties k and ϵ , Eqs. (5) and (6), are $k_w = \partial \epsilon_w / \partial y = 0$. The free-stream boundary conditions for k and ϵ are calculated with the Eqs. (5) and (6) neglecting the gradients in the y direction. The resulting ordinary differential equations for k_x are integrated in the x direction. The free-stream velocities and temperatures at the outer edge of the boundary layer are based on the experimental data and derived from the total pressure, total temperature, and the static pressure distribution along the wall. Constant total enthalpy in the free-stream, isentropic expansion, and constant static pressure across the boundary layer are assumed. Surface roughness is considered to be negligible.

Initial Conditions. For the calculations laminar initial profiles have been employed. To avoid Mach number influencing the boundary layer initial profiles the starting location of calculations was shifted upstream to a region of low Mach number ($M_s = 0.25$). The initial profiles for the turbulent kinetic energy and the dissipation rate are dependent on the turbulence level, the free-stream velocity, and the length scale of the turbulence eddies.

Calculated Heat Transfer Distribution. All calculations show boundary layer transition from laminar to turbulent state upstream of the Laval nozzle. Since transition onset is very sensitive to the free-stream turbulence especially in the low turbulence range, additional calculations were performed with very low levels of turbulence ($Tu = 1.0 \div 1.5$ percent).

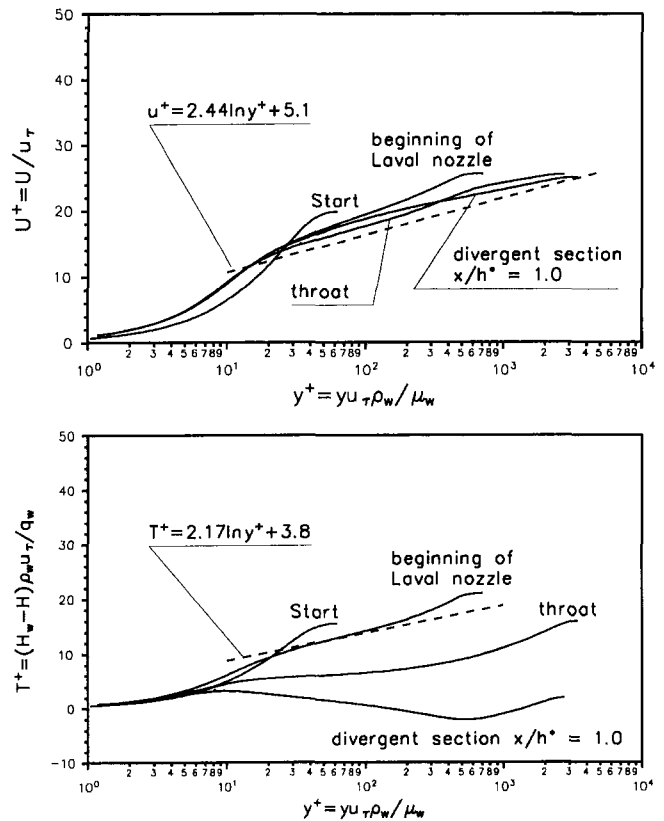


Fig. 9 Velocity and temperature profiles in the nozzle

All tests indicate an early transition. The boundary layer, therefore, is always assumed to be turbulent in the nozzle. Hence, modifications of the k – ϵ turbulence model to improve the description of the transition process as discussed by Sieger [21] are not necessary.

Calculated profiles of the mean velocity and mean temperatures for different locations in the nozzle are shown in Fig. 9. Velocity profiles confirm the turbulent state of the boundary layer at the entrance of the Laval nozzle (Fig. 9). For $30 \leq y^+ \leq 250$ the slope of the curve is higher than the one of the logarithmic law. Toward the throat, the slope decreases and the wake region broadens. In the divergent section no region of a logarithmic law appears. In general all calculated profiles are beyond the curve of the logarithmic law $u^+ = 2.44 \ln y^+ + 5.1$ for a turbulent flat plate boundary layer flow.

The temperature profiles in Fig. 9 show distinct differences between the calculations and the logarithmic law $T^+ = 2.17 \ln y^+ + 3.8$. There is no location in the Laval nozzle that can be described by the logarithmic law. The strong decrease in the static free-stream temperature as the flow becomes supersonic leads to a negative slope in the mean temperature profiles in the divergent section. However, heat is transferred from the boundary layer to the wall due to the dissipation of the kinetic energy. In the supersonic region the energy thickness decreases.

Comparison of Measurements and Calculations

A typical measured heat transfer distribution and the calculation with the modified version of ALFA [24, 21] are shown in Fig. 10. In addition, heat transfer coefficients calculated with an equation of Bartz [6]

$$\alpha_g = \frac{0.026}{h^{0.2}} \left(\frac{h^*}{r_{co}} \right)^{0.1} \left(\frac{\mu_{ref}^{0.2}}{Pr^{0.6}} \right) (\rho U)_{\infty}^{0.8} \left(\frac{\rho_{ref}}{\rho} \right)^{0.8} \left(\frac{\mu_{ref}}{\mu_0} \right)^{0.2} \quad (7)$$

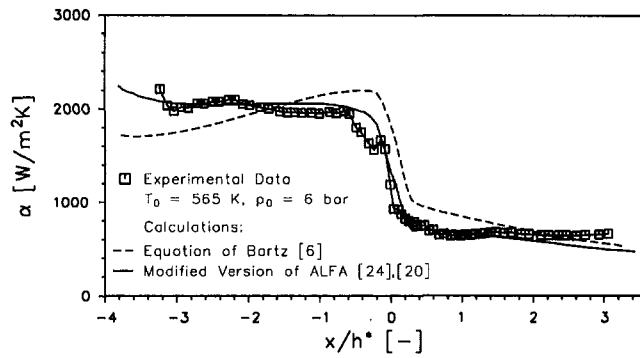


Fig. 10 Comparison of calculations and experimental data

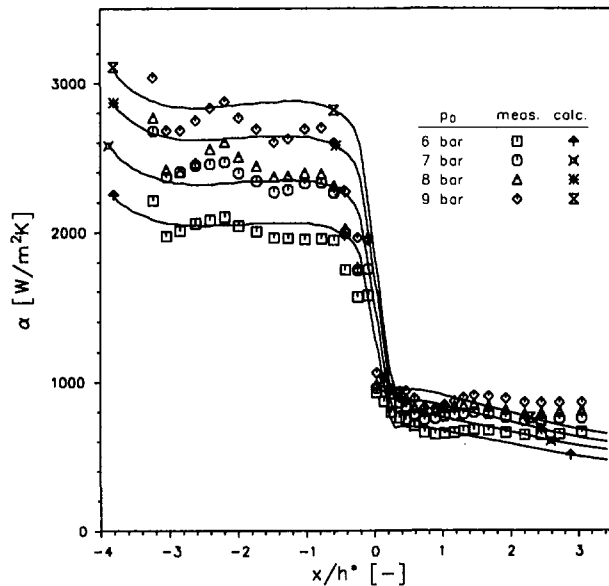


Fig. 11 Measured and calculated heat transfer distributions for $T_0 = 565$ K

based on the assumption of fully developed turbulent flow are also shown in Fig. 10. It can be clearly seen that the simple equation of Bartz is not suitable for the description of the heat transfer distribution along the nozzle, whereas the calculation with ALFA yields a much better conformity.

The measured and calculated heat transfer distributions for all operating conditions are shown in Figs. 11–13. For Mach numbers less than unity the thermal loading is very high. Calculated onset, slope, and final value of the strong decrease of the heat transfer coefficients near the throat are in excellent agreement with the measurements.

All experiments confirm the decrease of the heat transfer coefficients in the subsonic region and the rapid drop in heat transfer as the flow becomes supersonic. The decrease of the measured heat transfer coefficients continues in the supersonic section until $x/h^* = 0.8$; farther downstream the values stay nearly constant for $T_0 = 565$ K and $T_0 = 630$ K. The measurements for $T_0 = 700$ K indicate a nonuniform behavior in the supersonic region: for low total pressures, i.e., a high acceleration (see Fig. 7), measured heat transfer coefficients are below the calculated ones.

For the geometry and operating conditions under consideration the calculations confirm the location of the heat transfer maximum upstream of the nozzle throat. The calculated heat transfer distributions show a slight increase toward the nozzle throat, which is more clear for higher total pressures. As the flow becomes supersonic, a sudden reduction in heat transfer is predicted. In contrast to the measurements, the calculations show a sharp kink immediately downstream

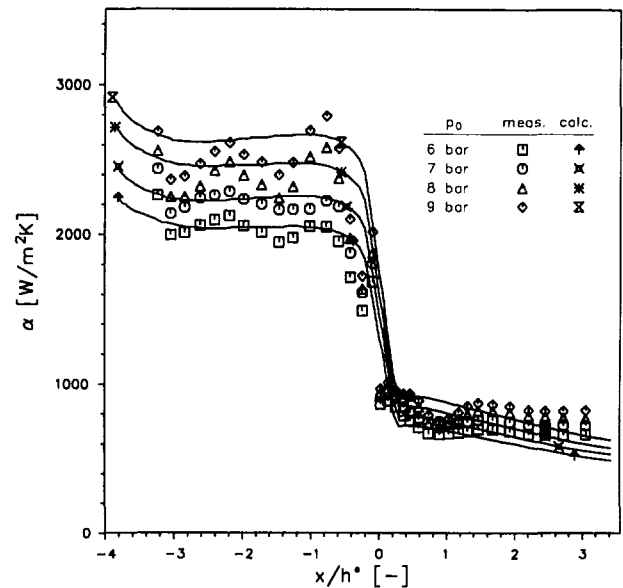


Fig. 12 Measured and calculated heat transfer distributions for $T_0 = 630$ K

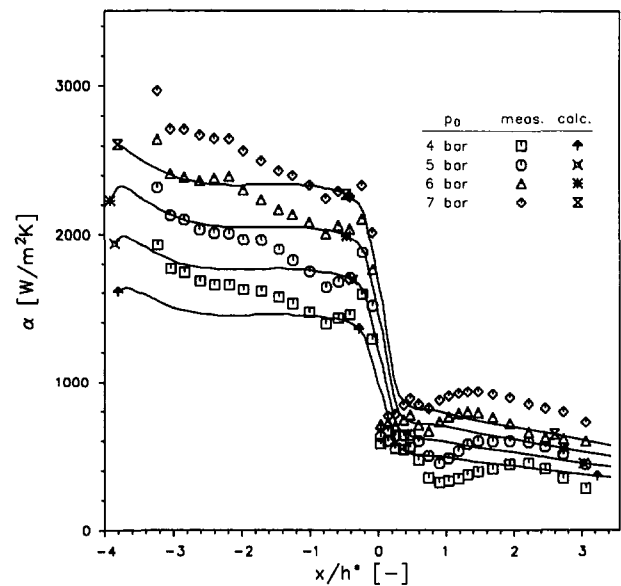


Fig. 13 Measured and calculated heat transfer distributions for $T_0 = 700$ K

of the throat. In the divergent section the calculations indicate a continuously decreasing heat transfer.

The deviations in the supersonic region cannot be fully explained at the moment. Probably three-dimensional flow effects in the divergent section caused by the small radius of curvature in the throat and the nonsymmetric nozzle contour are responsible for the deviations.

However, the comparison of calculated and measured heat transfer distributions clearly confirm the applicability of the boundary layer code and the turbulence model for describing the effects of strong acceleration and rapid changes in mainstream fluid properties, even when the “incompressible” formulation of the transport equations is employed.

Conclusions

Heat transfer measurements and calculations for high-speed nozzle flow have been performed. For the calculations the incompressible formulation of the transport equations

has been employed. Comparison of computed and measured heat transfer distributions show reasonably good agreement. The results indicate that the incompressible formulation of the transport equations with local averaged density and the low Reynolds-number $k-\epsilon$ turbulence model of the boundary layer code ALFA [24] can be used for the computation of heat transfer in subsonic, transonic, and low supersonic flows. For higher Mach numbers deviations of measured and calculated heat transfer distributions increase. Future work will be focused on laser-Doppler flow measurements in the transonic and supersonic region and investigation of turbulence models and their modifications for compressible flows.

Acknowledgments

The study was supported by the Sonderforschungsbereich 167 of the German Science Foundation (DFG) and the Motoren- und Turbinen-Union München GmbH. Dr.-Ing. R. Walther was actively involved in initiating the program.

References

- 1 Akima, H., "A New Method of Interpolation and Smooth Curve Fitting Based on Local Procedures," *Journal Assoc. Comp. Mach.*, Vol. 17, No. 4, 1970.
- 2 Back, L. H., and Cuffel, R. F., "Turbulent Boundary Layer and Heat Transfer Measurements Along a Convergent-Divergent Nozzle," ASME Paper No. 71-HT-4, 1971.
- 3 Back, L. H., Cuffel, R. F., and Massier, P. F., "Laminarization of a Turbulent Boundary Layer in Nozzle Flow—Boundary Layer and Heat Transfer Measurements With Wall Cooling," *ASME Journal of Heat Transfer*, Vol. 92, 1970, pp. 333–344.
- 4 Back, L. H., Massier, P. F., and Gier, H. L., "Convective Heat Transfer in a Convergent-Divergent Nozzle," *Int. J. Heat Mass Transfer*, Vol. 7, 1964, pp. 549–568.
- 5 Back, L. H., Massier, P. F., and Gier, H. L., "Comparison of Measured and Predicted Flows Through Conical Supersonic Nozzles, With Emphasis on the Transonic Region," *AIAA Journal*, Vol. 3, No. 9, 1965.
- 6 Bartz, D. R., "Turbulent Boundary-Layer Heat Transfer From Rapidly Accelerating Flow of Rocket Combustion Gases and of Heated Air," in: *Advances in Heat Transfer*, Vol. 2, Academic Press, New York-London, 1965.
- 7 Boldman, D. R., and Graham, R. W., "Heat Transfer and Boundary Layers on Conical Nozzles," NASA TN D-6594, 1972.
- 8 Boldman, D. R., Schmidt, J. F., and Ehlers, R. C., "Prediction of Local and Integrated Heat Transfer in Nozzles Using an Integral Turbulent Boundary Layer Method," NASA TN D-6595, 1972.
- 9 Dussauge, J. P., and Quine, C., "A Second Order Closure for Supersonic Turbulent Flows—Application to the Supersonic Mixing," *Lecture Notes in Engineering*, Springer Verlag, 1988.
- 10 FIDAP, "Fluid Dynamics Analysis Package Version 6.04," Fluid Dynamics International Inc., Evanston, IL, 1992.
- 11 Galmes, J. M., Dussauge, J. P., and Dekeyser, I., "Couches limites turbulentes supersoniques soumises à un gradient de pression: calcul à l'aide d'un modèle $k-\epsilon$," *Journal de Mécanique Théorique et Appliquée*, Vol. 2, No. 4, 1983.
- 12 Horstman, C. C., "Prediction of Hypersonic Shock Wave-Turbulent Boundary Layer Interaction Flow," AIAA Paper No. 87-1367, 1987.
- 13 Kays, W. M., and Moffat, R. J., "The Behavior of Transpired Boundary Layers," in: *Studies in Convection*, B. E. Launder, ed., Academic Press, 1975.
- 14 Lam, C. K. G., and Bremhorst, K. A., "Modified Form of the $k-\epsilon$ Model for Predicting Wall Turbulence," *ASME Journal of Fluids Engineering*, Vol. 103, 1981.
- 15 Leschziner, M. A., and Rodi, W., "Calculation of Annular and Parallel Jets Using Various Discretization Schemes and Turbulence Models," *ASME Journal of Fluids Engineering*, Vol. 103, 1981.
- 16 Maise, G., and McDonald, H., "Mixing Length and Kinematic Eddy Viscosity in a Compressible Boundary Layer," *AIAA Journal*, Vol. 6, No. 1, 1968.
- 17 Mayle, R., "The Role of Laminar-Turbulent Transition in Gas Turbine Engines," *ASME JOURNAL OF TURBOMACHINERY*, Vol. 113, No. 10, 1991.
- 18 Moretti, P. M., and Kays, W. M., "Heat Transfer to a Turbulent Boundary Layer With Varying Free-Stream Velocity and Varying Surface Temperature," *Int. J. Heat Mass Transfer*, Vol. 8, 1965.
- 19 Rodi, W., "Turbulence Models and Their Application in Hydraulic," *Int. Assoc. of Hydraulics Research Publication*, Delft, 1980.
- 20 Rüd, K., and Wittig, S., "Free-Stream Turbulence and Pressure Gradient Effects on Heat Transfer and Boundary Layer Development on Highly Cooled Surfaces," *ASME JOURNAL OF TURBOMACHINERY*, Vol. 107, 1985, pp. 54–59.
- 21 Sieger, K., Schulz, A., Wittig, S., and Crawford, M. E., "An Evaluation of Low-Reynolds Number $k-\epsilon$ -Turbulence Models for Predicting Transition Under the Influence of Free-Stream Turbulence and Pressure Gradient," in: *Proceedings of the Second International Symposium on Engineering Turbulence and Measurements*, Florence, Italy, 31 May–2 June, Elsevier, 1993.
- 22 Turner, A. B., "Local Heat Transfer Measurements on a Gas Turbine Blade," *Journal of Mechanical Engineering Sciences*, Vol. 13, 1971.
- 23 VDI, "VDI-Wärmeatlas, Berechnungsblätter für den Wärmeübergang," 4. Auflage, VDI-Verlag, Düsseldorf, 1984.
- 24 Wittig, S., Rodi, W., Sill, K. H., Rüd, Scheuerer, G., and Schulz, A., "Experimentelle und theoretische Untersuchung zur Bestimmung von Wärmeübergangszahlen an gekühlten Gasturbinenschaufeln," *FVV-Vorhaben*, No. 241, Abschlußbericht, 1982.
- 25 Wittig, S., Schulz, A., Bauer, H. J., and Sill, K. H., "Effects of Wakes on the Heat Transfer in Gas Turbine Cascades," in: *Heat Transfer and Cooling in Gas Turbines*, AGARD-CP-390, 1985.

Prediction of Turbulent Flow and Heat Transfer in a Ribbed Rectangular Duct With and Without Rotation

C. Prakash

R. Zerkle

General Electric Company
Aircraft Engines,
Mail Drop A322;
P.O. Box 156301,
One Neumann Way,
Cincinnati, OH 45215-6301

The present study deals with the numerical prediction of turbulent flow and heat transfer in a 2:1 aspect ratio rectangular duct with ribs on the two shorter sides. The ribs are of square cross section, staggered and aligned normal (90 deg) to the main flow direction. The ratio of rib height to duct hydraulic diameter equals 0.063, and the ratio of rib spacing to rib height equals 10. The duct may be stationary or rotating. The axis of rotation is normal to the axis of the duct and parallel to the ribbed walls (i.e., the ribbed walls form the leading and the trailing faces). The problem is three dimensional and fully elliptic; hence, for computational economy, the present analysis deals only with a periodically fully developed situation where the calculation domain is limited to the region between two adjacent ribs. Turbulence is modeled with the $k-\epsilon$ model in conjunction with wall functions. However, since the rib height is small, use of wall functions necessitates that the Reynolds number be kept high. (Attempts to use a two-layer model that permits integration to the wall did not yield satisfactory results and such modeling issues are discussed at length.) Computations are made here for Reynolds number in the range 30,000–100,000 and for Rotation number = 0 (stationary), 0.06, and 0.12. For the stationary case, the predicted heat transfer agrees well with the experimental correlations. Due to the Coriolis-induced secondary flow, rotation is found to enhance heat transfer from the trailing and the side walls, while decreasing heat transfer from the leading face. Relative to the corresponding stationary case, the effect of rotation is found to be less for a ribbed channel as compared to a smooth channel.

1.0 Introduction

1.1 Motivation. Effective turbine blade cooling is necessary to enhance the efficiency of advanced aircraft engines. In general, film cooling is imposed on the external surfaces of the blades, while forced-convection cooling is employed inside the blades by means of cooling passages as shown in Fig. 1. The present study pertains to the latter, i.e., flow and heat transfer in the internal blade cooling passages.

To trip the boundary layers for promoting turbulence and thereby enhancing heat transfer, various kinds of turbulators (ribs) are usually provided on the walls of the blade cooling passages. An example of a ribbed passage is shown in Fig. 2. The presence of the ribs leads to a complex flow field with regions of flow separation before and after the ribs. Further, since the turbine undergoes high rotation, the flow is strongly affected by the Coriolis and centrifugal forces. Needless to

say, therefore, the flow field, and hence the heat transfer at the walls, is quite complex.

Detailed information about the flow distribution in a ribbed rotating passage can be very valuable for a designer engaged in deciding where, how many, and what kind of ribs to employ. However, obtaining such information experimentally can be very expensive, and difficult, if not impossible.

The only other method for predicting flow and heat transfer is via numerical integration of the governing equations. However, practical flows are turbulent and require suitable turbulence models for the modeling of small-scale phenomena. Unfortunately, the available turbulence models are not universal. Hence, it is necessary that these models be first validated using data from well-defined experiments before they can be used to make routine calculations. The present study is to be viewed in this perspective. The work reported here is a natural progression from our previous study [1] where the effect of rotation on flow through a smooth channel was analyzed.

1.2 Turbulence Modeling Challenges. There are several features that make the task of predicting flow and heat

Contributed by the International Gas Turbine Institute and presented at the 38th International Gas Turbine and Aeroengine Congress and Exposition, Cincinnati, Ohio, May 24–27, 1993. Manuscript received at ASME Headquarters March 3, 1993. Paper No. 93-GT-206. Associate Technical Editor: H. Lukas.

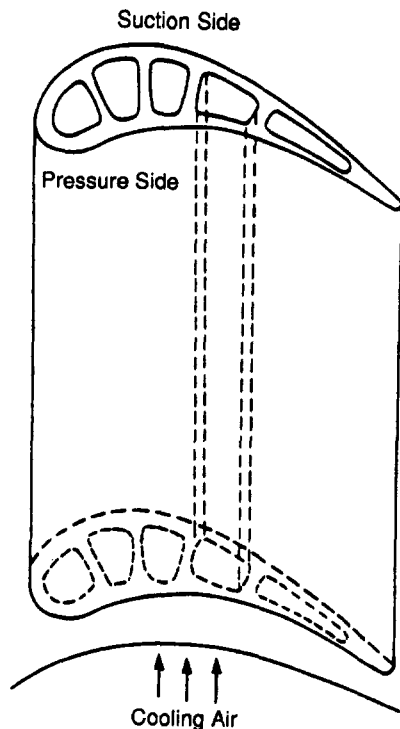


Fig. 1 Turbine blade internal cooling passages (Han [11])

transfer in a blade cooling passage particularly challenging. For instance, in many applications, the ribs have very small dimensions (low blockage ratio turbulators) and/or the Reynolds number is low. In such cases, even a modest computational grid around the ribs leads to the grid nodes being too close to the wall (i.e., low y^+) for accurate application of the wall-function treatment of turbulence modeling [2]. Hence, use of a low Reynolds number turbulence model becomes necessary. The difficulty with most of the low-Re models is that they require extremely fine grids and often become computationally prohibitive for the three-dimensional elliptic flows of interest here [3]. Indeed, the grid requirements with low-Re model can be so demanding that several efforts are currently underway to develop the so-called

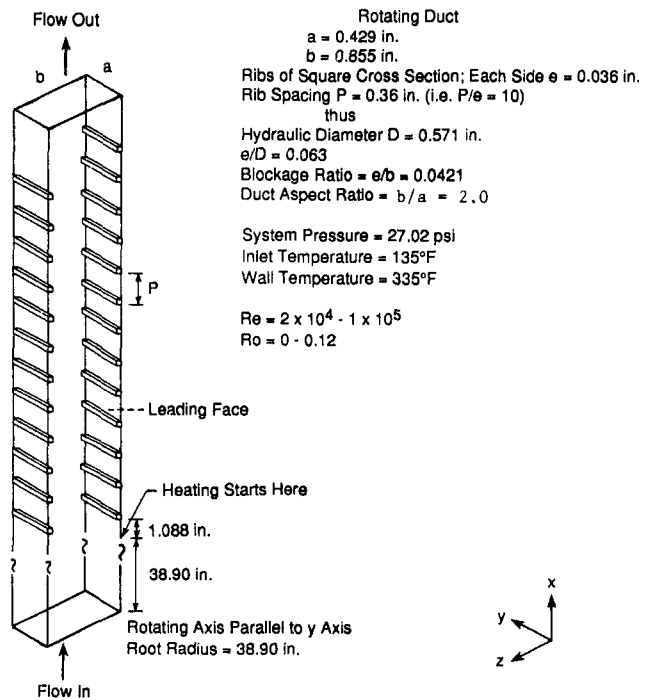


Fig. 2 Turbulated passage

two-layer models, which seek to provide the benefits of a low-Re model but on a much coarser grid. Several two-layer models have been reviewed by Rodi [4] and it appears that for three-dimensional elliptic flows even these may require very fine grids.

If centrifugal buoyancy is small, then the flow can become periodically fully developed (i.e., repeat cyclically). In such a situation, the computational domain is limited to the region between two adjacent ribs and it may be possible to provide adequate grid for a low-Re or a two-layer model. However, in practical situations, centrifugal buoyancy can be significant and it can lead to large flow reversals near the walls [1]. In such cases, the flow is not cyclically developed and one must analyze the entire channel with several ribs. For such a complete analysis, the grid required for the low-Re and the

Nomenclature

a, b = length of the shorter (ribbed) and longer (smooth) walls	P = rib pitch, i.e., interrib spacing	between the wall and the near-wall point = $\delta u_\tau / \nu$
B, C = pressure and temperature gradients in the flow direction (Eqs. (2), (3))	p, \bar{p} = pressure (Eq. (2))	δ = distance between the wall and the near-wall point
C_1, C_2, C_μ = turbulence model constants	Pr, Pr_t = laminar and turbulent Prandtl numbers	ϵ = rate of dissipation of turbulent kinetic energy
c_p = specific heat	q = heat flux	κ = von Karman constant
D = hydraulic diameter = $2ab/(a+b)$	Re = Reynolds number = $\bar{u}D/\nu$	λ = thermal conductivity
E = wall roughness parameter	Ro = Rotation number = $\Omega D/\bar{u}$	μ, μ_t = laminar and turbulent viscosity, respectively
e = rib height	s = local friction coefficient	ν, ν_t = laminar and turbulent kinematic viscosity, respectively
f = friction factor = $BD/(2\rho\bar{u}^2)$	St = local Stanton number	ρ = density
G = rate of generation of turbulent kinetic energy	T, \bar{T} = temperature (Eq. (3))	$\sigma_\kappa, \sigma_\epsilon$ = Prandtl numbers for κ and ϵ , respectively
h = heat transfer coefficient	u, v, w = velocity components in the x, y, z directions	τ_w = local shear stress at the wall
k = turbulent kinetic energy	\bar{u} = mean velocity = $\dot{m}/(\rho ab)$	Ω = angular rotation speed
\dot{m} = mass flow rate through the duct	u_τ = shear velocity at the wall = $\sqrt{\tau_w/\rho}$	Subscripts
Nu = Nusselt number = hD/λ	V = tangential velocity at the near-wall point	b = bulk
	x, y, z = coordinates	w = wall
	y^+ = dimensionless distance	

two-layer models can indeed be very large, preventing economical computations on a routine basis.

When the ribs are large (high blockage ratio), and/or the Reynolds number is high, then these difficulties do not arise and one may be able to use wall functions and work with reasonable grid sizes. However, two additional considerations become important: (a) Secondary cross-stream flows due to three-dimensional effects can become significant. These flows are caused by turbulence anisotropic effects and require advanced turbulence models (of Reynolds-stress-type) for prediction. (Such secondary flows, it should be pointed out though, may be less important in rotating channels as compared to stationary channels because of the swamping effect of the Coriolis flows in the former.) (b) Multiple length scale effects can become important, necessitating the use of advanced turbulence models that acknowledge the presence of two or more length scales.

On the basis of the key issues discussed above, four categories of problems can be defined:

- 1 Low Reynolds number/low blockage ratio
- 2 Low Reynolds number/high blockage ratio
- 3 High Reynolds number/low blockage ratio
- 4 High Reynolds number/high blockage ratio

Categories 1 and 2 require a low Reynolds number turbulence model while for 3 and 4 the wall-function procedure may be adequate. Further, categories 2 and 4 may require Reynolds stress models to account for anisotropic effects and, possibly, multiple-length-scale models. Clearly, problems of type 2 are the most demanding, those of type 3 least demanding, while types 1 and 4 are of moderate difficulty.

Finally, rotation, and associated buoyancy effects, may require refinements to the turbulence models and possibly the near-wall treatments.

1.3 Scope of the Present Study. The purpose of the previous section is to highlight that the problem of predicting flow in turbine blade cooling passages is by no means easy. Hence, it would be unreasonable to expect a single effort that would yield a turbulence model that can address all the difficulties outlined above. Instead, progress will have to come in several steps, with each effort representing an advance over the previous one. There is no doubt, of course, that the intermediate steps, though limited in scope, will continue to add to our understanding of the various physical aspects of the flow. The work described in this paper is to be taken in this spirit and regarded as a building block.

In terms of the classification provided in the previous section, the simulations presented in this paper correspond to category 3 (high Reynolds number/low blockage ratio . . . least demanding). Our intent here is to see how well the standard (isotropic) $k-\epsilon$ model performs in conjunction with the wall functions.

1.4 Literature Review. The literature pertaining to flow in rotating smooth ducts (no ribs) was reviewed extensively by the present authors in [1] and is not repeated here.

1.4.1 Ribbed Passages—Theoretical. The original theoretical analyses dealt with the development of heat transfer and friction correlations using concepts similar to those used for rough tubes [5].

Due to the difficulties discussed in Section 1.2, numerical predictions of turbulent flow in ribbed passages are few and recent. Chang and Mills [6] employed a low-Re turbulence model for a two-dimensional situation involving flow in a stationary circular tube with repeated rectangular ribs. This study provides an indication of the large grids that may be required by a low-Re model. Arman and Rabas [7] subsequently predicted flow and heat transfer in a stationary circular tube with repeated ribs using a two-layer model.

Recently Cunha [8] predicted flow and heat transfer in

rotating circular tubes with ribs. A one-equation (k -mixing length) turbulence model is employed. Near the wall, a wall-function type treatment is employed but use is made of experimentally determined roughness function expressions for ribbed channels. In this sense Cunha's study is not fundamental—i.e., it uses experimentally determined velocity/temperature defect correlations at the walls instead of establishing them from the equations of fluid motion.

1.4.2 Ribbed Passages—Experimental. Due to the practical importance of the problem, there have been several experimental investigations aimed at determining the overall heat transfer and pressure drop in ribbed passages. Earlier efforts dealt with the stationary ducts while some of the recent studies examine the effect of rotation.

Stationary. Burgraff's study [9] is an example of one of the earlier works. For the last several years, Prof. J. C. Han's laboratory at Texas A & M has been engaged in obtaining heat transfer and pressure drop data in ducts of varying aspect ratio, rib height, and orientation. A sampling of Han's studies is provided by [10–12]. Professor Taslim's group at Northeastern University has been another source of experimental data as exemplified by [13].

Rotating. Experimental studies including the effect of rotation are more recent and fewer. The currently active groups are those of Dr. Johnson at United Technology Research Center [14–15] and of Dr. Taslim at Northeastern [16–17].

2.0 Analysis

2.1 Background. The present study is directed by our goal to predict flow and heat transfer in the ribbed channel shown in Fig. 2. This configuration is the result of discussions with turbine cooling designers, and includes parameters of practical interest. As shown, the channel consists of a long, smooth, rotating (but unheated) entrance length on top of which is perched the ribbed section. Clearly, within the ribbed part of the channel, the flow is in a developing mode both hydrodynamically and thermally. Further, in the range of operating parameters, both Coriolis and centrifugal buoyancy are important.

2.2 The Problem Solved: Assumptions and Implications. Our final goal is to simulate the flow in the channel shown in Fig. 2. However, the present analysis is an intermediate step, a rationale for which may be found in the discussion of sections 1.2 and 1.3. Here we focus our attention on a periodically fully developed situation, which assumes that the flow repeats itself cyclically from one rib to the next. This assumption allows the calculation domain to be limited to the region between two adjacent ribs and the computational grid is reasonable. The calculation domain, and grid used, are shown in Fig. 3.

As for a fully developed duct flow, a periodically fully developed situation is intended to imply that conditions within a module are isolated from happenings outside the module either upstream or downstream. This requirement could be violated by centrifugal buoyancy effects if they lead to large-scale flow reversals as was found in [1] for a smooth channel. *For this reason, centrifugal-buoyancy effects are neglected in this analysis (i.e., density is assumed constant), and only Coriolis effects are considered.* In the same spirit, though with lesser implications, is the requirement of constant thermophysical properties (viscosity, conductivity, etc.) so that a periodically fully developed situation can be defined.

If buoyancy effects are weak and do not lead to large-scale flow reversals, then, under certain thermal boundary conditions (e.g., uniform wall heat flux), it may be possible to account for buoyancy within a periodically fully developed

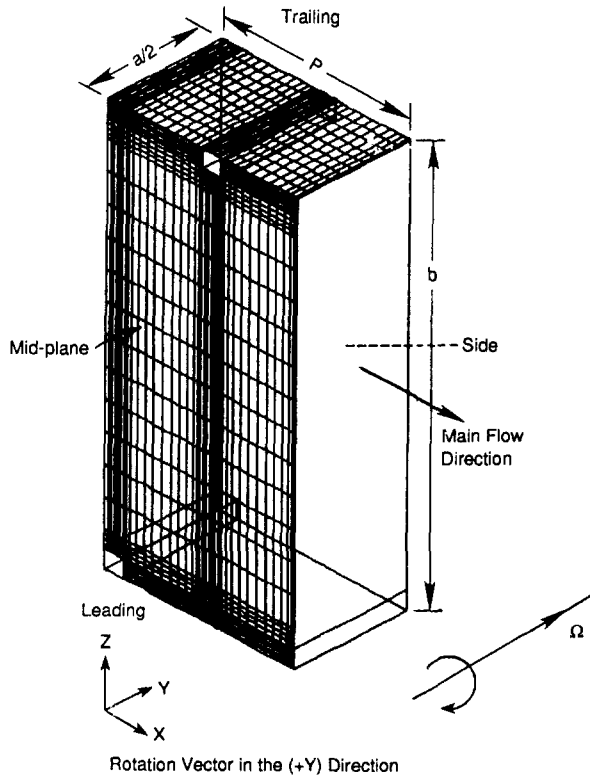


Fig. 3 Problem schematics and grid ($36 \times 32 \times 10 = 11,520$ nodes)

framework if certain assumptions are made (e.g., Boussinesq in conjunction with relative temperature differences within the computational module, etc.). However, based on experience with a smooth channel [1], it is felt that centrifugal-buoyancy effects are best handled via the simulation of the flow in the entire channel with several ribs including careful modeling of the exit boundary conditions. Such a complete analysis is being planned for the future.

2.3 Governing Equations. The coordinate system shown in Fig. 3 rotates with the duct. In such a system the flow is steady, but account must be taken of the Coriolis and centrifugal forces, which appear as additional source terms in the equations of motion. However, as already discussed, the fluid is assumed incompressible and buoyancy effects neglected. Hence, the centrifugal terms only modify the pressure and do not affect the flow field. As a result, as long as the pressure is interpreted as being the modified pressure, the centrifugal force terms need not be included in the governing equations. Further, as is common practice, we solve the time-averaged form of turbulent flow equations in conjunction with a suitable turbulence model [2-4]. The following equations pertain to the mean flow.

A comprehensive discussion of the periodically fully developed analyses is provided by Patankar et al. in [18], and all details are not repeated here. Basically, all flow variables repeat cyclically over the length of the computational module (the ribs spacing P). Thus:

$$\phi(x, y, z) = \phi(x + P, y, z) \quad (1)$$

where ϕ could be any velocity component (u, v, w), the turbulent kinetic energy (k), or the turbulent dissipation rate (ϵ). Further, the pressure can be decomposed as

$$p = -Bx + \bar{p} \quad (2)$$

where \bar{p} is cyclic (i.e., abides by Eq. (1)) while the term Bx is related to the net pressure loss (due to friction, form-drag, etc.) over the computational module.

In a periodic analysis, the flow rate is not known a priori.

Instead, one specifies B and iteratively adjusts it to get the desired flow rate.

Patankar et al. [18] also discuss the formulation of the thermal problem in a periodic framework. The case of uniform wall temperature is somewhat difficult because it leads to an eigenvalue problem. Therefore, taking advantage of the fact that boundary conditions have a lesser effect on turbulent heat transfer coefficients than laminar ones, we consider the simpler case of uniform heat flux at all wall surfaces (ribs as well as the walls). For such a case, the temperature field can be expressed as

$$T = Cx + \tilde{T} \quad (3)$$

where \tilde{T} is cyclic (i.e., follows Eq. (1)) while the first term is related to the net heat gain and can be obtained from an overall heat balance, i.e.,

$$C = Q/(\dot{m}c_p P) \quad (4)$$

where Q is the total heat input over the module, \dot{m} the throughflow rate, and c_p the specific heat.

With the above considerations, the governing equations are:

Continuity:

$$\text{div}(\mathbf{u}) = 0 \quad (5)$$

x-Momentum:

$$\rho \text{div}(\mathbf{u}u) = -\frac{\partial \bar{p}}{\partial x} + B - 2\rho\Omega w + \text{div}[(\mu + \mu_t)\text{grad}(u)] \quad (6)$$

y-Momentum:

$$\rho \text{div}(\mathbf{u}v) = -\frac{\partial \bar{p}}{\partial y} + \text{div}[(\mu + \mu_t)\text{grad}(v)] \quad (7)$$

z-Momentum:

$$\rho \text{div}(\mathbf{u}w) = -\frac{\partial \bar{p}}{\partial z} + 2\rho\Omega u + \text{div}[(\mu + \mu_t)\text{grad}(w)] \quad (8)$$

Energy:

$$\rho \text{div}(\mathbf{u}\tilde{T}) = -\rho u C + \text{div}\left[\left(\frac{\mu}{\text{Pr}} + \frac{\mu_t}{\text{Pr}_t}\right)\text{grad}(\tilde{T})\right] \quad (9)$$

In Eqs. (5)–(9), the symbols (div) and (grad) designate the divergence and the gradient operators. The variable μ_t represents the turbulent viscosity and Pr_t designates the turbulent Prandtl number.

To close this system of equations, expressions need to be provided for the turbulence viscosity μ_t and the turbulent Prandtl number Pr_t . The turbulent Prandtl number, Pr_t , is usually constant and is taken = 0.86 here. However, turbulent viscosity varies throughout the flow field and requires a more elaborate turbulence model. This issue will be discussed next.

2.4 Turbulence Model I: The Two-Layer Model. As already mentioned, the present study employs the standard k - ϵ model in conjunction with the wall functions [2]. This model will be discussed in the next section. A difficulty with this model, as indicated before, is that grid points should not get too close to the wall. Specifically, this model requires that the y^+ corresponding to the near-wall nodes should be greater than ~ 30 .

In our case the ribs are small, and our intention is to capture the details of the flow around the ribs. Hence, the grid around the ribs has to be of some modest size. The problem then arises that unless the Reynolds number is sufficiently high the y^+ corresponding to the near-wall nodes

become too small (i.e., < 30). Indeed, it is this issue that was discussed at length in section 1.2.

Recognizing this difficulty up front, we started this project using a two-layer model of turbulence, which is free of the above near-wall problems. Like the low-Re models [3], the two-layer models permit integration to the wall, but require a much coarser grid. We employed a two-layer model similar to the one used by Rodi's group [4].

The predictions with the two-layer model looked quite good for a two-dimensional stationary ribbed channel, i.e., for a case with no side-wall in the y direction (recall Fig. 2). Indeed, the predicted heat transfer agreed quite favorably with Han's correlation obtained from experiments on two-dimensional ($a/b \sim 12$) parallel plate channels [10].

However, when the two-layer model was applied to the three-dimensional situation, it did not yield satisfactory results. In particular, the heat transfer from the shorter side (the ribbed side) was much underpredicted. The flow field also showed some undesirable features including too long a recirculation zone behind the ribs.

We are currently exploring ways of improving the two-layer model predictions. In the interim, the two-layer model results are not included in this paper. Instead, we focus here on the predictions with the standard $k-\epsilon$ model with wall functions, and stay at the higher end of Reynolds numbers for which the near-wall y^+ problem is less severe.

2.5 Turbulence Model II: The Two-Equation $k-\epsilon$ Model.

2.5.1 Core Equations. The results presented in this paper were obtained using the $k-\epsilon$ model where the turbulence viscosity, μ_t , is obtained from the turbulent kinetic energy (k) and rate of dissipation of turbulent energy ϵ [2]. Specifically:

$$\mu_t = \rho C_\mu k^2 / \epsilon \quad (10)$$

k and ϵ are obtained from the following transport equations:

$$\text{div}(\rho \mathbf{u} k) = \text{div}[(\mu_t / \sigma_k) \text{grad}(k)] + G - \rho \epsilon \quad (11)$$

$$\text{div}(\rho \mathbf{u} \epsilon) = \text{div}[(\mu_t / \sigma_\epsilon) \text{grad}(\epsilon)] + C_1 \epsilon G / k - C_2 \rho \epsilon^2 / k \quad (12)$$

where

$$G = \mu_t \left\{ 2 \left[\left(\frac{\partial u}{\partial x} \right)^2 + \left(\frac{\partial v}{\partial y} \right)^2 + \left(\frac{\partial w}{\partial z} \right)^2 \right] + \left[\frac{\partial u}{\partial y} + \frac{\partial v}{\partial x} \right]^2 + \left[\frac{\partial u}{\partial z} + \frac{\partial w}{\partial x} \right]^2 + \left[\frac{\partial v}{\partial z} + \frac{\partial w}{\partial y} \right]^2 \right\} \quad (13)$$

The constants above have the following values:

$$\sigma_k = 1.0; \quad \sigma_\epsilon = 1.314; \quad C_\mu = 0.09$$

$$C_1 = 1.44; \quad C_2 = 1.92$$

2.5.2 Wall Functions. The $k-\epsilon$ equations provided above apply in the fully turbulent regions away from the walls where laminar effects can be neglected. To relate this outer solution to the wall, the relevant equations have to be integrated across the viscous sublayer. The wall functions, e.g., the log-law of the wall, are the outcome of such semi-empirical integrations. The purpose of these functions is to relate the wall shear and heat flux to the velocity and the temperature difference between the wall and the near-wall node [2].

We use the generalized wall function treatment of Rosten and Worrell [19], details of which are provided in the appendix. The following features of the method may be noted:

- The friction velocity ($u_\tau = V\sqrt{s}$) is replaced by a velocity scale calculated from the local turbulent kinetic energy at the near wall point. Here u_τ designates the friction coefficient and V the magnitude of the tangential velocity at the near-wall point.
- The kinetic energy at the near wall point is deduced from the regular transport equation with zero normal gradient at the wall. The generation term for the wall cells is calculated by an analytical integration based on the wall shear stress.
- The dissipation rate for the near wall cells is fixed to an average obtained from analytical integration.
- The wall heat transfer is expressed using Jayatilika's [20] Stanton number correlation.
- Most importantly: If the near-wall point lies in the viscous sublayer, laminar expressions are used for the friction coefficient and the Stanton number.*

2.6 Boundary Conditions. No inlet and exit conditions are required for a periodically fully developed analysis. At the walls, the no-slip condition is used in conjunction with the wall functions. For the temperature equation, since the heat flux is prescribed at the wall, the wall functions are used to determine the wall temperature from the computed near-wall temperature. The difference between the wall temperature so determined, and the local bulk temperature, is then used to compute the local heat transfer coefficient.

2.7 Dimensionless Parameters. The geometric parameters were kept fixed corresponding to Fig. 2. The Prandtl number was taken = 0.7 corresponding to air. The Reynolds number was varied in the range 30,000–100,000 and the Rotation number had values = 0 (stationary), 0.06, and 0.12. (see Nomenclature for the definition of the parameters).

2.8 Numerical Details. The control-volume-based finite difference method described by Patankar [20] was employed in the present study. It uses the primitive variables (u, v, w, p) as unknowns, a staggered grid, and the pressure correction algorithm. The iterative line-by-line TDMA was used to solve the discretized equations with a cyclic-TDMA employed in the x direction [18].

The grid deployed is shown in Fig. 3. There were 36 nodes in the main flow direction (x) of which 6 extend over the rib and 30 lie in the interrib space. In the direction normal to the ribbed walls (z), there is a total of 32 cells disposed symmetrically (16 each) around the midheight ($z = b/2$); of these, 6 cells extend over the rib height e , 4 cover an additional height e over the top of the rib, and 6 cover the remaining distance up to the midheight. In the direction normal to the smooth side wall (y), a total of 10 cells is used. In total, there were 11,520 nodes in this simulation.

Numerical computation of periodically fully developed flow is rendered difficult by the fact that no boundary information is available in the main flow direction along which the discretization coefficients are largest. Partly due to this reason, the code took ~ 1500 iterations of the SIMPLER algorithm [20] for convergence. On Cray-YMP, this translated to ~ 30 minutes of CPU time.

2.9 Grid Refinement. In the present problem, most of the real action is around the ribbed walls. However, due to the conflicting requirement of keeping near-wall y^+ reasonably large, the grid could not be refined excessively around the ribs. Far from the walls, i.e., in the core, the variables do not vary much and, hence, an excessively fine grid is not necessary. The grid shown in Fig. 3 is a result of all these practical considerations. Limited numerical experimentation suggested the grid used to be fairly adequate.

2.10 Smooth Channel Predictions. For a smooth channel, the periodically fully developed analysis is same as the

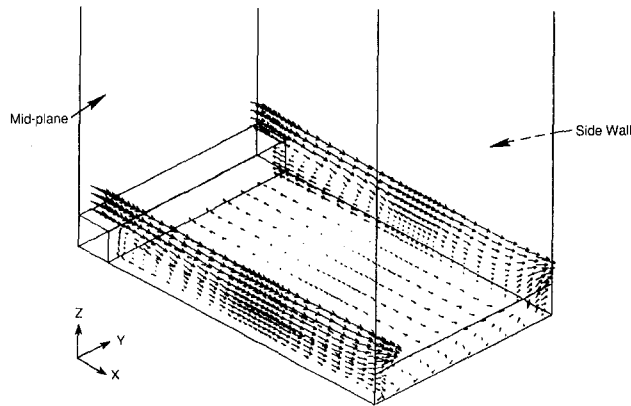


Fig. 4 Stationary ribbed channel. Flow field near the ribbed wall. $Re = 3.232 \times 10^4$.

simple fully developed flow in a duct. For each ribbed case considered, the corresponding smooth channel case was also computed for comparison.

3.0 Results I: The Stationary Case

3.1 The y^+ Issue. As already indicated, for the use of the $k-\epsilon$ model with wall functions, the near-wall nodes should be sufficiently far from the wall: specifically, $y^+ > 30$ is recommended. However, in most practical flows, this condition cannot be guaranteed at all points in the computational domain. For instance, in recirculating flows, the y^+ values become quite small around the reattachment point. Also, in three-dimensional duct flows, the velocities are quite small near the corners where, again, y^+ becomes small. The stance normally taken in these situations is that use of wall functions is probably not very harmful as long as the locations of low y^+ are not too many.

In the present problem, with small ribs, even a modest grid around the ribs leads to the potential for low y^+ at the near-wall nodes. To keep this issue in focus, the range of y^+ encountered on different surfaces is listed below:

	Variation of y^+	
	Re = 30,000	Re = 90,000
Top face of ribs	15	35
Back face of ribs	7	15
Front face of ribs	10	20
Interrib floor space	8	18
Smooth side-wall	20-50	40-120

These numbers are representative of the values over most of the listed surfaces. As already noted, lower values cannot be avoided in local regions such as the reattachment line and the corners.

The reader's attention is again drawn to the laminar limits imposed on the wall-function expressions (appendix) to take account of the possibility of low y^+ . Also it should be mentioned that $y^+ > 30$ is a general recommendation though values of y^+ of ~ 15 are considered not too objectionable.

Our experience has been that if the y^+ is pushed too low, then the effect is generally to overpredict both friction and heat transfer.

3.2 The Flow Field. Figure 4 shows the flowfield in the vicinity of the ribs. As can be noted, the flow is complex and consists of recirculation zones before and after the ribs.

3.3 Heat Transfer

3.3.1 Definition. The local heat transfer coefficient is defined as:

$$h = q(T_w - T_b) \quad (14)$$

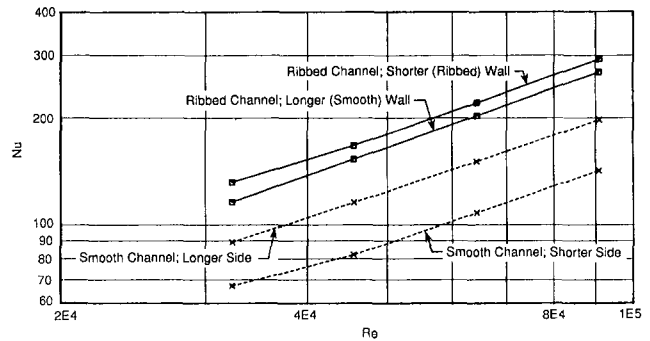


Fig. 5 Stationary channel; variation of average Nusselt number

where q is the heat flux (uniform), T_w the wall temperature (varying over the surface and computed using the wall-functions and near-wall node temperature), and T_b the bulk temperature at the same location.

The average heat transfer coefficient over a surface is defined as:

$$h = \int_{A_t} h dA / A_p \quad (15)$$

where A_t is the true heat transfer area, while A_p (not necessarily equal to A_t) is the projected base area.

All surfaces of the ribs as well as the interrib floor space are used in computing the average heat transfer over the ribbed faces, i.e., $A_t = (aP + 2ea)$. However, the projected base area A_p is taken to be just the base area, i.e., $A_p = aP$. Likewise, on the smooth side-wall, $A_t = (bP - 2e^2)$ while $A_p = bP$.

Note that due to the use of the projected base area, the heat transfer coefficient in Eq. (15) embodies within it heat transfer augmentation due to both factors, namely (i) additional heat transfer area provided by the ribs, and (ii) enhancement caused by the ribs by perturbing the flow and the turbulent fields.

3.3.2 Heat Transfer Augmentation by the Ribs. Computed heat transfer results for the stationary duct are shown in Fig. 5.

Consider the smooth channel case. Since the longer sides (side b) are closer to each other and the core, it is expected that the temperature gradients will be higher on these compared to the shorter sides (side a). Hence, the heat transfer coefficient on the longer side is expected to be higher than on the shorter side as the results of Fig. 5 indicate. It should be noted though that the predicted difference (~ 30 percent) is higher than expected. The expected difference is $\sim (2^{0.2} - 1) \sim 15$ percent, which is based on the application of the correlations $Nu_b \sim Re_b^{0.8}$ and $Nu_a \sim Re_a^{0.8}$ to the sides individually. Apparently, the $k-\epsilon$ model overpredicts heat transfer on the longer sides and underpredicts it on the shorter side (with the fortunate consequence that the average for the channel is predicted well as Fig. 6 will show). It would be appropriate to mention here that with the two-layer model of turbulence, the difference in average heat transfer coefficient for the two sides was found to be even larger.

For a ribbed channel, this situation changes. The effect of ribs is to enhance significantly (more than double) the heat transfer from the face on which they are employed (the shorter side a). The ribs also increase the heat transfer from the smooth side-walls (the longer side b) but the enhancement ($\sim 20-30$ percent) is much less than for the ribbed wall. As a result, for the ribbed channel, the shorter side (the ribbed wall) has a higher heat transfer coefficient than the longer side (the smooth side-wall).

3.3.3 Comparison. The computed results for the smooth and the ribbed channels are compared, in Figs. 6-9, with the

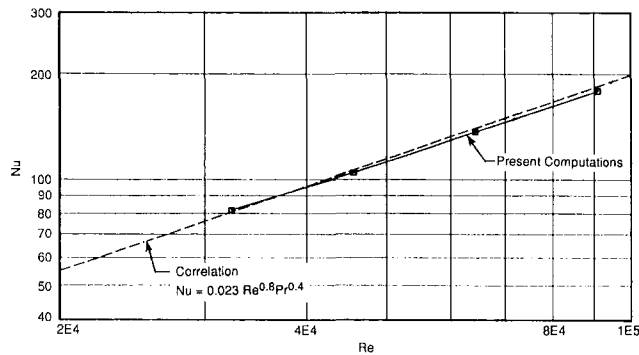


Fig. 6 Stationary, smooth channel; variation of average Nusselt number for channel (average of both sides)

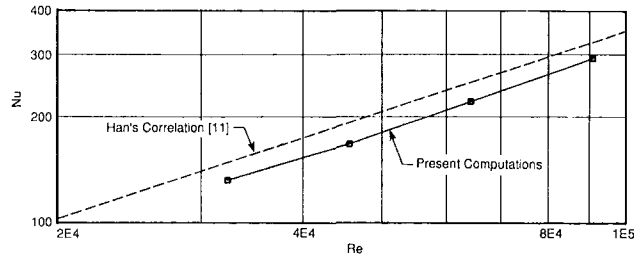


Fig. 7 Stationary ribbed channel; variation of average Nusselt number for the ribbed side

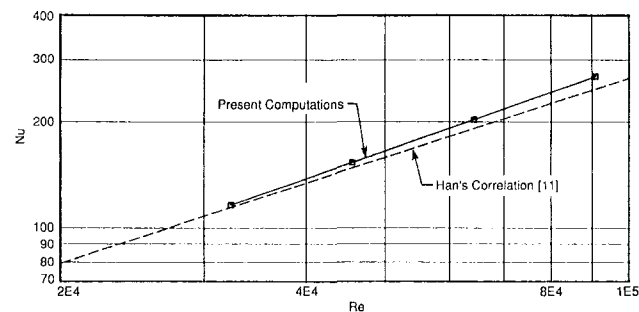


Fig. 8 Stationary ribbed channel; variation of average Nusselt number for the smooth side-wall

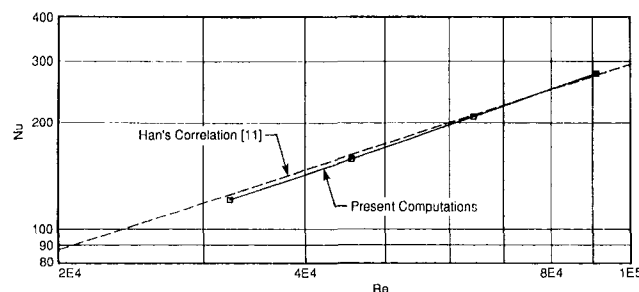


Fig. 9 Stationary ribbed channel; variation of average Nusselt number for the channel (average of ribbed and smooth sides)

correlations proposed by Han et al. [11] on the basis of extensive experimental data. As can be noted, the agreement is good.

It must be pointed out that care was taken in using Han's correlation [11] to ensure that the expressions were consistent with the use projected area in the definition of the average heat transfer coefficient (Eq. (15)).

3.4 Friction Factor. The computed friction factors are presented and compared with Han's [11] correlation in Fig. 10. The predictions correctly indicate the increase of friction

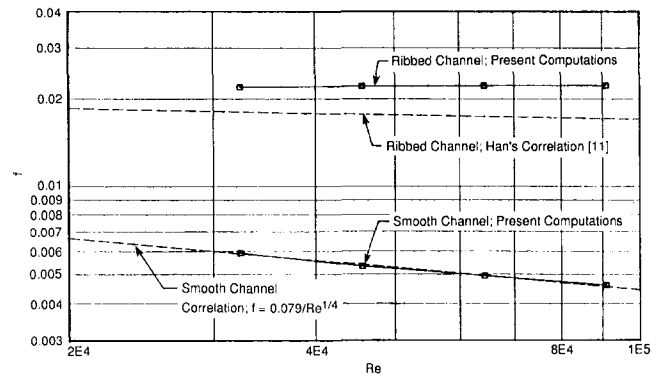


Fig. 10 Stationary channel; variation of friction factor

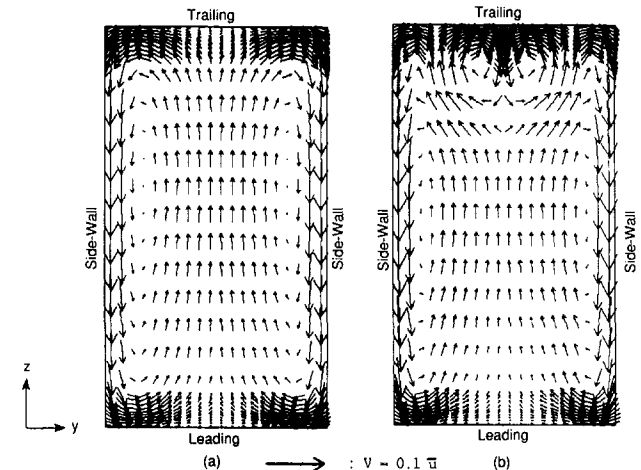


Fig. 11 Rotating smooth channel; Coriolis-induced cross-stream flow; $Re = 3.232 \times 10^4$; (A) $Ro = 0.06$, two-vortex solution; (B) $Ro = 0.12$, four-vortex solution

by the ribs. The levels of enhancement are also correctly predicted.

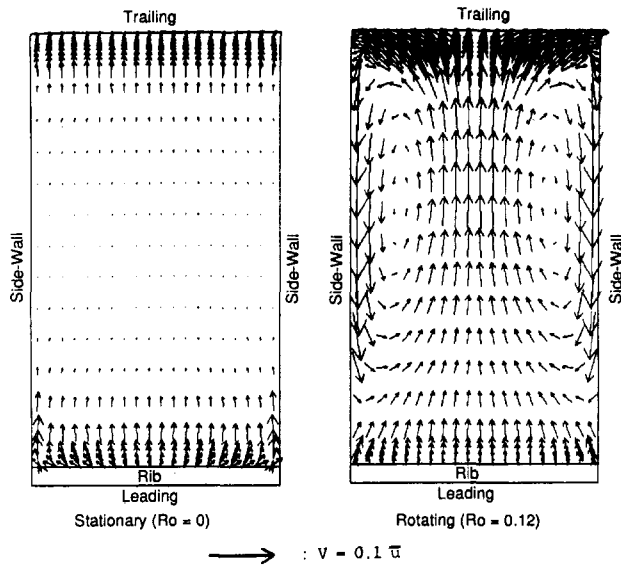
For the ribbed case, agreement with Han is only reasonable [within ~ 25 percent]. The present predictions indicate a friction factor that is nearly independent of the Reynolds number, which is typical of a rough pipe when the wall friction losses are small compared to losses due to form-drag, etc.

4.0 Results II: Effect of Rotation

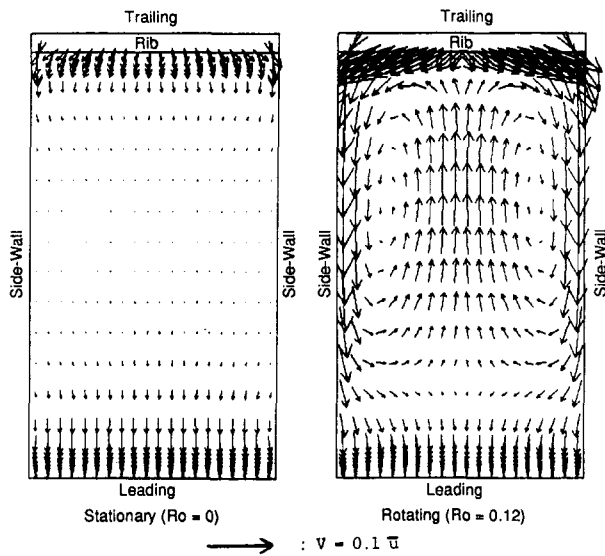
4.1 Comments. Attention will now be turned to examining the effect of rotation on flow and heat transfer. However, since the present cyclic analysis only considers Coriolis effects (i.e., buoyancy and entrance effects are not accounted for), a meaningful comparison with data is not possible and hence not made.

4.2 Flow Field. Recall Eq. (8) and note the Coriolis term ($2\rho\Omega u$) on the right-hand side. Since the throughflow velocity u is higher in the core and smaller near the walls, the consequence of this body force is to create a cross-stream flow, which is directed from the leading to the trailing wall near the core and from the trailing to the leading wall near the side-wall.

Figures 11(a) and 11(b) show the Coriolis-induced cross-stream flow for a smooth channel. At low Rotation numbers, the flow is characterized by two symmetric vortices while four-vortex solutions arise at higher rotation numbers. These two- and four-vortex solutions were discussed by Launder and Iacovides [21]. For $Ro = 0.06$, two-vortex solutions occurred at lower Reynolds numbers with a switch to four-vortex solution at higher Reynolds numbers. For $Ro = 0.12$, four-



(A)



(B)

Fig. 12 (A) Ribbed-channel; cross-stream flow over the rib on the leading wall. $Re = 3.232 \times 10^4$. (B) Ribbed-channel; cross-stream flow over rib on the trailing wall. $Re = 3.232 \times 10^4$.

vortex solutions were found for all Reynolds numbers considered.

The Coriolis induced cross-stream flow for the ribbed channel are shown in Figs. 12(a) and 12(b). The nonrotating cases are included for comparison. The vectors near the ribs also indicate the state of flow as it crosses over the ribs. For the range of parameters, no four-vortex solutions were found for a ribbed passage.

4.3 Heat Transfer. The Coriolis-induced secondary flow transports cooler, faster moving fluid from the core to the trailing face and hence heat transfer there is enhanced compared to a nonrotating case. For similar reasons, heat transfer is also enhanced at the side-wall. However, the rotating fluid gets warmer and slower by the time it gets to the leading wall with the result that heat transfer is decreased relative to a nonrotating case.

From Figs. 11 and 12, and general intuition, it is to be expected that the Coriolis effects are more pronounced in a smooth channel as compared to a ribbed channel. The reason

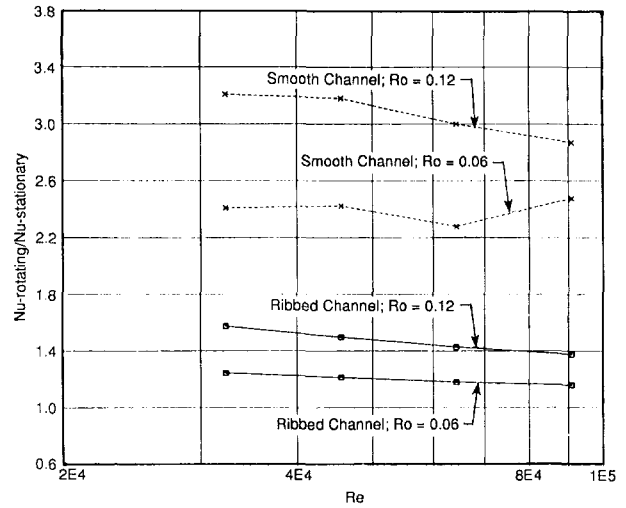


Fig. 13 Effect of rotation on average Nusselt number at trailing wall

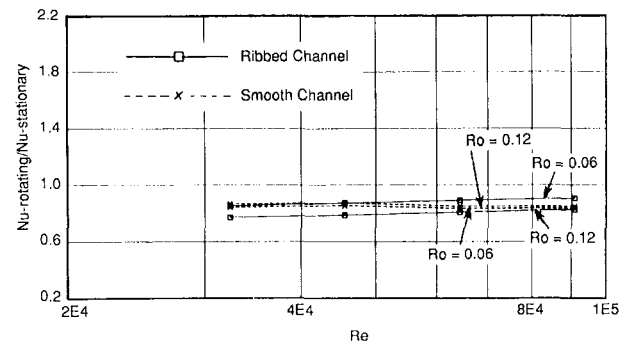


Fig. 14 Effect of rotation on average Nusselt number at the leading wall

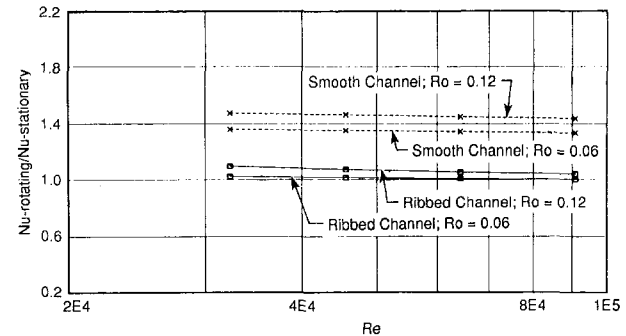


Fig. 15 Effect of rotation on average Nusselt number at the side-wall

is simply that in a ribbed channel there is much going on already in the interrib space (separation, re-attachment, etc.), which prevents Coriolis effects from reaching the walls.

These features are evidenced by Figs. 13–16 where the ratio

$$\frac{Nu_{rotating}}{Nu_{stationary}}$$

is presented on the different walls.

From Fig. 13, the heat transfer enhancement at the trailing wall can be noted. Also, as discussed above, the effect of rotation, relative to the stationary case, is less for a ribbed channel compared to a smooth channel. For a fixed rotation number, increasing the Reynolds number decreases the Nusselt number ratio (rotating/stationary) at the trailing face. The only exception to this statement is the smooth channel case for $Ro = 0.06$ where the rise occurred due to the

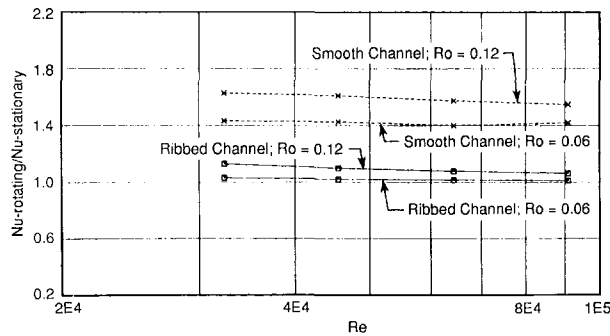


Fig. 16 Effect of rotation on average Nusselt number for channel (average of all sides)

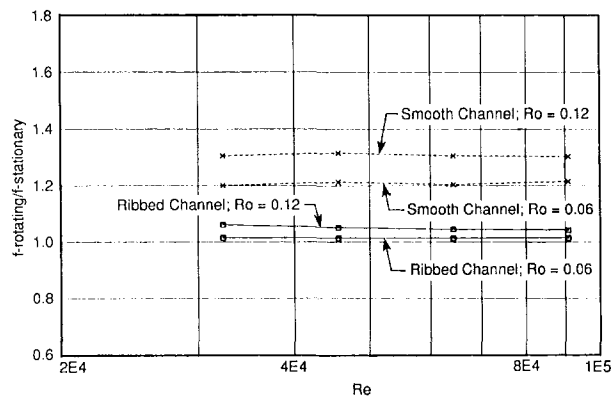


Fig. 17 Effect of rotation on the friction factor

switching of the solution from a two-vortex to four-vortex flow at higher Reynolds numbers (recall Fig. 11) with associated increase in heat transfer [21].

The effect of rotation in reducing heat transfer at the leading face may be noted from Fig. 14. Compared to the trailing face, the heat transfer ratio (rotating/stationary) for the leading face appears to be less sensitive to the parameters over the range considered, the ratio remaining largely around ~ 0.8 .

Rotation increases the heat transfer at the smooth side-wall also as is evidenced by Fig. 15. The increase, again, is more for a smooth channel as compared to a ribbed channel.

Since the heat transfer is enhanced at the trailing face and decreased at the leading face, there is a canceling effect when the average heat transfer for the entire channel is computed. This can be seen in Fig. 16 where the ratio (rotating/stationary) for the average Nusselt number is found to be closer to unity.

4.4 Friction Factor. The ratio of rotating to stationary friction factors is presented in Fig. 17.

For the smooth channel, wall friction is the primary loss mechanism and hence rotation has a noticeable effect on the friction factor.

For the ribbed channel, wall friction is less important, since form-drag, etc., make a major contribution to the pressure loss. Hence, since over the range of Rotation number considered the Coriolis flow has a rather weak influence on the separated flow around the ribs, rotation is found to have a small effect on the friction factor.

5.0 Concluding Remarks

5.1 Summary of Results. One purpose of the present paper is to highlight the turbulence modeling issues related to the numerical prediction of flow in turbine blade cooling passages. It is discussed that the problems can be categorized into four groups, namely (1) low Reynolds number/low

blockage ratio, (2) low Reynolds number/high blockage ratio, (3) high Reynolds number/low blockage ratio, and (4) high Reynolds number/high blockage ratio. Categories 1 and 2 require a low Reynolds number turbulence model while for 3 and 4 the wall-function treatment may be adequate. Likewise, an isotropic $k-\epsilon$ model may be adequate for types 1 and 3 while a Reynolds-stress turbulence model may be needed for 2 and 4 in order to account for the secondary cross-stream flows arising due to anisotropic effects. Clearly, problems of type 2 are most demanding, those of type 3 are least demanding, while types 1 and 4 are of moderate difficulty.

In terms of this classification, the present simulations correspond to category 3 (high Reynolds number/low blockage ratio . . . least demanding) and our intent here is to see how well the standard $k-\epsilon$ /wall-function model performs. The findings may be summarized as follows:

Stationary

(a) For the smooth channel, the friction factor and average heat transfer coefficient agree well with textbook correlations. However, the difference in the average heat transfer coefficient for the two sides is more than expected; i.e., the coefficient is overpredicted on the longer side and underpredicted on the shorter side (with the happy consequence that the average is close to data).

(b) For the ribbed channel, the heat transfer is underpredicted by ~ 20 percent on the ribbed wall and overpredicted by ~ 10 percent on the smooth side-wall. The friction factor is overpredicted by ~ 25 percent.

Rotating

(a) The Coriolis-induced secondary flows and their effect on heat transfer at the different walls (enhancement at the trailing and side walls, and decrease at the leading wall) is correctly predicted. It is also shown that the effect of rotation on the heat transfer is less for a ribbed channel compared to a smooth channel [16, 17].

(b) Unfortunately, since the present cyclic analysis does not include entrance and buoyancy effects, a meaningful comparison with the data has not been possible. For such a comparison, the entire channel (including several ribs) must be simulated, and such a study is currently in progress.

5.2 What's Next?

(a) The present analysis needs to be performed over a wide range of duct aspect ratios and rib heights to determine the range of blockage ratios over which the isotropic $k-\epsilon$ model with wall-functions may be adequate.

(b) The exercise should be extended for a full channel analysis including several ribs so that the effect of buoyancy can be studied.

(c) As discussed, a computationally affordable low Reynolds number model is deemed to be necessary, and efforts toward development of such models need no defending.

(d) Finally, to capture anisotropic effects, a Reynolds stress model is required.

We are currently involved in working on all of the aspects listed above.

Acknowledgments

The authors wish to express their appreciation to Dr. Mikio Suo for his guidance and support to our CFD methods development activities in gas turbine heat transfer at GE Aircraft Engines. We also wish to thank Mr. John Starkweather for his critical review and analysis of our work from the perspective of a turbine cooling designer.

References

- 1 Prakash, C., and Zerkle, R., "Prediction of Turbulent Flow and

Heat Transfer in a Radially Rotating Square Duct," ASME JOURNAL OF TURBOMACHINERY, Vol. 114, 1992, pp. 835-846.

2 Launder, B. E., and Spalding, D. B., "The Numerical Computation of Turbulent Flows," *Computer Methods in Applied Mechanics and Engineering*, Vol. 3, 1974, pp. 269-289.

3 Patel, V. C., Rodi, W., and Scheuerer, G., "Turbulence Models for Near-Wall and Low-Reynolds Number Flows: A Review," *AIAA Journal*, Vol. 23, No. 9, 1985, pp. 1308-1319.

4 Rodi, W., "Experience With Two-Layer Models Combining the $k-\epsilon$ Model With a One-Equation Model Near the Wall," Paper No. AIAA-91-0216, 1991.

5 Webb, R. L., Eckert, E. R. G., and Goldstein, R. J., "Heat Transfer and Friction in Tubes With Repeated-Rib Roughness," *Int. J. Heat Mass Transfer*, Vol. 14, 1971, pp. 601-617.

6 Chang, B. H., and Mills, A. F., "Application of a Low-Reynolds Number Turbulence Model to Flow in a Tube With Repeated Rectangular Rib Roughness," *PHOENICS Journal*, Vol. 4, No. 3, 1991, pp. 262-288.

7 Arman, B., and Rabas, T., "The Influence of the Prandtl Number on the Thermal Performance of Tubes With the Separation and Reattachment Mechanism," *Enhanced Heat Transfer*, ASME HTD-Vol. 202, 1992, pp. 77-88.

8 Cunha, F. J., "Turbulent Flow and Heat Transfer in Gas Turbine Blade Cooling Passages," ASME 92-GT-239, 1992.

9 Burgraff, F., "Experimental Heat Transfer and Pressure Drop With Two Dimensional Turbulence Promoters Applied to Two Opposite Walls of a Square Tube," *Augmentation of Convective Heat and Mass Transfer*, E. E. Bergles and R. L. Webb, eds., ASME, New York, 1970, pp. 70-79.

10 Han, J. C., Glicksman, L. R., and Rohsenow, W. M., "An Investigation of Heat Transfer and Friction for Rib-Roughened Surfaces," *Int. J. Heat Mass Transfer*, Vol. 21, 1978, pp. 1143-1156.

11 Han, J. C., "Heat Transfer and Friction Characteristics in Rectangular Channels With Rib Turbulators," *ASME Journal of Heat Transfer*, Vol. 110, 1988, pp. 321-328.

12 Han, J. C., and Park, J. S., and Lei, C. K., "Augmented Heat Transfer in Rectangular Channels of Narrow Aspect Ratios With Rib Turbulators," *Int. J. Heat Mass Transfer*, Vol. 32, No. 9, 1989, pp. 1619-1630.

13 Taslim, M. E., and Spring, S. D., "Experimental Heat Transfer and Friction Factors in Turbulated Cooling Passages of Different Aspect Ratios Where Turbulators Are Staggered," Paper No. AIAA-88-3014, 1988.

14 Wagner, J. H., Kim, J. C., and Johnson, B. V., "Rotating Heat Transfer Experiments With Turbine Airfoil Internal Flow Passages," ASME 86-GT-133, 1986.

15 Johnson, B. V., Wagner, J. H., Steuber, G. D., and Yeh, F. C., "Heat Transfer in Rotating Serpentine Passages With Trips Skewed to the Flow," ASME JOURNAL OF TURBOMACHINERY, Vol. 116, 1994, pp. 113-123.

16 Taslim, M. E., Bondi, L. A., and Kercher, D. M., "An Experimental Investigation of Heat Transfer in an Orthogonally Rotating Channel Roughened With 45 deg Criss-Cross Ribs on Two Opposite Walls," ASME JOURNAL OF TURBOMACHINERY, Vol. 113, 1991, pp. 345-353.

17 Taslim, M. E., Rahman, A., and Spring, S. D., "An Experimental Investigation of Heat Transfer Coefficients in a Spanwise Rotating Channel With Two Opposite Rib-Roughened Walls," ASME JOURNAL OF TURBOMACHINERY, Vol. 113, 1991, pp. 75-82.

18 Patankar, S. V., Liu, C. H., and Sparrow, E. M., "Fully Developed Flow and Heat Transfer in Ducts Having Streamwise-Periodic Variations of Cross-Sectional Area," *ASME Journal of Heat Transfer*, Vol. 99, 1977, pp. 180-186.

19 Rosten, H. I., and Worrell, J. K., "Generalized Wall Functions for Turbulent Flow," *PHOENICS Journal*, Vol. 1, 1988, pp. 81-109.

20 Jayatilika, C. L. V., "The Influence of the Prandtl Number and Surface Roughness on the Resistance of the Sub-layer to Momentum and Heat Transfer," *Prog. in Heat and Mass Transfer*, Vol. 1, 1969, pp. 193-329.

21 Iacovides, H., and Launder, B. E., "Parametric and Numerical Study of Fully Developed Flow and Heat Transfer in Rotating Rectangular Ducts," ASME JOURNAL OF TURBOMACHINERY, Vol. 113, 1991, pp. 331-338.

APPENDIX

Generalized Wall Functions [19]

Consider Fig. A-1, which shows a near-wall grid point P located at a distance δ from the wall. Let V_p and k_p represent the tangential velocity and the turbulent kinetic energy at the point P . The shear stress at the wall is obtained as:

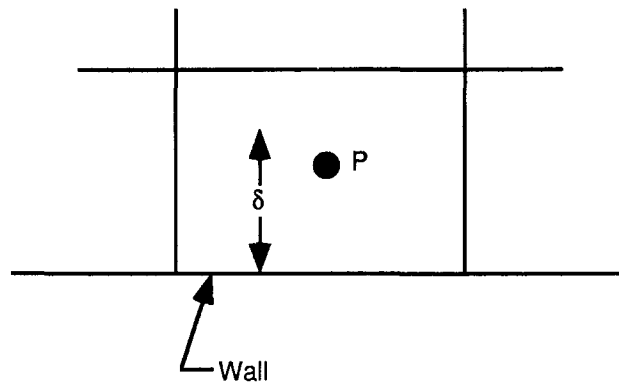


Fig. A-1 Near wall grid point

$$\frac{\tau_w}{\rho} = s V_p^2 \quad (A1)$$

where s is the friction coefficient given by

$$s = \text{greater of} \left[\frac{\kappa C_\mu^{1/4} k_p^{1/2}}{V_p \ln(E \delta C_\mu^{1/4} k_p^{1/2} / \nu)} ; \frac{\nu}{V_p \delta} \right] \quad (A2)$$

turbulent (s_{tur}) laminar limit (s_{lam})

In the above,

$$\kappa = \text{von Karman constant} = 0.435$$

and

$$E = \text{wall roughness parameter} = 9 \text{ (smooth wall)}$$

The turbulent kinetic energy, k_p , is obtained via the differential equation for k with the zero-gradient condition imposed at the wall.

The generation rate of k at the point p is computed as:

$$G_p = \rho (s V_p^2) V_p \quad (A3)$$

The dissipation rate at the point P is fixed as:

$$G_p = \frac{C_\mu^{3/4} k_p^{3/2} \ln(E \delta C_\mu^{1/4} k_p^{1/2} / \nu)}{\kappa} \quad (A4)$$

The heat flow at the wall is given by

$$q_w = (St \rho V_p) c_p (T_w - T_p) \quad (A5)$$

where T_w and T_p designate the temperature at the wall and the point P respectively, and St is the Stanton number given by

$$St = \text{greater of} \left[\frac{s_{tur}}{\left[\text{Pr}_t \left(1 + \frac{s_{tur} P V_p}{C_\mu^{1/4} \sqrt{k_p}} \right) \right]} ; \frac{\nu}{V_p \delta (\text{Pr})} \right] \quad (A6)$$

turbulent laminar limit

In the above, the P -function is given by

$$P = 9 \left(\frac{\text{Pr}}{\text{Pr}_t} - 1 \right) \left(\frac{\text{Pr}_t}{\text{Pr}} \right)^{1/4} \quad (A7)$$

Effect of Permeable Ribs on Heat Transfer and Friction in a Rectangular Channel

Jenn-Jiang Hwang

Associate Professor,
Department of Mechanical Engineering,
Chung-Hua Polytechnic Institute,
Hsinchu, Taiwan

Tong-Miin Liou

Professor,
Department of Power
Mechanical Engineering,
National Tsing Hua University,
Hsinchu, Taiwan

Heat transfer and friction characteristics in a rectangular channel with perforated ribs arranged in-line on two opposite walls are investigated experimentally. Five perforated rib open-area ratios (0, 10, 22, 38, and 44 percent) and three rib pitch-to-height ratios (10, 15, and 20) are examined. The Reynolds number ranges from 5000 to 50,000. The rib height-to-channel hydraulic diameter ratio and the channel aspect ratio are 0.081 and 4, respectively. Laser holographic interferometry is employed not only to measure the heat transfer coefficients of the ribbed wall but also to determine the rib apparent permeability. It is found that ribs with appropriately high open-area ratio and high Reynolds number are permeable, and the critical Reynolds number for evidence of flow permeability decreases with increasing rib open-area ratio. Results of local heat transfer coefficients further show that the permeable ribs have an advantage of obviating hot spots. Moreover, the duct with permeable ribs gives a higher thermal performance than that with solid ribs.

Introduction

To increase specific thrust and to reduce specific fuel consumption (SFC), high turbine entry gas temperature (1400–1600°C) has become the trend in advanced aero-engine design. Such a high gas temperature is far above the allowable metal temperature; therefore, turbine blades must be cooled in order to operate in the high gas temperature environment. Turbulence promoters inside cooling passages enhance the overall heat transfer to the cooling air. Researchers have modeled these ribbed cooling passages as straight rectangular channels with two opposite ribbed walls and two smooth walls. Earlier evident works include: Burggraf (1970) reported the results of turbulent airflow in a square duct ($AR = 1$) with transverse solid-type ribs ($\alpha = 90$ deg, $\beta = 0$) on two opposite walls for the Reynolds number range from 1.3×10^4 to 1.3×10^5 . The wall temperature distributions were measured by thermocouples. With a hydrodynamically fully developed condition at the heated duct entrance, the average Nusselt number of the ribbed side wall and the friction factor were approximately 2.38 times and 8.6 times the corresponding values for fully developed smooth duct flows. The average Nusselt number of the smooth side wall was 19 percent over that of the duct with four smooth walls. Similar trends were obtained for three channel entrance geometries (long duct, short duct, and bent entrance). Tanasawa et al. (1983) employed the resistance heating method and thermocouple technique to determine the heat transfer

coefficients in a channel with turbulence promoters. Three types of turbulence promoter, namely, fence-type, perforated plate-type, and slitted plate-type, were tested in their work. Results showed that the surfaces with perforated plate-type turbulence promoters gave an excellent performance under constant pumping power conditions. Note that the thin plates were insulated; therefore the additional surfaces caused by the existence of plates have no contribution to the heat transfer enhancement. Han (1984) conducted experimental works to examine the effects of the rib pitch-to-height ratio ($Pi/H = 10, 20, \text{ and } 40$) and the rib height-to-hydraulic diameter ratio ($H/De = 0.021, 0.042, \text{ and } 0.063$) on the heat transfer coefficient and friction of the fully developed airflow in a square duct with two opposite ribbed walls. The temperature distributions were measured by thermocouple. The results showed that the Stanton number and friction factor of the ribbed duct were about 1.5 to 2.2 times and 2.1 to 6 times, respectively, those of the smooth duct for the range of the test data. Later, Han (1988) investigated the effect of the channel aspect ratios ($AR = 1/4, 1/2, 1, 2, 4$) on the distributions of local heat transfer coefficients in channels with two opposite ribbed walls. Both the local and average Nusselt numbers were measured by the thermocouple technique and resistance (stainless steel foil) heating method. The results were obtained for the solid-type rib with angle of attack 90 deg. It was found that the increased ribbed-side-wall heat transfer in a smaller aspect ratio channel was higher than that in a large aspect ratio channel for a constant pumping power; however, the increased average heat transfer was slightly lower. Lockett and Collins (1990) conducted the double-exposure holographic interferometry measurement in a fully developed channel flow with square and rounded rib

Contributed by the International Gas Turbine Institute and presented at the 38th International Gas Turbine and Aeroengine Congress and Exposition, Cincinnati, Ohio, May 24–27, 1993. Manuscript received at ASME Headquarters March 10, 1993. Paper No. 93-GT-301. Associate Technical Editor: H. Lukas.

roughness on one wall. The ribs were solid. One rib pitch-to-height ratio ($Pi/H = 7.2$) and one rib-to-channel height ratio ($H/B = 0.106$) were investigated in their work. It was found that the heat transfer distribution was Reynolds number dependent for the rounded rib, but independent for the square rib. Lau et al. (1991) conducted experiments to study the effects of replacing the aligned 90 deg full ribs on two opposite walls of a square channel with angled discrete ribs (five equal segments of the angled full ribs staggered in alternate rows of three and two ribs) on turbulent heat transfer and friction for fully developed airflow. The temperature distributions were measured by thermocouple. Results showed that parallel 60 deg discrete ribs had the highest ribbed wall heat transfer, parallel 30 deg discrete ribs caused the lowest pressure drop, and crossed arrays of angled ribs had poor thermal performance and were not recommended. Liou and Hwang (1993) experimentally studied the effect of the rib shapes on the heat transfer and friction characteristics in periodic fully developed duct flows. Three rib shapes (square, triangular, and semicircular) with the same rib height ($H/De = 0.081$) were investigated in their work. The local as well as the average Nusselt numbers were determined by a real-time laser holographic interferometry (LHI). It was found that the three shaped ribs had comparable thermal performances under the constant pumping power constraint.

As indicated in the discussion above, the relevant geometric parameters involved in the investigations are passage aspect ratio, AR ; rib angle of attack, α ; rib pitch-to-height ratio, Pi/H ; blockage ratio, H/De ; rib shapes; and the manner by which ribs are positioned with respect to each other. However, a serious problem still remains and must be overcome: Previous measurements (Lockett and Collins, 1990; Liou and Hwang, 1992a, 1992b, 1993) and calculations (Liou et al., 1992, 1993) of detailed local Nusselt number distributions show that the hot spots ($Nu/\overline{Nu}_s < 1$) exist in the recirculating region behind the solid-type rib because the flow is nearly stagnant relative to the mainstream in this region. The hot spots will degrade blade materials. It is important to search for an efficacious rib configuration for improving heat transfer in the recirculating region. To fulfill

this motivation, the effect of replacing the solid-type ribs by the perforated ribs on the local heat transfer characteristics will be examined in this paper. The main objective of this paper is to study the effect of replacing the solid-type rib by perforated ribs on the local heat transfer characteristics. First, flow visualization is conducted to determine the permeability of the perforated ribs. A criterion of the rib permeability is proposed as a function of the rib open-area ratio and the Reynolds number. Then, laser holographic interferometry is employed to measure the local heat transfer coefficient distribution of the ribbed wall. Since the airflow partly passes through the permeable rib and directly impinges on the recirculating cell behind the rib, it is of interest whether the channel with permeable ribs can improve the heat transfer rate in this region. Finally, the thermal performances of the perforated ribbed ducts are quantified with respect to a corresponding smooth duct. It is questionable whether the perforated ribs can provide a better thermal performance than the solid-type ribs. The parameters investigated in this work are the rib open-area ratio, $\beta = 0, 10, 22, 38,$ and 44 percent; the rib pitch-to-height ratio, $Pi/H = 10, 15,$ and 20 ; and the Reynolds number, $5000 < Re < 50,000$. The rib height-to-channel hydraulic diameter ratio and the channel aspect ratio are fixed at values of 0.081 and 4 , respectively. The ribs are square with sharp-edged corners.

Experimental Apparatus

Instrumentation. In this work, the temperature distribution of airflow in the ribbed duct is measured by a real-time holographic interferometry (single exposure method, Liou and Hwang, 1992a). The overall arrangement of the holographic interferometer is illustrated in detail in Fig. 1. The coherent source used is a high-power, argon-ion laser, Spectra-Physic Model 2000. The photographic emulsion 8E56 made by Agfa-Gevaert Ltd. is found to be a suitable recording material for combining a good compromise between light sensitivity and resolution. The instantaneous interference field is digitized by a CCD camera (COHU, Model 6400) which allows 512×512 pixel resolution with 256 grey levels

Nomenclature

A = width of channel	the smooth duct (at the same pumping power)	U = average channel velocity without ribs
AR = channel aspect ratio = A/B	Pi = rib pitch	W = rib width
B = height of channel	Pr = Prandtl number	X_h = axial coordinate ($X_h = 0$ at inlet reference, Fig. 2)
c_p = specific heat at constant pressure	ΔP = pressure drop across the fully developed test section	X_N = axial coordinate ($X_N = 0$ at rib rear edge, Fig. 2)
De = hydraulic diameter = $2B/(1 + B/A)$	q_{conv} = convective heat flux from the wall	Y = transverse coordinate, Fig. 2
f = friction factor, Eq. (5)	Re = Reynolds number = $U \cdot De/\nu$	Z = spanwise coordinate, Fig. 2
H = rib height	Re_δ = Reynolds number based on the boundary layer thickness = $U \cdot \delta/\nu$	α = rib angle of attack
k_f = film temperature (T_f) air thermal conductivity	T = air temperature	β = open-area ratio of the perforated rib, Eq. (1)
L_h = wetted length in one pitch	T_b = local bulk mean air temperature	δ = boundary layer thickness air density
ΔL = channel length for fully developed pressure drop	\overline{T}_b = average bulk mean air temperature = $(\int_0^{L_h} T_b dX)/L_h$	ρ = air density
m = mass flow rate	T_f = film temperature = $(T_w + T_b)/2$	ϕ = radius of the hole distributed over the perforated rib
n = number of holes in a rib	T_{in} = air temperature at duct inlet (i.e., room temperature)	
Nu = local Nusselt number	T_w = local wall temperature	
\overline{Nu}_p = periodic fully developed (average) Nusselt number for the ribbed duct	\overline{T}_w = average wall temperature	
\overline{Nu}_s = average Nusselt number for the smooth duct (at the same mass flow rate)	dT/dY = air temperature gradient	
\overline{Nu}_s^* = average Nusselt number for		

Subscripts

b = bulk mean
N = rib index
n = number of the holes drilled through the perforated ribs
s = smooth
w = wall

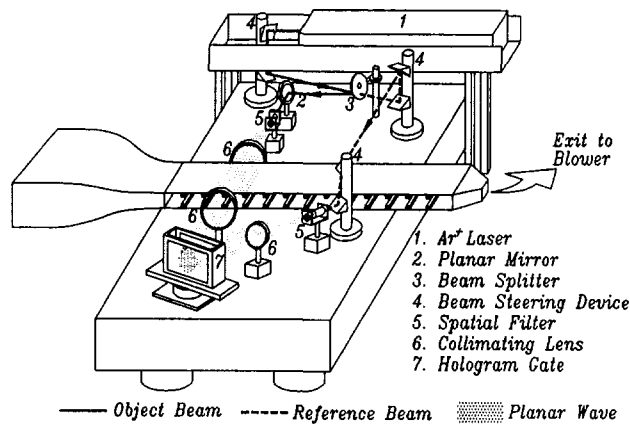


Fig. 1 Schematic drawing of flow system and experimental apparatus

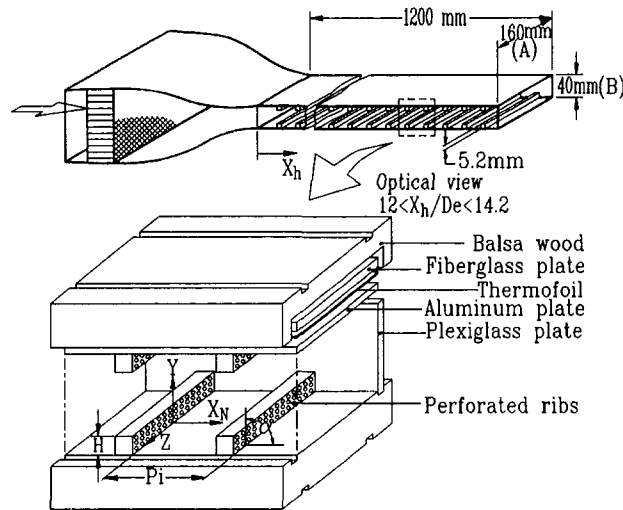


Fig. 2 Sketch of configuration, coordinates, and dimensions of the test section

per pixel and recorded on a VHS videocassette recorder for storage and further image processing.

While the flow field temperature is measured by LHI, the wall temperature of the test section is measured by thermocouples. Copper-constantan thermocouples (i.e., T-type) are used to measure the local wall temperature of the ribbed duct. The junction-bead of the thermocouple is about 0.15 mm in diameter. The temperature signals are transferred to a hybrid recorder (Yokogawa, DA-2500) with 30 channels. All of the data are then sent to a PC-AT via GPIB interface. The preprocessing of the raw data can be carried out by using a built-in BASIC program by which the nondimensional parameter can be calculated.

Test Model. Figure 2 shows the coordinate system, configuration, and dimension of the test duct. The test duct is 1200 mm long and has a rectangular cross section of 160 mm by 40 mm (YZ plane). As shown in Fig. 2, the perforated ribs are attached symmetrically to the top and bottom walls (aluminum plates, 3 mm in thickness) of the test ducts. The rib angle of attack is 90 deg. Aluminum plates and ribs are adopted in this work for their high conductivity and machinability. Thermofoils of thickness 0.18 mm are adhered uniformly between the aluminum plate and a 6-mm-thick fiberglass board to insure good contact. In addition, two pieces of balsa wood (20 mm in thickness) are used to prevent the heat loss from the upper and lower sides of the heated plates. The thermal resistance of the glue (0.13 mm thick or less) used at

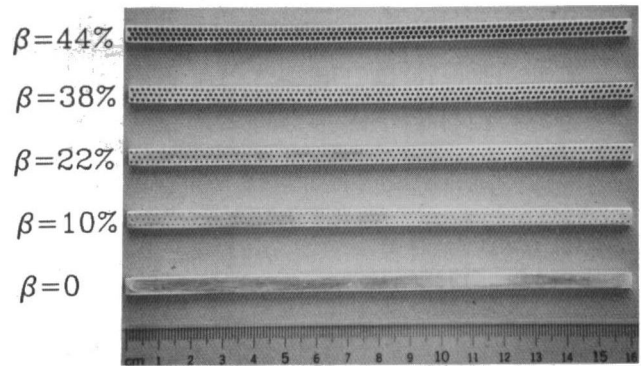


Fig. 3 Photographs of the investigated perforated ribs

each of the abovementioned interfaces is negligible (less than 2 percent). The region of optical view is instrumented with 28 thermocouples distributed along the spanwise centerline ($Z = 0$) of the heated plate and ribs for wall temperature measurements, as shown in Fig. 2. Two pressure taps are used to measure the static pressure for the fully developed duct flows.

Figure 3 shows a photograph of the perforated ribs investigated in this work. The rib open-area ratio (β) is defined as

$$\beta = (n \cdot \pi \cdot \phi^2) / (A \cdot H) \quad (1)$$

where n is the number of holes drilled through on the perforated rib, ϕ , the radius of the hole, A , the width of the channel (i.e., the length of the perforated rib), and H , the rib height. In this work, the rib open-area ratios investigated are 0, 10, 22, 38, and 44 percent; the rib pitch-to-height ratios are 10, 15, and 20; the Reynolds number, based on the duct hydraulic diameter and bulk mean velocity, extends from 5.0×10^3 to 5.0×10^4 ; and the rib-to-channel height ratio (or the ratio of the rib height-to-channel hydraulic diameter) is 0.13 (0.081).

Experimental Conditions and Data Analysis

The two dimensionality of the actual temperature field, the thermal boundary conditions of the test section, and analysis of the interference fringe have been described in detail by Liou and Hwang (1992a), and are not elaborated on in this paper.

Heat Transfer Coefficient. In this study the entire temperature field is revealed by the infinite-fringe interferometry and subsequently enables the calculations of local and average heat transfer coefficients of the heated surface. The convection heat transfer coefficient can be presented in terms of the local Nusselt number Nu , which is defined as

$$Nu = -(dT/dY)_w \cdot De / (T_w - T_b) \quad (2)$$

where the air temperature gradient $(dT/dY)_w$ is determined by curve fitting, based on a least-squares method through the near wall values for temperature and fringe shift; T_w is read from the thermocouple output; and T_b is calculated from an energy balance, $T_b = T_{in} + Q / (m \cdot c_p)$, where Q is the quantity of heat given to air from entrance to the considered cross section of the duct and can be obtained by the integrated form of $\int_0^A [k_f \cdot (dT/dY)_w \cdot A] \cdot dX$. The maximum uncertainty of local Nusselt number is estimated to be less than 6.5 percent by the uncertainty estimation method of Kline and McClintock (1953). The average Nusselt number is evaluated by the following equation:

$$\overline{Nu}_p = q_{conv} \cdot De / [k_f \cdot (\overline{T}_w - \overline{T}_b)] \quad (3)$$

where q_{conv} is the convective heat flux from the ribbed wall and is estimated by subtracting the heat loss from the sup-

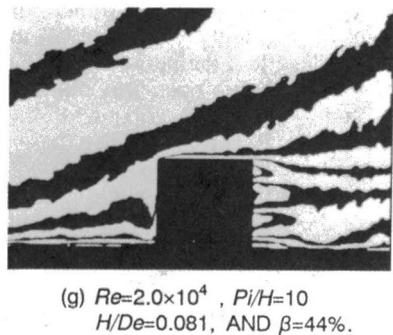
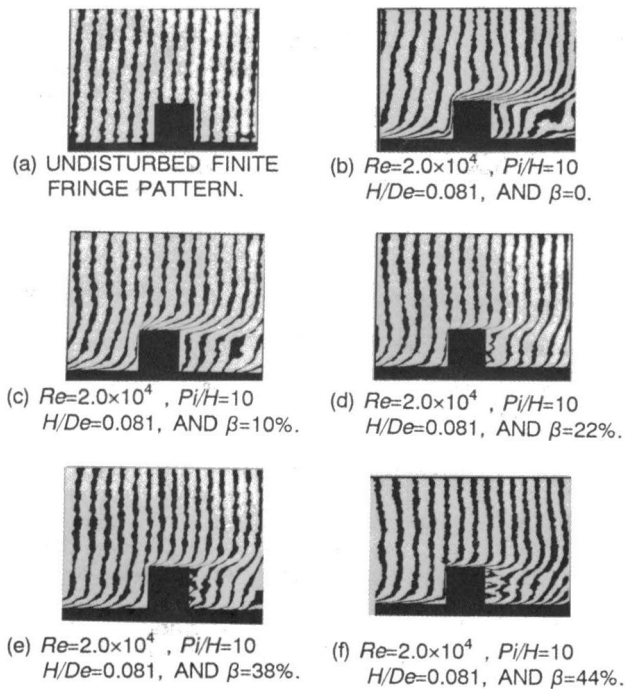


Fig. 4 Examples of the holographic interferograms for the ribbed-duct flows

plied electrical input (Liou and Hwang, 1992a). The maximum uncertainty of \overline{Nu}_p was estimated to be less than 9.8 percent. The local and average Nusselt numbers of the present study are normalized by the Nusselt number for fully developed turbulent flow in smooth circular tubes correlated by Dittus-Boelter as

$$Nu/\overline{Nu}_s = Nu/(0.023 \cdot Re^{0.8} \cdot Pr^{0.4}) \quad (4)$$

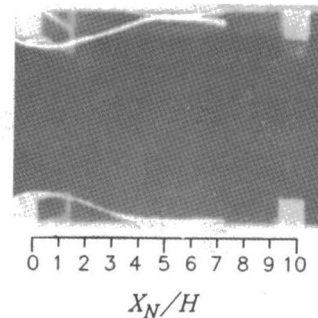
Friction Factor. The friction factor of the periodic fully developed flow is expressed as:

$$f = [(-\Delta P/\Delta L) \cdot De/4]/(\rho \cdot U^2/2) \quad (5)$$

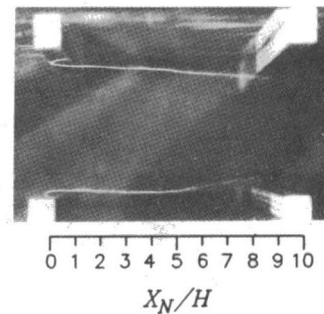
where the pressure gradient, $\Delta P/\Delta L$, is evaluated by taking the ratio of the pressure difference and the distance of two successive pressure taps. The maximum uncertainty of f is estimated to be less than 7.3 percent.

Results and Discussion

Interference Patterns. Typical examples of the interferograms taken from the temperature fields of the perforated-rib and the solid-type-rib geometries are shown in Figs. 4(a)–(g). Figures 4(a)–(f) show the finite-fringe (also called wedge-fringe) interferograms. If there are no disturbances in the field, parallel, equally spaced, and alternately dark and bright



(a) $\beta=0$, $Pi/H=10$, AND $H/De=0.081$ (LIU AND HWANG, 1992a)



(b) $\beta=44\%$, $Pi/H=10$, AND $H/De=0.081$

Fig. 5 Flow visualization using a light thread

fringes will appear on the interferogram, as shown in Fig. 4(a). When a disturbance is present with the test section, the optical path is no longer uniform. The fringes then are no longer straight, but curved. The disturbed finite-fringe interferograms for the different rib open-area-ratios are shown in Figs. 4(b)–(f) at $Re = 20,000$. For the solid-type rib ($\beta = 0$) in Fig. 4(b), there is no fluid passing through the rib, and the total fluid has to turn from the duct wall into the contraction between the two opposite ribs. It can be observed that the fringes are highly distorted in the regions of the flow over and behind the rib top. This indicates that the flow introduces a strong shear layer from the rib top, which drives the recirculating flow behind the rib (Fig. 5(a)). At the lowest rib open-area ratio, $\beta = 10$ percent (Fig. 4(c)), the distorted fringes seem to have no difference from those of the solid-type rib, and the fluid still passes through the rib contraction only. Basically, it is impermeable. As the rib open-area ratio is larger than 22 percent (Figs. 4(d)–(f)), the saw-shaped fringes found behind the rib reveal that a part of fluid passes through the rib and the separation bubble behind the rib is thus broken up. This can be supported by a comparison of the flow visualization between Fig. 5(a) and Fig. 5(b), which shows that the separation bubble behind the solid-type rib disappears for the perforated rib geometry. Moreover, the distorted region on the top of the perforated rib becomes thinner than that on the solid-type rib. This indicates that the high convective heat transfer from the rib-top surface is accompanied with the solid-type rib. The reason is that for the perforated rib a large amount of heat has been convected by the fluid that passes through the rib, which is conducted from the rib base, hence a reduction of the heat transfer rate on the rib top. This is reflected by the lower local Nusselt number distribution, and will be shown later. Figure 4(g) is a typical isotherm-pattern interferogram (infinite fringe set) for the perforated rib geometry. From the information of the whole-field air temperature distributions given by the interferograms (infinite fringe set), the local heat transfer coefficient of the perforated-ribbed walls can be calculated.

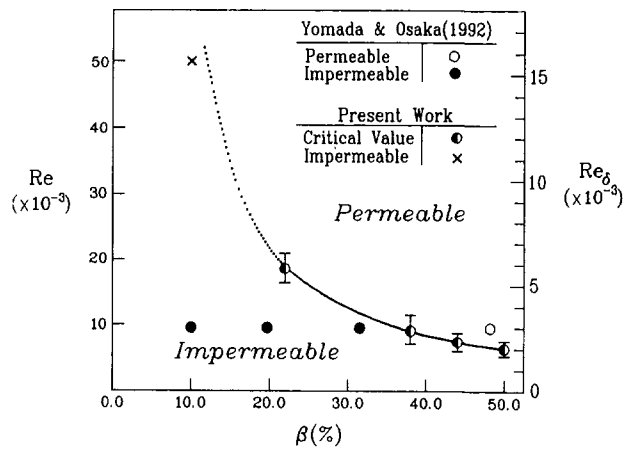


Fig. 6 Dependence of permeability limit as a function of Reynolds number and rib open-area ratio

Permeability Limit. In accordance with the flow visualization results given above, the permeability limit of the perforated rib is plotted as a function of the Reynolds number and the rib open-area ratio, as shown in Fig. 6. The half-solid symbols are the actual values obtained from the experiment, and the error bounds are caused by the unsteady or intermittent appearance of the separation bubble (or saw-shaped fringes). The solid curve passing through these symbols is a curve-fitting result. The permeability limit is a criterion of the change of the flow patterns. When the ribs are permeable (above the solid curve), the flow pattern of the multi-mixing-layers appears behind the rib, which is caused by the multi-jets emitting from the rear face of the rib. For data lying below the solid curve, the ribs are impermeable, and typical flow patterns of separation, reattachment, and recirculation are found. It can be seen from this figure that the impermeable zone is found to be in the region where the values of flow Reynolds number and the rib open area ratio are lower. The critical Reynolds number of initiation of flow permeability decreases with increasing the value of the rib open-area ratio. Note that for the range of the Reynolds number investigated, the ribs with $\beta = 10$ percent are impermeable. A critical value of β exists between 10 and 22 percent, which makes the rib permeable for the range of Reynolds number investigated. The solid and open circular points in Fig. 6 are the results obtained by using smoke-wire flow visualization (Yomada and Osaka, 1992). In their work, the authors used a single perforated rectangular plate to stand against a flat wall where turbulent boundary layer is developing. The Reynolds number based on the boundary layer thickness is 3150. It was concluded that the critical value of β is between 32.5 and 48.5 percent, and below which there is a recirculation cell behind the plate. As seen in Fig. 6, the results obtained in the previous work are very satisfactory for the solid-curve obtained in this work. Note that the boundary thickness in this work is half of the channel height because the investigated rib pairs are located at the fully developed region of the channel (Liou and Hwang, 1992b).

Local Nusselt Number. Figure 7 shows the distributions of the local Nusselt number ratio for various β (10, 22, 38, and 44 percent) and at a fixed Re (20,000). The dotted line shows the results of the solid-type ribbed wall. Similar to the solid-type rib results, the Nu/\bar{Nu}_s distributions for the perforated rib investigated show the presence of the local maximum of Nu/\bar{Nu}_s on the upstream tip of the rib due to forced convection augmented by flow acceleration. However, the value is lower than that of the solid-type rib and decreases with an increase of β . This is reasonable because for the

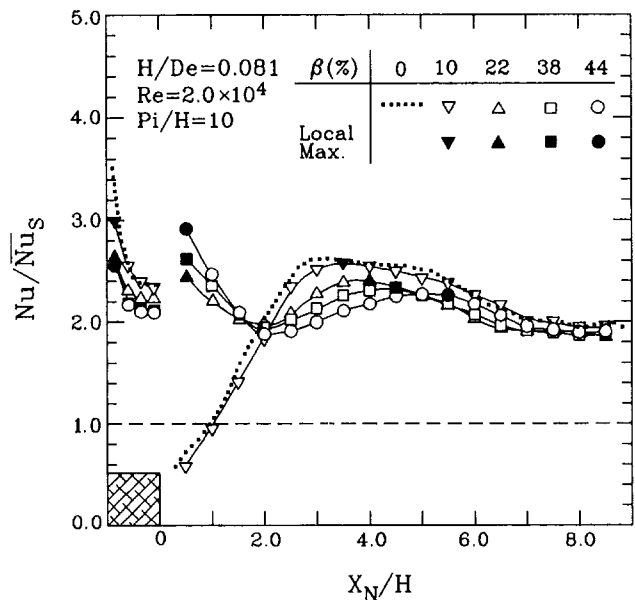


Fig. 7 Local Nusselt number distributions along the perforated ribbed surfaces

ribbed-wall with a large value of β , a large amount of heat conducted from the rib base has been convected by the airflow through the rib, and therefore, the conductive heat to the rib top (or convective heat from the rib-top surface to the test section) is reduced. In addition, the augmented forced convection between the two opposite ribs decreases as β increases due to the reduction of the blockage ratio. Concerning the results between the ribs, it can be observed that the difference between the permeable ($\beta \geq 22$ percent) and impermeable ($\beta \leq 10$ percent) rib geometries is evident. The results of the duct with solid-type ribs have been described in detail by Liou and Hwang (1992a). For the duct with permeable ribs, there are two-peak values of Nu/\bar{Nu}_s within the streamwise distance of the two successive ribs. The first local peak value is located at the duct wall just downstream of the rib, and it increases with an increase of β . Although the level of turbulence intensity is not measured quantitatively in this work, it is believed to be caused by the effect of the intense jet turbulence generating from the rear of the rib by the qualitative observation of the highly fluctuating fringes in this region. The second peak located in the middle of the successive ribs is considered to be the reason of an approach of the shear layer from the rib top to the duct wall. As β increases, the second peak of Nu/\bar{Nu}_s moves downward because the flow rate through the perforated walls increases with an increase of β . Note that the hot spots ($Nu/\bar{Nu}_s < 1$) around the concave corner behind the solid-type rib do not arise in the permeable-ribbed wall.

In this work the augmentation of the heat transfer is due to the combined effects of the extended surfaces and the enhanced turbulence (Liou et al., 1992). Considering the effect of the enhanced turbulence only, one may integrate the local heat transfer coefficient along the duct wall, i.e., $X_N/H = 0-9$ (Liou and Hwang, 1992a). As shown in Fig. 7, the value of the Nusselt number averaged over the duct wall between two successive ribs (i.e., $\bar{Nu}_{X_N/H=0-9}$) for the permeable rib geometry is higher than that for the solid-type rib geometry (Fig. 7, dotted line), typically $\bar{Nu}_{X_N/H=0-9} = 2.3$ and $2.1\bar{Nu}_s$ for $\beta = 44$ and 0 percent, respectively. This result reveals that the heat transfer augmentation due to the enhanced turbulence for the permeable rib geometry is higher than that for the solid-type rib geometry. Such a trend agrees with that in Tanasawa et al. (1983), in which thin, insulated

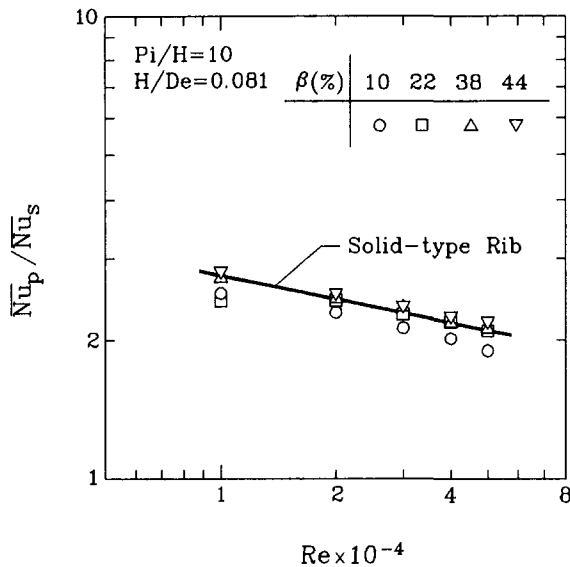


Fig. 8 Average Nusselt number versus Reynolds number

perforated plates were used as turbulence promoters, i.e., the effect of the extended area of the plate is not considered.

Average Nusselt Number and Friction Force. Ribs with a relatively high open-area ratio, and coolant flow passing through the ribs, are accompanied by a higher heat transfer area as compared with the solid-type ribs. To place the results on a common basis, the averaged Nusselt number (Eq. (4)) is based on the projected area of the corresponding ribless wall. Thus the magnitude of Nu can reflect the combined effects of the extended surfaces provided by the ribs and the enhanced turbulence by distortion the velocity and temperature fields caused by the presence of ribs (Liou et al., 1992). Figure 8 gives the average Nusselt number of the perforated-ribbed walls as a function of Reynolds number. The solid line (Liou and Hwang, 1992a) shows the results of the solid-type ribbed wall. It can be observed from this figure that for all the rib open area ratios investigated the heat transfer augmentation ($\overline{Nu}_p > \overline{Nu}_s$) is achieved. The increments of the average heat transfer coefficients for the permeable-ribbed wall are about the same as those for the solid-type-ribbed wall, typically 120–180 percent, as compared with the smooth-duct results for the range of the investigated Reynolds number. However, for the impermeable perforated-ribbed wall, i.e., $\beta = 10$ percent for all Re investigated and $\beta = 22$ percent at $Re = 10,000$, the heat transfer coefficients are slightly lower than those of the permeable or solid-type ribbed wall. The explanation of this fact is as follows: As shown in Fig. 7, the solid-type and impermeable perforated ribbed geometries have comparable heat transfer enhancements in the interrib region ($X_N/H = 0-9$). However, the heat transfer rate for the top wall ($X_N/H = -1-0$) of the impermeable perforated rib ($\beta = 10$ percent) is slightly lower than that of the solid-type rib. The lower heat transfer rate for the impermeable perforated ribs may be due to a reduction of the effective conductivity of the rib caused by the presence of the stagnant air in the holes. Thus, the averaged rib and duct-wall heat transfer coefficient for the impermeable perforated ribbed geometry is slightly lower as compared to that for the solid-type rib one. In fact, channels with solid-type ribs and impermeable perforated ribs may be considered simply as channels with relatively high and low conductivity ribs, respectively. The higher heat transfer enhancement associated with the channel with higher conductivity ribs is physically reasonable (Liou and Hwang, 1993).

The effect of the open-area ratio of the rib on the fully

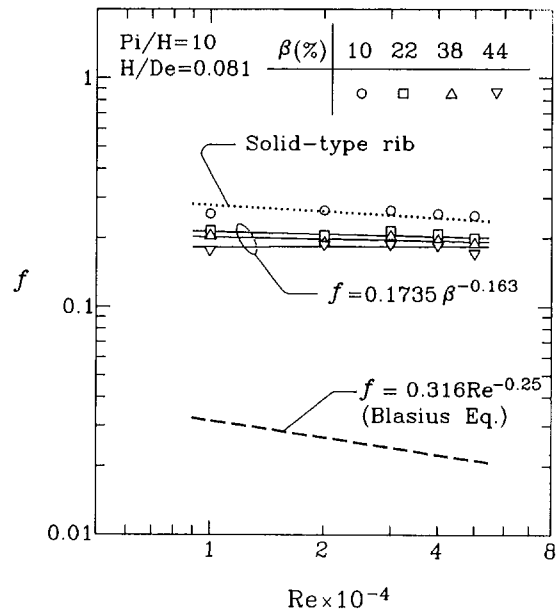


Fig. 9 Friction factor versus Reynolds number

developed friction factor is shown in Fig. 9. The pressure drops across the test channel are measured by the unheated flow conditions. The friction factor for the perforated rib is higher than its counterpart for the smooth channel (dashed-line, Blasius correlation), but lower than that for the solid-type rib (dotted line, Liou and Hwang, 1992b). It is almost constant regardless of the values of Re . In the case of $\beta = 10$ percent, the value of f is found to be almost the same as that of the solid-type rib. This reflects the fact of impermeability for $\beta = 10$ percent concluded before. In comparison with the results of the duct flows with solid-type ribs, the values of f are approximately 100, 85, 75, and 60 percent of that of the solid-type rib for $\beta = 10, 22, 38,$ and 44 percent, respectively, in the range of the Reynolds number investigated. As expected, for a given Reynolds number the friction factor decreases with increasing β because of less cross-sectional blockage for ribs with the larger β . The effects of Reynolds number and rib open-area ratio on the friction factor can be correlated as follows:

$$f = 0.1735 \cdot \beta^{-0.163} \quad (6)$$

Note that the correlation above is valid only for the permeable rib.

Performance Comparison. The general tendency found in the previous discussion of the solid-type rib is that the value of f is large when \overline{Nu}_p is large. From the results of the moderate heat transfer enhancement and lower pressure drop penalty achieved by the large value of β , a high thermal performance under the constant pumping power constraint may be expected to be accompanied by a large value of β . The pumping power required to feed the fluid through the duct is proportional to $f \cdot Re^3$. Thus in Fig. 10 the performance shown by the ratio of $\overline{Nu}_p/\overline{Nu}_s^*$ is plotted against $f^{1/3} \cdot Re$ (Tanasawa et al., 1983; Liou and Hwang, 1993). Figure 10 shows that the improvement in Nusselt number ratio of the permeable ribbed duct is more pronounced than that of the solid-type ribbed duct (dotted line). Note that at lower Reynolds number both the perforated and solid-type ribbed geometries give a higher thermal performance than those at higher Reynolds number. Therefore, the usage of the perforated ribs in the large rib open-area ratio and the lower Reynolds number range is recommended.

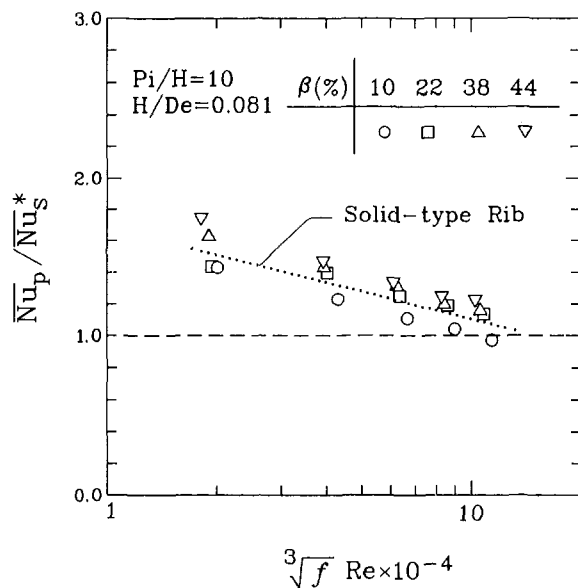


Fig. 10 Performances of the perforated ribbed ducts under constant pumping power

Concluding Remarks

Manufacturing of blades with permeable turbulators has been technically difficult up to now. However, it is important to understand the characteristics of heat transfer and fluid flow in channels with permeable ribs before the exact application. Moreover, information of flow over permeable ribbed walls is useful for the general area of heat exchangers. In this work, the turbulent heat transfer and friction in a channel with perforated rib on two opposite walls have been studied experimentally. The main findings are: A permeability criterion of the perforated rib is presented as a function of the rib open-area ratio and the Reynolds number. The critical Reynolds number of initiation of flow permeability decreases with increasing rib open-area ratio. The high rib open-area ratio and Reynolds number allow the ribs to be permeable. Results of the local heat transfer coefficient distributions reveal that the hot spots occurring in the region around the concave corner behind the solid-type rib do not arise in the corresponding region of the permeable-rib geometry. As compared with the conventional solid-type rib results, the average Nusselt number/friction factor of the perforated rib geometry are about 75/100, 100/85, 100/75, and 105/60 per-

cent, respectively, for $\beta = 10, 22, 38,$ and 44 percent. The moderate heat transfer coefficient and lower pressure drop accompanied by the large value of β reflect a higher thermal performance.

Acknowledgments

Support for this work was provided by the National Science Council of the Republic of China under contract No. NSC 82-0113-E-216-031-7.

References

- Burggraf, F., 1970, "Experimental Heat Transfer and Pressure Drop With Two-Dimensional Discrete Turbulence Promoters Applied to Two Opposite Walls of a Square Tube," *Augmentation of Convective Heat and Mass Transfer*, E. E. Bergles and R. L. Webb, eds., ASME, New York, pp. 70-79.
- Han, J. C., 1984, "Heat Transfer and Friction in Channels With Two Opposite Rib-Roughened Walls," *ASME Journal of Heat Transfer*, Vol. 106, pp. 774-782.
- Han, J. C., 1988, "Heat Transfer and Friction Characteristics in Rectangular Channels With Rib Turbulators," *ASME Journal of Heat Transfer*, Vol. 110, pp. 321-328.
- Kline, S. J., and McClintock, F. A., 1953, "Describing Uncertainties in Single-Sample Experiments," *Mechanical Engineering*, Vol. 75, Jan., pp. 3-8.
- Lau, S. C., McMillin, R. D., and Han, J. C., 1991, "Turbulent Heat Transfer and Friction in a Square Channel with Discrete Rib Turbulators," *ASME JOURNAL OF TURBOMACHINERY*, Vol. 113, pp. 360-366.
- Liou, T. M., and Hwang, J. J., 1992a, "Turbulent Heat Transfer and Friction in Periodic Fully Developed Channel Flows," *ASME JOURNAL OF TURBOMACHINERY*, Vol. 114, pp. 56-64.
- Liou, T. M., and Hwang, J. J., 1992b, "Developing Heat Transfer and Friction in a Rectangular Ribbed Duct With Flow Separation at Inlet," *ASME Journal of Heat Transfer*, Vol. 114, pp. 565-573.
- Liou, T. M., Hwang, J. J., and Chen, S. H., 1992, "Turbulent Transport Phenomena in a Channel With Periodic Rib Turbulators," *AIAA J. Thermophysics*, Vol. 6, pp. 513-521.
- Liou, T. M., and Hwang, J. J., 1993, "Effects of Ridge Shapes on Turbulent Heat Transfer and Friction in a Rectangular Channel," *Int. J. Heat Mass Transfer*, Vol. 36, No. 4, pp. 931-940.
- Liou, T. M., Hwang, J. J., and Chen, S. H., 1993, "Simulation and Measurement of Enhanced Turbulent Heat Transfer in a Channel With Periodic Rib on One Principal Wall," *Int. J. Heat Mass Transfer*, Vol. 36, No. 2, pp. 507-517.
- Lockett, J. F., and Collins, M. W., 1990, "Holographic Interferometry Applied to Rib-Roughness Heat Transfer in Turbulent Flow," *Int. J. Heat Mass Transfer*, Vol. 33, pp. 2439-2449.
- Tanasawa, T., Nishio, S., Tanano, K., and Tado, M., 1983, "Enhancement of Forced Convection Heat Transfer in a Rectangular Channel Using Turbulence Promoters," *Proceedings of ASME/JSME Thermal Engineering Joint Conference*, pp. 395-402.
- Yomada, H., and Osaka, H., 1992, "Flow Around a Permeable Rectangular Plate Standing Vertically on the Flat Wall, 2nd Report. Effects of the Aspect and the Open Area Ratios," *Trans. JSME*, Vol. 56, No. 546, pp. 120-128.

Surface Heating Effect on Local Heat Transfer in a Rotating Two-Pass Square Channel With 60 deg Angled Rib Turbulators

Y. M. Zhang

J. C. Han

J. A. Parsons

Department of Mechanical Engineering,
Turbine Heat Transfer Laboratory,
Texas A & M University,
College Station, TX 77843

C. P. Lee

General Electric Company,
Cincinnati, OH 45215

The influence of uneven wall temperature on the local heat transfer coefficient in a rotating, two-pass, square channel with 60 deg ribs on the leading and trailing walls was investigated for Reynolds numbers from 2500 to 25,000 and rotation numbers from 0 to 0.352. Each pass, composed of six isolated copper sections, had a length-to-hydraulic diameter ratio of 12. The mean rotating radius-to-hydraulic diameter ratio was 30. Three thermal boundary condition cases were studied: (A) all four walls at the same temperature, (B) all four walls at the same heat flux, and (C) trailing wall hotter than leading with side walls unheated and insulated. Results indicate that rotating ribbed wall heat transfer coefficients increase by a factor of 2 to 3 over the rotating smooth wall data and at reduced coefficient variation from inlet to exit. As rotation number (or buoyancy parameter) increases, the first pass (outflow) trailing heat transfer coefficients increase and the first pass leading heat transfer coefficients decrease, whereas the reverse is true for the second pass (inflow). The direction of the Coriolis force reverses from the outflow trailing wall to the inflow leading wall. Differences between the first pass leading and trailing heat transfer coefficients increase with rotation number. A similar behavior is seen for the second pass leading and trailing heat transfer coefficients, but the differences are reduced due to buoyancy changing from aiding to opposing the inertia force. The results suggest that uneven wall temperature has a significant impact on the local heat transfer coefficients. The heat transfer coefficients on the first pass leading wall for cases B and C are up to 70–100 percent higher than that for case A, while the heat transfer coefficients on the second pass trailing wall for cases B and C are up to 20–50 percent higher.

Introduction

It is well known that turbine engine thermal efficiency can be improved by increasing the turbine inlet gas temperatures. This causes an increase of heat load to the turbine components. Highly sophisticated cooling techniques such as film cooling and augmented internal cooling (shown in Fig. 1) have been employed for turbine blades in order to maintain acceptable safety requirements under extreme operating conditions. However, it is important to understand the effect of blade rotation on local heat transfer coefficient distributions inside the serpentine coolant passages. This paper focuses on the influence of surface heating condition on local heat transfer coefficients in a rotating, two-pass, square channel with 60 deg rib-turbulated walls.

Previous investigations of turbine blade internal coolant

passage heat transfer have concentrated on nonrotating models and have not accounted for the Coriolis force and the centrifugal buoyancy force effects on coolant motion and heat transfer (Han, 1984, 1988). However, some researchers reported the effect of rotation on the heat transfer characteristics in a straight channel with smooth walls and radial outward flow (Mori et al., 1971; Clifford et al., 1984; Haragama and Morris, 1988; Guidez, 1989; Morris and Ghavam-Nasr, 1991). Taslim et al. (1991a, 1991b) studied the effect of rotation on the heat transfer coefficients in a rectangular channel with ribbed walls and radial outward flow. Wagner et al. (1991a, 1991b, 1992) and Johnson et al. (1994) systematically investigated the effect of rotation on the local heat transfer coefficient in a serpentine coolant passage (three-pass) with smooth and ribbed walls, respectively, for parameters similar to typical engine conditions. Prakash and Zerkle (1992) predicted the flow and heat transfer coefficients in a rotating smooth channel with radial outward flow and agreed within 10–30 percent with the data of Wagner et al. (1991a).

In summary, for the case of a multipass smooth wall

Contributed by the International Gas Turbine Institute and presented at the 38th International Gas Turbine and Aeroengine Congress and Exposition, Cincinnati, Ohio, May 24–27, 1993. Manuscript received at ASME Headquarters March 17, 1993. Paper No. 93-GT-336. Associate Technical Editor: H. Lukas.

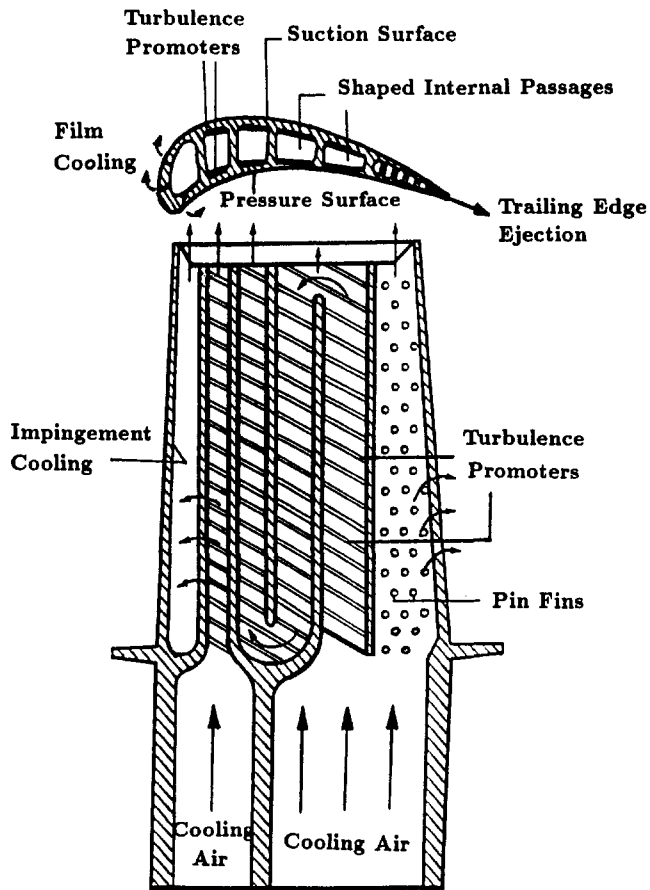


Fig. 1 Cooling concepts of a modern multipass turbine blade

channel, Wagner et al. (1991a, 1991b) reported that the rotating trailing surface heat transfer coefficient of the first coolant passage (radial outward flow) increased up to 3.5 times the nonrotating fully developed circular tube values (Rohsenow and Choi, 1961), but the leading surface heat transfer coefficient decreased to 40 percent of the fully developed circular tube values. However, the rotating trailing surface heat transfer coefficient of the second coolant pas-

sage (radial inward flow) decreased by 30 percent compared to the stationary values, while the leading surface heat transfer coefficient increased by 20 percent compared to the stationary results. For the case of a multipass, square channel with trips normal to the flow (90 deg ribs), Wagner et al. (1992) indicated that the maximum rotating heat transfer coefficient increased up to 4.0 times from the nonrotating fully developed circular tube values, which were slightly above the highest levels obtained with the rotating smooth wall model (~ 3.5 times). However, the minimum rotating heat transfer coefficients decreased to 80 percent of the stationary 90 deg ribbed wall model. For the case of a multipass square channel with trips skewed to the flow (45 deg ribs), Johnson et al. (1994) concluded that the maximum rotating heat transfer coefficient increased up to 5.0 times of the nonrotating circular tube values, while the minimum rotating heat transfer coefficient decreased to 40 percent of the stationary 45 deg ribbed wall model. They recommended that skewed trip strips (45 deg ribs) rather than normal trip strips (90 deg ribs) be used for the turbine blade coolant passage design.

Han et al. (1993, 1994) reported the effect of surface heating condition on local heat transfer coefficients in a one-pass and two-pass square channel with smooth walls (shown in Fig. 2). Their rotating smooth-wall heat transfer results agreed with those of Wagner et al. (1991a, 1991b) for the case of uniform wall temperature conditions. However, Han et al. (1993, 1994) found that, for the uniform wall heat flux and simulated engine wall heating conditions, the rotating leading surface heat transfer coefficient of the first coolant passage (radial outward flow) as well as the rotating trailing surface heat transfer coefficient of the second coolant passage (radial inward flow) were up to 100 percent greater than those for the uniform wall temperature conditions. Since wall heating condition significantly affects rotating smooth wall channel heat transfer, it is unknown how effects due to wall heating are changed when ribs are added to the channel walls. Therefore, the objective of this study is to investigate the effects of wall heating condition on local heat transfer coefficients in a rotating two-pass square channel with 60 deg angled ribs on the leading and trailing walls. Three wall heating conditions were tested: Case (A) four walls at the same temperature, Case (B) four walls at the same heat flux, and Case (C) the trailing wall hotter than the leading wall but with two side walls unheated and insulated (to simulate turbine engine operating conditions).

Nomenclature

A = heat transfer surface area
 D = hydraulic diameter; square channel width or height
 e = rib height
 h = heat transfer coefficient
 k = thermal conductivity of coolant (air)
 L = heated channel length (each pass)
 Nu = Nusselt number = hD/k
 Nu_0 = Nusselt number in fully developed tube flow
 P = rib pitch or streamwise spacing
 Pr = Prandtl number
 q_{net} = net heat transfer rate
 q'' = net heat transfer flux
 R = rotating radius
 \bar{R} = mean rotating radius
 Re = Reynolds number = $\rho DV/\mu$

Ro = rotation number = $\Omega D/V$
 T_b = local bulk mean coolant temperature
 T_{bi} = inlet bulk mean coolant temperature
 T_w = local wall temperature
 T_{wA} = local wall temperature of side A surface
 T_{wB} = local wall temperature of side B surface
 T_{wL} = local wall temperature of leading surface
 T_{wT} = local wall temperature of trailing surface
 V = mean coolant channel velocity
 X = channel axial distance from heated channel inlet
 X' = channel axial distance from second pass inlet

$\Delta \rho/\rho$ = coolant-to-wall density ratio based on local bulk mean coolant temperature = $(\rho_b - \rho_w)/\rho_b = (T_w - T_b)/T_w$
 $(\Delta \rho/\rho)_i$ = coolant-to-wall density ratio based on inlet bulk mean coolant temperature = $(\rho_{bi} - \rho_w)/\rho_{bi} = (T_w - T_{bi})/T_w$
 μ = coolant dynamic viscosity
 ρ = coolant density
 ρ_b = coolant density based on local bulk mean coolant temperature
 ρ_{bi} = coolant density based on inlet bulk mean coolant temperature
 ρ_w = coolant density based on local wall temperature
 Ω = rotational speed, rpm

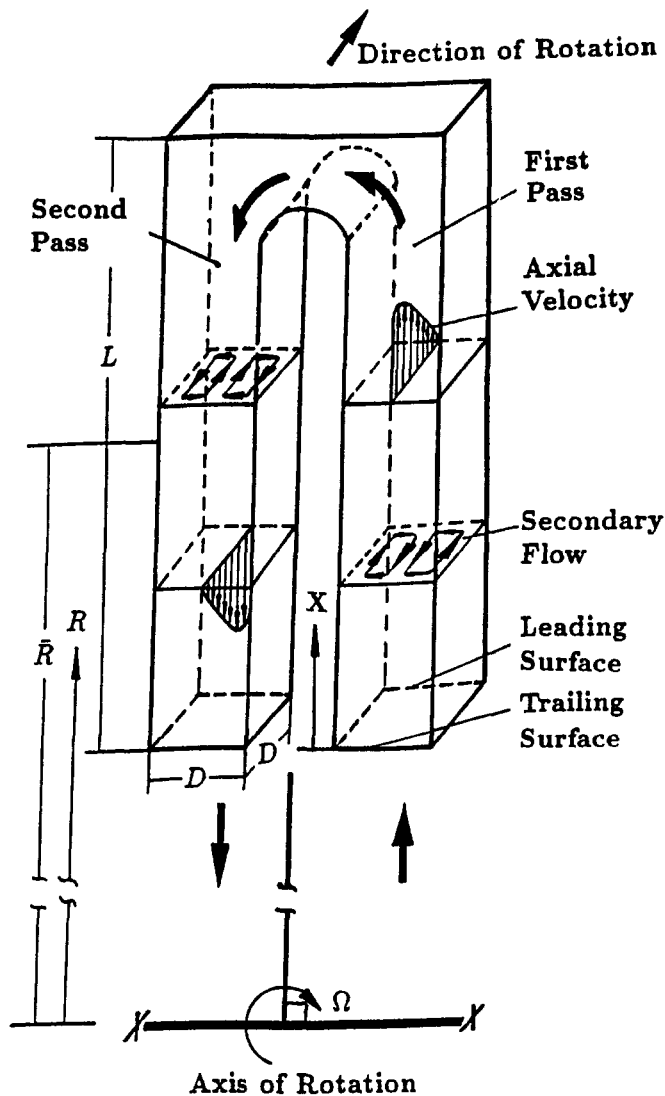


Fig. 2 Conceptual view of a two-pass rotating coolant flow profile

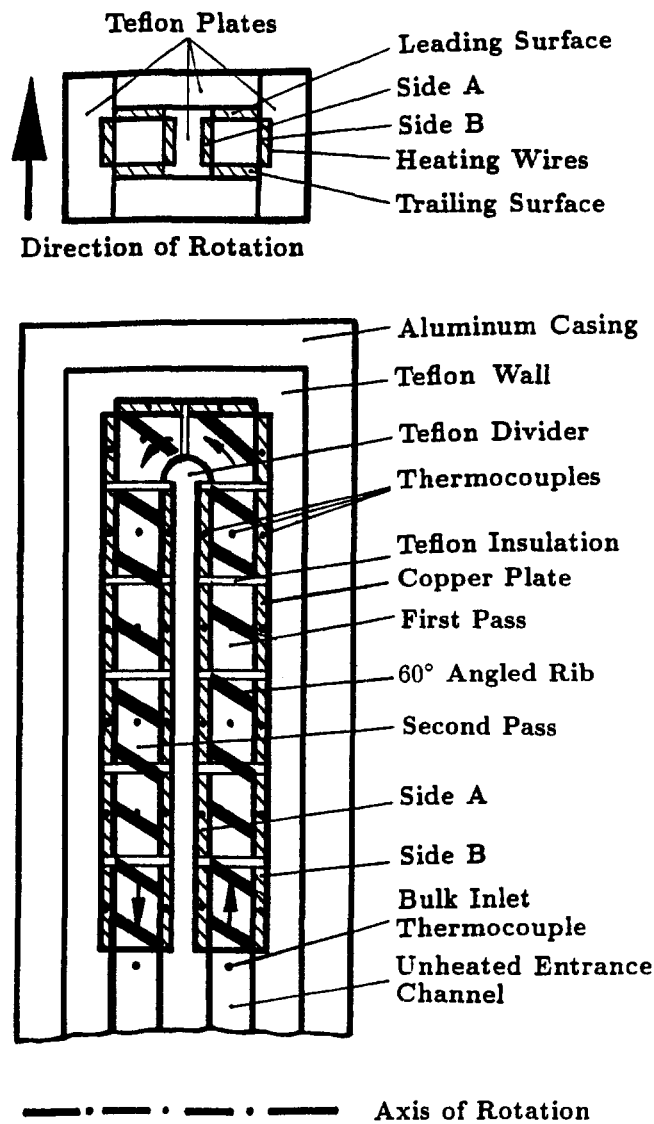


Fig. 3 Schematic of the two-pass heat transfer test model

Experimental Facility

The test stand has been previously described and illustrated in Han et al. (1993, 1994). A shortened description of the test stand follows. Regulated compressor air flows from an orifice meter and passes through a hollow rotating shaft and a hollow rotating arm, which is perpendicular to the shaft. It then goes into the test model (a ribbed, two-pass, square channel) and is exhausted into the atmosphere at the opposite end of the rotating shaft. Slip ring units transfer thermocouple outputs to a data logger interfaced to a personal computer, and transfer variac transformer outputs to wire resistance heaters uniformly cemented in grooves on the backside of the copper plates. The rotating shaft speed is measured by a digital photo tachometer.

It is better to have a test model for turbine cooling design that can determine the regionally averaged heat transfer coefficients in the channel streamwise flow direction. The two-pass square channel test model is divided into twelve short copper sections (see Fig. 3). Each copper section is composed of four copper plates and has an inner cross section of 1.27 cm by 1.27 cm (1/2 in. by 1/2 in.). Thin Teflon strips are machined along the periphery contact surface between copper sections for insulation to prevent possible heat conduction. The channel length-to-hydraulic diameter ratio is 24, while each pass length-to-hydraulic diameter ratio (L/D)

is 12. The ratio of the mean rotating arm radius to the channel hydraulic diameter (\bar{R}/D) is 30. The ribbed trailing and leading surfaces were made by gluing brass ribs of square cross section to the copper plates in a required distribution and orientation. The thickness of conductive glue is less than 0.01 cm and creates a negligible thermal insulation effect between the ribs and the copper plates. For this study, the rib height-to-hydraulic diameter ratio (e/D) is 0.125, the rib pitch-to-height ratio (p/e) is 10, and the rib flow-attack-angle (the angle between the rib and coolant flow direction) equals 60 deg. The 60 deg ribs on both the leading and trailing walls are in-line and parallel to each other. Each wall has its own heater powered by a variac transformer for controllable heat flux. The smooth side walls are isolated from the leading and trailing walls to eliminate heat conduction. The entire heated test duct is insulated by Teflon material. The local wall temperature of the test model is measured by 48 copper-constantan thermocouples distributed along the length and around the perimeter of the copper channel. Two more thermocouples measure the inlet and outlet bulk air temperature. There is an unheated Teflon entrance channel (partially shown in Fig. 3) that has the same cross section and length of one pass of the channel. This serves to establish hydrodynamically fully developed at the entrance to the heated channel.

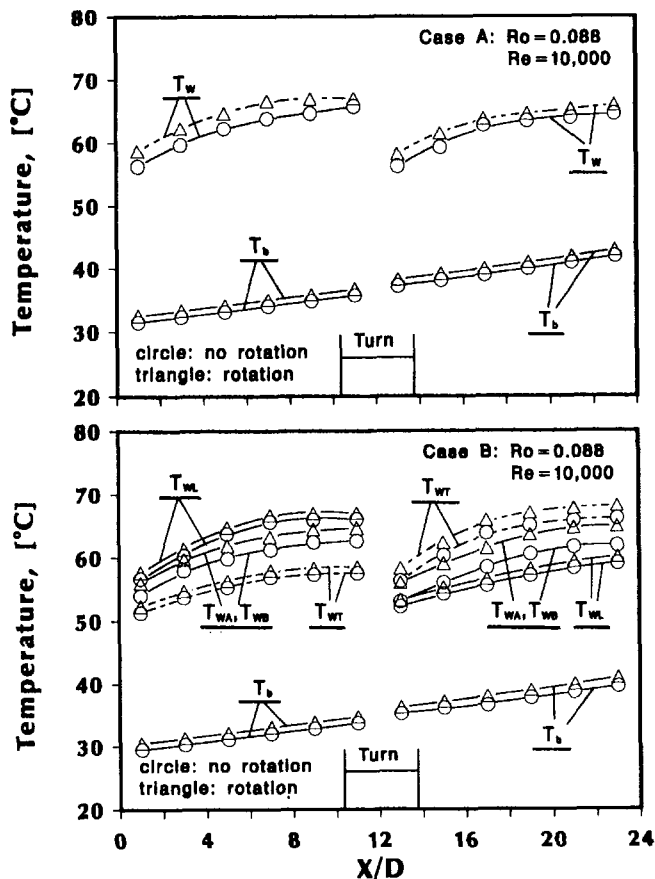


Fig. 4 Variation of the surface and coolant temperature with axial location for Cases A and B

Data Reduction

The local heat transfer coefficient is calculated from the local net heat transfer rate per unit surface area to the cooling air, the local wall temperature on each copper plate, and the local bulk mean air temperature as:

$$h = q_{\text{net}} / [A(T_w - T_b)] \quad (1)$$

Local net heat transfer rate (q_{net}) is the electrical power generated from the heaters, which is calculated from heater voltage and current measurements minus the heat loss to the outside of the test section. Heat loss tests, done without air flow, determine heat loss for each test model wall for both stationary and rotating conditions. Several different power input levels at steady state are used to obtain the heat loss relationships for each wall as a function of the wall temperature. Wall heat loss relationships are determined for the three different wall heating conditions (Cases A, B, and C). To place the results on a common basis, the heat transfer area used in Eq. (1) is always that of a smooth wall, i.e., the area increase due to the ribs is not included.

The local wall temperatures in Eq. (1) are obtained from the thermocouples in each copper plate. The local bulk mean air temperature in Eq. (1) uses the corresponding X/L for each thermocouple location in interpolating between the measured inlet (about 30°C) and exit bulk temperatures. The total net heat transfer rate from the test channel to the cooling air agreed with the bulk mean air temperature rise along the test channel for Reynolds numbers larger than 5000 (i.e., an energy balance was achieved). Figure 4 shows typical variations of local wall-to-bulk mean air temperature along the two-pass test channel for two different wall heating conditions (Cases A and B) at rotation numbers of 0.0 and 0.088 (0 and 800 rpm at $Re = 10,000$).

To reduce the influence of the flow Reynolds number on the heat transfer coefficient with rotation, the local Nusselt number of the present study is normalized by the Nusselt number for fully developed turbulent flow in smooth circular tubes with no rotation correlated by Dittus-Boelter/McAdams (Rohsenow and Choi, 1961) as:

$$Nu/Nu_0 = (hD/k) / [0.023 Re^{0.8} Pr^{0.4}] \quad (2)$$

with $Pr = 0.72$. Properties in the Nusselt and Reynolds numbers are based on the average of the inlet and outlet bulk mean air temperatures. The uncertainty of the local heat transfer coefficient depends on the local wall-to-coolant (air) temperature difference and the net heat input to the air for each copper plate. This uncertainty increases for decreasing both the local wall-to-air temperature difference ($T_w - T_b$) and the net heat input. Based on the method described by Kline and McClintock (1953), the typical uncertainty in the Nusselt number is estimated to be less than 8 percent for Reynolds numbers larger than 10,000. The maximum uncertainty, however, could be up to 20–25 percent for the lower heat transfer coefficient at the lowest Reynolds number tested ($Re = 2500$).

Experimental Results and Discussion

According to Wagner et al. (1991a, 1991b, 1992) and Han et al. (1993, 1994), the Nusselt number in a rotating channel is a function of the ratio of the rotating mean radius to channel hydraulic diameter, the ratio of the axial distance to channel hydraulic diameter, Reynolds number, Prandtl number, rotation number, wall-to-coolant temperature (density) difference ratio, flow direction (radial outward flow or radial inward flow), and the rib turbulator orientation, respectively. Their functional relationship can be expressed as:

$$Nu = f(\bar{R}/D, X/D, Re, Pr, Ro, \Delta\rho/\rho,$$

$$\text{flow direction, roughness}) \quad (3)$$

where, for the present study, $Pr = 0.72$ and $\bar{R}/D = 30$. Tests in this study have the following parameter values: $Re = 2500, 5000, 10,000, \text{ and } 25,000$; $\Omega = 0, 400, \text{ and } 800$ rpm; combining to produce $Ro = 0.0, 0.0176, 0.0352, 0.044, 0.088, 0.176, \text{ and } 0.352$. The inlet wall-to-coolant density ratio $(\Delta\rho/\rho)_i$ has the following values: Case A = 0.11; Case B = 0.10, 0.07, and 0.08 for the first pass leading, trailing, and side walls (the reverse is true for the second pass leading and trailing walls); and Case C = 0.10 and 0.08 for trailing and leading, respectively.

Effect of Rotation Relative to Nonrotation. Figure 5 shows the effect of rotation on the local Nusselt number ratio (Nu/Nu_0) for Case A. Note that the Nusselt number ratio is the ratio of the local Nusselt number to that of the nonrotating fully developed turbulent flow smooth tube value shown in Eq. (2). The results show that the local Nusselt number ratios on the trailing and leading ribbed walls are fairly uniform for nonrotation (around 3–4 through the entire two-pass channel for Reynolds numbers between 2500 and 25,000). In the first outflow pass ($0 < X/D < 12$), the rotation significantly enhances the Nusselt number ratios on the trailing ribbed wall and greatly decreases the Nusselt number ratios on the leading ribbed wall. In the second inflow pass ($12 < X/D < 24$), the rotation decreases the trailing wall Nusselt number ratios and increases the leading wall Nusselt number ratios as compared to that of the nonrotation values. This is because rotation induces the Coriolis forces that produce secondary cross-stream flows and thins out the first pass trailing and the second inflow pass leading boundary layers. It also thickens the first pass leading and the second pass trailing boundary layers (see the conceptual velocity profile in Fig. 2). Therefore, the heat transfer coefficients on

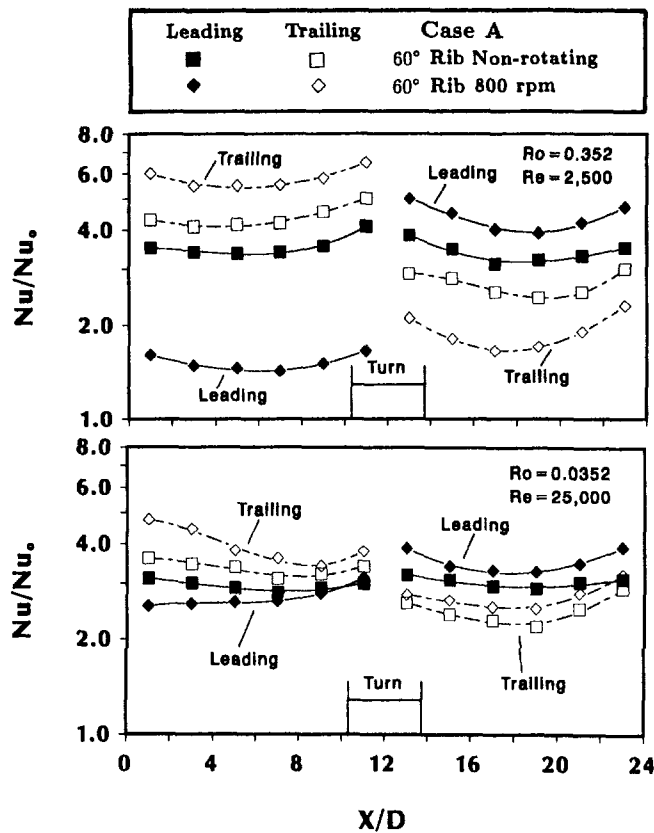


Fig. 5 Effect of rotation on Nusselt number ratio variation for Case A

the first pass trailing and the second pass leading walls with rotation are higher than those without rotation, whereas the heat transfer coefficients on the first pass leading and the second pass trailing with rotation are lower than those without rotation. However, the rotation effect is reduced when the rotation number decreases from $Ro = 0.352$ to $Ro = 0.0352$ (see Fig. 5).

Effect of Wall Heating Condition. Figure 6 shows the effect of varying the wall heating on the local Nusselt number ratio for rotation numbers $Ro = 0.0352$ and 0.352 . Nusselt number ratios on the leading ribbed wall for Cases B and C in the first pass ($0 < X/D < 12$) are 70 and 100 percent higher, respectively, than those for Case A at $Nu/Nu_0 = 1.5$. The Nusselt number ratios on the trailing ribbed wall for Case C are about 20 percent higher than those for Case A at $Nu/Nu_0 = 6.0$. The Nusselt number ratios on the trailing ribbed wall for Cases B and C in the second pass ($12 < X/D < 24$) are 20 and 50 percent higher, respectively, than for Case A at $Nu/Nu_0 = 2.0$, while the Nusselt number ratios on the leading ribbed wall for Case C are about 50 percent lower than those for Case A at $Nu/Nu_0 = 4.5$. However, the wall heating condition effect is reduced with decreased rotation number from $Ro = 0.352$ to 0.0352 (see Fig. 6).

For Case B of four walls at the same heat flux, the first pass trailing wall temperature ($T_w = 50\text{--}55^\circ\text{C}$ and $(\Delta\rho/\rho)_i = 0.07$) being lower than the leading ($T_w = 60\text{--}65^\circ\text{C}$ and $(\Delta\rho/\rho)_i = 0.1$) and side walls ($T_w = 55\text{--}60^\circ\text{C}$ and $(\Delta\rho/\rho)_i = 0.08$) can result in more cooler fluid near the trailing and side wall surfaces. It is assumed that the Coriolis-induced secondary cross stream flows carry these cooler fluids from the trailing and side wall surfaces toward the leading surface. Therefore, the leading surface heat transfer coefficients (i.e., Nusselt number ratios) for Case B are higher than those for Case A due to rotation. Similarly, for Case C of trailing hotter than leading surfaces ($T_w = 60\text{--}65^\circ\text{C}$ and $(\Delta\rho/\rho)_i = 0.1$

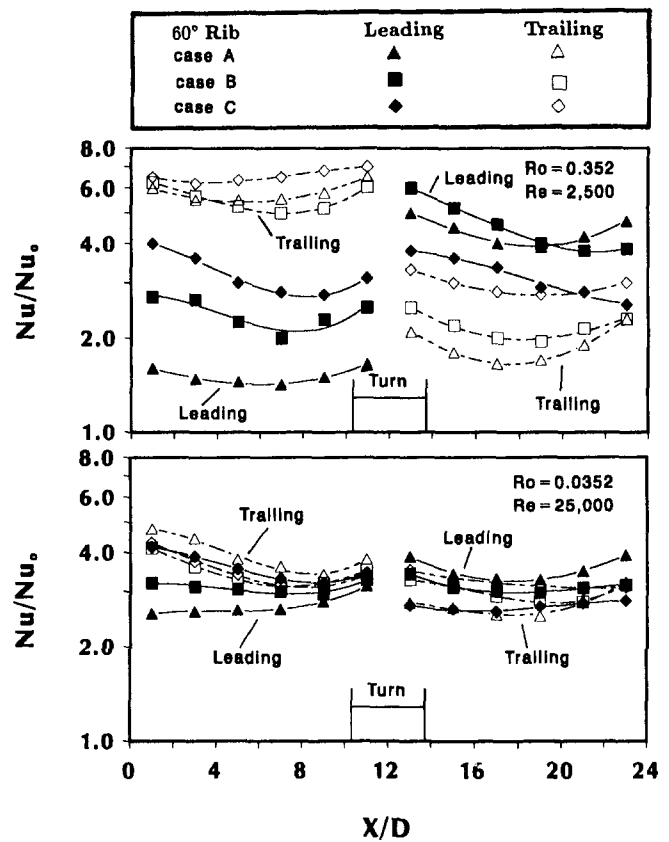


Fig. 6 Effect of wall heating condition on Nusselt number ratio variation for Cases A, B, and C at selected rotation numbers

for trailing and $T_w = 55\text{--}60^\circ\text{C}$ and $(\Delta\rho/\rho)_i = 0.08$ for leading) with two unheated and insulated sidewalls ($T_w = 45\text{--}50^\circ\text{C}$ and $(\Delta\rho/\rho)_i = 0.05$), the Coriolis-induced secondary cross-stream flows carry the cooler fluid from the side walls toward the leading surface. Therefore, the leading surface heat transfer coefficients for Case C are much higher than those for Case A due to rotation.

The leading wall temperature in the second pass for Case B is lower than the trailing and side walls and results in more cooler fluid near the leading surface. Meanwhile, the secondary cross-stream flows carry the cooler fluid from the leading and side walls back to the trailing surface. Therefore, due to rotation, the trailing surface heat transfer coefficients for Case B are higher than those for Case A. Similarly, for Case C of trailing hotter than leading surface with two unheated side walls, the secondary cross-stream flows carry the cooler fluid from the side walls toward the trailing surface. Therefore, due to rotation, the trailing surface heat transfer coefficients for Case C are much higher than those for Case A.

Effect of Reynolds Number. Figure 7 shows the effect of Reynolds number on the Nusselt number ratio at a given rotation number of $Ro = 0.088$. The rotation number $Ro = \Omega D/V$ can be held constant with various combinations of rotation speed (Ω) and axial flow velocity (V or Re). The rotation number $Ro = 0.088$ is based on two combinations of Ω and Re : $\Omega = 400$, $Re = 5000$; and $\Omega = 800$, $Re = 10,000$. The results show that the Nusselt number ratios increase slightly with an increasing Reynolds number by holding the rotation number constant. However, the amount of Nusselt number ratio increase for the first pass leading wall is relatively large.

Effect of Rotation Number and Wall Heating Condition and Comparison. Figure 8 shows the effect of rotation

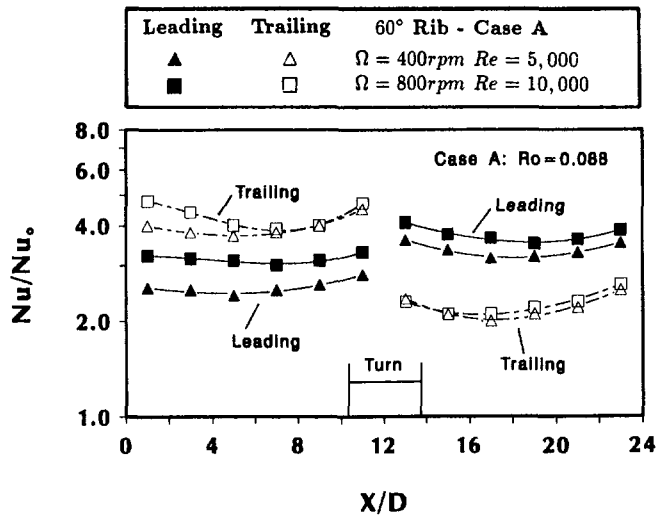


Fig. 7 Effect of Reynolds number on Nusselt number ratio variation for Case A

number on the Nusselt number ratio at six selected channel axial locations for the three studied heating conditions. The experimental results from Johnson et al. (1994) for the case of uniform wall temperature and with 45 deg ribbed walls, and from Han et al. (1993, 1994) for the case of four walls at the same temperature and smooth walls are also included for comparison. Results of Johnson et al. (1994) are based on the following conditions and locations: Ro calculated from $Re = 25,000$ and varying rotation speeds, $(\Delta\rho/\rho)_i = 0.13$, $\bar{R}/D = 49$, the first pass $X/D = 4.6, 8.5, 12.4$ (no ribs for $X/D < 3$), and the second pass $X/D = 21.6, 25.6$ (or for X' starting at the second pass inlet, $X'/D = 2.0, 6.0$). These data are taken from Fig. 6 of Johnson et al. (1994). The present data for the case of four walls at the same temperature are based on Ro calculated from $\Omega = 800\text{ rpm}$ and varying Reynolds numbers from 2500 to 25,000, $(\Delta\rho/\rho)_i = 0.11$, $\bar{R}/D = 30$, the first pass $X/D = 5, 9, 11$ (ribs start at $X/D = 0$), and the second pass $X/D = 13, 15, 19$ (or for X' , $X'/D = 1, 3, 7$).

The previous smooth wall results (shown in Fig. 8) indicate that the first pass trailing surface Nusselt number ratio increases with an increasing rotation number, while the first pass leading surface Nusselt number ratio decreases and then increases with an increasing rotation number. The smooth wall results also show that the difference between the leading and trailing surface heat transfer coefficients in the second pass is not as significant as that in the first pass. The leading and trailing surface heat transfer coefficients in the second pass are relatively independent of the rotation number as compared to that in the first pass.

The effect of rotation number on the 60 deg ribbed wall Nusselt number ratio shows trends similar to those on the smooth wall results except that the 60 deg ribs greatly enhance the surface Nusselt number ratios through the entire two-pass channel (Fig. 8). In the first pass, the Nusselt number ratios on the trailing ribbed wall increase up to 6.0 while the Nusselt number ratios on the leading ribbed wall decrease to 1.5 as compared to the nonrotating ribbed wall Nusselt number ratios of around 3 to 3.5. The Nusselt number ratios on the leading ribbed wall in the second pass increase from 3.0 to 4.0 while the Nusselt number ratios on the trailing ribbed wall decrease from 3.0 to 2.0 when the rotation number changes from 0 (nonrotating) to 0.352 (higher rotation). The difference between the leading and trailing Nusselt number ratios in the second pass is smaller than that in the first pass.

As previously discussed, Fig. 8 shows that the first pass Nusselt number ratios on the leading ribbed surface for

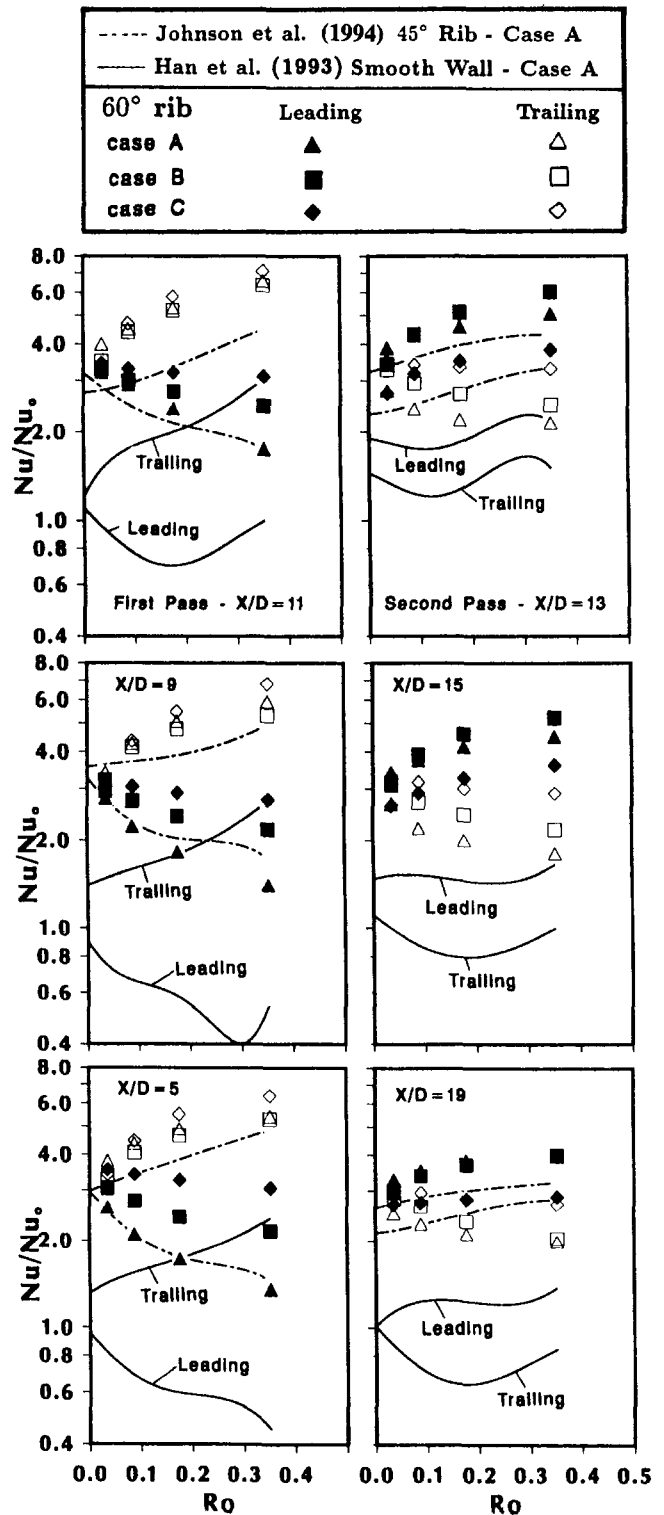


Fig. 8 Effect of rotation number on Nusselt number ratio variation at selected axial locations for Cases A, B, and C, and comparison with the previous results

Cases B and C are respectively higher than that for Case A. The second pass Nusselt number ratios on the trailing ribbed surface for Cases B and C are respectively higher than that for Case A. However, the second pass Nusselt number ratios on the leading ribbed surface for Case C are lower than that for Case A over the range of rotation numbers studied.

Figure 8 also shows the comparison between the present 60 deg rib data and Johnson et al. (1994) 45 deg rib results

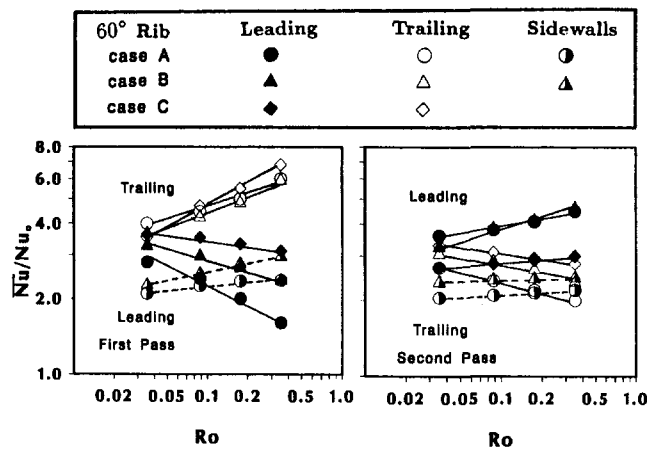


Fig. 9 Effect of rotation number on channel-averaged Nusselt number ratio variation for Cases A, B, and C

for the case of uniform wall temperature condition. In the first pass, the present Nusselt number ratios on the leading surface agree with those of Johnson et al., while the present Nusselt number ratios on the trailing surface are significantly higher than those of Johnson et al. over the range of rotation numbers studied. In the second pass, the present data on the leading surface are higher; however, the present data on the trailing surface are lower than those of Johnson et al. The difference between these two studies may be explained as follows. The 45 deg ribs of Johnson et al. are semicircular in cross section and have a rib height ratio of $e/D = 0.10$. The 60 deg ribs of this study are square in cross section and have a rib height ratio of $e/D = 0.125$. Since rotation creates a thinner boundary layer in the first pass trailing wall and a thicker boundary layer in the first pass leading wall, it is expected that the rib height, rib shape, and rib orientation/angle have a more significant effect on the thinner trailing wall boundary layer than that on the thicker leading wall boundary layer. Therefore, the present Nusselt number ratios on the ribbed trailing wall are higher than those of Johnson et al., while the leading wall Nusselt number ratios are about the same for the two studies. Similarly, in the second pass, the rotation induces a thinner boundary layer on the leading wall and a thicker boundary layer on the trailing wall. Therefore, due to the sharper and taller ribs of this study, the present data on the leading surface are higher than those of Johnson et al. However, the present data on the trailing surface are lower than those of Johnson et al., particularly at the higher rotation numbers. This may be due to the different combined effects of rotation, rib orientation (60 versus 45 deg), and second pass entrance geometry (sharp 180 deg turn versus gradual 180 deg bend).

Channel-Averaged Results. Figure 9 shows the variation of the channel-averaged Nusselt number ratio with rotation number for Cases A, B, and C. The channel-averaged Nusselt number (\bar{Nu}) for a wall is the average value of the entire wall local Nusselt number (Nu) from $X/D = 1$ to $X/D = 11$ for the first pass and from $X/D = 13$ to $X/D = 23$ for the second pass. The data are for $Ro = 0.352, 0.176, 0.088,$ and 0.0352 (based on $\Omega = 800$ rpm and $Re = 2500, 5000, 10,000,$ and $25,000$). The channel-averaged results show similar trends as those presented and discussed in Fig. 8. The wall heating condition has a significant effect on the first pass leading ribbed wall as well as on the second pass trailing ribbed wall results, whereas the difference between leading and trailing Nusselt number ratios in the second pass is smaller than that in the first pass. Figure 9 shows additional information. The channel-averaged Nusselt number ratios on the smooth side walls are enhanced up to 2–3 for both the first and second

pass. The smooth side wall Nusselt number ratios for Case B are slightly higher than those for Case A.

Effect of Buoyancy Parameter and Wall Heating Condition and Comparison. A buoyancy parameter $(\Delta\rho/\rho)(R/D)(Ro)^2$, also written as $(\Delta\rho/\rho)(\Omega R/V)(\Omega D/V)$, is used by Wagner et al. (1991a, 1991b, 1992), Johnson et al. (1994), and Han et al. (1993, 1994) to consider combined effects of Coriolis and buoyancy forces on heat transfer. The buoyancy parameter includes the effects of the local coolant-to-wall density ratio $((\Delta\rho/\rho) = (T_w - T_b)/T_w)$, related to buoyancy force, secondary cross-stream flow (Coriolis force, related to Ro), and rotating radius-to-hydraulic diameter ratio (R/D , related to buoyancy force). Figure 10 shows the Nusselt number ratio variation with buoyancy parameter at selected axial locations for the present 60 deg rib data at wall heating conditions A, B, and C. The results from Han et al. (1993, 1994) for smooth wall and from Johnson et al. (1994) for 45 deg rib ($R/D = 49$ and Ro between 0.0 and 0.34) are also included for comparison. In the present study, $R/D = 30$ and Ro is between 0.0 and 0.352. The buoyancy parameter effect on the Nusselt number ratios show trends similar to those presented and discussed in Fig. 8. The wall heating condition has a significant effect on the first pass leading surface as well as on the second pass trailing surface. This is because the rotation-induced secondary flows carry cooler fluid from the first pass trailing to leading and from the second pass leading to trailing, respectively, as discussed in the section "Effect of Wall Heating Condition." The present 60 deg rib data in the first pass trailing as well as in the second pass leading surface are higher than those of Johnson et al. 45 deg rib results. This is because, as previously discussed, the present taller and square-edged rib has more effect on the first pass thinner trailing wall boundary layer as well as on the second pass thinner leading wall boundary layer (due to rotation). However, the present 60 deg rib data in the second pass trailing surface are lower than the Johnson et al. 45 deg rib results. As discussed above, this is due to the difference in turn geometry and rib orientation between two studies.

Concluding Remarks

The influence of uneven wall temperature on the local heat transfer coefficients in a rotating two-pass square channel with in-line 60 deg angled ribs on leading and trailing walls has been observed for rotating numbers from 0.0 to 0.352 and Reynolds numbers from 2500 to 25,000. The findings are:

- 1 The trailing wall Nusselt number ratios for the first pass (Case A) are higher than the leading wall Nusselt number ratios, and increase with increasing rotation numbers. The leading wall Nusselt number ratios decrease with an increasing rotation number. The rotating ribbed wall heat transfer coefficients are two to three times higher than their corresponding rotating smooth wall values. The difference between the leading and trailing wall Nusselt number ratios increases with increasing rotation number. This is because the rotation creates a thinner boundary layer on the trailing wall and a thicker boundary layer on the leading wall.

- 2 The leading wall Nusselt number ratios in the second pass (Case A) are higher than the trailing wall Nusselt number ratios due to the reversing of the Coriolis force direction. The leading wall Nusselt number ratios increase and the trailing wall Nusselt number ratios decrease with increasing rotation number. Again, the rotating ribbed wall heat transfer coefficients are higher than their corresponding rotating smooth wall values. The difference between the leading and trailing wall Nusselt number ratios in the second pass is smaller than that in the first pass because the rota-

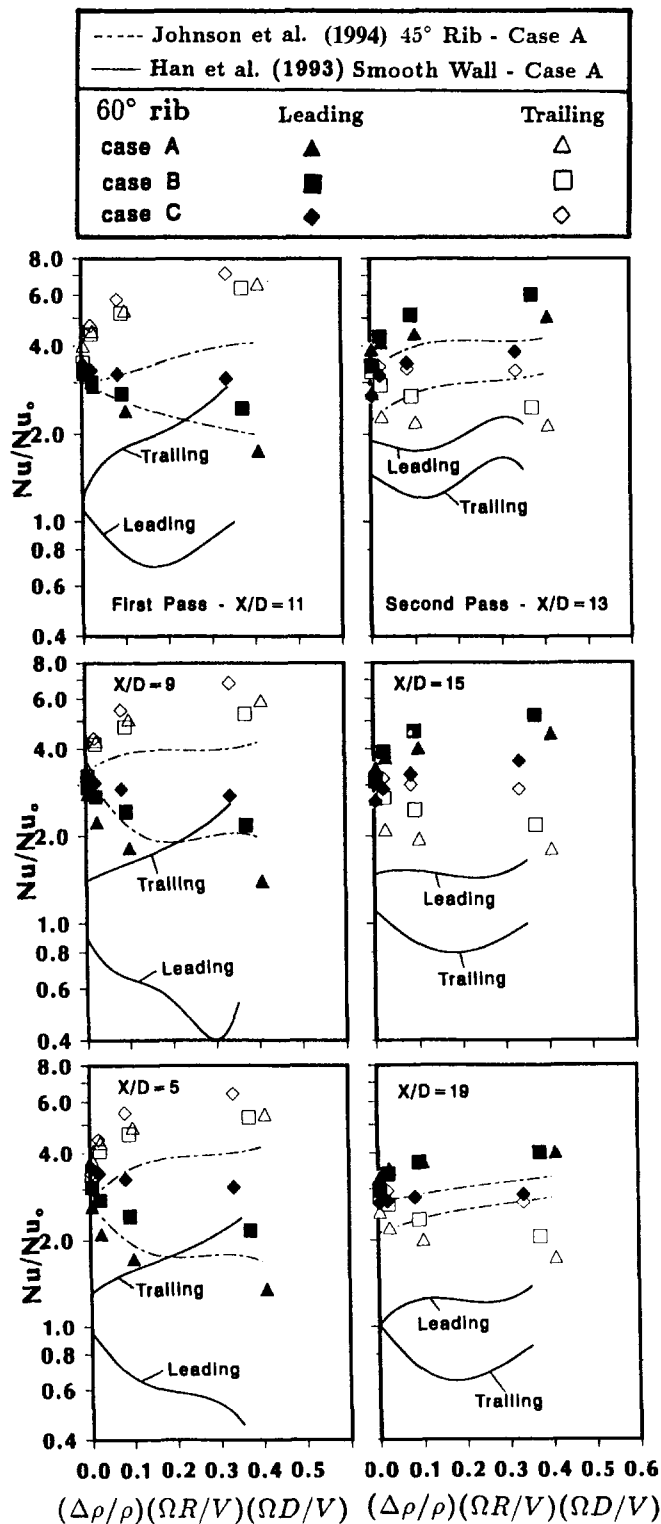


Fig. 10 Effect of buoyancy parameter on Nusselt number ratio at selected axial locations for Cases A, B, and C, and comparison with previous results

tion-induced buoyancy force opposes the inertia force in the second pass.

3 In the first pass, the Nusselt number ratios on the leading wall for Cases B and C are 70–100 percent higher than those for Case A. In the second pass, the Nusselt number ratios on the trailing wall for Cases B and C are 20–50 percent higher than those for Case A. This is because the rotation-induced secondary flows carry cooler fluid from

the trailing wall toward the leading wall (in the first pass), as well as from the leading and side walls toward the trailing wall (in the second pass).

4 The trends of the Nusselt number ratio versus the rotation number for both the present 60 deg ribs and Johnson et al. (1994) 45 deg ribs agree for Case A. In the first pass, the Nusselt number ratios on the leading thicker boundary layer wall for 60 deg ribs are about the same as the 45 deg rib values, while the Nusselt number ratios on the trailing thinner boundary layer wall for 60 deg ribs are higher than those for 45 deg ribs. However, due to different rib angles and turn geometry under rotation, the second pass Nusselt number ratios for 60 deg ribs are higher on the leading wall but lower on the trailing wall as compared to those for 45 deg ribs.

5 The channel-averaged Nusselt number ratios on the first pass trailing and second pass leading for all Cases (A, B, and C) increase with rotation number. However, the channel-averaged Nusselt number ratios on the first pass leading and second pass trailing decrease with rotation number. The channel-averaged Nusselt number ratios on the first pass and second pass smooth side walls increase from 2.0 to 3.0 over the range of rotation numbers studied.

Acknowledgments

This investigation was supported by General Electric Aircraft Engines, and by the Texas Higher Education Coordinating Board (Energy Research in Application Programs, TEES 70730).

References

- Clifford, R. J., Morris, W. D., and Harasgama, S. P., 1984, "An Experimental Study of Local and Mean Heat Transfer in a Triangular-Sectioned Duct Rotating the Orthogonal Mode," *ASME Journal of Engineering for Gas Turbines and Power*, Vol. 106, pp. 661–667.
- Guidez, J., 1989, "Study of the Convective Heat Transfer in Rotating Coolant Channels," *ASME JOURNAL OF TURBOMACHINERY*, Vol. 111, pp. 43–50.
- Han, J. C., 1984, "Heat Transfer and Friction in Channels With Two Opposite Rib-Roughened Walls," *ASME Journal of Heat Transfer*, Vol. 106, pp. 774–781.
- Han, J. C., 1988, "Heat Transfer and Friction Characteristics in Rectangular Channels With Rib Turbulators," *ASME Journal of Heat Transfer*, Vol. 110, pp. 321–328.
- Han, J. C., Zhang, Y. M., and Kalkuchler, K., 1993, "Uneven Wall Temperature Effect on Local Heat Transfer in a Rotating Two-Pass Square Channel With Smooth Walls," *ASME Journal of Heat Transfer*, Vol. 115, pp. 912–920.
- Han, J. C., Zhang, Y. M., and Lee, C. P., 1994, "Influence of Surface Heating Condition on Local Heat Transfer in a Rotating Square Channel With Smooth Walls and Radial Outward Flow," *ASME JOURNAL OF TURBOMACHINERY*, Vol. 116, pp. 149–158.
- Harasgama, S. P., and Morris, W. D., 1988, "The Influence of Rotation on the Heat Transfer Characteristics of Circular, Triangular, and Square-Sectioned Coolant Passages of Gas Turbine Rotor Blades," *ASME JOURNAL OF TURBOMACHINERY*, Vol. 110, pp. 44–50.
- Johnson, B. V., Wagner, J. H., Steuber, G. D., and Yeh, F. C., 1994, "Heat Transfer in Rotating Serpentine Passages With Trips Skewed to the Flow," *ASME JOURNAL OF TURBOMACHINERY*, Vol. 116, pp. 113–123.
- Kline, S. J., and McClintock, F. A., 1953, "Describing Uncertainties in Single-Sample Experiments," *Mechanical Engineering*, Jan., pp. 3–8.
- Mori, Y., Fukada, T., and Nakayama, W., 1971, "Convective Heat Transfer in a Rotating Radial Circular Pipe (2nd Report)," *International Journal of Heat and Mass Transfer*, Vol. 14, pp. 1807–1824.
- Morris, W. D., and Ghavami-Nasr, G., 1991, "Heat Transfer Measurements in Rectangular Channels With Orthogonal Mode Rotation," *ASME JOURNAL OF TURBOMACHINERY*, Vol. 113, pp. 339–345.
- Prakash, C., and Zerkle, R., 1992, "Prediction of Turbulent Flow and Heat Transfer in a Radially Rotating Square Duct," *ASME JOURNAL OF TURBOMACHINERY*, Vol. 114, pp. 835–846.
- Rohsenow, W. M., and Choi, H., 1961, *Heat, Mass and Momentum Transfer*, Prentice-Hall, Inc., New Jersey, pp. 192–193.
- Taslim, M. E., Rahman, A., and Spring, S. D., 1991a, "An Experimental Investigation of Heat Transfer Coefficients in a Spanwise Rotating Channel With Two Opposite Rib-Roughened Walls," *ASME JOURNAL OF TURBOMACHINERY*, Vol. 113, pp. 74–82.
- Taslim, M. E., Bondi, L. A., and Kercher, D. M., 1991b, "An Experi-

mental Investigation of Heat Transfer in an Orthogonally Rotating Channel Roughened With 45 Degree Criss-Cross Ribs on Two Opposite Walls," ASME JOURNAL OF TURBOMACHINERY, Vol. 113, pp. 346-353.

Wagner, J. H., Johnson, B. V., and Hajek, T. J., 1991a, "Heat Transfer in Rotating Passages With Smooth Walls and Radial Outward Flow," ASME JOURNAL OF TURBOMACHINERY, Vol. 113, pp. 42-51.

Wagner, J. H., Johnson, B. V., and Kopper, F. C., 1991b, "Heat Transfer in Rotating Serpentine Passages With Smooth Walls," ASME JOURNAL OF TURBOMACHINERY, Vol. 113, pp. 321-330.

Wagner, J. H., Johnson, B. V., Graziani, R. A., and Yeh, F. C., 1992, "Heat Transfer in Rotating Serpentine Passages With Trips Normal to the Flow," ASME JOURNAL OF TURBOMACHINERY, Vol. 114, pp. 847-857.

Experimental Study of the Effects of Bleed Holes on Heat Transfer and Pressure Drop in Trapezoidal Passages With Tapered Turbulators

M. E. Taslim

T. Li

Department of Mechanical Engineering,
Northeastern University,
Boston, MA 02115

S. D. Spring

General Electric—Aircraft Engines,
Lynn, MA 01910

Trailing edge cooling cavities in modern gas turbine blades often have trapezoidal cross-sectional areas of relatively low aspect ratio. To enhance cooling effectiveness in these passages, they are roughened with tapered turbulators. Furthermore, to provide additional cooling for the trailing edge, the cooling air may be ejected through trailing edge slots as it moves radially along the cooling passage. The tapered turbulators, in conjunction with the presence of these slots along the smaller base of the trapezoidal cavity, create both spanwise and longitudinal variations in heat transfer coefficient on the turbulated walls. Moreover, the continuous variation of cooling air velocity along these passages causes a continuous change in static pressure, which also requires investigation. Liquid crystals are used in this experimental investigation to study the effects of tapered turbulators on heat transfer coefficients in trailing edge passages with and without bleed holes. The tapered turbulators are configured on two opposite walls of the trapezoidal test section in a staggered arrangement with an angle of attack to the mainstream flow, α , of 90 deg. Nine different test geometries consisting of two passage aspect ratios, AR , were tested over a range of turbulator aspect ratios, AR_t , blockage ratios, e_{max}/D_h , pitch-to-height ratios, S/e_{max} , and Reynolds numbers. Channel pressure losses were also measured and both heat transfer and friction factor results for several geometries are compared. It is concluded that (a) there exists a large spanwise variation in heat transfer coefficient in test sections with no bleed holes, (b) adding bleed holes to the smaller base of the trapezoidal cavity gives a spanwise velocity component to the mainstream flow and reduces this variation, and (c) Nusselt numbers measured in the test sections with bleed holes correlate well with local Reynolds number.

Introduction

Various methods have been developed over the years to keep turbine blade temperatures below critical levels. The main objective in turbine blade cooling is usually to achieve maximum heat transfer coefficients while minimizing the coolant flow rate.

One such method is to route coolant air through turbulated serpentine passages within the airfoil and convectively remove heat from the blade. The coolant is then ejected either at the tip of the blade, through the cooling slots along the trailing edge, or through the cooling holes along the airfoil surface.

Geometric parameters such as passage aspect ratio (AR), turbulator height to passage hydraulic diameter or blockage ratio (e/D_h), turbulator angle of attack (α), the manner in which the turbulators are positioned relative to one another (in-line, staggered, criss-cross, etc.), turbulator pitch-to-height ratio (S/e) and turbulator shape (round versus sharp corners, fillets, turbulator aspect ratio (AR_t), and skewness toward the flow direction) have pronounced effects on both local and overall heat transfer coefficients. Some of these effects were studied by different investigators such as Burggraf (1970), Chandra (1988), Chandra and Han (1989), Han (1984), Han et al. (1978, 1985, 1992), Metzger et al. (1983, 1990), Taslim and Spring (1978a, b), Taslim et al (1991b, c), Webb et al. (1971), and Zhang et al. (1993). The available data in open literature, however, is mostly for circular, square, or rectangular channels roughened with ribs of uniform cross-sectional area.

Contributed by the International Gas Turbine Institute and presented at the 38th International Gas Turbine and Aeroengine Congress and Exposition, Cincinnati, Ohio, May 24–27, 1993. Manuscript received at ASME Headquarters March 3, 1993. Paper No. 93-GT-212. Associate Technical Editor: H. Lukas.

As dictated by the external shape of blade trailing edges, trailing edge cooling cavities often have very narrow trapezoidal shapes with characteristically small passage aspect ratios. Furthermore, the narrow trapezoidal shape often necessitates that when turbulators are used, their heights must taper in the direction of the small trapezoid base. Moreover, the cooling air is often ejected through a series of holes or slots along the blade trailing edge and/or a few tip holes at the blade tip. This complex geometry creates a complex flow field. Both longitudinal and spanwise variations in air velocity and heat transfer coefficient are expected. Experimental as well as theoretical work in this area encompassing all those above-mentioned effects is rare if not nonexistent. Abuaf et al. (1986) reported the results of an experimental investigation of the pressure drop and heat transfer coefficient distributions in serpentine passages with and without turbulence promoters. They investigated a three-legged passage with slanted bleed holes along the third leg. Air entered the test section at three inlet ports along the first leg and liquid crystals along with thin foil heaters were used to measure the heat transfer coefficient. Tests were run with and without wooden ribs mounted on the liquid crystals at an angle 90 deg with the flow direction. Lau et al. (1989a, b) reported on turbulent heat transfer and friction in pin fin channels with lateral flow ejection. Kumaran et al. (1991) reported on augmented heat transfer in a pin fin channel with short or long ejection holes. None of these cases, however, resembles the geometries or the flow pattern tested in the present work. The main objective in this investigation was to measure the friction factors and heat transfer coefficients in trapezoidal test sections roughened with tapered turbulators of different geometry as well as with and without trailing edge bleed.

Test Sections

Figure 1 shows schematically the layout and cross-sectional area of a typical test section, while turbulator geometry details are shown in Fig. 2. Table 1 contains the specifications of all nine staggered rib geometries tested in this investigation. A liquid crystal technique was employed to measure the heat transfer coefficients in these test sections

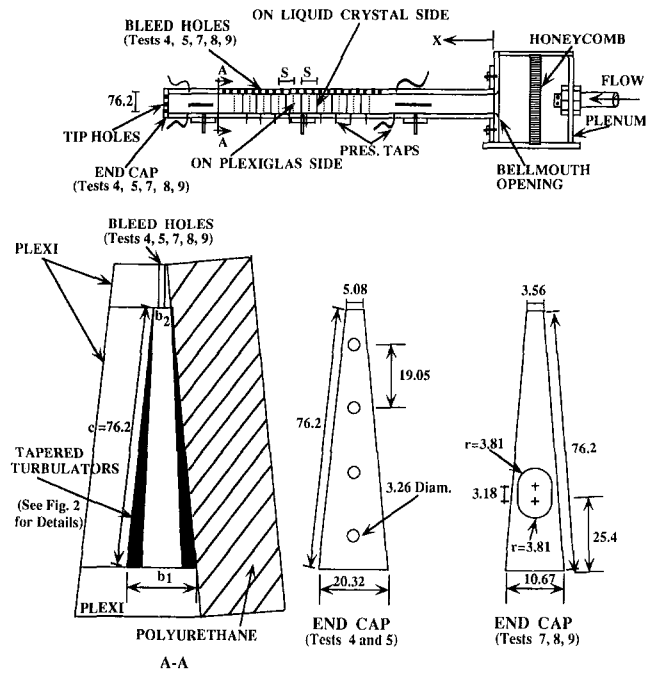


Fig. 1 Schematic diagram of test sections (dimensions in mm; not to scale)

(see Moffat, 1990). In this technique, the most temperature-sensitive color displayed by the liquid crystals is chosen as the reference color corresponding to a known temperature. By proper adjustment of the Ohmic power to a very thin foil heater immediately underneath the liquid crystals, the reference color is moved from one location to another such that the entire area of interest is eventually covered with the reference color at one time or another. This process results in a series of photographs, each corresponding to a certain location of the reference color. Among the advantages of liquid crystal thermography is to depict the flow "footprints" and local values of heat transfer coefficient on the surface

Nomenclature

AR = passage aspect ratio = $(b_1 + b_2)/2c$
 AR_t = turbulator aspect ratio (height/width)
 b_1 = wide base of trapezoidal cross section (see Fig. 1)
 b_2 = narrow base of the trapezoidal cross section (see Fig. 1)
 c = side of the trapezoidal cross section (turbulated side, 7.62 cm for all cases)
 d = bleed hole diameter
 D_h = hydraulic diameter based on nonturbulated cross section
 e_{max} = maximum height of the tapered turbulator
 \bar{f} = Darcy friction factor = $\Delta P(D_h/L)/(1/2)\rho U_m^2$
 \bar{h} = average heat transfer coefficient on an area between a pair of turbulators

k = air thermal conductivity
 L = length of the turbulated portion of the test section
 \dot{m} = air mass flow rate
 \bar{Nu} = average Nusselt number on an area between a pair of turbulators = $\bar{h}D_h/k$
 Nu_s = Nusselt number in a smooth passage (based on D_h)
 P = unturbulated passage perimeter
 P_d = static pressure in the duct at the bleed hole location
 P_j = jet static pressure (lab pressure)
 P_t = total pressure at the bleed hole location
 Pr = Prandtl number
 Re = Reynolds number (based on D_h)

Re_{local} = local Reynolds number = $4\dot{m}_{local}/P\mu$
 S = turbulator pitch (center-to-center)
 t = bleed hole length (wall thickness)
 T_f = film temperature = $0.5(T_s + T_m)$
 T_m = air mixed mean temperature
 T_s = surface temperature
 U_m = air mean velocity
 w = turbulator width
 X = distance between camera and test section entrance
 α = angle of attack (= 90 deg for all cases)
 ΔP = pressure drop across the turbulated portion of the test section
 μ = air dynamic viscosity
 ρ = air density

under investigation. This simultaneous “flow visualization” enhances the understanding of the underlying physics and helps the investigator in interpretation of the results. Furthermore, unexpected asymmetries in flow are revealed as well as the slightest heat and flow leaks, nonuniformities in surface heat flux, imperfections associated with the attachment of the heater to the test section surface, and nonuniformities in wall material thermal conductivity.

All test sections, with a length varied from 96.5 to 116.8 cm, had symmetric trapezoidal cross-sectional areas. Three walls of these channels, namely the two bases and one side wall, were made of 1.27-cm-thick clear acrylic. The fourth wall, on which the heaters and liquid crystal sheets were attached and all measurements were taken, was made of a 5-cm-thick machinable polyurethane slab. This wall, for all cases tested, had a fixed width of 7.62 cm. Thus, any varia-

tion of test section aspect ratio was accomplished by varying the size of the two bases. For those geometries with bleed holes (the holes were drilled on the smaller base of the trapezoid), the test section was capped at the exit and holes were drilled on the end wall to simulate the tip holes in a blade. Turbulators were also machined out of acrylic and glued onto two opposite walls in a staggered arrangement. All turbulators had rounded edges as shown in Fig. 2.

The entrance region of all test sections was left unturbulated to simulate the cooling passage in the dovetail region of an airfoil. Heat transfer measurements were performed for an area between a pair of turbulators in the middle of the turbulated zone for the test sections with no bleed holes and at two locations, close to the beginning and end of turbulated zone, for those test sections with the bleed holes. The corresponding X/D_h at the test location is given for each geometry in the results section.

Three or four, depending on the length of the test section, 7.62 cm × 27.94 cm custom-made etched-foil heaters with a thickness of 0.15 mm were placed on the polyurethane wall where measurements were taken using a special double-stick 0.05-mm-thick tape with minimal temperature deformation characteristics. The heaters covered the entire test section length including the nonturbulated entry length. However, they did not extend over the actual turbulator surface nor on the acrylic sidewalls. Thus the reported heat transfer coefficients are the averages over the wall surface area between a pair of turbulators. The heat transfer coefficients on the turbulator surfaces are reported by investigators such as Metzger et al. (1988) and Taslim et al. (1994). It is noted that an experimental investigation by El-Husayni et al. (1994) on heat transfer in a turbulated channel with one, two, and four heated walls showed that, in a stationary turbulated channel, the heat transfer coefficient is not sensitive to the number of heated walls. The 0.127-mm-thick liquid crystal sheet was then placed on the heaters. Static pressure taps were mounted on all three acrylic walls of each test section to measure the pressure drop across the turbulated portion of the test section. The reported friction factor is the overall passage average, \bar{f} , and not just the turbulated surfaces.

The test sections were covered on all sides, except for a small window at the location where the pictures were taken, by 5-cm-thick styrofoam sheets to minimize heat losses to the environment. The radiational heat loss from the heated wall to the unheated walls as well as losses to ambient air was taken into consideration when heat transfer coefficients were calculated.

A 35-mm programmable camera, in conjunction with proper filters and background lighting to simulate daylight conditions, was used to take photographs of isochrome patterns formed on the liquid crystal sheet. Surface heat flux in the test section was generated by the heaters through a custom-designed power supply unit. Each heater was individually controlled by a variable transformer.

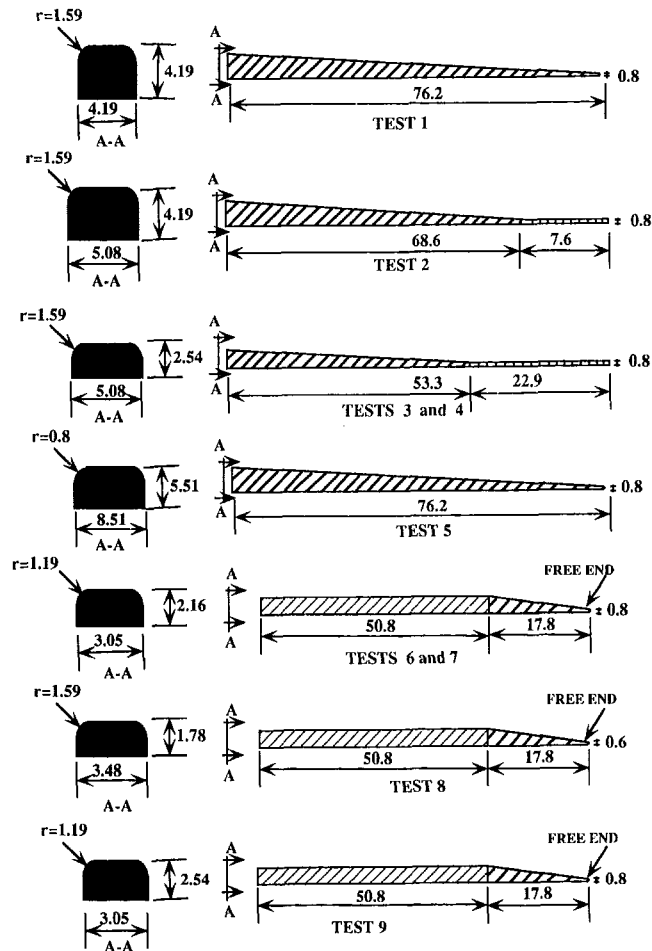


Fig. 2 Turbulator geometries (dimensions in mm; not to scale)

Table 1 Specifications

TEST	e_{max} (mm)	w (mm)	S/e_{max}	e_{max}/D_h	AR	α	Remarks
1	4.19	4.19	6.67	0.139	0.167	90° St	Tapered, No Bleed
2	4.19	5.08	6.67	0.139	0.167	90° St	Tapered, No Bleed
3	2.54	5.08	11.00	0.117	0.167	90° St	Tapered, No Bleed
4	2.54	5.08	11.00	0.117	0.167	90° St	Tapered, Bleed Holes
5	5.51	8.51	7.28	0.254	0.167	90° St	Tapered, Bleed Holes
6	2.16	3.05	8.51	0.164	0.093	90° St	Tapered end, No Bleed
7	2.16	3.05	8.51	0.164	0.093	90° St	Tapered end, Bleed Holes
8	1.78	3.48	10.36	0.137	0.093	90° St	Tapered end, Bleed Holes
9	2.54	3.05	7.22	0.193	0.093	90° St	Tapered end, Bleed Holes

Procedure

Before testing, the liquid crystal sheets were calibrated as follows: A water bath was used to attain uniform isochromes on a small piece of the liquid crystal sheet used throughout this investigation. The temperature corresponding to each color was measured using a precision thermocouple and photographs were taken at laboratory conditions simultaneously so as to simulate closely the actual testing environment. A reference color along with its measured temperature of 36.9°C was then chosen to be used throughout the experiments. It should be noted that all possible shades of the selected reference color did not show a temperature difference more than 0.3°C.

An accurate account for the air mass flow rate through each individual bleed hole was a major task in this investigation. First, discharge coefficient for each hole had to be determined. Exhaustive literature survey and measurements were performed to assure an accurate treatment of the discharge coefficient. Among several references including Kreith (1984), the NASA report by Rohde et al. (1969) and experimental results by Hay et al. (1983) represented the closest geometry to the present investigation where the approach flow was perpendicular to the bleed hole axis and bleed hole corners were sharp. Furthermore, the hole t/d , the approach flow Mach number, and the "velocity head ratio," defined as

$$\frac{(P_t - P_d)}{(P_t - P_j)}$$

for the present geometry were within the range of those reported by the above-mentioned investigators. The velocity head ratio in the present tests varied from 25 to 200 while the approach flow Mach number changed from 0.02 to 0.114. Therefore, using the Rohde et al. data, the discharge coefficient varied from 0.78 to 0.84, representing an approximately 7.5 percent variation. Calculating the discharge coefficient for individual holes and measuring the static pressure variation along the flow direction, the mass flow rate through each individual hole was determined. This method is basically similar to that used by other investigators such as Kumaran et al. (1991), without assuming a constant discharge coefficient for all bleed holes. The sum of mass flow rates through all bleed holes for each case was checked against the total mass flow rate entering the test section and the agreement was always within ± 5 percent. A contact micromanometer with an accuracy of 0.025 mm of water column measured the pressure differences between the static pressure taps along the sidewall opposite to that with the bleed holes. The static pressure at each location was assumed to be the same for the entire cross section at that location. This was based on the readings of the two sets of three pressure taps mounted on three walls of the test section before and after the bleed hole portion (see Fig. 1). A critical venturimeter, with choked flow for all cases tested, measured the total mass flow rate entering the test section. This device is widely accepted as one of the most accurate flow measuring devices. With the known surface heat flux along the test section and the air temperature at the test section inlet, through a successive application of the energy balance starting from the test section inlet and the first bleed hole to the end of the test section, the variation of the air mixed mean temperature along the test section was calculated taking into account the small heat losses through the test section walls to the ambient air.

For a typical test run, the Reynolds number was set by precisely fixing the mass flow rate. The heat flux was induced by turning on the main power supply and adjusting heater power until the first band of reference color was observed on the liquid crystal sheet in the area of interest. Each heater

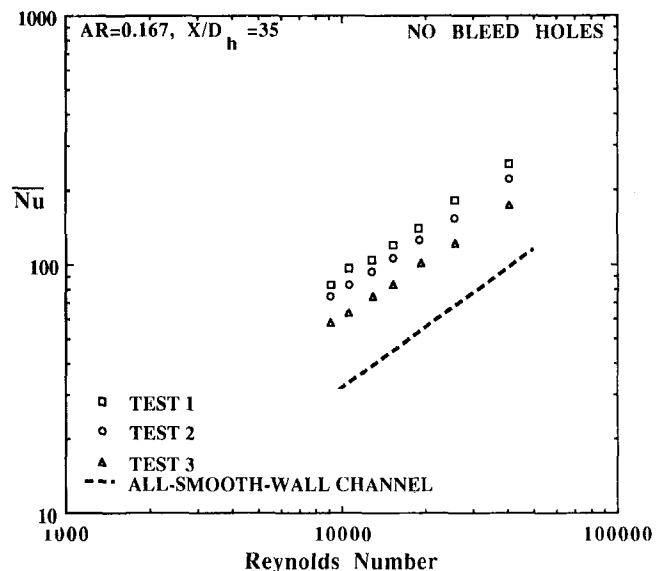


Fig. 3 Surface average Nusselt versus Reynolds number for tests 1, 2, and 3 (no bleed)

was adjusted individually such that uniform heat flux was accomplished over the entire tested surface. Enough time was given so that the system came to thermal equilibrium, at which time a photograph was taken and data recorded. The power to the heaters was then increased such that the reference color was moved to a location next to the previous one and another picture was taken. This procedure was continued until eventually the entire surface between a pair of turbulators was covered by the reference color at one time or another. The process was repeated for all Reynolds numbers. Each photograph was digitized in order to measure the area covered by the reference color. This was done by using a magnetic tablet and a commercial software package installed on an IBM-PC-AT. Once the areas were measured, an area-weighted average heat transfer coefficient was calculated.

For verification of the liquid crystal technique accuracy, an all-smooth-wall channel was tested with heaters on one wall. The results, which were within ± 5 percent of the well-known Dittus-Boelter (1930) correlation, are reported in Taslim (1990). Furthermore, these authors' previous results (Taslim et al., 1991c) of turbulated channels of various geometries using the same technique compared favorably with those of Metzger et al. (1990).

Maximum experimental uncertainties, following the method of Kline and McClintock (1953), were determined to be ± 7 and ± 8 percent for the heat transfer coefficient and friction factor, respectively.

Results and Discussion

The all-smooth-wall channel Nusselt versus Reynolds number curve, shown in Fig. 3, and other heat transfer results to be presented in the following paragraphs, are from the well-known Dittus-Boelter (1930) correlation given by $Nu_s = 0.023Re^{0.8}Pr^{0.4}$. With this correlation, the enhancement in turbulated heat transfer coefficients versus smooth wall can be readily evaluated. Air properties for Nusselt and Reynolds number calculations are based on the local film temperature, T_f , for all cases.

Results of the first three tests, which were performed with no bleed holes, are shown in Figs. 3 and 4. As is shown in the table of specifications, while the passage geometry remained unchanged, three different tapered turbulator geometries were tested. The variation in turbulator geometry represents real effects that can exist in airfoils due to casting tolerance

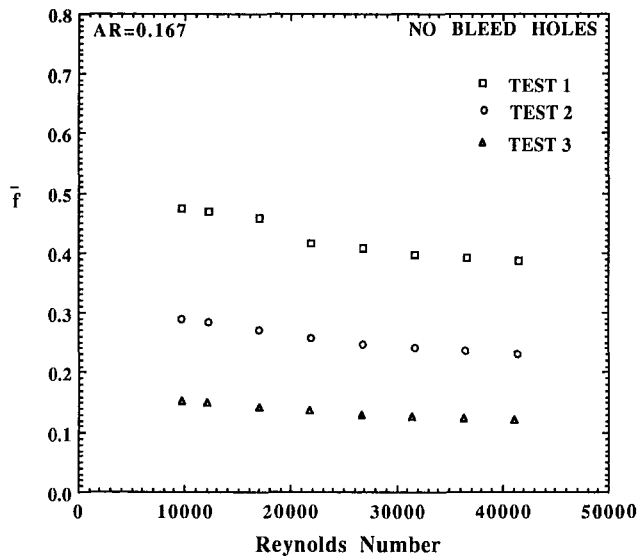


Fig. 4 Channel average friction factor versus Reynolds number for tests 1, 2, and 3 (no bleed)

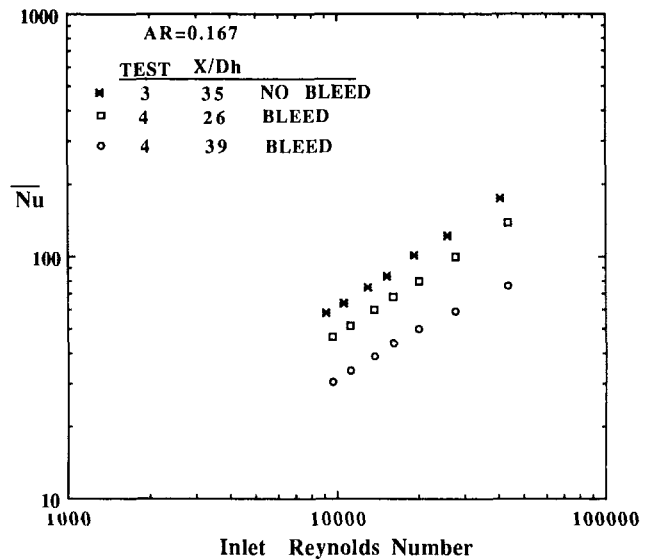


Fig. 6 Surface average Nusselt versus inlet Reynolds number for tests 3 (no bleed) and 4 (bleed)

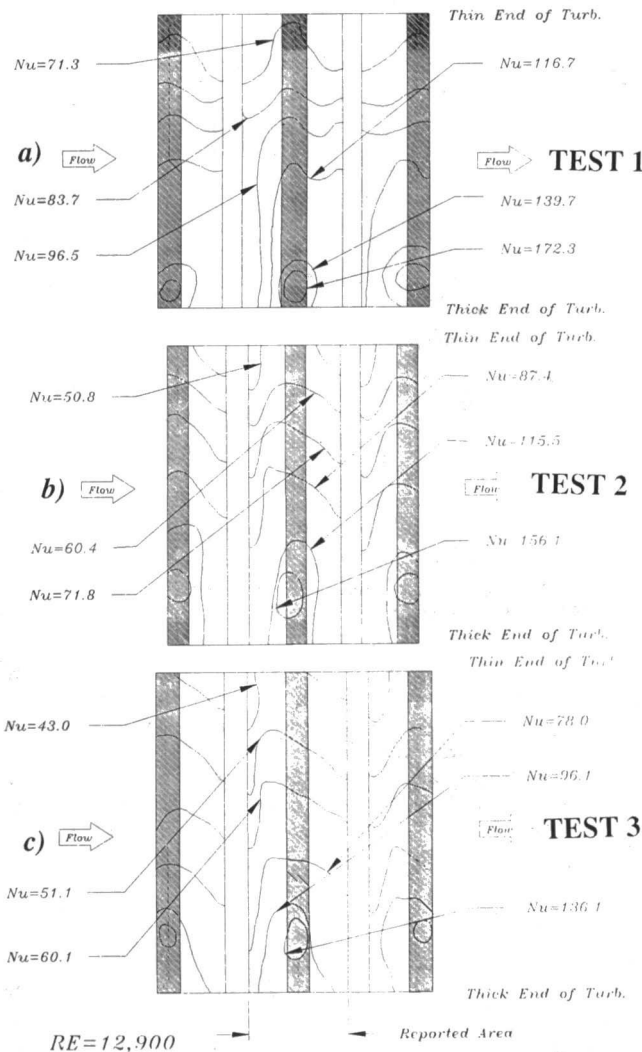


Fig. 5 Local iso-Nu contours for tests 1, 2, and 3 with no bleed

variations. Several observations can be made about the surface average values in Fig. 3. Although the turbulators in tests 1 and 2 had the same maximum height, test 2 showed a decrease in both the heat transfer enhancement and friction

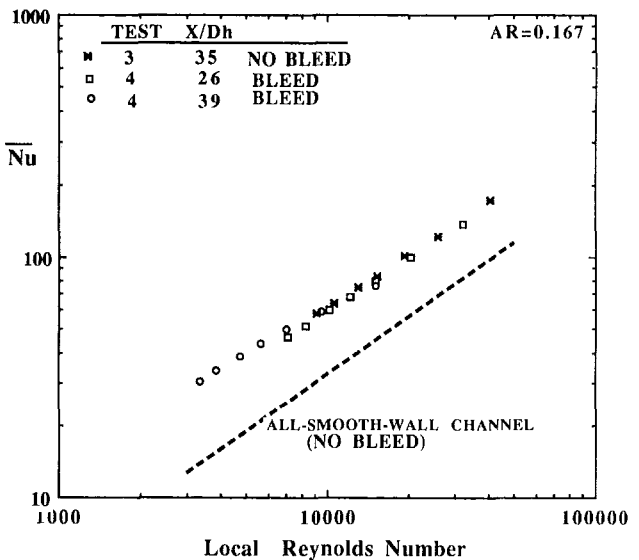


Fig. 7 Surface average Nusselt versus local Reynolds number for test 3 (no bleed) and test 4 (bleed)

factor due to its lower turbulator aspect ratio and decreased overall average blockage ratio. This is consistent with previous work on the effects of turbulator aspect ratio on heat transfer and pressure drop (Taslim and Spring, 1991a, b). Furthermore, the results indicate that the effects of pertinent geometric parameters on heat transfer and pressure drop, demonstrated in rectangular passages with nontapering turbulator geometries, are the same for trapezoidal passages with tapered turbulators when evaluated on a surface average basis.

Some representative iso-Nu contours (contours of constant Nusselt number) for tests 1, 2, and 3 are shown in Fig. 5. Here a remarkable variation in heat transfer coefficient in the spanwise direction is revealed and local values can be seen to vary 20–80 percent from the average. Several factors contribute to this variation. First, some level of spanwise variation in air axial velocity is expected since most of the air passes through the wider end of the trapezoidal cross section. Second, local turbulator blockage and aspect ratios (e/D_h , AR_t), decrease and turbulator pitch-to-height ratio (S/e) increases in the spanwise direction; the trends of these varia-

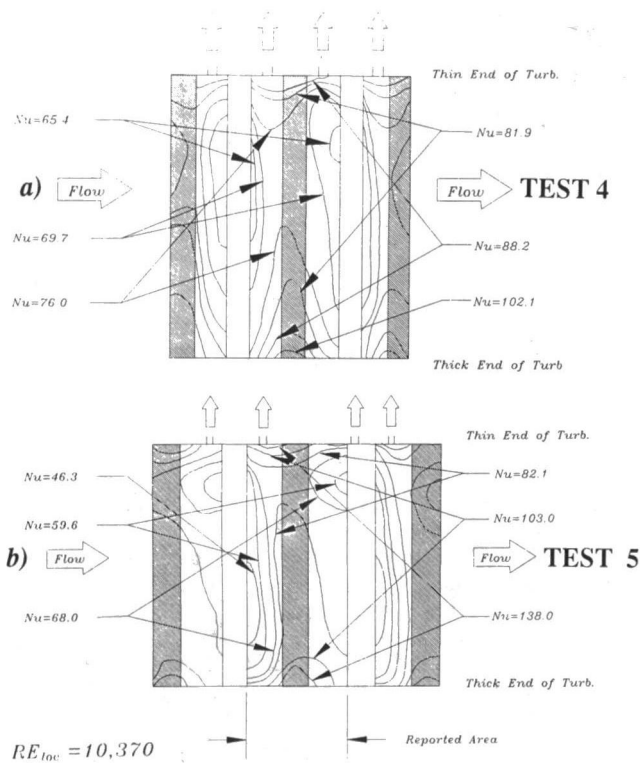


Fig. 8 Local iso-Nu contours for tests 4 and 5

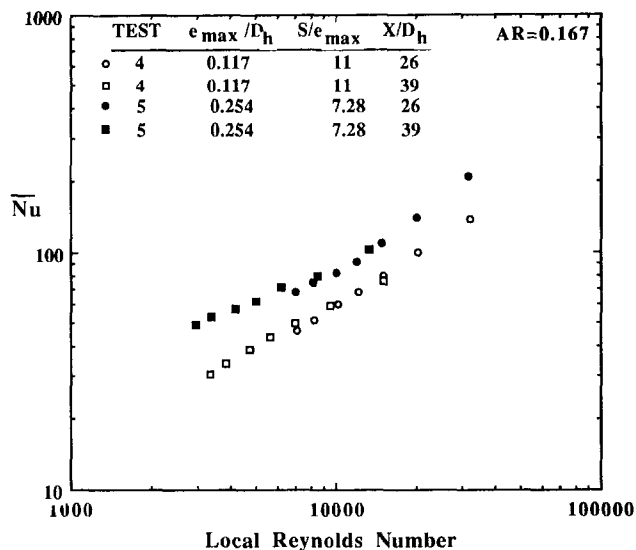


Fig. 9 Surface average Nusselt versus local Reynolds number for tests 4 and 5 (with bleed)

tions are known (Taslam and Spring, 1991a, b) to have deteriorating effects on the heat transfer coefficient. Hence the passage geometry itself sets up a bias, which is added to that of the tapering turbulator geometry. Spanwise variations in heat transfer coefficient have significant effects on design applications when the trailing edge cooling cavity corresponds to a significant portion of the blade surface area.

To investigate the effects of bleed holes on the heat transfer performance and pressure drop, 24 holes of 2.8 mm diameter were drilled along the narrow base of test section 3. At the same time, the exit end was capped and four holes of 3.26 mm diameter were drilled in the end cap. Heat transfer coefficients for a range of Reynolds numbers at two different axial locations, corresponding to $X/D_h = 26$ and 38.8, are presented in Fig. 6. To make a direct comparison, the results of test 3 (identical passage and turbulator geometries but no

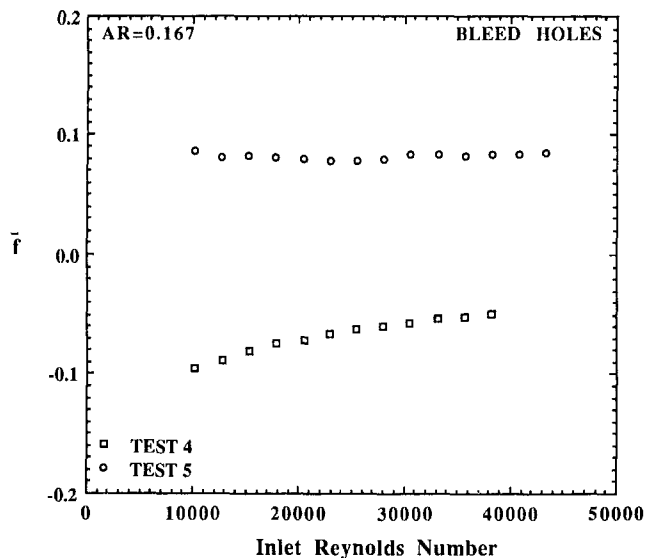


Fig. 10 Channel average friction factor versus inlet Reynolds number for tests 4 and 5 (with bleed)

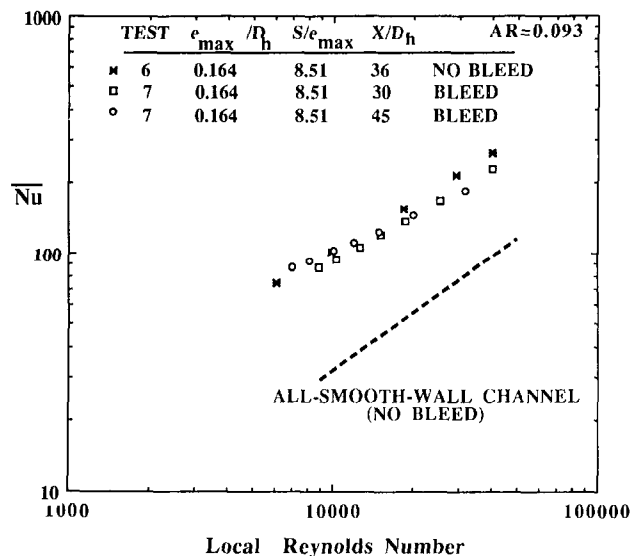


Fig. 11 Surface average Nusselt versus local Reynolds number for test 6 (no bleed) and test 7 (bleed)

bleed holes) are presented on the same figure. The decrease in the heat transfer coefficient along the test section is obviously due to the continuous loss of flow through the side holes. Note that the comparison is based on the inlet Reynolds number. The same average Nusselt numbers are presented in Fig. 7 in terms of local Reynolds number (Re_{local}). It is noted that Nusselt numbers measured at two locations on the turbulated wall correlate very well with local Reynolds number. Representative iso-Nu contours for this case are shown in Fig. 8(a). A comparison between Figs. 5(c) and 8(a) shows that the spanwise variation in heat transfer coefficient for the case with bleed holes is not as large as that with no bleed holes. This is due to the spanwise velocity component of the air. It should be noted that while the spanwise variation is changing, the average values for identical local Reynolds numbers remain relatively constant.

For test 5 with trailing edge bleed holes, the passage geometry remained identical to that of test 4 but larger turbulators with a more optimum spacing were used. Results of tests 4 and 5 are shown in Fig. 9. Again, it is observed that the Nusselt number correlates well with the local Reynolds number for both X/D_h locations of test 5. Again, the turbula-

tors with higher blockage ratio and more optimum spacing produced higher heat transfer coefficients. The friction factor results versus inlet Reynolds number are presented in Fig. 10. The negative f presented for test 4 is merely to show the increase in static pressure along the test section as the average velocity decreases due to the loss of air through the

bleed holes. Test section 5 produced a drop in static pressure due to high blockage turbulators inspite of bleed holes.

In this study, the first five tests involved changing turbulator and bleed geometries, all at a constant passage geometry. As is known, turbine blade trailing edge cooling cavities often have aspect ratios less than 0.1. The last four tests were

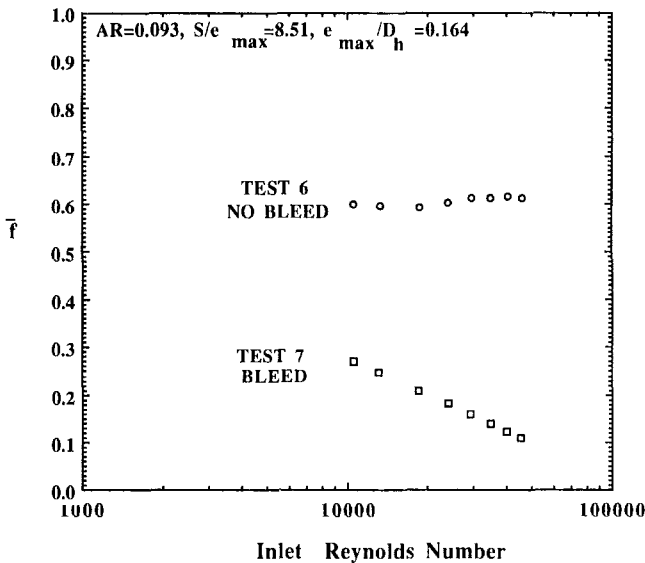


Fig. 12 Channel average friction factor versus inlet Reynolds number for test 6 (no bleed) and test 7 (bleed)

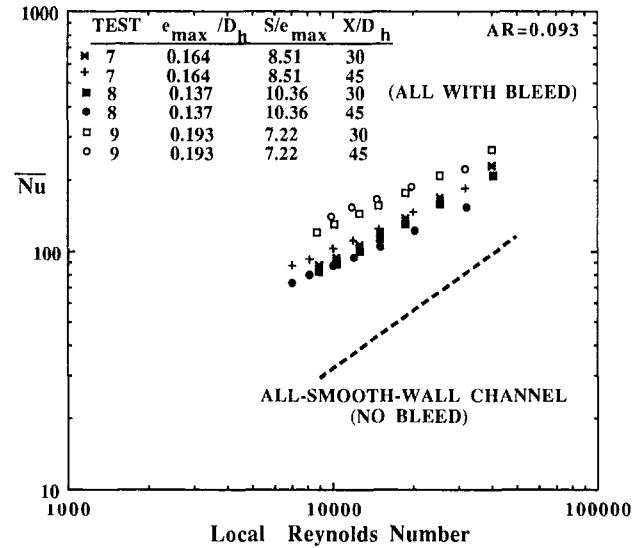


Fig. 13 Surface average Nusselt versus local Reynolds number for tests 7, 8, and 9 (with bleed)

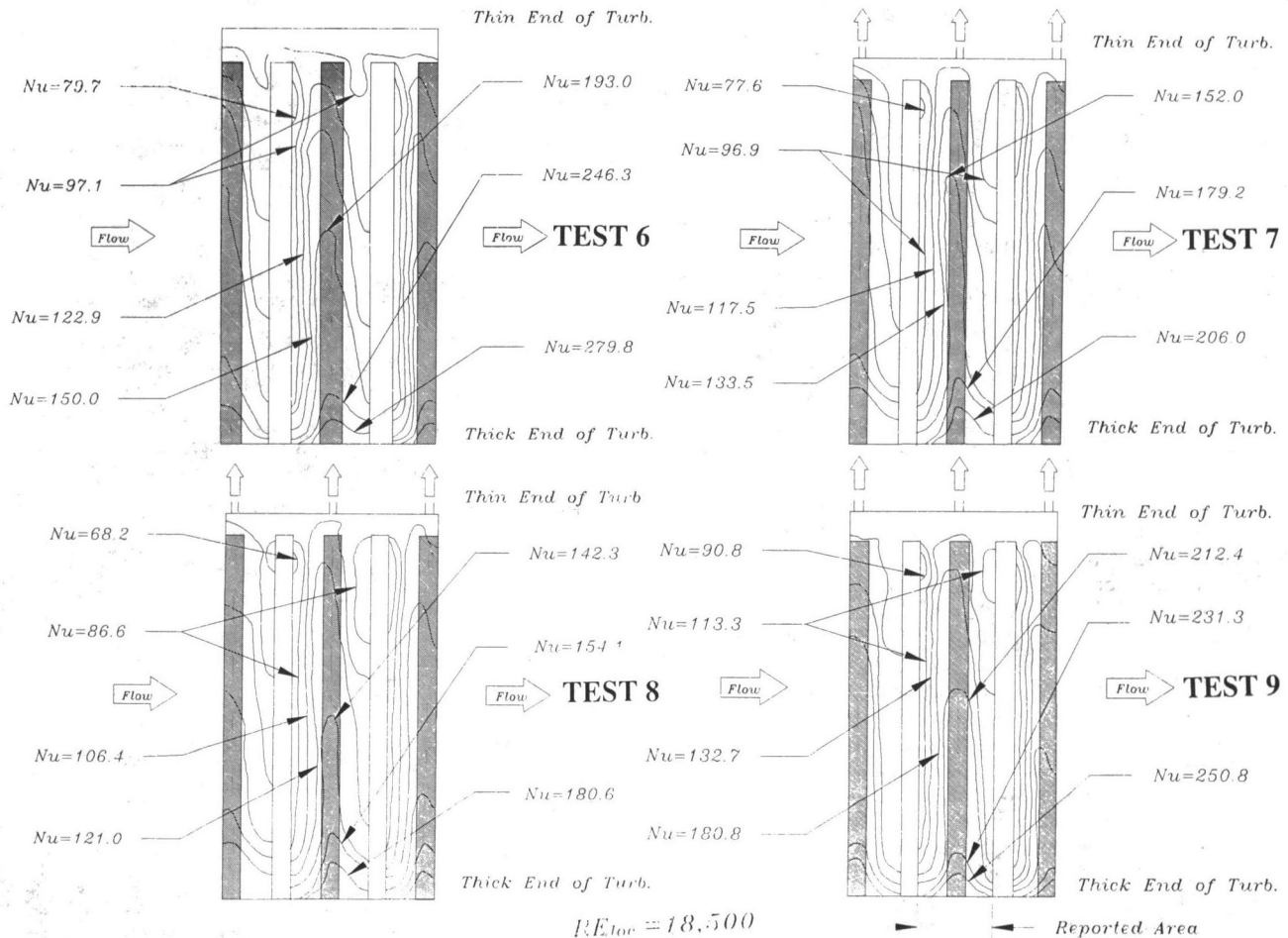


Fig. 14 Local iso-Nu contours for tests 6 (no bleed), and 7, 8, and 9 (with bleed) at $Re_{local} = 18,500$

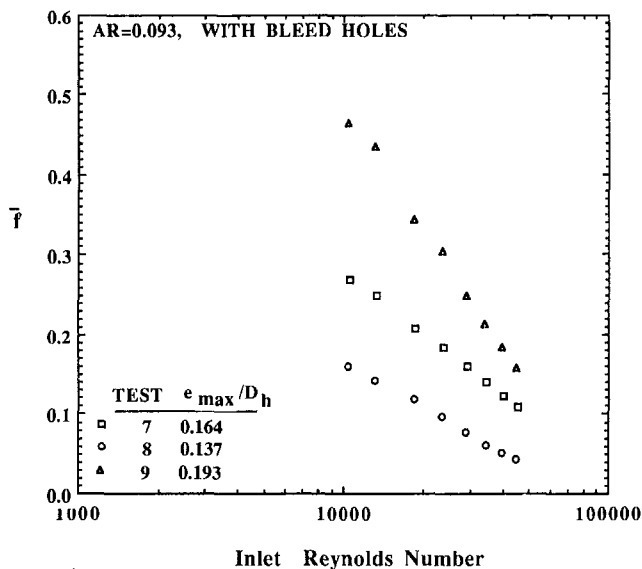


Fig. 15 Channel average friction factor versus inlet Reynolds number for tests 7, 8, and 9 (with bleed)

performed in a test section where the aspect ratio was decreased to 0.093. Here, three different turbulator geometries were tested in a constant passage geometry to show the effects on heat transfer coefficient for simulated real casting tolerances with and without trailing edge bleed. Details of the turbulator geometries are given in Fig. 2. These turbulators, which were only 6.86 cm long, covered 90 percent of the test section in the spanwise direction, initiating from the wide base of the trapezoid and terminating at 0.762 cm from the narrow base. Furthermore, only a length of 1.778 cm at the end of turbulators was tapered. Test section 6 was tested with no bleed holes. The geometry of test section 7 was identical to that of test section 6 except for 25 equally spaced holes with a diameter of 1.59 mm drilled along the narrow base of the trapezoid in the turbulated section and installation of an end cap with a tip hole, shown in Fig. 1. Results of heat transfer and pressure drop are shown in Figs. 11 and 12. Once again, the Nusselt numbers at two X/D_h locations for test 7 with bleed holes correlate well with the local Reynolds number. This trend is similar to that for tests 3 and 4 presented in Fig. 7. All discussions on tests 3 and 4 pertain to these two tests as well. Geometries 6 and 7 produce higher heat transfer coefficients due to a combination of higher blockage ratio, more optimum spacing, and lower passage aspect ratio. Again the trend is consistent with previous trends of these three parameters, which are known to enhance heat transfer in rectangular test sections. Friction factor results for tests 6 and 7 are shown in Fig. 12. As was the case with test 5, the pressure drop caused by high blockage turbulators was more than the static pressure rise along the test section due to bleed holes.

Results for tests 7, 8, and 9 are shown in Figs. 13–15. The test section geometry was the same for all three tests. Only turbulator geometry was changed. Figure 13 shows that the Nusselt numbers for all geometries correlate well with the local Reynolds number and that enhancement in heat transfer increases as turbulator blockage increases and spacing is made more optimum. The trend of friction factor variation in Fig. 15 is consistent with that of Nusselt number. Finally, iso-Nu lines for these four tests, presented in Fig. 14, indicate that once again the spanwise variation in heat transfer coefficient for the test sections with bleed holes is not as large as that with no bleed holes. In addition, a region of relatively high heat transfer coefficient is observed downstream of the turbulator free end (see Fig. 2). Vortices shed from the free

end of the turbulators are believed to contribute to this phenomenon.

Conclusions

Two low-aspect-ratio trapezoidal test section geometries, simulating the trailing edge cooling cavities of turbine blades, roughened with seven different turbulator geometries, were tested for heat transfer and pressure variations. The test sections were tested both with and without bleed holes. From this study, it is concluded that for trapezoidal test sections with tapered turbulators:

1 The effects of pertinent geometric parameters (e/D_h , S/e , AR , etc.) on heat transfer behavior is consistent with previously reported results obtained from circular or rectangular test sections when surface average values are compared.

2 There exists a large spanwise variation in heat transfer coefficient in test sections without bleed holes since a major portion of the flow passes through the wider end of the cross section and interacts with the high blockage end of the turbulators. For the geometries tested, a variation of -40 to $+80$ percent with respect to the area-weighted average was measured.

3 Bleed holes on the trailing edge side of the cavity give a spanwise velocity component to the main flow and consequently cause a more uniform distribution of spanwise heat transfer coefficient. For the geometries tested, the variation in local heat transfer coefficient given in part 2 for no bleed case, reduced to -10 to $+41$ percent for the cases with bleed holes.

4 Nusselt numbers measured at two locations along the test sections with bleed holes correlate well with the local Reynolds number.

Acknowledgments

The authors wish to express gratitude to R. E. Gladden, J. M. Hill, and M. Suo for their support during this investigation.

References

- Abuaf, N., Gibbs, R., and Baum, R., 1986, "Pressure Drop and Heat Transfer Coefficient Distributions in Serpentine Passages With and Without Turbulence Promoters," *The Eighth International Heat Transfer Conference*, C. L. Tien, V. P. Carey and J. K. Ferrel, eds., pp. 2837–2845.
- Burggraf, F., 1970, "Experimental Heat Transfer and Pressure Drop With Two Dimensional Turbulence Promoters Applied to Two Opposite Walls of a Square Tube," *Augmentation of Convective Heat and Mass Transfer*, A. E. Bergles and R. L. Webb, eds., ASME, pp. 70–79.
- Chandra, P. R., 1988, "Effect of Rib Angle on Local Heat/Mass Transfer Distribution in a Two Pass Rib-Roughened Channel," *ASME JOURNAL OF TURBOMACHINERY*, Vol. 110, pp. 233–241.
- Chandra, P. R., and Han, J. C., 1989, "Pressure Drop and Mass Transfer in Two-Pass Ribbed Channels," *AIAA J. Thermophysics*, Vol. 3, No. 3, pp. 315–319.
- Dittus, F. W., and Boelter, L. M. K., 1930, "Publications in Engineering," Vol. 2, University of California, Berkeley, CA, p. 443.
- El-Husayni, H., Taslim, M. E., and Kercher, D. M., 1994, "Experimental Heat Transfer Investigation of Stationary and Orthogonally Rotating Asymmetric and Symmetric Heated Smooth and Turbulated Channels," *ASME JOURNAL OF TURBOMACHINERY*, Vol. 116, pp. 124–132.
- Han, J. C., Glicksman, L. R., and Rohsenow, W. M., 1978, "An Investigation of Heat Transfer and Friction for Rib Roughened Surfaces," *Int. J. Heat Mass Transfer*, Vol. 12, pp. 1143–1156.
- Han, J. C., 1984, "Heat Transfer and Friction in Channels With Two Opposite Rib-Roughened Walls," *ASME Journal of Heat Transfer*, Vol. 106, No. 4, pp. 774–781.
- Han, J. C., Park, J. S., and Lei, C. K., 1985, "Heat Transfer Enhancement in Channels With Turbulence Promoters," *ASME Journal of Engineering for Gas Turbines and Power*, Vol. 107, pp. 628–635.
- Han, J. C., Zhang, Y. M., and Lee, C. P., 1992, "Influence of Surface Heat Flux Ratio on Heat Transfer Augmentation in Square Channels With Parallel, Crossed, and V-Shaped Angled Ribs," *ASME JOURNAL OF TURBOMACHINERY*, Vol. 114, pp. 872–880.

- Hay, N., Lampard, D., and Benmansour, S., 1983, "Effects of Cross-flows on the Discharge Coefficient of Film Cooling Holes," *ASME Journal of Engineering for Power*, Vol. 105, pp. 243-248.
- Kline, S. J., and McClintock, F. A., 1953, "Describing Uncertainty in Single-Sample Experiments," *Mechanical Engineering*, Vol. 75, Jan., pp. 3-8.
- Kreith, F., ed., 1984, *Fluid Flow, Data Book*, Genium Publishing Corp., Section 406.1.
- Kumaran, T. K., Han, J. C., and Lau, S. C., 1991, "Augmented Heat Transfer in a Pin Fin Channel With Short or Long Ejection Holes," *Int. J. Heat Mass Transfer*, Vol. 34, No. 10, pp. 2617-2628.
- Lau, S. C., Han, J. C., and Kim, Y. S., 1989a, "Turbulent Heat Transfer and Friction in Pin Fin Channels With Lateral Flow Ejection," *ASME Journal of Heat Transfer*, Vol. 111, No. 1, pp. 51-58.
- Lau, S. C., Han, J. C., and Batten, T., 1989b, "Heat Transfer, Pressure Drop and Mass Flow Rate in Pin Fin Channels With Long and Short Trailing Edge Ejection Holes," *ASME JOURNAL OF TURBOMACHINERY*, Vol. 111, pp. 117-123.
- Metzger, D. E., Fan, C. S., and Pennington, J. W., 1983, "Heat Transfer and Flow Friction Characteristics of Very Rough Transverse Ribbed Surfaces With and Without Pin Fins," *Proc. ASME-JSME Thermal Engineering Joint Conference*, Vol. 1, pp. 429-436.
- Metzger, D. E., Chyu, M. K., and Bunker, R. S., 1988, "The Contribution of On-Rib Heat Transfer Coefficients to Total Heat Transfer From Rib-Roughened Surfaces," *Transport Phenomena in Rotating Machinery*, J. H. Kim, ed., Hemisphere Publishing Co.
- Metzger, D. E., Fan, C. S., and Yu, Y., 1990, "Effects of Rib Angle and Orientation on Local Heat Transfer in Square Channels With Angled Roughness Ribs," *Compact Heat Exchangers: A Festschrift for A. L. London*, Hemisphere Publishing Co., pp. 151-167.
- Moffat, R. J., 1990, "Experimental Heat Transfer," *Proc. 9th Int. Heat Transfer Conf.*, Vol. 1, pp. 187-204.
- Rohde, J. E., Richards, H. T., and Metzger, G. W., 1969, "Discharge Coefficient for Thick Plate Orifices With Approach Flow Perpendicular and Inclined to the Orifice Axis," NASA TN D-5467.
- Taslim, M. E., and Spring, S. D., 1988a, "An Experimental Investigation of Heat Transfer Coefficients and Friction Factors in Passages of Different Aspect Ratios Roughened With 45° Turbulators," *Proc. ASME National Heat Conference*, Houston, TX.
- Taslim, M. E., and Spring, S. D., 1988b, "Experimental Heat Transfer and Friction Factors in Turbulated Cooling Passages of Different Aspect Ratios, Where Turbulators are Staggered," Paper #AIAA-88-3014.
- Taslim, M. E., 1990, "Application of Liquid Crystals in Heat Transfer Coefficient Measurement," *Proceedings of IEEE ELECTRO/90*, Boston, MA.
- Taslim, M. E., Rahman, A., and Spring, S. D., 1991b, "An Experimental Investigation of Heat Transfer Coefficients in a Spanwise Rotating Channel With Two Opposite Rib-Roughened Walls," *ASME JOURNAL OF TURBOMACHINERY*, Vol. 113, pp. 75-82.
- Taslim, M. E., Bondi, L. A., and Kercher, D. M., 1991c, "An Experimental Investigation of Heat Transfer in an Orthogonally Rotating Channel Roughened 45 Degree Criss-Cross Ribs on Two Opposite Walls," *ASME JOURNAL OF TURBOMACHINERY*, Vol. 113, pp. 346-353.
- Taslim, M. E., and Wadsworth, C. M., 1994, "An Experimental Investigation of the Rib Surface-Averaged Heat Transfer Coefficient in a Rib-Roughened Square Passage," ASME Paper No. 94-GT-162; accepted for publication in the *Transactions of the ASME*.
- Webb, R. L., Eckert, E. R. G., and Goldstein, R. J., 1971, "Heat Transfer and Friction in Tubes With Repeated-Rib-Roughness," *Int. J. Heat Mass Transfer*, Vol. 14, pp. 601-617.
- Zhang, Y. M., Gu, W. Z., and Han, J. C., 1993, "Heat Transfer and Friction in Rectangular Channels With Ribbed or Ribbed-Grooved Walls," *ASME Journal of Heat Transfer*, accepted for publication.

Detailed Heat Transfer Coefficient Measurements and Thermal Analysis at Engine Conditions of a Pedestal With Fillet Radii

Z. Wang

P. T. Ireland

T. V. Jones

Department of Engineering Science,
University of Oxford,
Oxford, United Kingdom

The heat transfer coefficient over the surface of a pedestal with fillet radii has been measured using thermochromic liquid crystals and the transient heat transfer method. The tests were performed at engine representative Reynolds numbers for a geometry typical of those used in turbine blade cooling systems. The heat conduction process that occurs in the engine was subsequently modeled numerically with a finite element discretization of the solid pedestal. The measured heat transfer coefficients were used to derive the exact boundary conditions applicable to the engine. The temperature field within the pedestal, calculated using the correct heat transfer coefficient distribution, is compared to that calculated using an area-averaged heat transfer coefficient. Metal temperature differences of 90 K are predicted across the blade wall.

Introduction

Short pin-fin and pin-fin arrays are frequently used in turbine blade internal cooling systems to enhance cooling and stiffen the structure. The present work has shown that a knowledge of the detailed heat transfer coefficient distribution is required to predict the cooling effect of such devices accurately. The heat flow process has been numerically modeled at typical engine conditions with the detailed heat transfer distribution measured by the transient heat transfer method being used as the thermal boundary conditions.

One outcome of the blade manufacturing process is that pin-fins found in internal cooling passages blend into the passage wall instead of joining the end wall to form an abrupt edge (Fig. 1). Large-scale (100 times engine size) perspex models were used in the present study to represent the engine pedestal geometry accurately. Previous researchers (Ireland and Jones, 1986; Metzger et al., 1986; Van Fossen, 1982; Zukauskas, 1972) have considered pin-fins without fillet radii. The effect of this simplification in model geometry on the detailed distribution of heat transfer coefficient has not been assessed. Chyu (1990) used the mass to heat transfer analogy method to measure the difference in the average mass transfer from arrays of pin fins with and without fillet radii. He concluded that the average Sherwood number on the pin fin surface for a staggered array was less with fillet radii than for straight pin fins. The presence of fillet radii had little effect on the Sherwood number for

in-line configurations. The present work has measured local values of h and enables the extent of the effect of the blend radius to be estimated.

Previous experimental studies of heat transfer to pin-fins have been performed without representing the temperature distribution in the pedestal material caused by the finite blade conductivity. Such tests have employed highly conductive models or have applied the mass to heat transfer analogy. Preliminary estimates of the temperature change across an engine pin fin indicated that the pin fin temperature difference could be of the order of 10–20 percent of the coolant to free-stream cooling potential. This value of the expected temperature change is typical of those occurring in engine cooling passages as discussed by Holland (1991) who gives a typical Biot number for a high-pressure turbine of 0.2. The recently acquired knowledge of the local heat transfer coefficient distribution has enabled the temperature change through the conducting blade material to be properly accounted for as reported below.

Heat Transfer Coefficient Measurements

Experimental Method. The distribution of heat transfer coefficient in this study was measured by a transient heat transfer liquid crystal method (Byerley et al., 1992; Shen et al., 1991). Thermochromic liquid crystals that exhibit color display over a certain temperature range are used as a full cover surface thermometer. The liquid crystal compounds are encapsulated in spheres of approximately 10 μm diameter and sprayed onto the model surface to form a thermally thin layer (Jones et al., 1992). In each test, the model temperature is initially uniform at room temperature. The experiment

Contributed by the International Gas Turbine Institute and presented at the 38th International Gas Turbine and Aeroengine Congress and Exposition, Cincinnati, Ohio, May 24–27, 1993. Manuscript received at ASME Headquarters March 17, 1993. Paper No. 93-GT-329. Associate Technical Editor: H. Lukas.

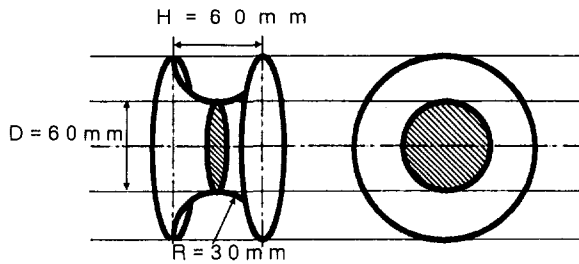


Fig. 1 Large-scale model of a pedestal with fillet radii

commences when the model is suddenly exposed to a flow of air at a temperature higher than the liquid crystal color change temperature. As the experiment proceeds, the liquid crystal coating on the model surface displays color when the local surface reaches the liquid crystal color change temperature. The surface temperature rise is a function of the local heat transfer coefficient given by the following equation:

$$\theta = 1 - \exp \beta^2 \operatorname{erfc} \beta \quad (1)$$

where

$$\beta = \frac{h\sqrt{t}}{\sqrt{\rho ck}} \quad (2)$$

and

$$\theta = \frac{T_s - T_{\text{init}}}{T_{\text{gas}} - T_{\text{init}}} \quad (3)$$

T_{init} and T_{gas} are the initial temperature and the gas temperature. T_s corresponds to the liquid crystal color change temperature and t is the time at which the color display appears at the location where h is measured. T_{init} and T_{gas} are measured during the experiment and the local heat transfer coefficient can be calculated from the equation above. In this study, the color change times were found using a frame grabber fitted to a PC and the intensity history analysis method detailed by Wang et al. (1990) and Wang (1991) was used to process the data.

Experimental Apparatus. The experimental apparatus is shown in Fig. 2. The air from the heater is initially directed through the bypass that takes the same flow rate as that passing through the test section during the experiment. The test commences when the hot flow is switched by two fast-acting valves through the test section (shown by the solid arrows in Fig. 2). The test section is a high-aspect-ratio channel ($60 \times 600 \times 1500$ mm). The pedestal with fillet radii is placed on the duct centerline sufficiently far from the duct inlet for the flow to be fully developed. The pedestal spans the channel shortest dimension. The midspan ($z/H = 0.5$) diameter of the pedestal at 60 mm is the same as the channel width, H , and the radius of the fillets is half of the pedestal

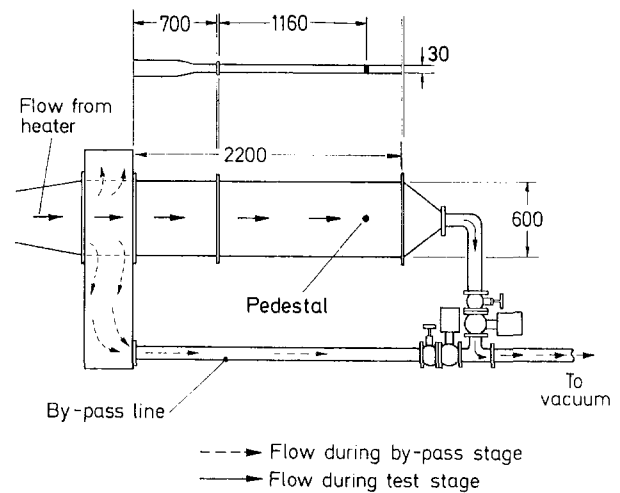


Fig. 2 Experimental apparatus

length. There is no straight section on the pedestal. The channel and the pedestal were manufactured from perspex. A liquid crystal coating that displayed color over two distinct temperature ranges was used in this work to calculate h twice at each selected location. A thin layer of black ink was applied on top of the liquid crystal film to eliminate transmitted light. The data presented below are the average of these two values. The experimental uncertainty was calculated, following the approach of Byerley (1992) and Ireland (1987), as being less than 7 percent.

Heat Transfer Coefficient Results. The dimensionless heat transfer coefficient on the channel wall at a location remote from the pedestal is plotted in Fig. 3. The experimental data are very close to the prediction from Kays and Crawford (1980) for fully developed channel flow. The measured heat transfer coefficients divided by the base level are depicted as contours in Fig. 4. The locations at which the crystal color change times were evaluated are indicated by the asterisks. There are about 120 data points on the pedestal surface and 80 points distributed over the end wall. This measurement density was sufficient to resolve all the features in the heat transfer coefficient distribution from the recorded video data.

The interpolated enhancement factor distributions (projected onto the channel wall) at different Reynolds numbers are shown in Fig. 5. It can be seen that the heat transfer is enhanced above the duct level on both the pedestal and the end wall surface. Similar regions of high convective transfer near the cylinder to wall junction have been measured using the mass transfer method of Goldstein and Karni (1984) and Sparrow et al. (1984). The highest heat transfer is found at

Nomenclature

A = area of the pedestal base
 d = pedestal diameter in local plane
 D = pedestal diameter (on $z/H = 0.5$ plane)
 Fr = Frossling number
 h = heat transfer coefficient
 H = pedestal length
 k = thermal conductivity
 Nu = Nusselt number
 Q = heat flow through extended pedestal base
 $Q1$ = reference (flat wall) heat flow

Re = Reynolds number
 t = time
 T = temperature
 u = velocity
 x = distance upstream of pedestal centerline
 z = distance normal to channel wall
 β = dimensionless time
 η = fin efficiency
 θ = dimensionless surface temperature
 ν = kinematic viscosity
 β = dimensionless time

$\sqrt{\rho ck}$ = thermal product of perspex

Subscripts

CL = centerline plane ($z = H/2$)
 $cool$ = coolant
 ext = external
 gas = gas
 $init$ = initial
 max = maximum
 mb = mixed bulk
 s = surface
 z = in plane at distance z from channel wall

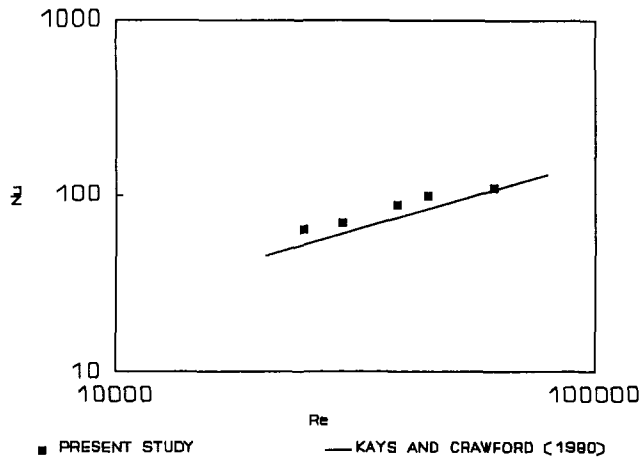


Fig. 3 Measured channel Nusselt number as a function of Reynolds number

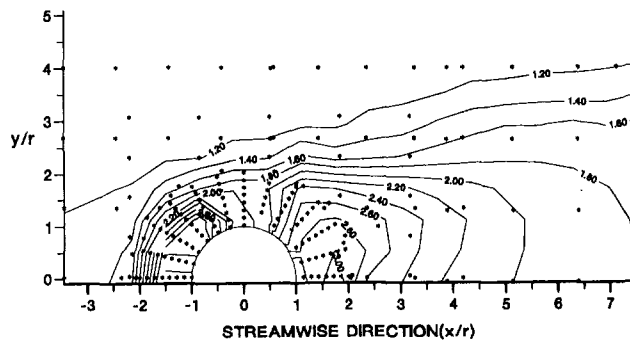


Fig. 4 Heat transfer enhancement factor measured over the pedestal surface

the front stagnation point. The reduction in enhancement factor at the stagnation point with Reynolds number (Fig. 6), would be expected if the boundary layer on the front surface of the pedestal is laminar. The heat transfer coefficient under these conditions is proportional to the square root of Reynolds number while for the turbulent channel flow, h varies with Reynolds number to the 0.73 (Ireland, 1987).

On the end wall, the heat transfer is lower than on the pedestal and, at the side, is within 20 percent of the base level at a distance of $1.5D$ from the pedestal centerline. For comparison the heat transfer enhancement on the end wall adjacent to a straight pedestal ($H/D = 1$) (from Ireland, 1987) at similar Reynolds numbers is shown in Fig. 7. Figure 8 shows the heat transfer coefficient plotted against distance from the pedestal along the upstream line of channel symmetry. In the case of the straight pedestal, this line starts ($x/D = 0.5$) at the cylinder to end wall junction. The same coordinate on the blended pedestal is at the stagnation point on the pedestal surface ($z/H = 0.5$). It is of interest to note that the heat transfer coefficient at the root of the straight pedestal is much higher than at the front of the filleted pedestal. The peak at the root of the straight pedestal has been shown (Ireland, 1987) to be close to the attachment point of the main horseshoe vortex. One other significant difference between the two heat transfer distributions is that, at about $x/D = 0.7$, the heat transfer coefficient distribution for the straight pedestal exhibits a local minimum and local maximum. This feature, marked as X in Fig. 7, appears as the kinks in the otherwise smooth contours of enhancement factor. This locally high heat transfer ring was interpreted as being caused by a second (separation) vortex parallel to the main horseshoe vortex. The trough in heat transfer was associated with the separation vortex, which resides between

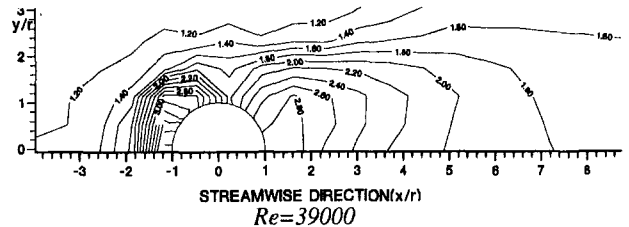
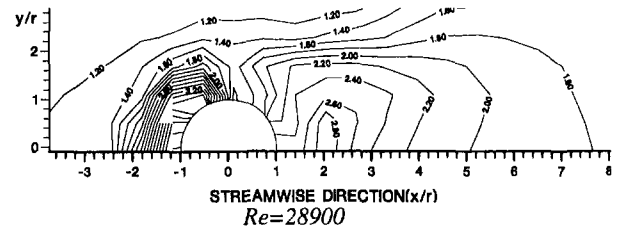


Fig. 5 Interpolated heat transfer coefficient distribution over the pedestal surface

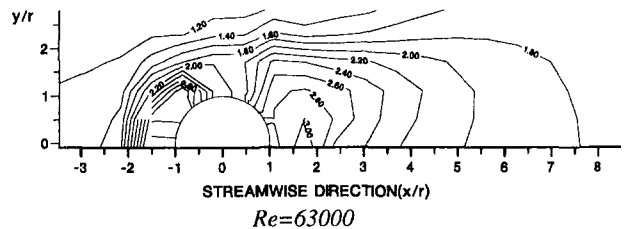
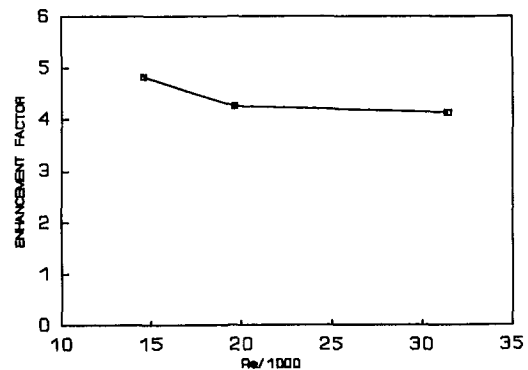


Fig. 6 Stagnation point heat transfer enhancement factor as a function of pedestal Reynolds number



the main and the separation vortices. The absence of similar kinks in Fig. 5 together with Fig. 8 indicate that the vortex structure has been modified by the presence of the fillet radius. The heat transfer distribution in the fillet pedestal case is shown in Fig. 8 monotonically decreasing in the upstream direction. However, at x/D is 0.7, the heat transfer coefficient decreases at a lesser rate with distance. The flow phenomenon that causes this change in gradient has not been resolved. It will be shown below, that the heat transfer enhancement at the front fillet radius appears to be mainly caused by attachment of the flow on the stagnation line and the growth of a new boundary layer.

Over the front of the pedestal where the boundary layer would be expected to be laminar, the Nusselt number should increase with the square root of Reynolds number. For a straight cylinder, the Reynolds number and Nusselt number

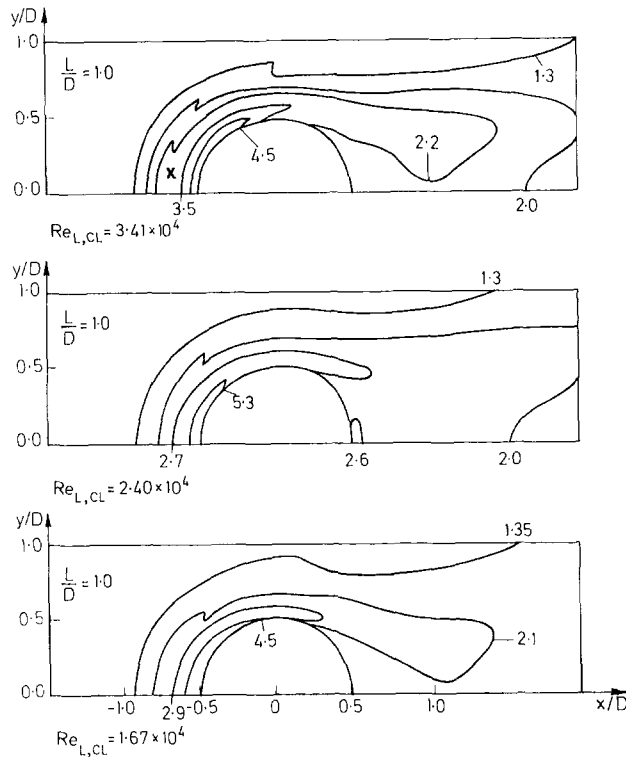


Fig. 7 Enhancement factor over the end wall near a prismatic pedestal after Ireland (1987)

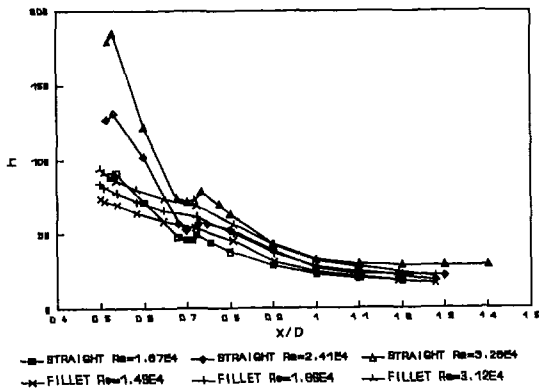


Fig. 8 (W/m^2K) on a line leading upstream of the pedestal as a function of distance from the pedestal center

would be based on the cylinder diameter. In the case of the pedestal with fillet radii, it is of interest to consider the Nusselt number divided by the square root of Reynolds number (the Frossling number)

$$Fr = \frac{Nu}{\sqrt{Re}} = \frac{h\sqrt{d\nu}}{k\sqrt{u_{CL}}} \quad (4)$$

over the front of the pedestal. The diameter most appropriate to add value to comparisons with other data is not immediately obvious.

The Frossling number, based on the midspan diameter D , at different Reynolds numbers and in a midspan plane is plotted as a function of angle from the leading edge in Fig. 9. The insensitivity of Fr to Reynolds number under the laminar boundary layer is apparent. In this figure, the Reynolds number is based on the diameter of the midspan circumference. Compared to the results obtained on both long pedestals and short straight pedestals, the heat transfer distribution at the midspan of the blended pedestal is similar and the levels are comparable. The stagnation point value is higher than

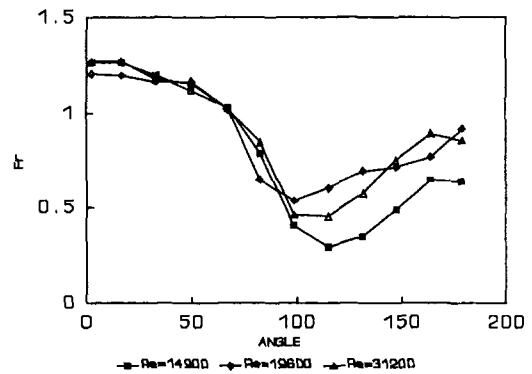
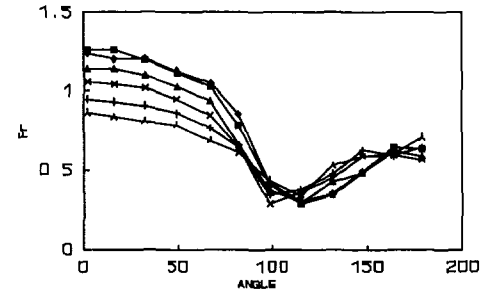
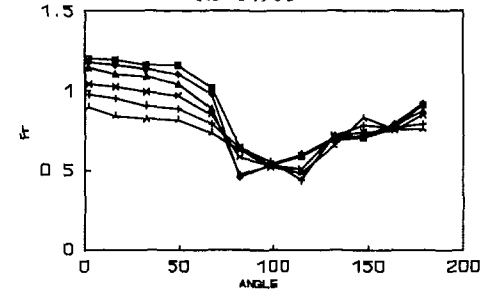


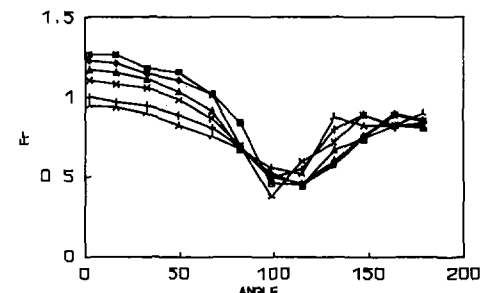
Fig. 9 Fr (based on D) around the midspan of the pedestal with fillet radii



$Re=14900$



$Re=19600$



$Re=31200$

Fig. 10 Fr (based on D) around planes at different distances from the channel wall

the theoretical straight cylinder value of 0.99. A similar increase was observed on a straight pedestal in the same channel (Ireland, 1987) and was thought to be due to turbulence.

The Frossling number distribution around circular planes aligned parallel to, but at different distances from, the channel wall is presented in Fig. 10. It can be seen that the heat

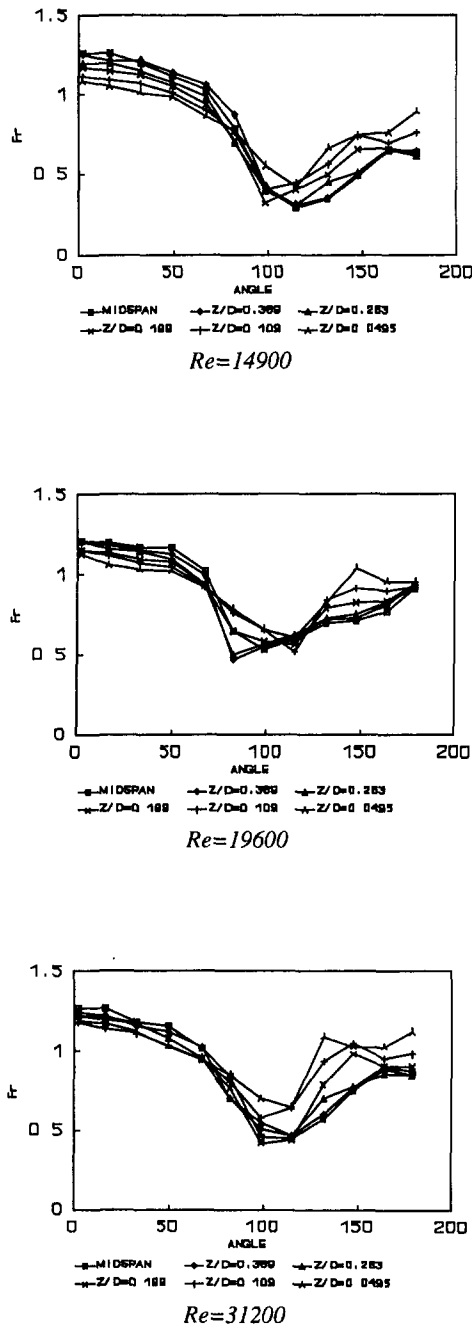


Fig. 11 Fr based on local plane diameter

transfer coefficients decrease toward the endwall. There are three main differences between the flow around the midspan plane and that closer to the wall. Close to the wall:

- (a) the local circle has a bigger diameter;
- (b) the approach flow is lower in the channel boundary layer where the air stream is slower and cooler;
- (c) the flow is no longer two dimensional.

To investigate (a), the Frossling number was then recalculated for each plane, using the value of diameter, d , local to that plane, Fig. 11. The uniform Fr at the front of the pedestal indicates that the flow can be treated as essentially two dimensional in this region. Strong secondary flows are either not present over most of the pedestal front or have very little effect on heat transfer levels. In this figure, the velocity used to calculate Fr is u_{CL} . Measurements confirmed that the channel velocity profile and temperature profile at a distance $2.6D$ ahead of the pedestal were fully developed.

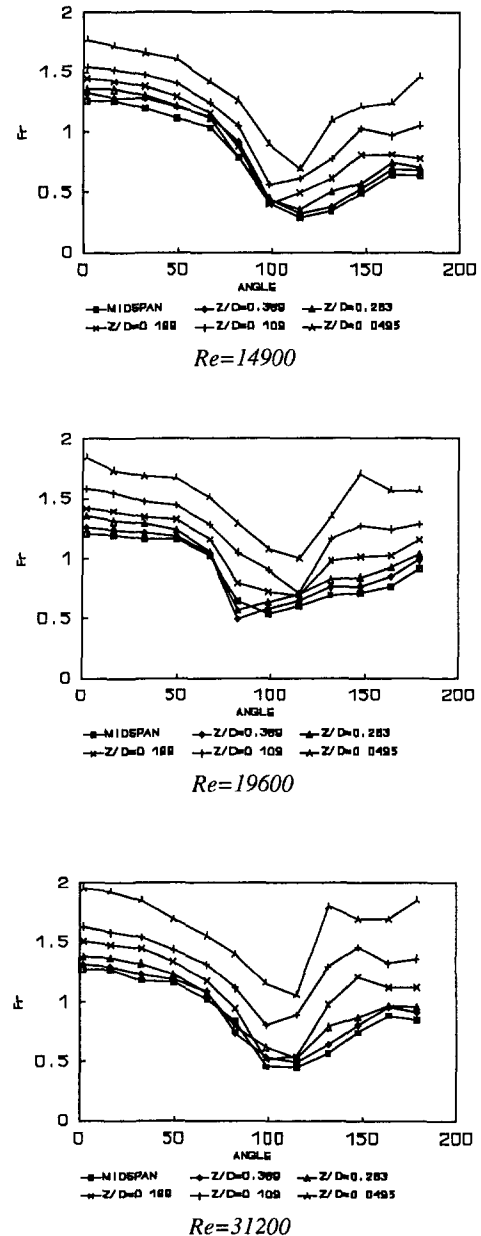


Fig. 12 Fr based on local plane diameter with factors applied to account for upstream gas temperature and velocity profiles

The effect of allowing for the upstream velocity and temperature profiles was also investigated. If the flow around the front of the pedestal does not migrate in the z direction and the flow around any circular slice of the pedestal is thus two dimensional, Fr based on local values of diameter, upstream temperature, and upstream velocity would collapse. The data were divided by a factor $(z/0.5H)^{1.5}$, which accounts for the seventh power law velocity and temperature profiles. The agreement between data from different planes can be seen to worsen (Fig. 12). The fact that the centerline velocity and temperature are the better values to collapse the Fr data is of interest and suggests that most of the front of the pedestal is swept by the flow originating remote from the channel wall.

At around 90 deg from the upstream line of symmetry, a narrow region of low heat transfer is found on the pedestal, which aligns with the pedestal axis and extends some distance from the midspan plane. This is caused by a region of separated flow, which has been identified many times on straight infinitely long cylinders. Interestingly the zone of low heat transfer extends almost to the end of the fillet where the surface is close to flat.

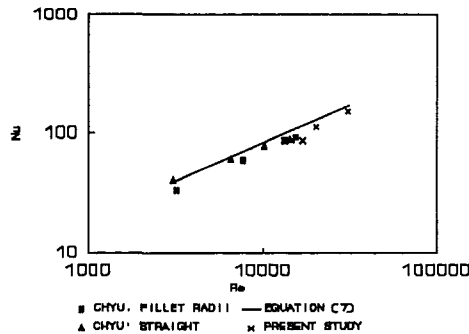


Fig. 13 Average Nu based on mixed bulk gas temperature as a function of Re based on mixed bulk channel velocity

Behind the pedestal, at about 150 deg, near to the junction between the fillet radius and the end wall, a high heat transfer region can be seen. This is the result of the reattachment of the horseshoe vortex to the surface. The divergence of the heat transfer contours downstream of this position is due to the gradual expansion of the horseshoe vortex leading to a double lobe shaped (only half is shown) enhancement region, which is similar to that found behind straight pedestals. In general, the region where heat transfer is enhanced behind the pedestal with fillet radii is wider and longer compared to a straight cylinder with a diameter the same as the midspan diameter. This would be expected since the pedestal with fillet radii presents more blockage. Extra heat transfer enhancement is obtained at the expense of increased pressure drop (Wang, 1991).

The heat transfer coefficient averaged over the surface of the pedestal with fillet radii is compared to the results of Chyu (1990) in Fig. 13. The data from this reference were taken from the first row of staggered arrays of straight pedestals and pedestals with fillet radii. The average Nusselt number has been calculated from the Sherwood number by multiplying by a factor of 0.6, which is the ratio of Schmidt number to Prandtl number raised to 0.4. Reynolds number used in the plot is based on the local mixed bulk velocity ahead of the pedestal and the

$$Re = \frac{U_{mb} D}{\nu} \quad (6)$$

pedestal diameter. Account has been taken of the difference in the minimum area and the channel area in determining Re for the first row data from (1989). Chyu's data reveals slightly lower Nusselt numbers for the blended pedestal compared to the straight pedestal. A similar reduction in average value was found for the heat transfer data. The data from the present work (the crosses) have been calculated based on the mixed bulk air temperature. The line is from a correlation (Eq. (7)) for pedestal average mixed bulk Nusselt number established for straight pedestals in isolated and row configurations from Ireland (1987).

$$Nu = 0.282 Re^{0.617} \quad (7)$$

It can be seen that the convective transfer data for the pedestal with fillet radii is lower than the straight cylinder correlation.

Conduction Analysis

In simple thermal analysis of pedestals no account is taken of the temperature variation through the body of the pedestal. The pedestal is essentially treated as having infinite thermal conductivity and an average value of the heat transfer coefficient is assumed to act over the surface of the pedestal. If the pedestal has a length-to-diameter ratio greater than 0.5, then

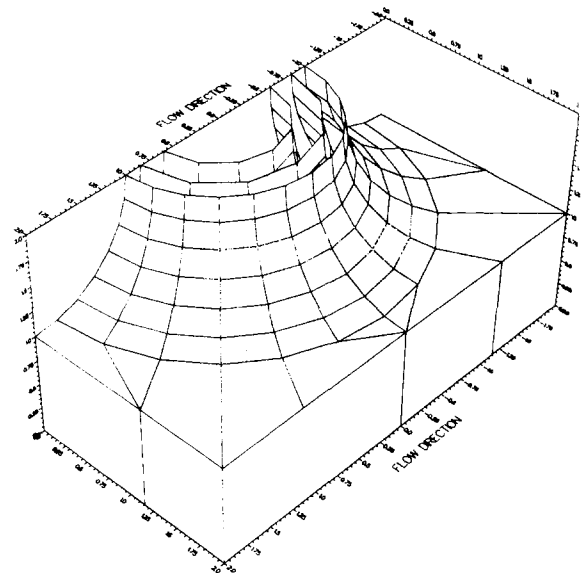


Fig. 14 Finite element calculation domain

the wetted area is increased. The change in area exposed to the flow is easily accounted for by defining an effective heat transfer coefficient (Brigham and Van Fossen, 1983). A slightly more sophisticated analysis of the temperature field inside the pedestal treats the conduction process as one dimensional and assumes a uniform heat transfer coefficient distributed over the pedestal surface. For a straight pedestal, the fin efficiency can be shown to be

$$\eta = \frac{\tanh\left(\sqrt{\frac{h}{kD}} H\right)}{\sqrt{\frac{h}{kD}} H} \quad (8)$$

where k is the pedestal conductivity. For values of the internal heat transfer coefficient and conductivity typical of engine conditions, the fin efficiency predicted by Eq. (8) can be as low as 80 percent. The effect of the nonuniform distribution of heat transfer coefficient is not so easily assessed. The measured heat transfer coefficient peaks at locations farthest from the passage wall. Since the heat flux is higher at these locations, the temperature drop through the pedestal would be expected to have a higher effect on the fin efficiency than is calculated for the uniform heat transfer coefficient case. In the present work, the temperature distribution in the pedestal and the blade wall was calculated at typical engine conditions. The cooling effect is assessed from the calculated temperature field. The accurately predicted cooling effect can then be compared with the results of the simplified calculation. A finite element analysis package was used to perform the conduction analysis. The domain in which the conduction analysis was carried out is shown in Fig. 14. A square base, one pedestal diameter thick, has been included to simulate the blade wall. On the blade internal surface, the heat transfer distribution calculated from the Nusselt number measured by the experiments was used as the exact boundary condition. At the external surface, i.e., the flat side of the base, a uniform heat transfer coefficient typical of engine values was used for all the computed cases. Typical values of the internal and external gas temperatures (510 K and 1500 K, respectively) were used in the analysis. The heat flux is assumed to be zero at all other surfaces. Calculations using averaged heat transfer coefficient over the pedestal surface were also performed for comparison. The conductivity of 25 W/mk was chosen as being typical of

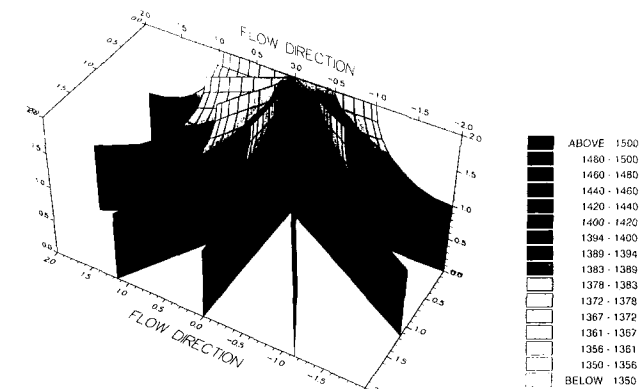
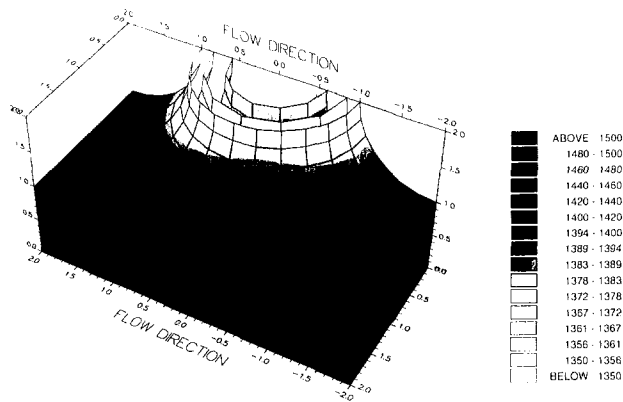


Fig. 15 Calculated temperature (in Kelvin) field for typical engine conditions

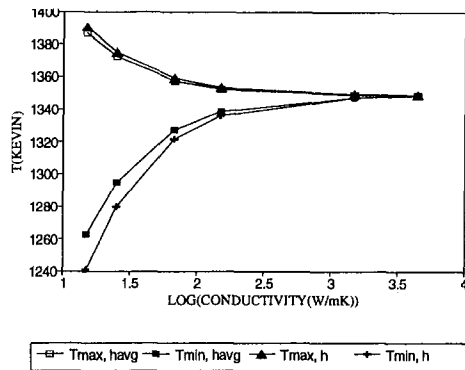


Fig. 16 Maximum and minimum temperatures

turbine blade material. The high-conductivity cases were performed to show the influence of the blade conductivity.

The computed temperature field for one set of boundary conditions is shown in Fig. 15. The lowest temperature is found, as expected, at the front facing stagnation point of the pedestal while the highest temperature is on the external (base) surface below the pedestal. Figure 16 shows the highest and lowest temperatures for both averaged and detailed heat transfer coefficients at different blade conductivities. The pedestal Reynolds number has been kept constant at 39,000. The graph shows that in this arrangement, typical of turbine cooling system, the temperature gradient across the blade is as high as 90 K at an engine representative conductivity of 25 W/Mk. It can also be seen that a lower maximum temperature and a higher minimum temperature are predicted using the averaged heat transfer coefficients. As the conductivity increases the difference disappears.

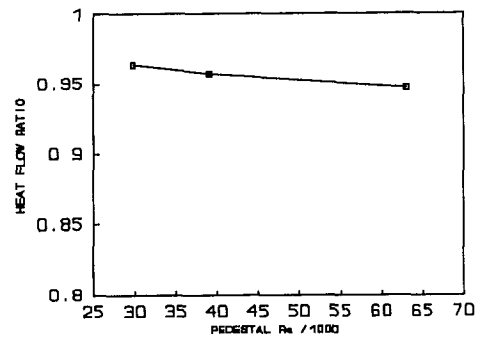


Fig. 17 Heat flow ratio for a plain wall showing only the effect of the finite blade conductivity

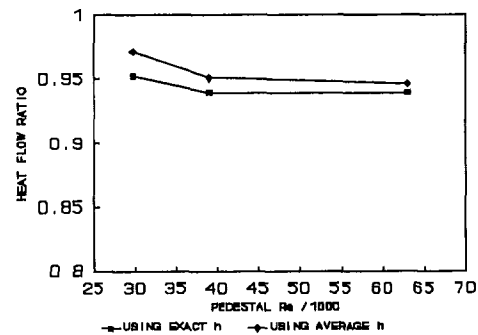


Fig. 18 Heat flow ratio as a function of pedestal Re for averaged and exact h distributions applied to the finite element domain

In order to evaluate the cooling efficiency of the device, the total heat flow through the square base of the pedestal for fixed gas and coolant temperatures was calculated. Since the external heat transfer coefficient is prescribed and the temperature over the face is uniform, the maximum temperature (at the base of the pedestal) is only a function of the heat flow through the device:

$$T_{\max} = T_{\text{gas}} - \frac{Q}{Ah_{\text{ext}}} \quad (9)$$

To normalize the heat flow, a base level heat flow, Q_1 , was computed for each Reynolds number. Q_1 is the heat flow through the bottom of a $1D$ thick plate and is calculated for a conductivity of 25 W/mk when an area-weighted heat transfer coefficient boundary condition is applied at the (now) flat cooling passage wall. In other words, Q_1 is the heat flow predicted by the simplified method, which does not account for the temperature drop through the pedestal. Before determining the exact effect of the fin efficiency, a one-dimensional approach was used to calculate the effect of the finite blade conductivity on the normalized heat flow. In the analysis used to calculate Fig. 17, the area-weighted heat transfer coefficient was applied at the inside surface of a flat wall $1D$ thick and $1D$ square. The calculated heat flow is divided by the heat flow through a $1D$ square wall of infinite conductivity. Even without simulating the effect of the extended shape of the pedestal, it can be seen that the heat flow is reduced by as much as 5 percent for the range of Reynolds numbers considered. Figure 18 compares the heat flux ratio between that predicted from the distributed heat transfer coefficient to that from the averaged heat transfer coefficient. Both the exact and the uniform average heat transfer coefficient were applied to the finite element domain. It can be seen that, when the geometry and conductivity are accurately modeled, the predicted heat flux can be lower than Q_1 by up to 6 percent.

Conclusions

Detailed distributions of heat transfer coefficient on and around a pedestal with fillet radii have been measured using a transient heat transfer method. The distribution has been compared with previous work and it has been shown that the local heat transfer levels are significantly different to the straight cylinder case. In particular, the vortex system does not locally enhance heat transfer to the same levels measured at the root of a straight pedestal. To accurately assess the effect of the different distribution on engine metal temperatures, the exact detailed distribution was used in a conduction analysis. The influence of pedestal conductivity and the effect of the nonuniform heat transfer coefficient distribution has been quantified for typical engine conditions. It has been shown that temperature differences of about 90 K exist across the pedestal surface.

Acknowledgments

This work has been carried out with the support of the United Kingdom Ministry of Defence and Rolls-Royce plc. The technical assistance of Mr. P. J. Timms was also much appreciated. The liquid crystals were supplied by Hallcrest LCT and the finite element software was written by PAFEC Ltd.

References

Brigham, B. A., and Van Fossen, G. J., 1983, "Length to Diameter Ratio and Row Number Effects in Short Pin Fin Heat Transfer," ASME Paper No. 83-GT-138.

Byerley, A. R., Jones, T. V., and Ireland, P. T., 1992, "Internal Cooling Passage Heat Transfer Near the Entrance to a Film Cooling Hole: Experimental and Computational Results," ASME Paper No. 92-GT-241.

Chyu, M. K., 1990, "Heat Transfer and Pressure Drop for Short Pin-Fin Arrays With Pin Endwall Fillet," *ASME Journal of Heat Transfer*, Vol. 112, pp. 926-932.

Goldstein, R. J., and Karni, J., 1984, "The Effect of a Wall Boundary Layer on Local Mass Transfer From a Cylinder in Crossflow," *ASME Journal of Heat Transfer*, Vol. 106, pp. XX-OO.

Holland, M. J., 1991, "Rotor Blade Cooling in HP Turbines," Rolls-Royce report, GN30498.

Ireland, P. T., and Jones, T. V., 1986, "Detailed Measurements of Heat Transfer on and Around a Pedestal in Fully Developed Passage Flow," *Proceedings of 8th International Heat Transfer Conference*, San Francisco, pp. 975-980.

Ireland, P. T., 1987, "Internal Cooling of Turbine Blades," D.Phil Thesis, University of Oxford, United Kingdom.

Jones, T. V., Wang, Z., and Ireland, P. T., 1992, "Liquid Crystals in Aerodynamic and Heat Transfer Testing," *Proceedings of Optical Methods and Data Processing in Heat and Fluid Flow*, I.Mech.E., London.

Kays and Crawford, 1980, *Convective Heat and Mass Transfer*, 2nd ed., McGraw-Hill, New York, p. 141.

Metzger, D. E., Shepard, W. B., and Haley, S. W., 1986, "Row Resolved Heat Transfer Variations in Pin Fin Arrays Including the Effects of Non-uniform Arrays and Flow Convergence," ASME Paper No. 86-GT-132.

Shen, J.-R., Ireland, P. T., Wang, Z., and Jones, T. V., 1991, "Heat Transfer Coefficient Enhancement in a Gas Turbine Blade Cooling Passage Due to Film Cooling Holes," *Proceedings of the Institution of Mechanical Engineers, Turbomachinery*, I.Mech.E., London, pp. 219-226.

Sparrow, E. M., Stahl, T. J., and Traub, P., 1984, "Heat Transfer Adjacent to the Attached End of a Cylinder in Crossflow," *International Journal of Heat Transfer*, Vol. 27, pp. 233-242.

Van Fossen, G. J., 1982, "Heat Transfer Coefficients for Staggered Arrays of Short Pin Fins," *ASME Journal of Heat Transfer*, Vol. 104, pp. 268-274.

Wang, Z., Ireland, P. T., and Jones, T. V., 1990, "A Technique for Measuring Convective Heat Transfer at Rough Surfaces," ASME Paper No. 90-GT-300.

Wang, Z., 1991, "The Application of Thermochromic Liquid Crystals to Detailed Turbine Blade Cooling Measurements," D.Phil Thesis, University of Oxford, United Kingdom.

Zukauskas, A. A., 1972, "Heat Transfer From Tubes in Cross Flow," *Advances in Heat Transfer*, Vol. 8, pp. 116-133.

Flow Between Contrarotating Disks

X. Gan

M. Kilic¹

J. M. Owen

School of Mechanical Engineering,
University of Bath,
Bath BA2 7AY, United Kingdom

The paper describes a combined experimental and computational study of laminar and turbulent flow between contrarotating disks. Laminar computations produce Batchelor-type flow: Radial outflow occurs in boundary layers on the disks and inflow is confined to a thin shear layer in the midplane; between the boundary layers and the shear layer, two contrarotating cores of fluid are formed. Turbulent computations (using a low-Reynolds-number $k-\epsilon$ turbulence model) and LDA measurements provide no evidence for Batchelor-type flow, even for rotational Reynolds numbers as low as 2.2×10^4 . While separate boundary layers are formed on the disks, radial inflow occurs in a single interior core that extends between the two boundary layers; in the core, rotational effects are weak. Although the flow in the core was always found to be turbulent, the flow in the boundary layers could remain laminar for rotational Reynolds numbers up to 1.2×10^5 . For the case of a superposed outflow, there is a source region in which the radial component of velocity is everywhere positive; radially outward of this region, the flow is similar to that described above. Although the turbulence model exhibited premature transition from laminar to turbulent flow in the boundary layers, agreement between the computed and measured radial and tangential components of velocity was mainly good over a wide range of nondimensional flow rates and rotational Reynolds numbers.

1 Introduction

Contrarotating turbine stages may be incorporated in future generations of ultra-high-bypass-ratio engines to drive the contrarotating fans. Contrarotating turbine blades obviate the need for a row of stator blades, thereby reducing the weight and size of the engine. Figure 1 shows a schematic diagram of the flow structure between contrarotating disks where fluid flows radially outward in boundary layers on the disks to be replaced by a radial inflow of fluid in the midplane.

Batchelor (1951) considered the solutions of the Navier–Stokes equations for the laminar flow between infinite disks. For the case of contrarotating disks, he predicted that, at high rotational Reynolds numbers, there would be radial outflow in thin boundary layers on the disks and inflow in a thin shear layer (or “transition layer” as he termed it) in the midplane; between the boundary layers and the shear layer would be two cores of contrarotating fluid. He made the prescient statement, “This singular solution may not be realizable experimentally, of course, but it has some intrinsic interest.”

Stewartson (1953) obtained numerical solutions of the Navier–Stokes equations for low rotational Reynolds num-

bers and also conducted some rudimentary experiments with two cardboard disks that suggested Batchelor-type flow did not occur: although there were separate boundary layers on the disks, the core of fluid between the boundary layers showed little sign of rotation. It should be pointed out, however, that the disks were only 150 mm in diameter and there were no peripheral shrouds.

The Batchelor–Stewartson controversy has been the subject of many studies (see, for example, Owen and Rogers,

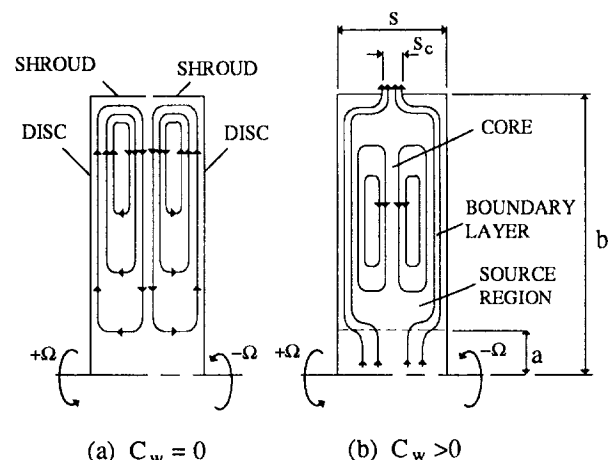


Fig. 1 Schematic diagram of flow between contrarotating disks

¹Now at Uludağ Üniversitesi, Mühendislik Fakültesi, Makina Bölümü, Bursa, Turkey.

Contributed by the International Gas Turbine Institute and presented at the 38th International Gas Turbine and Aeroengine Congress and Exposition, Cincinnati, Ohio, May 24–27, 1993. Manuscript received at ASME Headquarters March 10, 1993. Paper No. 93-GT-286. Associate Technical Editor: H. Lukas.

1989), and it is now recognized that there are multiple solutions of the infinite-disk equations, of which Batchelor's and Stewartson's are but two. Zanbergen and Dijkstra (1987) provide a very comprehensive review of this subject. For finite disks, however, the solution is usually unique, and the occurrence of Batchelor-type flow or Stewartson-type flow depends on, among other things, whether the disks are open or enclosed.

Dijkstra and van Heijst (1983) carried out a combined theoretical and experimental study of laminar flow between two finite disks, one of which was shrouded. Their study was confined to $-0.825 \leq \Gamma < 0$, where $\Gamma = \Omega_1/\Omega_2$, the ratio of speeds of the two disks. The two cells of contrarotating fluid formed for $\Gamma < 0$ were not symmetric about the midplane (unlike the two cells shown in Fig. 1 for $\Gamma = -1$); a stagnation point formed on the slower disk with flow radially outward at smaller radii and inward at larger radii, and the radial location of this stagnation point increased with decreasing Γ . No reliable experimental or computational results were obtained for $-1 \leq \Gamma < -0.825$, and wavy instabilities were observed in the experimental rig in this range. The numerical results indicated, at large radii, the presence of a shear layer with two contrarotating cores, as predicted by Batchelor; near the axis, however, Stewartson-type flow was computed, and the angular speed of the fluid was negligible outside the boundary layers.

Daniels et al. (1991) reported extensive experimental measurements in a pressurized rotating disk rig, with a stationary peripheral shroud, for $G = 0.328$, $Re_\phi = 4 \times 10^6$, 8×10^6 , and 1.7×10^7 , $\Gamma = -1$, 0 , and $+1$, and superposed flow rates in the range $-0.14 \leq \lambda_T \leq +0.14$ (the negative sign indicating radial inflow). For $\Gamma = -1$, the moment coefficient C_m was virtually independent of the magnitude and direction of the flow rate. For $\lambda_T = 0$, the moment coefficient for $\Gamma = -1$ was approximately twice that for $\Gamma = 0$ (the rotor-stator case); the insertion of a stationary disk between the two contrarotating ones reduced the moment to the same level as the rotor-stator system.

Morse (1988) used an elliptic solver with a low-Reynolds-number $k-\epsilon$ turbulence model to compute the flow inside rotating-disk systems for $G = 0.1$, $-1 \leq \Gamma \leq +1$, and $10^5 \leq Re_\phi \leq 10^7$. For $-1 < \Gamma \leq 0$, like Dijkstra and van Heijst, Morse found that the flow was not symmetric about the midplane and that there was a stagnation point on the slower

disk. For $\Gamma = -1$, like Daniels et al., Morse found that the moment coefficient was approximately twice the value of that for $\Gamma = 0$. For $Re_\phi \geq 10^6$ he correlated his computed moment coefficient by

$$C_m = 0.0319 Re_\phi^{-0.1375} \quad (1.1)$$

Like the system of Daniels et al., the one modeled by Morse had a stationary peripheral shroud.

The present paper describes a combined experimental and computational study of flow between contrarotating disks with $\Gamma = -1$. The computational method is outlined in Section 2, the apparatus is described in Section 3, and a comparison between computed and measured velocities is made in Section 4.

2 Computational Method

The code used was a modified version of a finite-volume, multigrid, elliptic solver developed at Sussex University. Simplec pressure-correction smoothing is used with a V-cycle, full-approximation-storage (FAS), multigrid scheme as employed by Lonsdale (1988) and extended by Vaughan et al. (1989).

The Reynolds-averaged, axisymmetric, steady-state Navier-Stokes equations, in cylindrical-polar coordinates, are given in Appendix A. The low-Reynolds-number $k-\epsilon$ turbulence model, which is a variant of that proposed by Morse (1988, 1991a, b), is given in Appendix B. Transition from laminar to turbulent flow is handled implicitly by the model without the need to specify transitional criteria or to "trip the flow" artificially. Further details of the method are given by Wilson et al. (1992), who used a Meiko 16-node parallel computing surface; for the computations described below, only one i860 processor was used.

For the case of zero superposed flow ($C_w = 0$), advantage was taken of the geometric symmetry about the midplane, $z/s = 0.5$. Numerical solutions of the equations were obtained in only half the cavity, $0 \leq z/s \leq 0.5$, and velocities for $0.5 < z/s \leq 1$ were calculated from symmetry (for V_r) and antisymmetry (for V_ϕ): the computed velocities were then compared with measured values for $0 \leq z/s \leq 1$. For the solid boundaries ($r = a$ and b , and $z = 0$), no-slip conditions were used for the velocities; for the midplane, $z/s = 0.5$, V_z and V_ϕ were taken to be zero and the symmetry condition

Nomenclature

A^+ = coefficient in near-wall damping function
 a = inner radius of disk
 b = outer radius of disk
 C_m = moment coefficient
 $= M/[(1/2)\rho\Omega^2b^3]$
 C_w = nondimensional flow rate
 $= m/\mu b$
 $C_\mu, C_{\epsilon 1}, C_{\epsilon 2}$ = constants in turbulence model
 D = term in k equation
 E, F = terms in ϵ equation
 G = gap ratio = s/b
 G_c = shroud-clearance ratio
 $= s_c/b$
 k = turbulent kinetic energy
 m = mass flow rate
 M = moment on one side of disk
 p = static pressure
 P = production rate of turbulent kinetic energy

r = radial coordinate
 Re_ϕ = rotational Reynolds number
 $= \rho\Omega b^2/\mu$
 Re_t = turbulence Reynolds number
 $= \rho k^2/\mu\epsilon$
 s = axial gap between disks
 s_c = axial clearance between shrouds
 U_r = friction velocity
 $= (\tau_w/\rho)^{0.5}$
 $\rho V_i' V_j'$ = Reynolds stress tensor
 V_r, V_ϕ, V_z = time-averaged velocity components in r, ϕ, z directions
 x = nondimensional radius
 $= r/b$
 y = distance normal to wall
 y^+ = wall-distance Reynolds number
 $= \rho U_r y/\mu$
 z = axial coordinate measured from disk 1
 Γ_r, Γ_z = effective diffusivities

Γ = ratio of angular speeds of contrarotating disks
 $= \Omega_1/\Omega_2$
 ϵ = turbulent energy dissipation rate
 λ_T = turbulent flow parameter
 $= C_w Re_\phi^{-0.8}$
 μ = dynamic viscosity
 μ_t = turbulent viscosity
 μ_{eff} = effective viscosity
 ρ = density
 $\sigma_k, \sigma_\epsilon$ = turbulent Prandtl numbers for k and ϵ
 τ_w = total wall shear stress
 ϕ = tangential coordinate
 Φ = generalized dependent variable
 Ω = angular speed of disk

Subscripts

1, 2 = left-hand, right-hand disk
 fd = free disk

was used for V_r . In the small clearance ($G_c = 0.016$) between the contrarotating shrouds, V_r and V_z were taken to be zero and V_ϕ varied linearly from $+\Omega b$ to $-\Omega b$ ($V_\phi = \Omega b(s - 2z)/s_c$). The dimensions of the computational domain were the same as those for the experimental rig, where $G = 0.12$ and $a/b = 0.128$, and a 65×113 (axial \times radial) nonuniform grid was used with grid-expansion factors employed to ensure close spacing near regions of large gradients. Morse (1991b) recommended that the grid point closest to a wall should be located to ensure $y^+ < 0.5$; this condition was achieved for the computations discussed below.

For the case of superposed flow ($C_w > 0$), computations were conducted for the entire cavity ($0 \leq z/s \leq 1$, and $0 \leq r \leq b$) with an 89×113 (axial \times radial) nonuniform grid. The air was assumed to enter the cavity axially without swirl ($V_r = 0$, $V_\phi = 0$, $V_z = (1/2)m/\pi a^2 \rho$) at the center of each disk ($0 \leq r \leq a$) and to leave radially ($V_z = 0$, $V_r = m/2\pi b s_c \rho$, $V_\phi = \Omega b(s - 2z)/s_c$) through the clearance between the contrarotating shrouds. For the solid boundaries, the no-slip condition was used; for the axis of rotation ($r = 0$), $V_\phi = 0$, $V_r = 0$, and symmetry conditions were used for V_z .

The inlet conditions assumed in the computation did not precisely match those on the rig, in which, as described in Section 3, there were rotating, porous cylindrical tubes, of radius a , at the center of the disks, and air was admitted to the tubes axially through a central hole in disk 1, the "upstream disk." Some computations were conducted with other inlet configurations that were intended to model more closely the conditions on the rig. However, in view of the relatively good agreement achieved between the computed and measured velocities, particularly at large radii well away from the inlet, the additional complications were regarded as unnecessary and the results for these inlet conditions are not reported here. The symmetric boundary conditions specified above allowed numerical solutions to be obtained using only half the cavity ($0 \leq z/s \leq 0.5$), as for the zero-flow case; the results of the computations for half the cavity did not differ from those presented below for the entire cavity.

The convergence criterion was based on the normalized

root-mean-square (rms) value of the change in residuals from one iteration to the next. For the results presented here, the maximum change in the normalized rms value was set to 10^{-4} ; tests conducted with smaller values showed no significant changes in the computed velocity profiles or moment coefficients. For turbulent flow, the computing time for a single i860 processor, using a three-level multigrid, was approximately one hour for the half cavity and 1 1/2 hours for the entire cavity.

3 Experimental Apparatus

3.1 Rotating Disk Rig. Figure 2 shows a schematic diagram of the rig used for the experimental measurements described below. The disks, which were 762 mm in diameter, could be rotated independently up to 4000 rpm by means of two thyristor-controlled electric motors, and the speed could be measured to an accuracy of ± 1 rpm. For the tests considered here, the downstream disk was made from steel, and the upstream disk and the shrouds were made from transparent polycarbonate, which limited the maximum speed to 1500 rpm. Each shroud was attached to the periphery of a disk using a 10-mm-thick silicon-rubber foam; this altered the effective outer radius of the cavity (measured to the inside of the shrouds) to $b = 391$ mm. The axial clearance, s_c , between the shrouds tended to increase with increasing rotational speed and was estimated to be as large as 4 mm at 1500 rpm.

Air could be admitted to the center of the cavity from a "uniform sink" of 100 mm diameter. This was made from two rotating gauze tubes, each attached to one of the disks; as discussed in Section 4.2, the gauze tubes did not completely eliminate the skew in the inlet flow. For the superposed-flow case ($C_w > 0$), air was supplied at the center of the upstream disk through a hollow rotating shaft of 60 mm internal diameter, which in turn was connected to a stationary tube attached to a centrifugal fan. The flow rate was determined, with an uncertainty of ± 3 percent, by means of an orifice plate in the stationary tube upstream of the disks. Seals

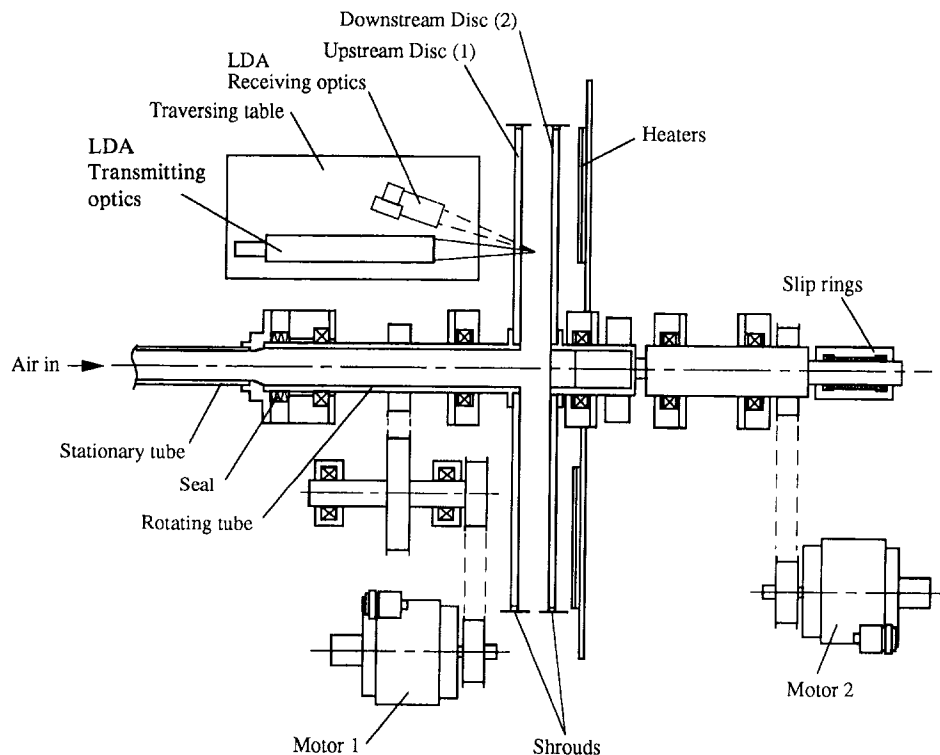


Fig. 2 Schematic layout of the rotating-disk rig and LDA system

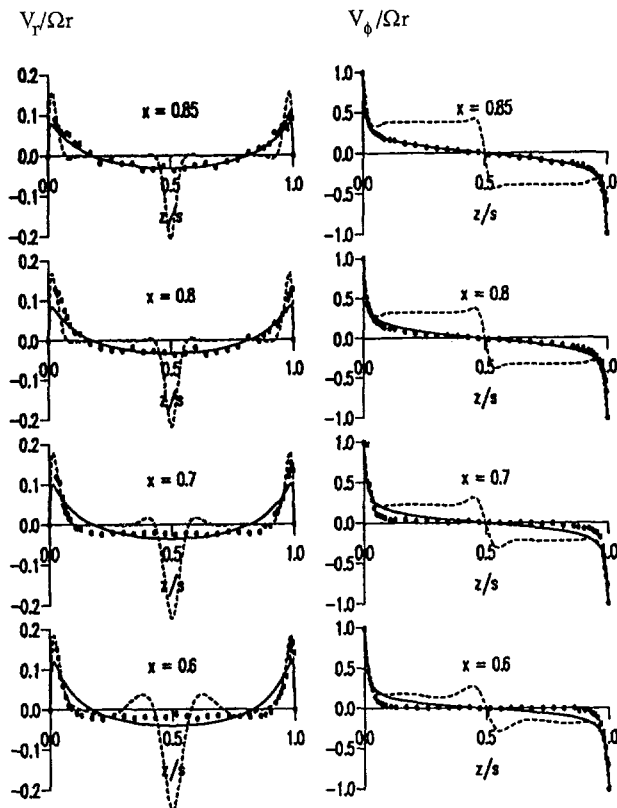


Fig. 3 Axial distribution of $V_r/\Omega r$ and $V_\phi/\Omega r$; $G = 0.12$, $C_w = 0$, $Re_\phi = 2.31 \times 10^5$; --- laminar computations, — turbulent computations, \circ experimental measurements

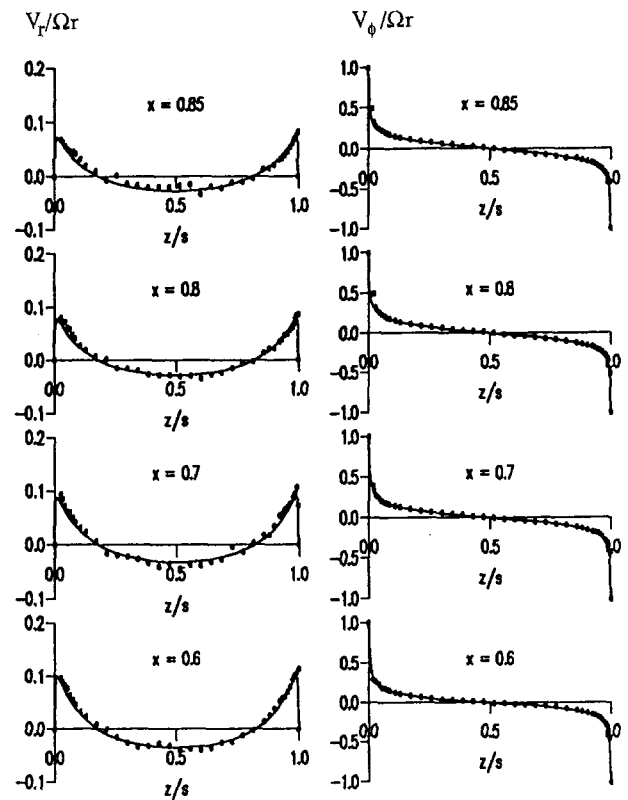


Fig. 4 Axial distribution of $V_r/\Omega r$ and $V_\phi/\Omega r$; $G = 0.12$, $C_w = 0$, $Re_\phi = 7.26 \times 10^5$; — turbulent computations, \circ experimental measurements

between the rotating and stationary tubes reduced the leakage flow rate to a negligible level.

3.2 Optical Instrumentation. A single-component laser Doppler anemometry (LDA) system was used to measure the radial and tangential components of velocity between the disks. The system comprised a 4 W Spectra-Physics 164A argon-ion laser, connected by a fiber-optic cable to TSI transmitting optics, together with TSI frequency shift and receiving optics. The wavelength was 514.5 nm and the power at the control volume was up to 350 mW. The optics were configured in an off-axis back-scatter mode, as shown in Fig. 2, "looking through" the upstream polycarbonate disk. The beam spacing was 50 mm, and a converging lens of 120 mm focal length produced a probe volume of 0.34 mm length and 34 μm diameter, and the fringe spacing was 1.39 μm . The Doppler signal could be frequency-shifted in the range 2 kHz to 10 MHz.

The signal was processed using a TSI IFA-750 burst correlator, which was capable of measuring frequencies up to 90 MHz with signal-to-noise ratios (SNR) as low as -5 dB. The processor was used in conjunction with a Viglen PC, which also provided positional control of the x - y traversing table on which the optics were mounted. As soon as the Doppler signal had been validated by the processor, the PC automatically controlled the movement of the optics to their next position. It was necessary, however, to rotate the transmission optics manually through 90 deg to measure the second component of velocity.

The optical axis was normal to the disks, and the probe volume could be positioned with an axial uncertainty of 0.13 mm by the use of a "target" attached to the (stationary) steel disk. Neither disk was flat: The steel disk had a "run-out" of ± 0.25 mm and the polycarbonate disk ± 1.1 mm. Despite the run-out, it was possible to make velocity measurements as close as 0.5 mm from the polycarbonate disk, but "flare"

made it impossible to get closer than 1.5 mm from the steel disk.

The signal from the correlator could be used to make accurate measurements close to the polycarbonate disk: the presence of the disk caused a second peak in the spectrum of the Doppler frequency, and this peak was filtered out to enable the "true" frequency to be determined. It was also possible to obtain Doppler signals (from "scattering sites" within the disk material) when the probe volume was completely inside the polycarbonate disk; this was used to align the optics. The radial direction was determined by rotating the probe volume until the radial component of velocity was zero; rotation of the optics through 90 deg then allowed the tangential component to be measured. With the probe volume inside the polycarbonate disk, the tangential component of velocity could be validated to within 0.5 percent of the independently measured angular speed of the disk.

Oil particles of around 1 μm diameter, produced from a Dantec particle generator, were used to "seed" the air. For the case where there was no superposed flow, the particles were released in the air surrounding the disks, and sufficient numbers were ingested into the cavity, through the clearance between the shrouds, to produce acceptable Doppler signals. (The ingress of external air and particles was not observed to make the flow inside the cavity either unsteady or nonaxisymmetric.) For the case where there was a superposed flow, the particles were released into the intake of the centrifugal fan.

4 Comparison Between Computed and Measured Velocities

4.1 Zero Superposed Flow ($C_w = 0$). Figures 3, 4, and 5 show the results for $Re_\phi = 2.31 \times 10^5$, 7.26×10^5 , and 1.17×10^6 , respectively, with $C_w = 0$.

Figure 3 shows a comparison between the laminar and turbulent computations and the measured velocities. The

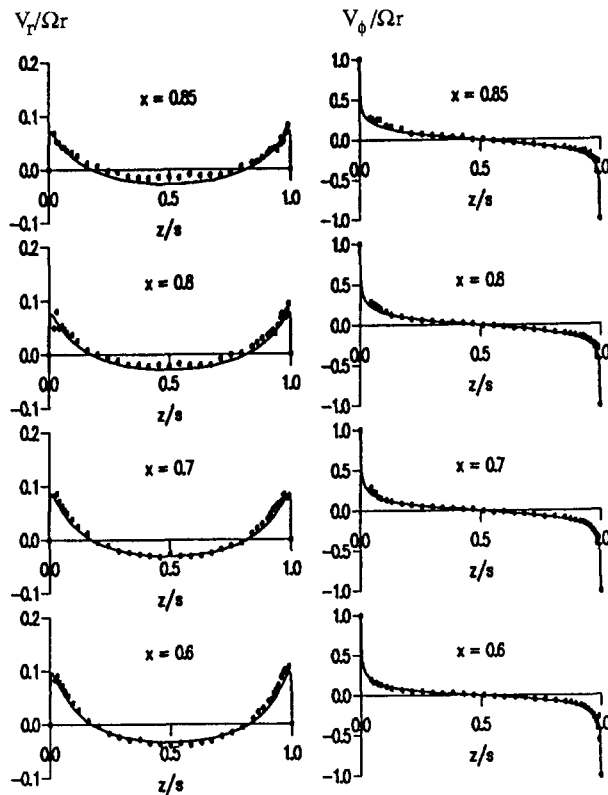


Fig. 5 Axial distribution of $V_r/\Omega r$ and $V_\phi/\Omega r$; $G = 0.12$, $C_w = 0$, $Re_\phi = 1.17 \times 10^5$; — turbulent computations, \circ experimental measurements

laminar computations show the classic Batchelor-type flow referred to in Section 1: Radial outflow occurs in boundary layers on the disks and inflow occurs in a thin shear layer in the midplane; between the shear layer and the boundary layers are two contrarotating cores of fluid. The turbulent computations and the experimental measurements show Stewartson-type flow: Between the boundary layers there is a single interior core in which rotation is weak.

The radial components of velocity in Fig. 3 show good agreement between the laminar computations and the measured values in the boundary layers for $x \leq 0.70$ ($x^2 Re_\phi \leq 1.1 \times 10^5$). For $x = 0.85$ ($x^2 Re_\phi = 1.7 \times 10^5$), there is good agreement between the turbulent computations and the measured values in the boundary layers. For all values of x , the turbulent computations in the core are in better agreement with the measurements than the laminar computations are. (No evidence of Batchelor-type flow, or of laminar flow in the core, was found even for measurements made at local rotational Reynolds numbers as low as $x^2 Re_\phi = 2 \times 10^4$.) The experimental results suggest that the flow in the boundary layers is laminar for $x^2 Re_\phi \leq 1.1 \times 10^5$ and turbulent for $x^2 Re_\phi \geq 1.7 \times 10^5$. For the free disk (see Owen and Rogers, 1989), laminar flow becomes unstable around $x^2 Re_\phi = 2 \times 10^5$ and transition is usually complete by 3×10^5 ; a highly polished disk can delay transition, and surface roughness or atmospheric disturbances can advance it.

The fact that Batchelor-type flow was not observed is attributed to its inherent instability. In the shear layer, the computed laminar velocity profiles exhibit points of inflexion, which are associated with instability (see, for example, Schlichting, 1979). Also, in the boundary layers on the shrouds, two contrarotating flows meet head-on in the midplane, creating a source of turbulence. Even though these effects create turbulent flow in the core, laminar flow can still occur in the boundary layers on the disks, as shown by both the experimental measurements and the turbulent com-

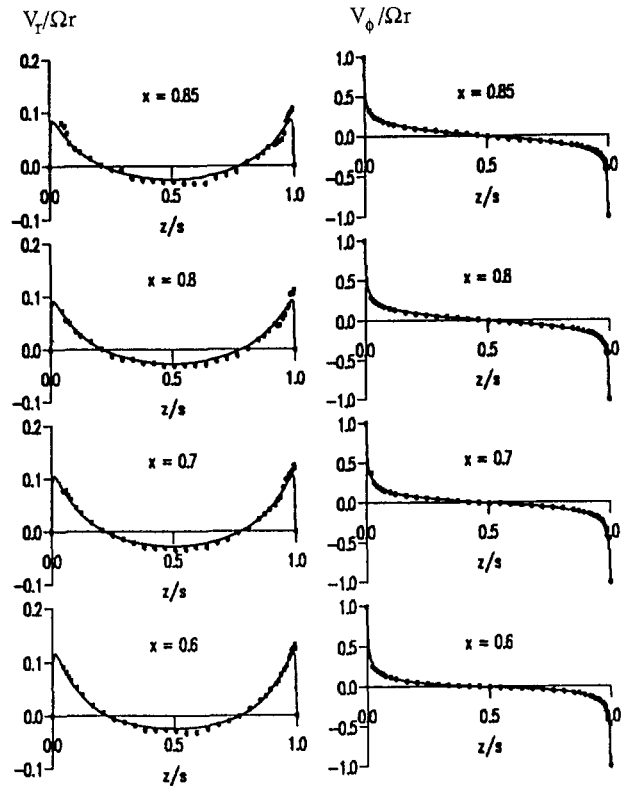


Fig. 6 Axial distribution of $V_r/\Omega r$ and $V_\phi/\Omega r$; $G = 0.12$, $C_w = 2310$, $Re_\phi = 6.66 \times 10^5$; $\lambda_T = 0.0506$; — turbulent computations, \circ experimental measurements

putations. The computations show premature transition on the disks but in all other respects they agree well with the measurements.

Figures 4 and 5 show good agreement between the turbulent computations and the measured radial and tangential components of velocity at all values of x . For these cases, where $x^2 Re_\phi \geq 2.6 \times 10^5$, the flow is completely turbulent. It can be seen that the thickness of the turbulent boundary layer (based on the point where $V_r = 0$) does not appear to depend significantly on either x or Re_ϕ .

4.2 Superposed Radial Outflow ($C_w > 0$). Figures 6, 7, and 8 show the results for $Re_\phi \approx 7 \times 10^5$ and $C_w = 2310$, 6320, and 9280, respectively; these correspond to $\lambda_T = 0.0506$, 0.132, and 0.199, which cover the range of the turbulent flow parameter that is likely to be of interest to the gas turbine designer. For these results, $x^2 Re_\phi \geq 2.4 \times 10^5$ and the flow is completely turbulent.

Figure 6, for $\lambda_T = 0.0506$, shows that the form of the velocity profiles is similar to that in Fig. 4, for $\lambda_T = 0$. The only significant difference is that the maximum value of $V_r/\Omega r$ is, not surprisingly, slightly higher in Fig. 6 than in Fig. 4. The agreement between the measured and computed velocity profiles in Fig. 6 is mainly good, although the measured values of $V_r/\Omega r$ near the downstream disk ($z/s = 1$) tend to be higher than the computed values. This is attributed to the inlet flow impinging on the downstream disk, an effect that the gauze tubes reduce but do not eliminate.

Figure 7, for $\lambda_T = 0.132$, shows further evidence of the skew in the experimental results, particularly at the smaller values of x . At the larger values of x , the agreement between the computed and measured radial components of velocity is mainly good, and the agreement between the computed and measured tangential components is very good for all x .

Figure 8, for $\lambda_T = 0.199$, shows that for $x \leq 0.7$ there is no radial inflow in the core: The flow is everywhere positive. Apart from the effects of skew and scatter in the measured

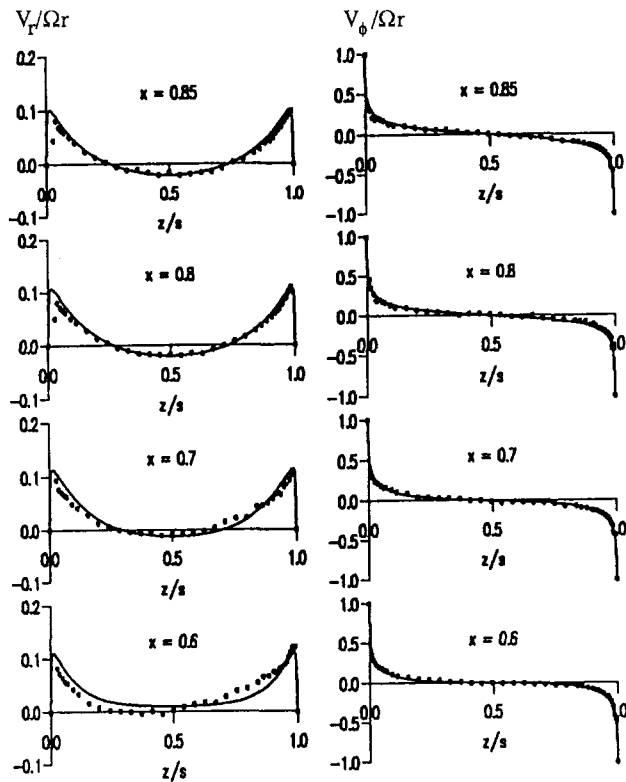


Fig. 7 Axial distribution of $V_r/\Omega r$ and $V_\phi/\Omega r$: $G = 0.12$, $C_w = 6320$, $Re_\phi = 7.08 \times 10^5$; $\lambda_T = 0.132$; — turbulent computations, \circ experimental measurements

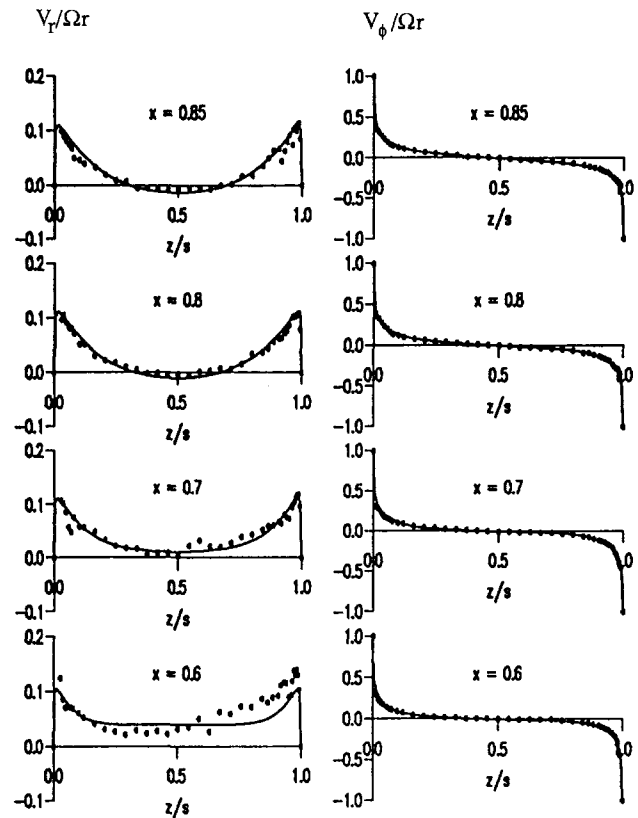


Fig. 8 Axial distribution of $V_r/\Omega r$ and $V_\phi/\Omega r$: $G = 0.12$, $C_w = 9280$, $Re_\phi = 6.84 \times 10^5$; $\lambda_T = 0.199$; — turbulent computations, \circ experimental measurements

radial component of velocity, agreement between the computed and measured values is good.

It is interesting to compare the results with those of the free disk (see Owen and Rogers, 1989). For turbulent flow, the free-disk entrainment rate can be approximated by

$$\frac{m_{fd}}{\mu r} = 0.219(x^2 Re_\phi)^{4/5} \quad (4.1)$$

where the subscript *fd* refers to the free disk. For contrarotating disks, the entrained flow rate will be double that of a single disk. If x_e is the nondimensional radius at which the superposed flow rate equals that entrained by the free disk, it follows from Eq. (4.1) that, for two disks,

$$x_e = \left(\frac{\lambda_T}{0.438} \right)^{5/13} \quad (4.2)$$

For $\lambda_T = 0.132$ and 0.199 , Eq. (4.2) gives $x_e = 0.63$ and 0.74 , respectively, which are consistent with the values of x at which the radial velocity becomes zero in the core, as shown in Figs. 7 and 8. Thus, for $x < x_e$, there is a source region in which the superposed flow rate is greater than that entrained by the disks and, as a consequence, the radial component of velocity is everywhere positive. For $x > x_e$, where the superposed flow rate is less than that entrained by the disks, recirculation occurs and the radial component of velocity in the core is negative.

The computed moment coefficient for these three cases showed very little effect of flow rate (as also found experimentally by Daniels et al., 1991), and were within 1 percent of the average value, which was $C_m = 0.0049$. It is interesting to compare this moment coefficient with both the Morse correlation, given by Eq. (1.1), and the free-disk correlation given by Owen and Rogers (1989) where

$$C_{m,fd} = 0.491(\log_{10} Re_\phi)^{-2.58} \quad (4.3)$$

For $Re_\phi = 6.8 \times 10^5$, the average rotational Reynolds number, these two correlations give $C_m = 0.050$ and 0.052 , respectively. It should be remembered, however, that Morse's correlation was obtained for contrarotating disks with a *stationary* shroud, for $Re_\phi \geq 10^6$ and for zero superposed flow. It appears to matter little whether the shroud is rotating or whether there is a superposed flow. For all these cases, the moment coefficient for the contrarotating disks is within a few percent of the free-disk value.

5 Conclusions

For the case of zero superposed flow, laminar computations show a Batchelor-type flow structure: Radial outflow occurs in the boundary layers on the disks and inflow occurs in a thin shear layer in the midplane; between the shear layer and the boundary layers are two contrarotating cores of fluid. Turbulent computations and experimental measurements show Stewartson-type flow: between the boundary layers there is a single interior core in which rotation is weak. The flow in the core was always found to be turbulent (even for local Reynolds numbers as low as $x^2 Re_\phi = 2 \times 10^4$), but experimental measurements showed that the flow in the boundary layers remained laminar up to $x^2 Re_\phi = 1.1 \times 10^5$, and fully turbulent flow occurred for $x^2 Re_\phi \geq 1.7 \times 10^5$. The turbulence model exhibited premature transition but, for fully turbulent flow, there was good agreement between the computed and measured velocities.

For the case of a superposed radial outflow, with $0.0506 \leq \lambda_T \leq 0.199$, there is a source region, the radial extent of which can be estimated using the free-disk entrainment rate. Inside the source region, the radial component of velocity is everywhere positive; outside, recirculation occurs with radially inward flow in the interior core. Agreement between the turbulent computations and measured velocities was mainly

good, apart from some of the radial components of velocity at small radii where the measurements showed that the flow was skewed toward the downstream disk. The superposed flow had a negligible effect on the computed moment coefficients, which were a few percent lower than the equivalent free-disk value.

The work described above was carried out for $\Gamma = -1$. The effect of varying Γ in the range $-1 \leq \Gamma \leq 0$ is described by Kilic et al. (1994a, b, c).

Acknowledgments

The authors wish to thank the UK Ministry of Defence and the Science and Engineering Research Council (SERC) for supporting the work described in this paper; in particular, the Meiko parallel computer and much of the TSI LDA system was provided by SERC. We also wish to thank the Turkish Government and the University of Uludag, Bursa, for providing financial support for Dr. Kilic.

References

- Batchelor, G. K., 1951, "Note on a Class of Solutions of the Navier-Stokes Equations Representing Steady Rotationally-Symmetric Flow," *Quart. J. Mech. Appl. Math.*, Vol. 4, pp. 29-41.
- Daniels, W. A., Johnson, B. V., and Graber, D. J., 1991, "Aerodynamic and Torque Characteristics of Enclosed Co/counter Rotating Disks," *ASME JOURNAL OF TURBOMACHINERY*, Vol. 113, pp. 67-74.
- Daily, J. W., and Necc, R. E., 1960, "Chamber Dimension Effects on Induced Flow and Frictional Resistance of Enclosed Rotating Disks," *ASME Journal of Basic Engineering*, Vol. 82, pp. 217-232.
- Daily, J. W., Ernst, W. D., and Asbedian, V. V., 1964, "Enclosed Rotating Disks With Superimposed Throughflow," Dept. Civil Engng., Hydrodyn. Lab, MIT, Cambridge, MA, Rep. No. 64.
- Dijkstra, D., and van Heijst, G. J. F., 1983, "The Flow Between Two Finite Rotating Disks Enclosed by a Cylinder," *J. Fluid Mech.*, Vol. 128, pp. 123-154.
- Gan, X., 1991, "Velocity Measurement Between Rotating Discs," Report No. 2180, School of Mechanical Engineering, University of Bath, United Kingdom.
- Itoh, M., Yamada, Y., and Nishioka, K., 1985, "Transition of the Flow Due to an Enclosed Rotating Disk," *Trans. Japan Soc. Mech. Eng.*, Vol. 51, pp. 452-460 [in Japanese].
- Itoh, M., Yamada, Y., Imao, S., and Gonda, M., 1992, "Experiments on Turbulent Flow Due to an Enclosed Rotating Disk," *Exp. Thermal Fluid Science*, Vol. 5, pp. 359-368.
- Kilic, M., Gan, X., and Owen, J. M., 1994a, "Transitional Flow Between Contra-rotating Discs," *J. Fluid Mech.*, Vol. 281, pp. 119-135.
- Kilic, M., Gan, X., and Owen, J. M., 1994b, "Superposed Flow Between Two Discs Contra-rotating at Differential Speeds," *Int. J. Heat Fluid Flow*, Vol. 15, pp. 438-446.
- Kilic, M., Gan, X., and Owen, J. M., 1994c, "Turbulent Flow Between Two Discs Contra-rotating at Differential Speeds," *ASME Paper 94-GT-54*; accepted for publication in the *ASME JOURNAL OF TURBOMACHINERY*.
- Lam, C. K. G., and Bremhorst, K. A., 1981, "Modified Form of the $k-\epsilon$ Model for Predicting Wall Turbulence," *ASME Journal of Fluids Engineering*, Vol. 103, pp. 456-460.
- Lonsdale, G., 1988, "Solution of a Rotating Navier-Stokes Problem by a Nonlinear Multigrid Algorithm," *J. Comp. Phys.*, Vol. 74, pp. 177-190.
- Morse, A. P., 1988, "Numerical Prediction of Turbulent Flow in Rotating Cavities," *ASME JOURNAL OF TURBOMACHINERY*, Vol. 110, pp. 202-212.
- Morse, A. P., 1991a, "Assessment of Laminar-Turbulent Transition in Closed Disk Geometries," *ASME JOURNAL OF TURBOMACHINERY*, Vol. 113, pp. 131-138.
- Morse, A. P., 1991b, "Application of a Low Reynolds Number $k-\epsilon$ Turbulence Model to High-Speed Rotating Cavity Flows," *ASME JOURNAL OF TURBOMACHINERY*, Vol. 113, pp. 98-105.
- Owen, J. M., and Rogers, R. H., 1989, *Flow and Heat Transfer in Rotating-Disc Systems. Vol. 1: Rotor-Stator Systems*, Research Studies Press, United Kingdom; Wiley Inc., USA.
- Schlichting, H., 1979, *Boundary-Layer Theory*, McGraw-Hill, New York.
- Stewartson, K., 1953, "On the Flow Between Two Rotating Coaxial Discs," *Proc. Camb. Phil. Soc.*, Vol. 49, pp. 333-341.
- Vaughan, C. M., Gilham, S., and Chew, J. W., 1989, "Numerical Solutions of Rotating Disc Flows Using a Non-linear Multigrid Algorithm," *Proc. 6th Int. Conf. Num. Meth. Lam. Turb. Flow*, Swansea, Pineridge Press, United Kingdom, pp. 66-73.
- Wilson, M., Kilic, M., and Owen, J. M., 1992, "Computation of Flow in Rotating Disc Systems," presented at the ICHMT Int. Symp. on Heat Transfer in Turbomachinery, Athens.
- Zanbergen, P. J., and Dijkstra, D., 1987, "Von Karman Swirling Flows," *Ann. Rev. Fluid Mech.*, Vol. 19, pp. 465-491.

Table A.1

Φ	Γ_z	Γ_r	S_Φ
v_z	$2\mu_{eff} - \mu$	μ_{eff}	$-\frac{\partial}{\partial z}(p + \frac{2}{3}\rho k)$ $+ \frac{1}{r} \frac{\partial}{\partial r}(r\mu_t \frac{\partial v_r}{\partial z})$ $-\frac{2}{3} \frac{\partial}{\partial z}(\mu_{eff} \nabla \cdot \mathbf{v})$
v_r	μ_{eff}	$2\mu_{eff} - \mu$	$-\frac{\partial}{\partial r}(p + \frac{2}{3}\rho k)$ $-(2\mu_{eff} - \mu) \frac{v_r}{r^2}$ $+ \frac{\rho v_\phi^2}{r} + \frac{\partial}{\partial z}(\mu_t \frac{\partial v_z}{\partial r})$ $-\frac{2}{3} \frac{\partial}{\partial r}(\mu_{eff} \nabla \cdot \mathbf{v})$
v_ϕ	μ_{eff}	μ_{eff}	$-\frac{\rho v_r v_\phi}{r} - \mu_{eff} \frac{v_\phi}{r^2}$ $-\frac{v_\phi}{r} \frac{\partial \mu_t}{\partial r}$
k	$\mu + \frac{\mu_t}{\sigma_k}$	$\mu + \frac{\mu_t}{\sigma_k}$	$P - \rho \epsilon - D$
ϵ	$\mu + \frac{\mu_t}{\sigma_\epsilon}$	$\mu + \frac{\mu_t}{\sigma_\epsilon}$	$\frac{\epsilon}{k}(c_{\epsilon 1} P - c_{\epsilon 2} \rho \epsilon)$ $+ E - F$

APPENDIX A

Conservation Equations

The axisymmetric equations of motion and continuity can be written in the following form using a cylindrical-polar coordinate system (r, ϕ, z) with velocity components (V_r, V_ϕ, V_z) :

$$\frac{\partial}{\partial z}(\rho V_z \Phi) + \frac{1}{r} \frac{\partial}{\partial r}(r \rho V_r \Phi) = \frac{\partial}{\partial z} \left(\Gamma_z \frac{\partial \Phi}{\partial z} \right) + \frac{1}{r} \frac{\partial}{\partial r} \left(r \Gamma_r \frac{\partial \Phi}{\partial r} \right) + S_\Phi$$

$$\frac{1}{r} \frac{\partial}{\partial r}(\rho r V_r) + \frac{\partial}{\partial z}(\rho V_z) = 0$$

where Φ represents the components of velocity V_r, V_ϕ, V_z and the turbulence quantities k and ϵ . S_Φ contains all source terms including the pressure gradient. Γ_r and Γ_z are the effective diffusivities comprising both laminar and turbulent components. The relevant expressions are given in Table A.1. The boundary conditions for $V_r, V_\phi,$ and V_z are specified in Section 2. For k and ϵ , the following values were used: For

all solid boundaries, $k = \epsilon = 0$; between the shrouds,

$$\frac{\partial k}{\partial r} = \frac{\partial \epsilon}{\partial r} = 0;$$

on the midplane (for $C_w = 0$),

$$\frac{\partial k}{\partial z} = \frac{\partial \epsilon}{\partial z} = 0;$$

for the central inlet (for $C_w > 0$),

$$k = 10^{-4} V_z^2, \quad \epsilon = \frac{k^2}{100\nu}$$

(The conditions for the inlet for $C_w > 0$ are the same as those used by Morse 1989).

APPENDIX B

Low-Reynolds-Number $k-\epsilon$ Turbulence Model

The terms given in Table B.1 are based on the model used by Morse (1988, 1991a, b), in which D , E , and F are extra terms added to the high-Reynolds-number form of the model to represent near-wall behavior. The production rate P of turbulence kinetic energy (k) is given by:

$$P = \mu_t \left[2 \left(\left(\frac{\partial V_z}{\partial z} \right)^2 + \left(\frac{\partial V_r}{\partial r} \right)^2 + \left(\frac{V_r}{r} \right)^2 \right) + \left(\frac{\partial V_z}{\partial r} + \frac{\partial V_r}{\partial z} \right)^2 + \left(\frac{\partial V_\phi}{\partial z} \right)^2 + \left(r \frac{\partial}{\partial r} \left(\frac{V_\phi}{r} \right) \right)^2 \right]$$

The empirical coefficients appearing in the model are given by:

$$\begin{aligned} C_\mu &= 0.09; \quad C_{\epsilon 1} = 1.44; \\ C_{\epsilon 2} &= 1.92 - 0.43 \exp(-\text{Re}_t^2/36) \\ \sigma_k &= 1.0; \quad \sigma_\epsilon = 1.22 \end{aligned}$$

The turbulent viscosity includes a near-wall damping function f_μ where

$$\mu_t = C_\mu f_\mu \rho k^2 / \epsilon$$

The version of f_μ used by Morse for single-grid codes was found by the present authors to give convergence difficulties in the multigrid code. The problem was overcome by using a version of f_μ employed by Lam and Bremhorst (1981) where

$$f_\mu = \left[1 - \exp(-A_\mu \text{Re}_y) \right]^2 \left(1 + \frac{A_t}{\text{Re}_t} \right)$$

$$\text{Re}_t = \rho k^2 / \mu \epsilon$$

and

$$\text{Re}_y = \rho k^{1/2} y / \mu$$

For the computations presented in this paper, $A_\mu = 0.029$, $A_t = 25$, and f_μ was never allowed to exceed unity.

Table B.1

$D = 2\mu \left[\left(\frac{\partial k^{1/2}}{\partial z} \right)^2 + \left(\frac{\partial k^{1/2}}{\partial r} \right)^2 \right]$
$E = \frac{2\mu\mu_t}{\rho} \left[\left(\frac{\partial^2 v_r}{\partial z^2} \right)^2 + \left(\frac{\partial^2 v_\phi}{\partial z^2} \right)^2 \right]$ $+ \frac{2\mu\mu_t}{\rho} \left[\left(\frac{\partial^2 v_z}{\partial r^2} \right)^2 + \left(\frac{\partial^2 v_\phi}{\partial r^2} \right)^2 \right]$
$F = 2\mu \left[\left(\frac{\partial \epsilon^{1/2}}{\partial z} \right)^2 + \left(\frac{\partial \epsilon^{1/2}}{\partial r} \right)^2 \right]$

Table B.2

$\overline{\rho(v_r')^2} = \frac{2}{3}\rho k - 2\mu_t \frac{\partial v_r}{\partial r}$	$\overline{\rho v_r' v_\phi'} = -\mu_t r \frac{\partial}{\partial r} \left(\frac{v_\phi}{r} \right)$
$\overline{\rho(v_\phi')^2} = \frac{2}{3}\rho k - 2\mu_t \frac{v_r}{r}$	$\overline{\rho v_r' v_z'} = -\mu_t \left(\frac{\partial v_r}{\partial z} + \frac{\partial v_z}{\partial r} \right)$
$\overline{\rho(v_z')^2} = \frac{2}{3}\rho k - 2\mu_t \frac{\partial v_z}{\partial z}$	$\overline{\rho v_\phi' v_z'} = -\mu_t \frac{\partial v_\phi}{\partial z}$

The values for A_μ and A_t , which differ from those used by Lam and Bremhorst, were chosen to give good agreement with velocity profiles and moment coefficients obtained from measurements in a number of rotor-stator systems for $10^5 \leq \text{Re}_\phi \leq 4.4 \times 10^6$ (see Daily and Nece (1960), Daily et al. (1964), Itoh et al. (1985, 1992) and Gan (1991)). Once appropriate values had been selected, the turbulence model was tested on a wide range of rotating-disk systems including the free disk, rotor-stator systems, rotating cavities, and contrarotating disks, with and without superposed flow, up to $\text{Re}_\phi = 10^7$. No convergence problems were experienced, and the turbulence model produced results that were in good agreement with available data. Although other models have been, and are being, tested, it is the authors' intention to apply turbulence models to, rather than develop models for, rotating-disk systems.

The approximations for the Reynolds stresses $\rho V_i' V_j'$ appearing in the time-averaged Navier-Stokes equations for axisymmetric flow are given in Table B.2.